Bio-Inspired Design for Mechanical and Biomechanical Applications

Bio-Inspired Design for Mechanical and Biomechanical Applications

A DISSERTATION PRESENTED
BY
AUGUST G. DOMEL
TO
THE SCHOOL OF ENGINEERING AND APPLIED SCIENCES

IN PARTIAL FULFILLMENT OF THE REQUIREMENTS
FOR THE DEGREE OF
DOCTOR OF PHILOSOPHY
IN THE SUBJECT OF
ENGINEERING SCIENCES

HARVARD UNIVERSITY
CAMBRIDGE, MASSACHUSETTS
DECEMBER 2018

Dissertation Advisor: Professor Katia Bertoldi August G. Domel

Bio-Inspired Design for Mechanical and Biomechanical Applications

ABSTRACT

Over the course of billions of years, nature has evolved materials, structures, and morphologies that exhibit a wide range of unique functionalities. Some of these traits are of particular interest to scientists and engineers because inspiration can be drawn from these traits, and applied to a wide range of man-made systems. Thus, bio-inspired design is of great interest to researchers in hopes of improving upon man-made innovations. Bio-inspired design comes in all shapes and forms, but the present thesis focuses on inspiration from two specific aquatic animals: sharks and octopuses.

First, inspiration is taken from the morphology of the skin of sharks to design surfaces and structures for engineering applications. Using a combination of 3D printing, experiments, and numerical simulations, this thesis shows that the tiny, tooth-like structures (denticles) that cover the skin of a shark can be used to enhance lift and reduce drag when placed on an airfoil as a bio-inspired, low-profile vortex generator. In addition, this thesis shows that whole surfaces of these denticles with the right set of geometric parameters can be used to reduce drag and improve efficiency in dynamically moving surfaces. Through this bio-inspired design process, insights into the structure and purpose of the denticles on a living shark are attained as well.

Second, inspiration is taken from cephalopods, specifically octopuses, to design an extremely versatile soft gripping robot for a wide range of applications. With the novel bending and suction design presented for the soft robot, a wide range of objects can be grasped and manipulated, from flat rigid objects to heavier curved objects.

Throughout the course of this thesis, I will demonstrate that using a combination of various manufacturing techniques, experiments, and numerical simulations, the bio-inspired designs presented here not only have important applications in man-made systems such as aerial devices (including airplanes, wind turbines, and drones) and robotics for manufacturing, but also even give insight into understanding their functionality for the animal itself.

Contents

Listing of Figures

sensor with the substrate surfaces fastened on it. We set the initial position of the actuator to ensure the suckers attachment on the surface. A robotic arm fixed to the base of the actuator was programmed to move straight upwards at a constant speed of 0.1 mm/s until the suckers completely detached from the substrate surface. Vertical peeling forces plotted against time of (B) α = 9° actuator and (C) α = 4.5° actuator on surfaces of various roughness (R_a: < 1 μm, 20 μm, 200 μm). Side-view photographs (D) showing the sequential pull-off of an α = 4.5° actuator with its suckers actuated from a smooth planar surface and its corresponding load-displacement curve (E). (F) The attachment forces of the α = 9° actuator with stiff suckers (Young‘s Modulus: 660 kPa) and flexible suckers (Young's Modulus: 260 kPa) and α = 4.5° actuator with flexible suckers on planar surfaces of various roughness (R_a: < 1 μm, 20 μm, 200 μm). Scanning a wide range of input pressures with the α = 4.5° actuator permits the identification of the optimal input pressure (and therefore curvature) for maximizing pull-off force from non-planar substrates (G). The vertical dashed line indicates the “critical” pneumatic pressure values for maximizing the pull-off forces of the α = 4.5° actuator for the curvature of this specific surface (260 mm^{-1}). Side-view photographs showing the sequential pull-off of an α = 4.5° actuator with its suckers actuated from a smooth curved surface (H) and its corresponding load-displacement curve (I), which is very similar to that shown in (E). 224

DEDICATED TO MY FAMILY.

Acknowledgments

Throughout the course of my Ph.D., many people have given me invaluable guidance and support. There are far too many people to name who have provided support along the way, but I want to take this chance to thank everyone for their help and generosity, including Harvard University, my lab mates, my fellow cohort, Harvard's John A. Paulson School of Engineering and Applied Sciences, the Wyss Institute, the Graduate School of Arts and Sciences, and Dudley House. I would also like to give a big thanks to all of my collaborators on my various projects, including Li Wen, Mehdi Saadat, Hossein Haj-Hariri, Ning An, Gino Domel, and Zhexin Xie. I would also like to thank my thesis committee member Prof. Zhigang Suo for his feedback and guidance, especially in the early stages of my thesis. In addition to these great researchers, I would like to take the time to thank a few more people in particular.

I was truly blessed to have had the opportunity to work with Prof. Katia Bertoldi throughout my Ph.D. She is not only a magnificent researcher and engineer, but also a great mentor and person. Her guidance throughout my Ph.D. was invaluable, and she always helped me through the more challenging points. She was always so understanding, kind, motivating, and always pushed me to be the best student I could be. Without her, absolutely none of this would have been possible. In addition, we worked very closely with Prof. George Lauder. I would like to thank him for everything as well. He, too, was not only a brilliant researcher and scientist, but also was a great mentor and person. Working with

Prof. Lauder was a true pleasure and great experience, and I consider myself very lucky to have had the chance to work with him. I would also like to thank James Weaver as well. His guidance and help in my various projects was essential, and he too was both a great researcher and in general a great person to work with. I really believe that I was very lucky to have met, been advised by, and worked with all of these brilliant and wonderful people – thanks for everything!

Finally, I would like to thank my family for all of their support in this process. Everything that I have done would not have been possible without the support of my loving family, including my father, Gus Domel, my mother, Gina Domel, my sister, Tommasina, and my three brothers, Antonio, Gino, and Reno. I would like to additionally thank Sarah McGough for all of her love and support over the past several years.

1

Introduction

Nature, over the course of billions of years, has developed materials and structures that have unique and interesting properties. Because nature has had an enormous head start on the design process compared to human innovation, it is prudent to look to the structures and materials designed by nature in order to provide design insights for the development of novel technologies.

Taking inspiration from nature to inform and direct design is something that scientists and engineers have been successfully achieving and utilizing for many years (1-18). For example, for man-made aerial systems, bio-inspiration has been widely studied by engineers to improve aerodynamics (4-5). Specifically, the tubercles on the humpback whale's fin were shown to delay stall when placed on an airfoil compared to an analogous airfoil without tubercles (4). In addition, the feathers of swifts have been shown to help reduce flow separation on an airfoil in certain flow regimes (5). Outside of aerodynamics, bio-inspiration has been used for many other applications as well (6-11). For example, new tough hybrid materials have been developed by imitating natural composites that exhibit extreme toughness (6). Nature-inspired surface coatings for metals have also shown great promise for protecting against corrosion (7-10). Furthermore, to

create novel and better adhesive discs, scientists and engineers have looked to the highly modified dorsal fin of the remora for design inspiration (11). It is clear from all of these examples that bio-inspiration has an important place in the designing of future structures and materials.

Throughout this thesis, bio-inspiration will be used to help design for various engineering applications. Specifically, for the first portion of this thesis, inspiration will be drawn from the tooth-like structures (denticles) that cover the skin of a shark to design new structures and surfaces that can enhance the performance of man-made aerial devices and other dynamic systems. Recently, shark skin-inspired surfaces have been studied for their drag reducing properties. 3D printed parameterized models inspired by shark skin and even very simplified riblet surfaces modeled after shark skin have been shown to have great hydrodynamic benefits (12-18). Expanding upon these initial findings, in this thesis, shark skin-inspired structures and surfaces are designed to greatly enhance the performance of man-made mechanical and biomechanical systems in novel ways not previously considered (Chapters 2-4). It will even be discussed how the findings of these various designs have implications in new ways of understanding the complex and possibly multifunctional purpose that the morphology of these denticles serve a shark in locomotion (Chapters 2-4).

For the last portion of this thesis, inspiration will be drawn from octopus arms to create a multi-functional gripping soft robot. Octopuses can perform very complex tasks, including catching prey of many shapes and sizes and even retrieving objects from constrained environments (19-23). They are able to do

this by combining the highly coordinated bending motion of their arms with the integration of the array of suckers on their arms (19-23). Because of this, they often serve as a model for the development of robust soft robotic prototypes (24-31). In Chapter 5 of this thesis, it will be shown how the novel combination of bending and suction can be used to create an effective octopus arm-inspired soft robot. In addition, a range of possible taper angles, based on measurements acquired from several octopus species, will be studied to understand how the taper angle affects two very important aspects of the soft robot's performance, bending curvature and applied bending force.

Over the course of this thesis, one will see that the research detailed here looks to these different aspects of nature (specifically, sharks and octopuses) to arrive at designs for different structures, surfaces, and robots that not only offer novel and strong solutions for various engineering applications, but also provide insight into understanding the complex morphologies and functions of these different parts of the animals themselves. This is done with a combination of numerical and experimental approaches and by utilizing different 3D printing and molding techniques.

1.1 REFERENCES

[1] Bar-Cohen, Y. (2005). Biomimetics. *Biomimetics*, pp 495–513. Boca Raton, FL: CRC Press.

[2] Benyus, J. M. (1997). Biomimicry. *Innovation Inspired by Nature*. New York: Harper Collins.

[3] Patek, S. N. (2014). Biomimetics and evolution. *Science,* 345, 1448–1449.

[4] Fish, F. E., Weber, P. W., Murray M. M., Howle, L. E. (2011). The tubercles on humpback whales' flippers: application of bio-inspired technology. *Integr Comp Biol*, 51(1), 203–213.

[5] van Bokhorst, E., de Kat, R., Elsinga, G. E., Lentink, D. (2015). Feather roughness reduces flow separation during low Reynolds number glides of swifts. *J Exp Biol,* 218(Pt 20), 3179–3191.

[6] Munch, E., Launey, M. E., Alsem, D. H., Saiz, E., Tomsia, A. P., and Ritchie, R. O. (2008). Tough, bio-inspired hybrid materials. *Science*, 322(5907), 1516–1520.

[7] Yao, X., Song, Y., and Jiang, L. (2011). Applications of bio-inspired special wettable surfaces. *Advanced Materials*, 23(6), 719–734.

[8] Hintze, P. E., and Calle, L. M. (2006). Electrochemical properties and corrosion protection of organosilane self-assembled monolayers on aluminum 2024-T3. *Electrochimica Acta*, 51(8-9), 1761–1766.

[9] Sinapi, F., Forget, L., Delhalle, J., and Mekhalif, Z. (2003). Self-assembly of (3-mercaptopropyl)trimethoxysilane on polycrystalline zinc

substrates towards corrosion protection. *Applied Surface Science*, 212-213, 464–471.

[10] Zamborini, F. P., & Crooks, R. M. (1998). Corrosion Passivation of Gold byn-Alkanethiol Self-Assembled Monolayers: Effect of Chain Length and End Group. *Langmuir: The ACS Journal of Surfaces and Colloids*, 14(12), 3279–3286.

[11] Wang, Y., Yang, X., Chen, Y., Wainwright, D. K., Kenaley, C. P., Gong, Z., … Wen, L. (2017). A biorobotic adhesive disc for underwater hitchhiking inspired by the remora suckerfish. *Science Robotics*, 2(10), eaan8072.

[12] Oeffner, J., Lauder, G. V. (2012). The hydrodynamic function of shark skin and two biomimetic applications. *J Exp Biol,* 215, 785–795.

[13] Lauder, G. V., et al. (2016). Structure, biomimetics, and fluid dynamics of fish skin surfaces. *Physical Review Fluids,* 1(6). doi:10.1103/physrevfluids.1.060502.

[14] Wen, L., Weaver, J. C., Lauder, G. V. (2014). Biomimetic shark skin: design, fabrication and hydrodynamic function. *J Exp Biol,* 217, 1656–1666.

[15] Bechert, D. W., Bruse, M., Hage, W. (2000). Experiments with three-dimensional riblets as an idealized model of shark skin. *Exp Fluids,* 28, 403–412.

[16] Dean, B., Bhushan, B. (2010). Shark-skin surfaces for fluid-drag reduction in turbulent flow: a review. *Philos Trans A Math Phys Eng Sci,* 368, 4775–4806.

[17] Fu, Y. F., Yuan, C. Q., and Bai, X. Q. (2017). Marine drag reduction of

shark skin inspired riblet surfaces. *Biosurface and Biotribology,* 3.1, 11-24.

[18] Sareen, A., et al. (2014). Drag reduction using riblet film applied to airfoils for wind turbines. *Journal of Solar Energy Engineering,* 136.2, 021007.

[19] Vail, A. L., Manica, A., Bshary, R. (2013). Referential gestures in fish collaborative hunting. *Nat. Commun.*, 4, 1765.

[20] Richter, J. N. , Hochner, B., Kuba, M. J. (2015). Octopus arm movements under constrained conditions: adaptation, modification and plasticity of motor primitives. *J. Exp. Biol.,* 218, 1069-1076.

[21] Smith, A. (1996). Cephalopod sucker design and the physical limits to negative pressure. *J. Exp. Biol.,* 199, 949-958.

[22] Sumbre, G., Gutfreund, Y., Fiorito, G., Flash, T., Hochner, B. (2001). Control of octopus arm extension by a peripheral motor program. *Science,* 293, 1845-1848.

[23] Margheri, L., Laschi, C., Mazzolai, B. (2012). Soft robotic arm inspired by the octopus: I. From biological functions to artificial requirements. *Bioinspir. Biomim.,* **7**, 025004.

[24] Calisti, M., Giorelli, M., Levy, G., Mazzolai, B., Hochner, B., Laschi, C., Dario, P. (2011). An octopus-bioinspired solution to movement and manipulation for soft robots. *Bioinspir. Biomim.,* 6, 036002.

[25] Mazzolai, B., Margheri, L., Cianchetti, M., Dario, P., Laschi, C. (2012). Soft-robotic arm inspired by the octopus: II. From artificial requirements to innovative technological solutions. Bioinspir. Biomim., 7, 025005.

[26] Laschi, C., Cianchetti, M., Mazzolai, B., Margheri, L., Follador, M., Dario, P. (2012). Soft robot arm inspired by the octopus. *Adv. Robot.,* 26, 709-727.

[27] Pikul, J. H., Li, S., Bai, H., Hanlon, R. T., Cohen, I., Shepherd, R. F. (2017). Stretchable surfaces with programmable 3D texture morphing for synthetic camouflaging skins. *Science,* 358, 210-214.

[28] Walker, I. D., Dawson, D. M., Flash, T., Grasso, F. W., Hanlon, R. T., Hochner, B., Kier, W. M., Pagano, C. C., Rahn, C. D., Zhang, Q. M. (2005). Continuum robot arms inspired by cephalopods*. Proceedings of the 2005 SPIE Conference on Unmanned Ground Vehicle Technology IV*, 5804, 303-315.

[29] Cianchetti, M., Calisti, M., Margheri, L., Kuba, M., Laschi, C. (2015). Bioinspired locomotion and grasping in water: the soft eight-arm OCTOPUS robot. *Bioinspir. Biomim.*, 10, 035003.

[30] Katzschmann, R. K., Marchese, A. D., Rus, D. (2015). Autonomous object manipulation using a soft planar grasping manipulator. *Soft Robotics*., 2, 155-164.

[31] Marchese, A. D., Rus, D. (2016). Design, kinematics, and control of a soft spatial fluidic elastomer manipulator. *Int. J. Robot*., Res. 35, 840-869.

This project was done in collaboration with Mehdi Saadat, under the supervision of Prof. Katia Bertoldi, Prof. George Lauder, James Weaver, and Dean Hossein Haj-Hariri. This work has already been published, and the relevant citation for the work is: Domel, A. G., Saadat, M., Weaver, J. C., Haj-Hariri, H., Bertoldi, K., & Lauder, G. V. (2018). Shark skin-inspired designs that improve aerodynamic performance. Journal of the Royal Society, Interface / the Royal Society, 15(139).

2

Shark Skin-Inspired Designs that Improve Aerodynamic Performance

2.0 ABSTRACT

There have been significant efforts recently aimed at improving the aerodynamic performance of airfoils through the modification of their surfaces. Inspired by the drag reducing properties of the tooth-like denticles that cover the skin of sharks, we describe here experimental and simulation-based investigations into the aerodynamic effects of novel denticle-inspired designs placed along the suction side of an airfoil. Through parametric modeling to query a wide range of different designs, we discovered a set of denticle-inspired surface structures that achieve simultaneous drag reduction and lift generation on an airfoil, resulting in lift-to-drag ratio improvements comparable to the best-reported for traditional low-profile vortex generators and even outperforming these existing designs at low angles of attack with improvements of up to 323%. Such behavior is enabled by two concurrent mechanisms: (*i*) a separation bubble in the denticle's wake altering the flow pressure distribution of the airfoil to enhance suction and (*ii*) streamwise vortices that replenish momentum loss in the boundary layer due to skin friction. Our findings not only open new avenues for improved aerodynamic design, but also provide new perspective on the role of the complex and potentially multifunctional morphology of shark denticles for increased swimming efficiency.

2.1 INTRODUCTION

Systems that move suspended within a fluid, such as airplanes, wind turbines, drones and helicopters, all benefit from increased lift-to-drag ratios which results in lower energy consumption (1). Motivated by this need, two main strategies have been proposed to maximize the lift and minimize the drag. On one hand, several active flow control methods, which involve the addition of auxiliary power into the system, have been demonstrated for both drag reduction and lift augmentation (2-6). On the other hand, it has also been shown that passive flow control strategies based on geometric modifications are capable of altering lift and drag (7-12, 13-17). These include vortex generators (7-13), Gurney flaps (13,14,15) and winglets (16,17), which reduce drag and increase lift by passively altering the flow to favorably affect the pressure gradients along the airfoil. Although active methods typically yield better results than the passive ones, they require the supply of external energy and in fully automated systems, rely on complex sensor technology and algorithm development. By contrast, passive techniques are easy to implement and free from any kind of external energy requirements.

Nature, through the course of evolution, has arrived at structures and materials, whose traits often offer inspiration for the design of synthetic systems with unique properties (18,19,20). Specifically, biological systems have evolved a wide range of drag reducing mechanisms that have inspired the design of synthetic surfaces (18-27). Shark skin is one such example and is covered with rigid bony denticles (or scales) that exhibit a plate-like upper section with ridges,

which narrows to a thin neck that anchors into the skin (see Figure 2.1*A,B*). These intricate structures have inspired the development of several drag reducing surfaces (25), ranging from highly simplified ridge-like geometries [26,27] to complex 3D printed models that replicate the structural complexities of individual denticles [21-23]. These denticle-inspired surfaces have resulted in a drag reduction of 10% compared to corresponding smooth control surfaces (21-25).

Here, we focus on airfoils and study experimentally how 3D models of shark denticles arranged on their suction side can passively alter fluid flow. While previous studies have mostly only focused on the effect of shark denticles on drag reduction (21-27), here we demonstrate that the denticles can simultaneously enhance lift and reduce drag, resulting in large lift-to-drag ratios. We study the mechanisms leading to this behavior and find that shark denticles generate both a recirculation zone (in the form of a short separation bubble in the wake of the denticle) that alters the pressure distribution of the airfoil to enhance suction, as well as streamwise vortices that reduce drag by replenishing momentum to the flow which would otherwise be lost to skin friction. Guided by these observations, we developed a continuous streamlined geometric perturbation that utilizes these two mechanisms in a way that further enhances the lift-to-drag ratio.

2.2 METHODS

2.2.1 DESIGN OF AIRFOILS WITH SHARK DENTICLES

In this study we focused on a smooth airfoil, arrayed representative models of shark denticles on its suction side (upper surface), and investigated their effect on the aerodynamic performance of the system (see Figure 2.1).

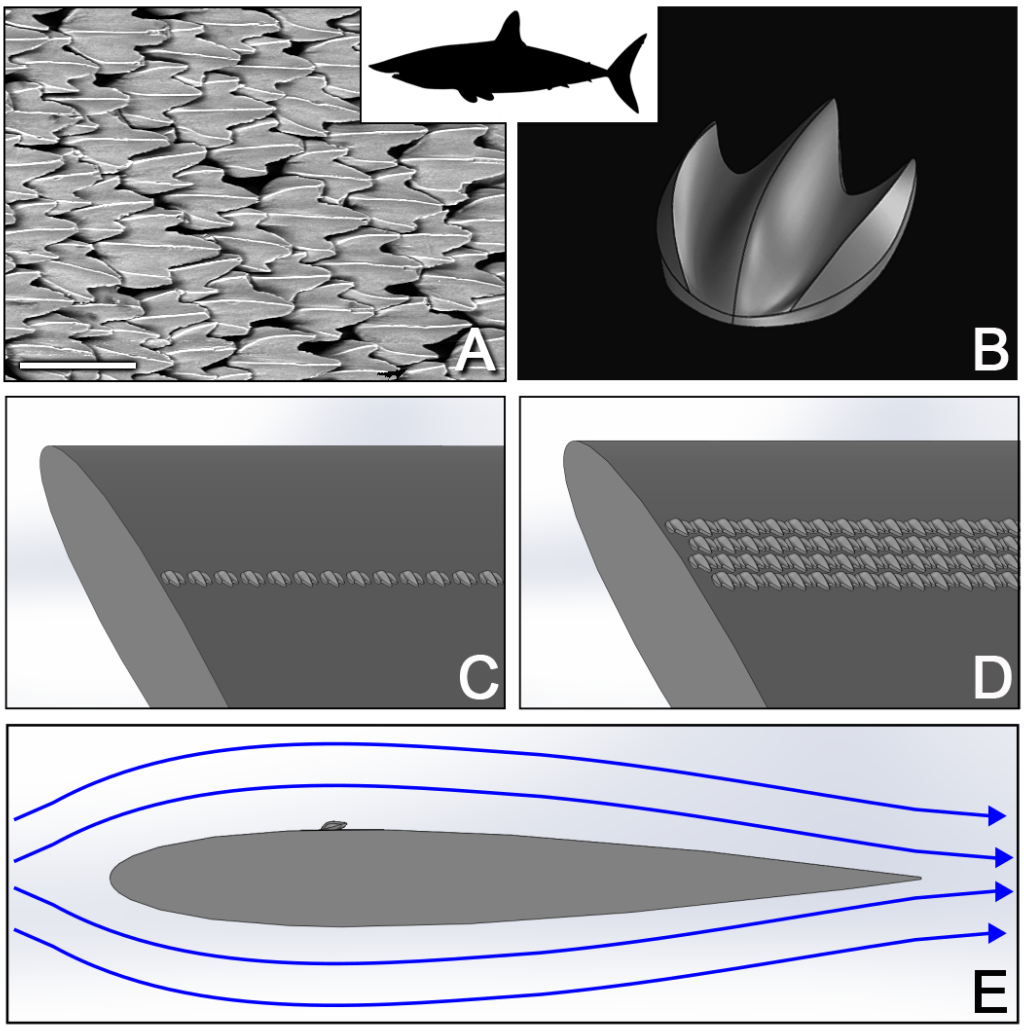

Figure 2.1: Inspiration, design and testing of shark denticle-inspired vortex generators. (A) Environmental scanning electron microscope (ESEM) image of denticles from the shortfin mako shark (scale bar: 200μm) used in this study and (B) its corresponding parametric 3D model. (C)-(D) These denticles were arranged in a wide range of different configurations on the suction side

of a NACA0012 airfoil, two examples of which are shown here. (E) All of the airfoils were then tested in fluid flow to evaluate the effect of the denticles on lift and drag.

More specifically, we considered a symmetric NACA0012 airfoil with aspect ratio W/L=2.8 (L=68mm being the chord length and W denoting the span length – see Section A.1 of Supporting Information for more details). We arranged on its suction side 3D representative models of a shark denticle based on micro-computed tomography (micro-CT) scans of denticles from *Isurus oxyrinchus* (23). In Figure 2.2 we show different views of the representative denticle model and indicate the key geometric parameters that define its shape: the chordwise length of the middle ridge (l_c), the chordwise length of the side ridges (l_r), the spanwise length between the outside ridges (l_s), the height of the middle ridge (h_1), the height of the side ridges (h_2), and the tilt angle (θ).

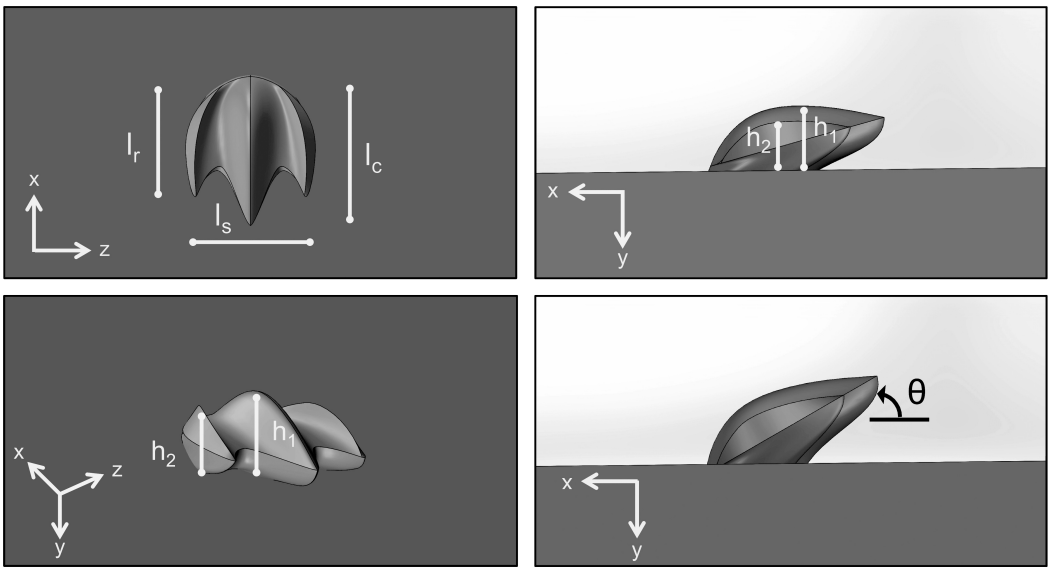

Figure 2.2: Representative model of the shark denticle. (A) Top, (B) side, and (C) isometric view of the representative model of the shark denticle used in this study, along with the corresponding geometric parameters. (D) A tilt angle of 15° was used for all foils except one.

In order to explore the parameter space as much as physically possible and to converge on a best design, we created 20 airfoils characterized by different arrangements (including either single or multiple rows of denticles), sizes, and tilt angles of these denticles (see Supporting Information Section A.1 for more details). Based on measurements of the shark denticles, in our study we kept l_c/l_s = 1.37, l_c/l_r = 1.25, h_1/h_2 = 1.40, and l_c/h_1 = 2.95 constant for all foils. All airfoils were fabricated from a transparent photopolymer (RGD81 - Stratasys Ltd, Eden Prairie, MN, USA) using an Objet Connex500 3D printer (see Figure 2.3 for images of all 3D printed foils). More details on the diversity of airfoil designs tested can be found in Supporting Information Section A.1.

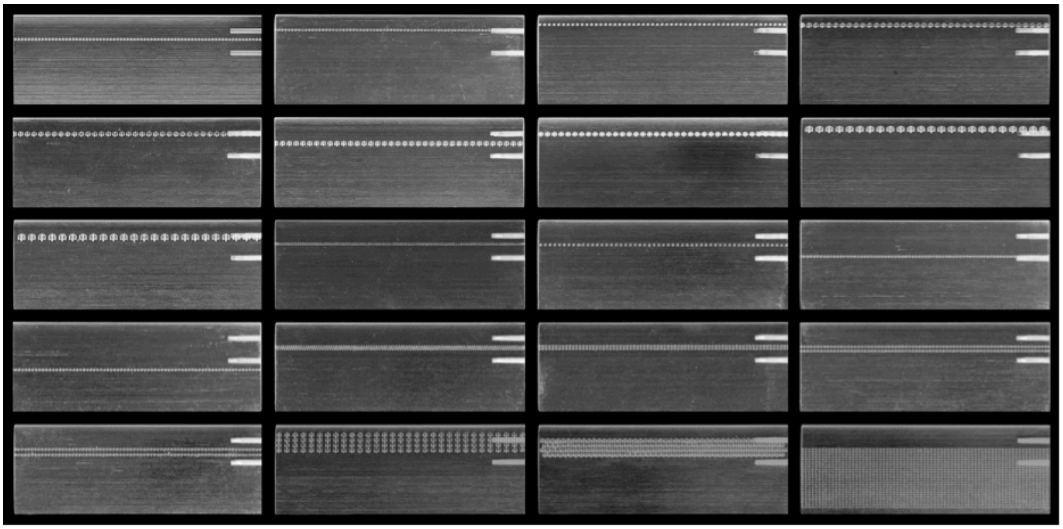

Figure 2.3: Image of all 20 shark denticle foils tested. The two holes on the upper right of each foil were used to attach the foil to the testing apparatus. A number of different denticle sizes, rows, and row positions were tested (see Supplemental Information Section A.1 for more details).

2.2.2 Experimental Testing

Given the relevant Reynolds number ranges for aerodynamic applications (<10,000 to >1,000,000) and the dimensional limitations of the 3D printer used to

fabricate our test models, these requirements necessitated the use of a water tank for measuring the performance metrics of our airfoils. Each foil's performance was tested in steady state within a water flow tank (kinematic viscosity υ=1x10^{-6} m^2/s) in the laminar regime with a flow speed of U=0.58m/s, which corresponds to a chord Reynolds number of $Re_c=UL/\upsilon \approx 4\text{x}10^4$ (21-23). The foils were tested at angles of attack, α, from 0° to 24° (post-stall and within the limits of the experimental setup) in increments of $\Delta\alpha$=2°. At each angle, the force experienced by the foils parallel to the flow, F_D, and perpendicular to the flow, F_L, were recorded. From these measurements, the dimensionless coefficients of lift (C_L) and drag (C_D) were calculated as

$$C_L = \frac{2F_L}{\rho A U^2} \ , \ \ C_D = \frac{2F_D}{\rho A U^2} \qquad [2.1]$$

where A=W×L= 12,920mm^2 is the airfoil planform area (regardless of foil orientation) and $\rho \approx 1000$kg/m^3 is the density of water. Since at the moderate Reynolds number considered in this study the force measurements can be quite sensitive to the different parameters of the experiment (28), at least 6 trials were conducted for each of the 20 foils and each presented data point is the average of many tests (with standard error reported). For some foils discussed in this main text, Particle Image Velocimetry (PIV) was also conducted using this water tank. In order to perform the PIV measurements, 10g of neutrally-buoyant, silver-covered glass particles were added to the water tank, and a 10W continuous-wave argon-ion laser (Innova 300, Coherent Laser Group, CA, USA) was focused at the mid-point of the foil. With this 1-2mm thick laser sheet shining on the center of the foil, high speed videos at 2000Hz and at a resolution of 1024 pixels by 1024

pixels were taken using a Photron mini-UX100 high-speed video camera. The videos were then finally post-processed using LaVision's DaVis software (v 7.3.1) to obtain the streamlines. See Supporting Information Section A.2 for more details on the experimental methods.

2.3 Results and Discussion

As previously shown in many studies focused on vortex generators (8,11,12,29), we find that both the geometry of the denticles and their arrangement have a profound effect on the aerodynamic response of the airfoils (Figures B.9-S26). While most foils behaved roughly similar to the denticle-free control, a few of them exhibited significantly enhanced performance (see Supporting Information Section A.3 for details). In Figure 2.4 we report results of the experiments for the best performing foil, which comprises a single row of denticles (each of which covers a footprint of roughly 2mm by 2mm and has a middle-ridge height of 0.7mm) placed at 26% along the chord and with a spanwise separation of 1mm (see Figure 2.1*C*). Note that the 26% chordwise placement is consistent with previous work on NACA0012 airfoils, which has shown that the minimum pressure happens right after this location, making the flow susceptible to separation (29).

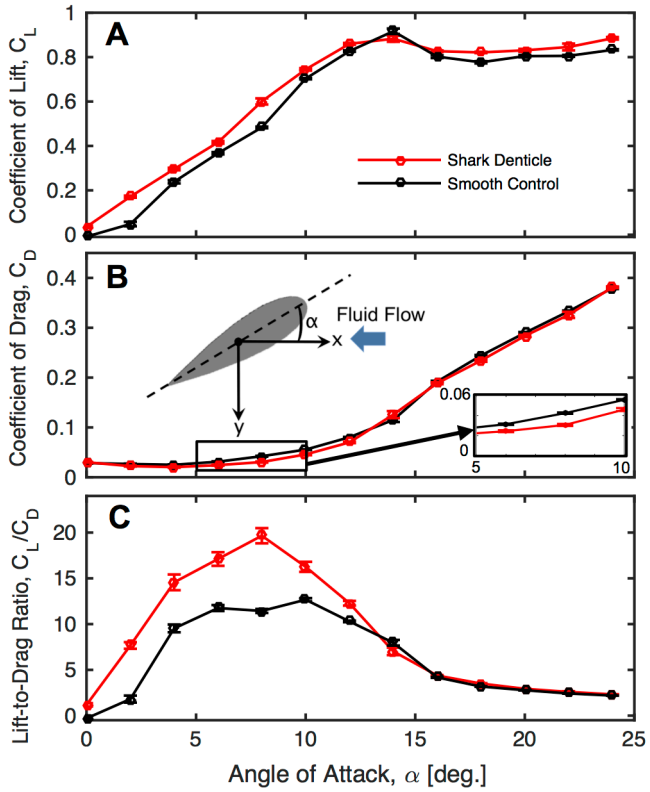

Figure 2.4: Experimental results for the best shark denticle airfoil. Evolution of (A) lift coefficient, (B) drag coefficient and (C) lift-to-drag ratio as a function of the angle of attack. In all plots the results for the best shark denticle foil (red lines) are compared to those for the corresponding smooth control (black lines). Each data point is based on nine total tests and standard error bars are included (note that most error bars are small enough to be contained within the data marker). The inset in (B) is a schematic depicting the angle of attack (a) of the airfoil (-x being the direction of fluid flow and -y being the direction of lift).

The results shown in Figure 2.4 for the best denticle-containing foil exhibit three key features. First, we observe an increase in lift at almost all angles of attack for the foil with shark denticles compared to the corresponding smooth control (i.e. $C_L^{shark}/C_L^{control}$ = 3.55, 1.24, 1.13, 1.24, 1.06, 1.04, 0.96, 1.03, 1.06 at α=2°, 4°, 6°, 8°, 10°, 12°, 14°, 16°, 18°, respectively - see Figure 2.4*A*). We even find that positive lift is generated at zero angle of attack for the shark denticle foil (C_L^{shark} = 0.04 at α=0°), whereas, as expected, we see no lift being generated by

the smooth, symmetric control foil for α=0°. Second, the airfoil with shark denticles reduces drag compared to the smooth control at almost all angles of attack smaller than the angle at which stall occurs ($C_D^{shark}/C_D^{control}$ = 1.06, 0.84, 0.81, 0.78, 0.72, 0.83, 0.87 at α=0°, 2°, 4°, 6°, 8°, 10°, 12°, respectively - see Figure 2.4*B*) with drag reduction comparable to previously designed synthetic shark skin surfaces (21-25). Third, as shown in Figure 2.4*C*, because of the two combined effects described above, we observe substantial enhancements in the lift-to-drag ratio ($C_{L/D}=C_L/C_D$). More specifically, we find that $C_{L/D}^{shark}/C_{L/D}^{control}$ = 4.23, 1.53, 1.46, 1.72, 1.28, and 1.19 at α=2°, 4°, 6°, 8°, 10°, and 12°, respectively. Such increases are comparable to those observed for the best-reported vane-type low-profile vortex generators for $\alpha\geq$4° (8,11,12). However, the shark denticle morphology outperforms the more traditional designs at low angles of attack (α<4°) (see Section A.5 in Supporting Information for more details), a condition that is often experienced in use by many systems including drones, turbines, automobiles, and airplanes.

The experimental results shown in Figure 2.4 indicate that there are two driving forces behind the improved lift-to-drag ratio found for the best denticle-containing foil: (*i*) the enhanced lift, and (*ii*) the drag reduction at angles of attack prior to stall (i.e. 2°<α<12°). By looking at the response of all 20 foils tested (see Figures B.9-S26 of Supporting Information), we find that all of them except two (foils #8 and #20) display lift enhancement at low angles of attack (with airfoils #11, #14, and #16 showing only very small improvements). These results suggest that such a benefit is rather robust, only marginally affected by the location, size

and quantity of the geometric perturbations added to the airfoils. In contrast, we find that the lift improvements at high angles of attack prior to stall, as well as the drag reduction, are sensitive to the location, size and quantity of the denticles (see Supporting Information Section A.3 for more details).

To further understand the effect of the denticles on the aerodynamic performance of the airfoils, first we focused on the robust lift enhancement at low angles of attack. Guided by a previous numerical study that demonstrated that a simple 2D bump arranged on a flat plane can generate a negative pressure coefficient (30), we constructed a foil in which the row of denticles was replaced with a simple 2D bump profile (with non-zero curvature only in the chordwise direction). This bump was arranged in the same chordwise location and had height and leading edge curvature that match those of the shark denticles (see Figure 2.5 for details on the morphology of this airfoil as well as Supporting Information Section A.1). Furthermore, the bump had a streamlined design on its downstream side to reduce its generated pressure drag.

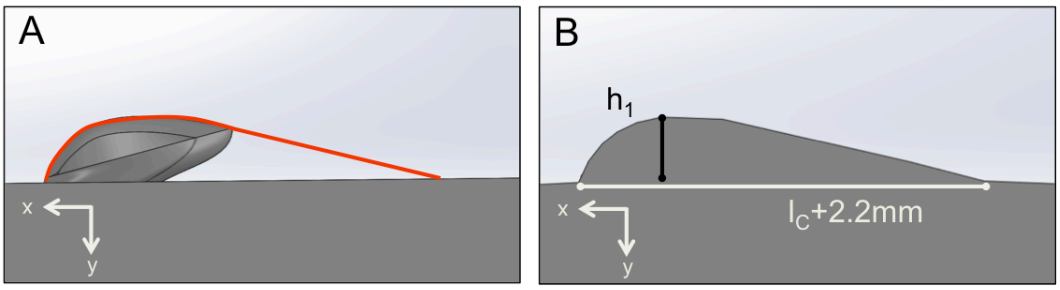

Figure 2.5: 2D bump profile. (A) Comparison between the profile of the 2D bump (red line) and the representative model of the shark denticle. (B) Side view of the 2D bump profile.

The experimental lift, drag, and lift-to-drag ratio for this 2D bump profile on a foil are presented in Figure 2.6 (corresponding numerical results for all of

these values are reported in the Supporting Information Section A.6). If we look specifically at the lift coefficient reported in Figure 2.6*A*, we see that this simple 2D bump profile enhances lift at low angles of attack ($C_L^{2Dbump}/C_L^{control}$=3.08 and 1.17 at α=2° and α=4° respectively) and generates non-zero lift at α=0° (C_L^{2Dbump}=0.09 at α=0°). Interestingly, while at α=2° and α=4° the foil with the 2D bump profile generates close to the same amount of lift as the one with the shark denticles (C_L^{2Dbump}/C_L^{shark}=0.87 and 0.94 at α=2° and 4°, respectively), it results in over twice the amount of lift at zero angle of attack (C_L^{2Dbump}/C_L^{shark} =2.41 at α=0°). These results confirm that the complex shape of the shark denticles arranged on the foil is not necessarily crucial to achieve lift enhancement at low angles of attack, and suggests that a continuous chordwise curved profile can further enhance C_L. However, the results reported in Figure 2.6*A* also demonstrate that the foil with the simple 2D bump profile loses its lift benefits relative to the control at higher angles of attack unlike the shark denticle foil ($C_L^{2Dbumb}/C_L^{control}$ = 0.88, 0.95, 0.91 at α=10°, 12°, 14°, respectively). At these angles right before and at stall, it is actually producing less lift than the control. Moreover, we also note that the 2D bump profile does not alter the drag greatly compared to the smooth control (except at α=10° and 12° – see Figure 2.6*B*). Because of these two latter effects, and when compared to the best denticle-containing foil, we find that the 2D bump profile exhibits a significantly lower lift-to-drag ratio across nearly all measured angles of attack (see Figure 2.6*C*).

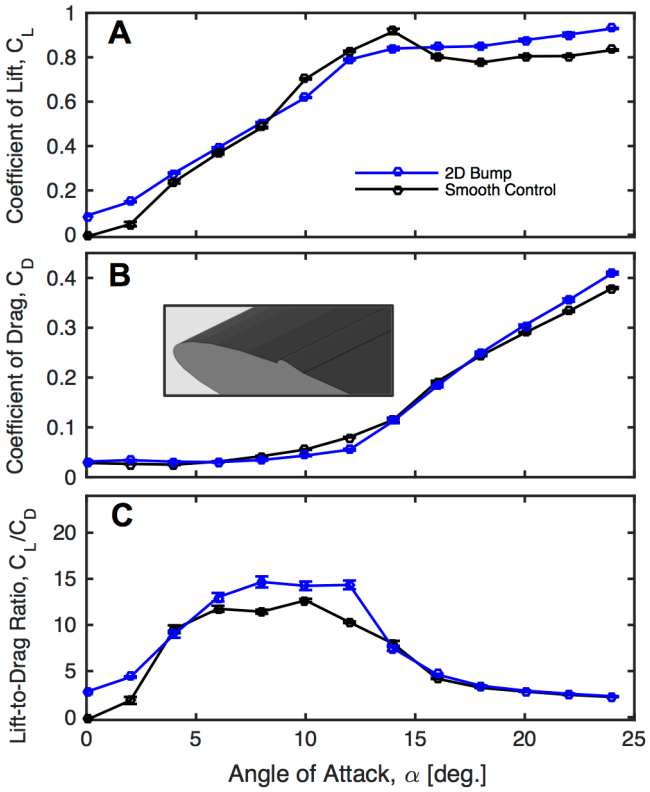

Figure 2.6: Experimental results for the 2D bump profile on an airfoil. Evolution of (A) lift coefficient, (B) drag coefficient and (C) lift-to-drag ratio as a function of the angle of attack. In all of the plots, the results for the 2D bump profile on an airfoil (blue lines) are compared to those for the corresponding smooth control (black lines). Each data point is based on nine total tests and standard error bars are included (note that most error bars are small enough to be contained within the data marker). The inset in (B) depicts the morphology of the 2D bump profile.

The reason behind the lift benefit at low angles of attack seen by both the shark denticle and 2D bump profile in comparison to the control can be further understood by inspecting the flow streamlines obtained via Particle Image Velocimetry (PIV) (see Section A.2 of the Supporting Information for more information on the PIV setup). The streamlines at α=0° and 4° shown in Figure 2.7 reveal that, in the presence of both the shark denticles and the 2D bump profile, a short separation bubble forms behind their trailing edge. While typically

separation bubbles are thought to negatively affect the performance of an airfoil (8, 10), it has also been shown that short separation bubbles (that fully reattach to the airfoil) can help to maintain a higher level of suction a bit further down the chord of the airfoil, providing a region over which the pressure distribution along the chord plateaus rather than dropping off further (31). As such, the short separation bubbles observed in our experiments likely provide additional suction that helps enhance lift.

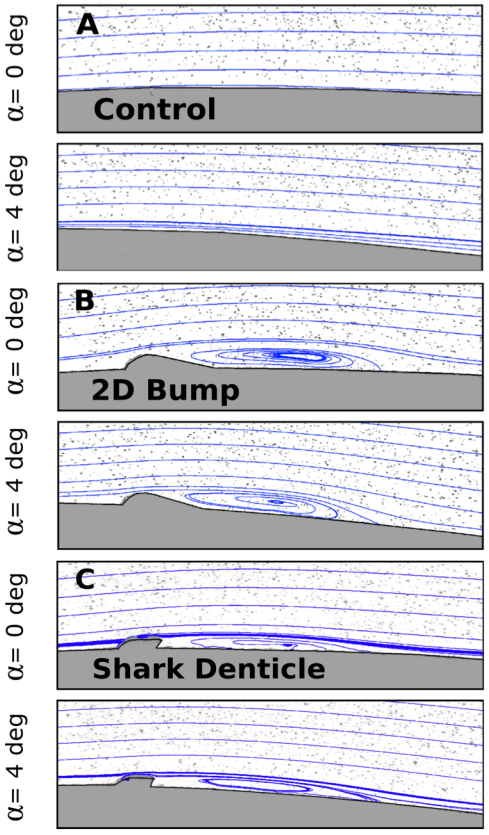

Figure 2.7: Flow streamlines obtained via Particle Image Velocimetry (PIV). PIV streamlines for the (A) smooth, (B) 2D bump profile, and (C) shark denticle foils are shown at a=0° and 4°, angles at which lift is being significantly enhanced by the 2D bump profile and shark denticle foils. A short separation bubble develops behind both the shark denticle and 2D bump foils, helping to provide further suction and therefore lift for these foils compared to the control.

Having understood how the 2D bump profile and the shark denticles influence lift at low angles of attack, we then turned our attention to lift enhancement at higher angles of attack and drag reduction. The lack of drag reduction seen throughout the majority of angles of attack and loss of lift enhancement at $\alpha>4°$ for the 2D bump foil suggests strongly that the spanwise curvature of the denticles may play an important role. More specifically, guided by previous studies that showed that geometric perturbations capable of producing streamwise vortices could reduce drag (and prevent losses of lift at higher angles of attack near stall) (8,10,11,12), we hypothesized that the spanwise curvature of the shark denticles results in the formation of streamwise vortices. In order to confirm this hypothesis, and since the visualization of such vortices via PIV proved challenging due to both the small-scale spatial resolution required and the orientation of the denticles' grooves, we performed Computational Fluid Dynamics (CFD) analyses. The simulations were carried out with ANSYS® CFX, using a combination of a finite-volume and finite-element approach to discretize the Navier-Stokes equations, which were solved by an unsteady fully-implicit, fully-coupled multigrid solver with the Shear Stress Transport (SST) turbulence model (see CFD Analysis in Supporting Information Section A.6 for more details) (32). The numerical results reported in Figure 2.8 for an individual shark denticle on a flat plate not only confirm that the shark denticle morphology creates a short separation bubble in its wake (see Figure 2.8*A*) as shown previously via PIV, but also confirm that the shark denticle acts as a vortex generator, as shown clearly by the streamwise vortices forming in the wake of the denticle (see Figure 2.8*B*).

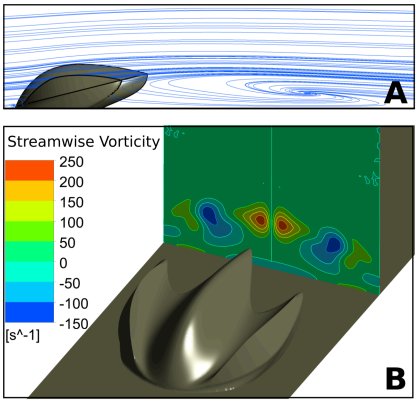

Figure 2.8: CFD analyses of a shark denticle model on a flat plate. (A) Numerical snapshot showing the flow streamlines. Our analyses predict the formation of a short separation bubble in the wake of the denticle. (B) Contours of the streamwise vorticity (the rate at which the streamwise-moving fluid is rotating just after the denticle) on a plane perpendicular to the flow just downstream from the denticle. The separation bubble and streamwise vortices shown in (A) and (B) help to enhance lift and reduce drag when the shark denticle is correctly placed on an airfoil (see Supporting Information Section A.3 for more details).

These streamwise vortices are likely responsible for drag reduction and also likely help to maintain lift at higher angles of attack by bringing higher momentum fluid from the outer part of the boundary closer to the wall and thus help replenish the momentum in the boundary layer which would have been lost to skin friction. It is further known that the interaction among these vortices is crucial in determining their aerodynamic advantages (33,34). For instance, placing the vortex generators too close to each other in the spanwise direction can lead to destructive interference of the streamwise vortices, which ultimately reduces the performance of the airfoil (33,34). This observation helps explain the high sensitivity of the drag coefficient to the morphology and placement of the denticles that we found in our experiments.

Guided by all these results, we then tried to improve the aerodynamic performance of the airfoil by designing a geometric perturbation that takes

advantage of the multiple mechanisms that were seen to be beneficial in the foils with the shark denticles and the 2D bump. More specifically, we designed a geometric perturbation that combines the ridges of the shark denticle with the continuous chordwise curved profile of the 2D bump to achieve the lift-to-drag ratio benefits of the shark denticle, while yet also improving the lift further at very low angles of attack (especially α=0°) in the way seen by the 2D bump profile. While this new morphology's chordwise cross-section is designed similarly to that of the 2D bump, its spanwise curvature and morphology resembles that of the denticle except for the fact that it has a continuous sinusoidal-like nature as opposed to the finite nature of the shark denticles placed side-by-side on a airfoil (see Figure 2.9 for details on the morphology of this profile as well as Supporting Information Section A.1). We refer to this new continuous streamlined morphology as the "continuous shark-inspired profile."

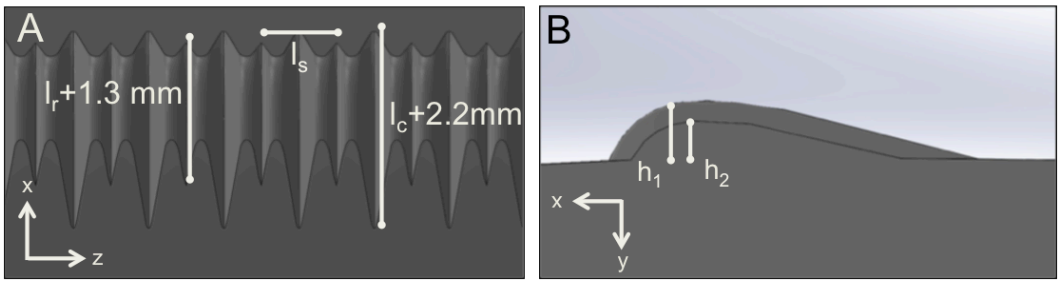

Figure 2.9: Continuous shark-inspired profile. (A) Top and (B) side views of the continuous shark-inspired profile.

In Figure 2.10 we report the experimental results for the aerodynamic response of an airfoil with this continuous shark-inspired profile placed at 26% along the chord. First, focusing on lift at low angles of attack, we find that this airfoil generates roughly the same amount of lift as the one with the 2D bump

profile, and over twice that of the one with shark denticles at α=0° ($C_L^{cont.}/C_L^{2Dbump}$=1.03 and $C_L^{cont.}/C_L^{shark}$=2.47 – see Figure 2.10*A*). We also see that the foil with this continuous shark-inspired profile results in coefficients of lift similar to those seen for the cases of the 2D bump profile and shark denticles at other low angles of attack ($C_L^{cont.}/C_L^{2Dbump}$=1.19, 1.09 and $C_L^{cont.}/C_L^{shark}$=1.04, 1.03 at α=2° and 4°, respectively). Second, our results indicate that this continuous shark-inspired profile does not lose these lift benefits as much at higher angles of attack prior to stall. Third, we find that the continuous shark-inspired profile leads to even more drag reduction than the shark denticles (see Figure 2.10*B*). This is especially evident at angles of attack just before stall, with $C_D^{cont.}/C_D^{control}$ =0.54 and 0.53 at α=10° and 12°, respectively (resulting in $C_D^{cont.}/C_D^{shark}$=0.65 and 0.62 at α=10° and 12°, respectively). This may in part be helped by the streamlined nature of the continuous shark-inspired profile. Finally, it is important to note that the observed high lift and low drag lead to large lift-to-drag ratio increases ($C_{L/D}^{cont.}/C_{L/D}^{control}$ = 3.61, 1.39, 1.52, 1.86, 1.83, and 1.83 at α=2°, 4°, 6°, 8°, 10°, and 12°, respectively – see Figure 2.10*C*).

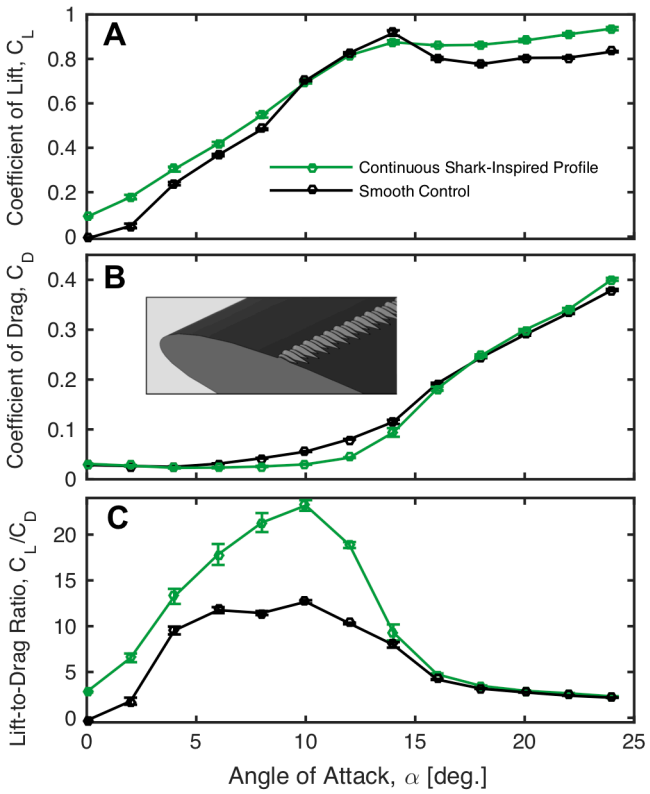

Figure 2.10: Experimental results for the airfoil with a continuous shark-inspired profile. Evolution of (a) lift coefficient, (b) drag coefficient and (c) lift-to-drag ratio as a function of the angle of attack. In all plots, the results for the continuous shark-inspired profile (green lines) are compared to those for the corresponding smooth control (black lines). Each data point is based on nine total tests and standard error bars are included (note that most error bars are small enough to be contained within the data marker).

Specifically, we see from Figure 2.11 (which shows a comparison of the lift-to-drag ratio improvements of all three main foils discussed in this manuscript) that the continuous shark-inspired profile outperforms the 2D bump profile at all angles of attack and the shark denticle at just about all angles of attack (see Section A.4 of the Supporting Information for more details). This is because the continuous shark-inspired profile is able to produce the same lift benefits as the 2D bump at low angles of attack (especially α=0°) without losing

these lift benefits as much at higher angles of attack (like the 2D bump does), in addition to greatly reducing drag at higher angles (like the shark denticle is able to). Note that in Figure 2.11 we also indicate with a filled in marker the angle at which the maximum lift-to-drag ratio occurs for each foil. Again, we find that the continuous shark-inspired profile produces the greatest improvement at this angle.

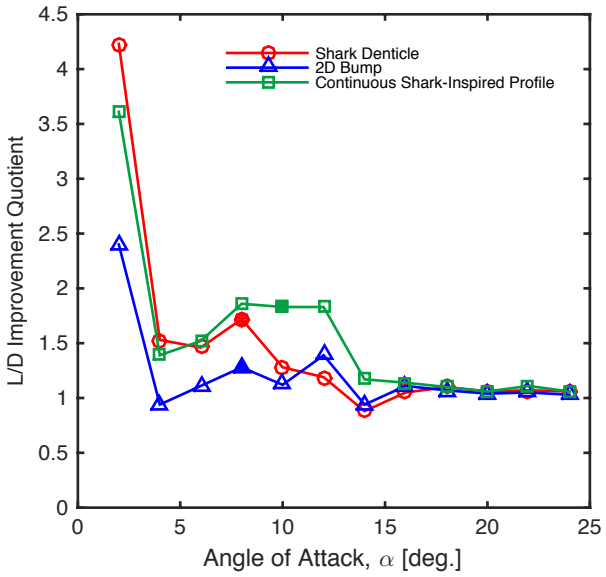

Figure 2.11: Comparison between the three main foils analyzed in this text. The red, blue, and green markers correspond to $C_{L/D}^{shark}/C_{L/D}^{control}$, $C_{L/D}^{2Dbump}/C_{L/D}^{control}$ and $C_{L/D}^{cont.}/C_{L/D}^{control}$, respectively. The solid markers represent the angle at which the max L/D for that foil occurs.

In addition to these great lift-to-drag ratio improvements, this continuous shark-inspired profile has another important advantage over the other foils discussed here. Although there has been increased interest in recent years aimed at reproducing the hydrodynamic performance of shark denticles for use on engineered surfaces, one major obstacle to the mass production of these shark skin-inspired geometries has been the structural complexity of the denticles. While it has been demonstrated previously that it is possible to replicate these

forms through the use of 3D printing (23), this approach is unfortunately not scalable, and the undercuts and overhangs present on the native denticles prevent the direct molding of these specific geometries using conventional manufacturing strategies. The continuous shark-inspired profile described here circumvents these problems and is easily amendable to roll-to-roll embossed fabrication, bringing this technology one step closer to large-scale adoption for aquatic and aerospace applications.

2.4 Conclusion

In this study, we have taken inspiration from shark denticles to design a set of profiles that significantly improve the aerodynamics of airfoils. In contrast to previous studies on shark skin that have mostly focused on drag reduction/thrust improvement (21-27), we showed that the denticles also generate lift, resulting in high lift-to-drag ratio improvements. Specifically, we found comparable results to those of the best previously reported low-profile vortex generators at higher angles of attack near stall, and even much higher improvements at low angles of attack ($\alpha<4°$) (8, 11, 12). The remarkable results shown here were achieved by utilizing two mechanisms. First, the shark-inspired profiles trip the boundary layer and generate a short (reattaching) separation bubble that provides extra suction along the chord and thereby enhances lift. Second, the spanwise curvature of the denticles helps to generate streamwise vortices that can lead to drag reduction and prevent lift losses at higher angles of attack. While in this study we have considered the ideal case of the denticles'

ridges perfectly parallel to the flow, future work will investigate how sensitive the aerodynamic response of the airfoils is to the orientation of the denticles with respect to the flow.

It is important to note that the flow regime considered in this study ($Re_c \approx 4x10^4$) is relevant for many systems, including interior portions of wind turbine blades, helicopter blades, drones, and autonomous underwater vehicles. Moreover, some of the mechanisms discovered here can hold also for higher flow regimes and can be used to improve movement through air and water. Finally, the results discussed here may have implications for understanding the function of shark denticle morphology. Shark skin denticles have been shown to alter the position and strength of the leading edge vortex in experimental studies (21), and it is likely that the lift effects observed here contribute to a thrust enhancement effect of shark skin resulting in increased self-propelled swimming speeds (23).

2.5 REFERENCES

[1] Raymer, D. (2012). *Aircraft Design: A Conceptual Approach* (5th ed.). New York: AIAA.

[2] Amitay, M,, Smith, B,, Glezer, A. (1998). Aerodynamic flow control using synthetic jet technology. *36th AIAA Aerospace Sciences Meeting and Exhibit,* doi:10.2514/6.1998-208.

[3] Kiedaisch, J., Nagib, H., Demanett, B. (2006). Active Flow Control Applied to High-Lift Airfoils Utilizing Simple Flaps. *3rd AIAA Flow Control Conference,* doi:10.2514/6.2006-2856.

[4] Pack, L., Schaeffler, N., Yao, C., Seifert, A. (2002). Active Control of Flow Separation from the Slat Shoulder of a Supercritical Airfoil. *1st Flow Control Conference,* doi:10.2514/6.2002-3156.

[5] Kiedaisch, J, Demanett, B., Reinhard, P., Nagib, H. (2007). Active Flow Control for High Lift Airfoils: Dynamic Flap Actuation. *45th AIAA Aerospace Sciences Meeting and Exhibit,* doi:10.2514/6.2007-1120.

[6] Amitay, M., Parekh, D. E., Smith, D. R., Kibens, V., Glezer, A. (2001). Aerodynamic flow control over an unconventional airfoil using synthetic jet actuators. *AIAA Journal,* 39, 361–370.

[7] Lin, J. C., Howard, F. G., Selby, G. V. (1990). Small submerged vortex generators for turbulent flow separation control. *J Spacecr Rockets,* 27, 503–507.

[8] Lin, J. C. (2002). Review of research on low-profile vortex generators to control boundary-layer separation. *Prog Aerosp Sci,* 38, 389–420.

[9] Yao, C., Lin, J., Allen, B. (2002). Flowfield Measurement of Device-Induced Embedded Streamwise Vortex on a Flat Plate. *1st Flow Control Conference* (American Institute of Aeronautics and Astronautics, Reston, Virigina). doi:10.2514/6.2002-3162.

[10] Kerho, M., Hutcherson, S., Blackwelder, R. F., Liebeck, R. H. (1993). Vortex generators used to control laminar separation bubbles. *J Aircr,* 30, 315–319.

[11] Lin, J. C., Robinson, S. K., McGhee, R. J., Valarezo, W. O. (1994). Separation control on high-lift airfoils via micro-vortex generators. *J Aircr,*

31, 1317–1323.

[12] Lin, J. (1999). Control of turbulent boundary-layer separation using micro-vortex generators. *30th Fluid Dynamics Conference* (American Institute of Aeronautics and Astronautics, Reston, Virigina). doi:10.2514/6.1999-3404.

[13] Storms, B. L., Jang, C. S. (1994). Lift enhancement of an airfoil using a Gurney flap and vortex generators. *J Aircr,* 31, 542–547.

[14] Myose, R., Papadakis, M., Heron, I. (1998). Gurney Flap Experiments on Airfoils, Wings, and Reflection Plane Model. *J Aircr,* 35, 206–211.

[15] Wang, J. J, Li, Y. C., Choi, K-S. (2008). Gurney flap—Lift enhancement, mechanisms and applications. *Prog Aerosp Sci,* 44, 22–47.

[16] Guerrero, J. E., Maestro, D., Bottaro, A. (2012). Biomimetic spiroid winglets for lift and drag control. *Comptes Rendus Mécanique,* 340, 67–80.

[17] Whitcomb, R. T. (1976). National Aeronautics and Space Administration. *A Design Approach and Selected Wind-tunnel Results at High Subsonic Speeds for Wing-tip Mounted Winglets*.

[18] Bar-Cohen, Y. (2005). Biomimetics. *Biomimetics*, pp 495–513. Boca Raton, FL: CRC Press.

[19] Benyus, J. M. (1997). Biomimicry. *Innovation Inspired by Nature*. New York: Harper Collins.

[20] Patek, S. N. (2014). Biomimetics and evolution. *Science,* 345, 1448–1449.

[21] Oeffner, J., Lauder, G. V. (2012). The hydrodynamic function of shark skin and two biomimetic applications. *J Exp Biol,* 215, 785–795.

[22] Lauder, G. V., et al. (2016). Structure, biomimetics, and fluid dynamics of

fish skin surfaces. *Physical Review Fluids,* 1(6). doi:10.1103/physrevfluids.1.060502.

[23] Wen, L., Weaver, J. C., Lauder, G. V. (2014). Biomimetic shark skin: design, fabrication and hydrodynamic function. *J Exp Biol,* 217, 1656–1666.

[24] Bechert, D. W., Bruse, M., Hage, W. (2000). Experiments with three-dimensional riblets as an idealized model of shark skin. *Exp Fluids,* 28, 403–412.

[25] Dean, B., Bhushan, B. (2010). Shark-skin surfaces for fluid-drag reduction in turbulent flow: a review. *Philos Trans A Math Phys Eng Sci,* 368, 4775–4806.

[26] Fu, Y. F., Yuan, C. Q., and Bai, X. Q. (2017). Marine drag reduction of shark skin inspired riblet surfaces. *Biosurface and Biotribology,* 3.1, 11-24.

[27] Sareen, A., et al. (2014). Drag reduction using riblet film applied to airfoils for wind turbines. *Journal of Solar Energy Engineering,* 136.2, 021007.

[28] Tank, J., Smith, L., Spedding, G. R. (2017). On the possibility (or lack thereof) of agreement between experiment and computation of flows over wings at moderate Reynolds number. *Interface Focus,* 7:20160076.

[29] Mueller-Vahl, H., Pechlivanoglou, G., Nayeri, C. N., Paschereit, C. O. (2012). Vortex Generators for Wind Turbine Blades: A Combined Wind Tunnel and Wind Turbine Parametric Study. In Volume 6: Oil and Gas Applications; Concentrating Solar Power Plants; Steam Turbines; Wind Energy, (doi:10.1115/gt2012-69197).

[30] Baskaran, V., Smits, A. J., Joubert, P. N. (1987). A turbulent flow over a

curved hill Part 1. Growth of an internal boundary layer. *J Fluid Mech,* 182, 47-83.

[31] Roberts, W. (1979). Calculation of laminar separation bubbles and their effect on airfoil performance. *17th Aerospace Sciences Meeting,* 18, 25-31 doi:10.2514/6.1979-285.

[32] ANSYS® Academic Research, Release 14.0, Help System, ANSYS CFX-Solver Theory Guide, ANSYS, Inc.

[33] Ashill, P., Fulker, J., Hackett, K. (2002). Studies of flows induced by Sub Boundary Layer Vortex Generators (SBVGs). *40th AIAA Aerospace Sciences Meeting & Exhibit,* doi:10.2514/6.2002-968.

[34] Tai, T. (2002). Effect of micro-vortex generators on V-22 aircraft forward-flight aerodynamics. *40th AIAA Aerospace Sciences Meeting Exhibit,* doi: 10.2514/6.2002-55.

This work was done in collaboration with Prof. George Lauder, Prof. Katia Bertoldi, James Weaver, Gino Domel, and Mehdi Saadat. This work has already been published, and the relevant citation for the work is: Domel, A. G., Domel, G., Weaver, J. C., Saadat, M., Bertoldi, K., & Lauder, G. V. (2018). Hydrodynamic properties of biomimetic shark skin: effect of denticle size and swimming speed. Bioinspiration & Biomimetics. https://doi.org/10.1088/1748-3190/aad418.

3

Hydrodynamic Properties of Biomimetic Shark Skin: Effect of Denticle Size and Swimming Speed

3.0 ABSTRACT

Biomechanists and biologists alike have yet to fully understand the complex morphology and function of shark denticles, morphologically intricate tooth-like structures embedded into the skin of sharks. Denticles vary in many ways (such as size and shape) depending on shark species, and studies on denticle hydrodynamics have suggested that they may aid in drag reduction as well as increase both lift and thrust. Although previous studies have analyzed the effect of different denticle patterns on hydrodynamic performance, no previous work has focused on the effects of denticle size. Here, we report on the hydrodynamic properties of 3D printed shark skin foils with rigid denticles embedded into a flexible substrate. The patterning of these denticles was based on previously reported designs exhibiting the greatest hydrodynamic performance (which also most closely mimics real shark skin). The size of the denticles and the speed of the flow were varied, and the foils were evaluated under both static and dynamic conditions. Static tests showed drag reduction compared to a smooth control foil (without denticles) for the smallest denticle size, while medium and large denticles exhibited increased drag. Under dynamic testing conditions, the smallest denticles increased the self-propelled swimming speed, while the largest denticles

reduced swimming performance. At higher speeds, the smallest denticles were also able to reduce power consumption compared to the control, demonstrating that their hydrodynamic effect depends on both denticle size and swimming speed. Our results thus provide new insights into the role of denticle size in shark swimming hydrodynamics across a range of locomotory modes, while simultaneously providing new design guidelines for the production of high performance low drag surface coatings for aquatic and aerospace applications.

3.1 INTRODUCTION

Sharks are an extremely diverse group of vertebrates with nearly 450 species that inhabit a wide variety of habitats from the open ocean to near-shore and benthic environments (1-4). One fascinating aspect of shark biology that has been extensively studied is the function of their skin, which is covered with many thousands of tooth-like denticles or scales, and has been postulated to play an important role in locomotion (5-10). Each denticle is covered in an enamel-like coating and often exhibits multiple surface ridges, which are generally aligned along the direction of water flow over the body and fins (Figure 3.1). There is considerable diversity in the patterning of skin denticles, in the alignment of denticle ridges across the surface, and variation in the spacing and hence overlap among adjacent denticles (2,7). Denticles can also vary considerably in shape, both along the body of an individual, and among different species. Denticles can be round and peg-like, diamond-shaped with ridges and pointed posterior

margins, or they can lack surface ornamentation and have a smooth and rounded posterior edge (5).

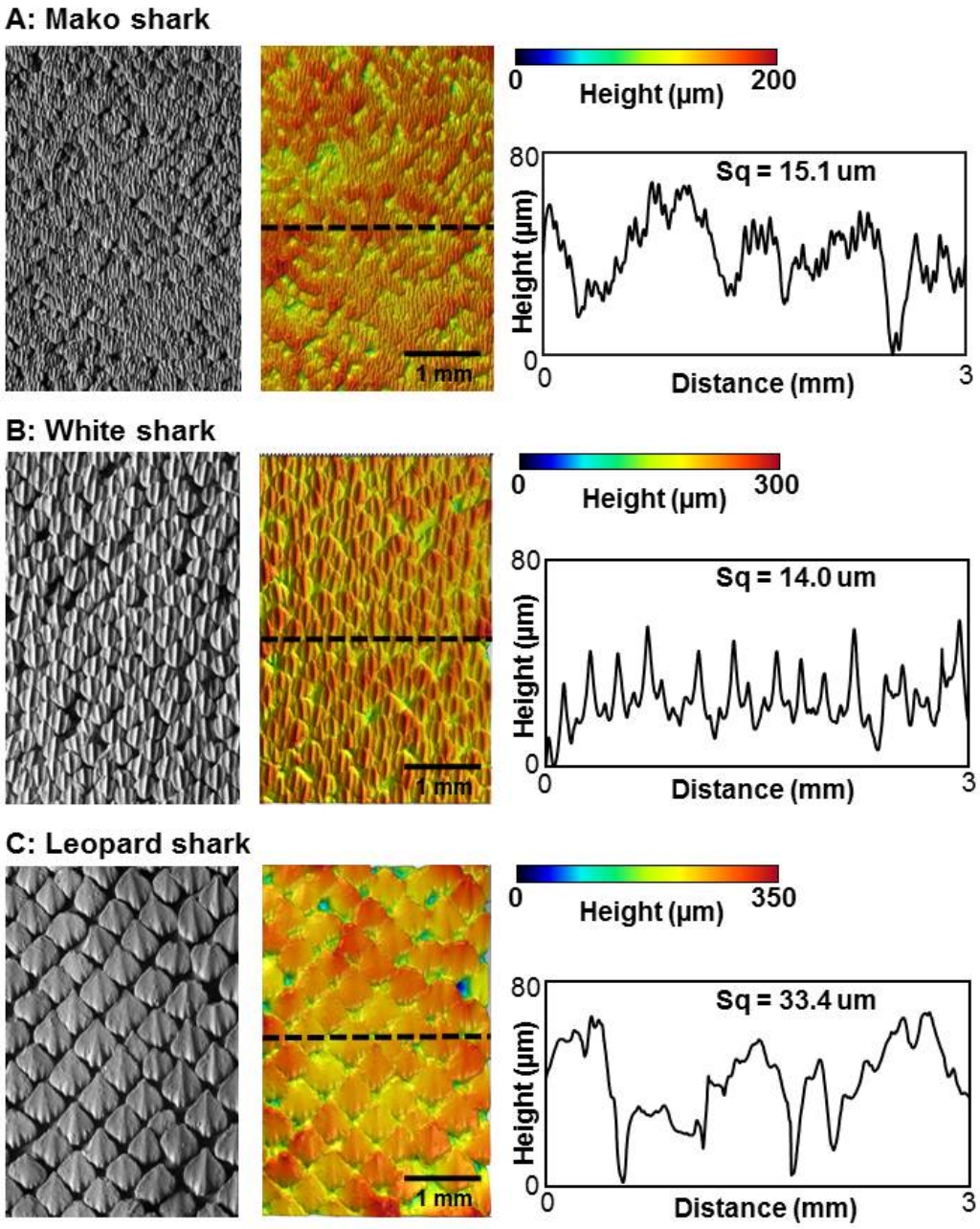

Figure 3.1: Variations in denticle surface patterning in three species of sharks. The denticle surface of each species was imaged in three dimensions using gel-based surface profilometry (see Methods). Data are shown for a mako shark (*Isurus oxyrinchus*), white shark (*Carcharodon carcharias*), and leopard shark (*Triakis semifasciata*). For each species, a surface image is shown (left), the same image with height indicated in color (middle), and a height profile at the location

of the dashed line (right). Water flow over the skin surface is from bottom to top. Measurements of surface roughness (Sq, see Methods) are given above each profile.

A primary axis of variation in shark denticles lies in their size, and individual denticles in different species can vary from larger than one millimeter to as small as 120 μm (2,5,11). Changes in denticle size affect the overall surface patterning and roughness characteristics as shown in Figure 3.1, where variation in denticle patterning is compared among three species of sharks. Species such as the leopard shark Triakis semifasciata, have individual denticles greater than 0.5 mm in length, while shortfin mako sharks (Isurus oxyrinchus) have among the smallest denticle sizes (200 μm in length). White sharks (Carcharodon carcharias, Figure 3.1) possess intermediate sized denticles as do many other open ocean species. Denticle size also affects overall surface roughness and the frequency characteristics of height variation over the surface, with the larger denticles of leopard sharks exhibiting twice the skin surface roughness of mako sharks (Figure 3.1).

In recent years, a number of studies have aimed to understand the functional significance of shark denticles by computationally simulating steady flow over denticles, although such studies have arrived at contradictory conclusions as to the possible drag reduction effect of denticle shapes (12,13. Denticles in at least a few species also appear to be relatively loosely anchored in the skin, and it has been suggested that these passively mobile denticles may change boundary layer characteristics of water flow over the body (14,15). Experimental studies of highly simplified denticle models (such as simple linear ridges) have demonstrated drag reduction under static test conditions with

constant flow (6,16,17), but the hydrodynamic conditions of these tests may not reflect the dynamic and time-varying flows experienced by the skin of sharks as they swim.

Another approach to understanding the functional significance of denticles has been to use either real pieces of shark skin (18) or 3D printed biomimetic shark skin models (9,19,20) attached to a robotic flapping controller which moves the skin and models in a biologically realistic manner (with appropriate frequencies and surface curvature). Testing shark skin in this way and under conditions of self-propulsion in the laboratory allows denticle-covered surfaces to experience both drag and lift forces naturally during oscillatory motion, and recent work has demonstrated that these surfaces can increase lift when added to airfoil surfaces (10) and increase thrust generation in a flapping propulsive system. These experimental tests of shark skin under conditions of propulsion also have the benefit of allowing calculation of the cost of transport and power consumption by different arrangements of denticles on the skin surface during swimming, and of direct comparisons to a manufactured smooth control surface of the same mass (20).

However, to date, these experimental studies have not considered the effects of denticle size alone. To address this question, we first 3D printed biomimetic model membranes of shark skin at different size scales along with corresponding smooth controls of the same mass. Second, we conducted static testing at different imposed flow speeds to determine how denticle size affects drag forces using 3D printed denticle membranes as compared to smooth control

surfaces at a variety of Reynolds numbers. Third, we conducted a series of dynamic tests at two Reynolds numbers in which 3D printed shark skin membranes with differently sized denticles swam under conditions of self-propulsion to investigate the relationship between denticle size and power consumption during propulsion. We used these data to test the hypothesis that smaller denticles reduce power consumption of propulsion compared to surfaces covered with larger denticles.

3.2 Materials and Methods

3.2.1 Creating the Shark Denticle Model

Using micro-computed tomography (micro-CT) data (XradiaVersaXRM-500, Zeiss, Oberkochen, Germany) obtained from denticles from the short fin mako (Isurus oxyrinchus), and as described previously by Lauder et al. (2016) and Wen et al. (2014, 2015), we created the representative shark denticle model shown in Figure 3.2 using Mimics 3D (Materialise Inc., Leuven, Belgium) to segment the raw data and SolidWorks for generation of the final parametric model (SolidWorks Corp., Waltham, MA, USA) (9,19,20). In Figure 3.2, l_c is the chordwise length of the denticle, l_s is the spanwise length, and l_r is length of the side ridges (the denticle is symmetric about its middle ridge – see Figure 3.2*A*). Moreover, h_1 is the height of the middle ridge from where it anchors into the skin surface, and h_2 is the height of the side ridge (see Figure 3.2*B* and Figure 3.2*C*). We kept $l_c/l_s = 1.37$, $l_c/l_r = 1.25$, $h_1/h_2 = 1.2$, and $l_c/h_1 = 1.67$ constant for all representative denticles. An l_c of 2.1 mm was used for the membrane with the

smallest denticles, l_c=3.15 mm for the medium denticles, and l_c =4.2 mm for the largest denticles. This model denticle was then arrayed in a staggered-overlapped pattern on the membrane surface, a pattern which was found to be most hydrodynamically beneficial by Wen et al. (2015) (20). This staggered-overlapped pattern is shown in Figure 3.2*D*, where S_s is the spacing between denticles in the streamwise direction, and S_l is the spacing between denticles in the lateral direction (S_s/S_l = 1 was kept constant throughout this study).

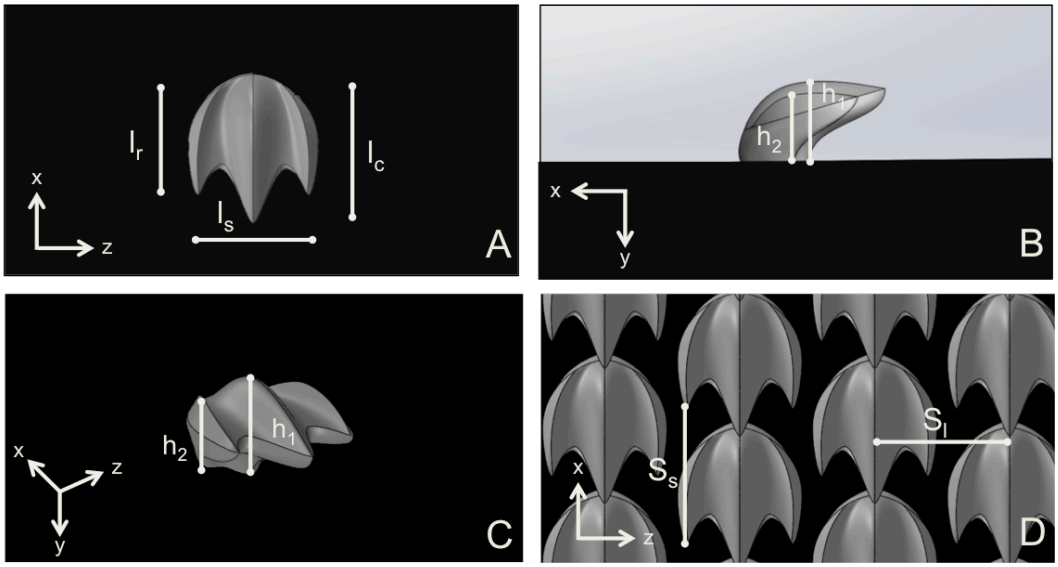

Figure 3.2: (A) Top, (B) side, and (C) isometric view of the representative shark denticle model used in this study. (D) The shark denticle model was then arrayed in a staggered-overlapped pattern. Dimensions used to design the denticle foils included l_c, l_r, l_s, h_1, h_2, S_i and S_s. l_c is the chordwise length of the denticle, l_s is the spanwise length, and l_r is length of the side ridges (the denticle is symmetric about its middle ridge). h_1 is the height of the middle ridge from where it anchors into a surface, and h_2 is the height of the side ridge. We kept l_c/l_s = 1.37, l_c/l_r = 1.25, h_1/h_2 = 1.2, l_c/h_1 = 1.67, and S_s/S_l = 1 constant for all biomimetic denticles and surfaces in this study.

3.2.2 Manufacturing Biomimetic Shark Skin Surfaces

In this study, we aimed to understand how denticle size affected the hydrodynamics of shark skin surfaces. Since these surfaces would be tested not

only statically, but also dynamically using a robotic flapping device, the surfaces had to be flexible. To meet this need, we employed multi-material 3D printing using a Objet Connex500 3D Printer (Stratasys Ltd, Eden Prairie, MN, USA) for the production of three composite shark skin surfaces that consisted of an array of rigid denticles embedded in a flexible membrane as a single integrated model (Figure 3.3). The membrane surface itself was printed out of a black flexible rubber-like material (FLX980; with Young's modulus E~1 MPa), while the denticles were printed out of a clear rigid thermoplastic-like material (RGD810; with Young's modulus E~1 GPa). Three different flexible biomimetic shark skin surfaces were created, each with a different size of denticles arrayed in the same staggered-overlapped pattern shown in Figure 3.2*D*. All three membranes had the same chord and span length (157 mm and 68 mm, respectively), and thus had the same Reynolds number based on the foil cord length, Re_C, at a given flow speed (as described by Wen et al. (2015)) (20). For all subsequent descriptions of these models, we refer to the membrane with the smallest denticles as "1x", the membrane with medium denticles as "1.5x" and the largest as "2x". The thickness of the flexible 1x membrane was set to 1.44 mm, and this value was scaled up with each additional membrane proportional to the size of the denticles. For each of the three different biomimetic shark skin membranes with differently sized denticles, two membranes were 3D printed. Each of the two membranes for a given denticle size was adhered to each side of a yellow plastic shim-stock "backbone" with thickness of 0.508 mm and flexural stiffness of 9.8×10^{-4} Nm^{-2}, resulting in a composite foil with denticles on both sides. Thus, the final foil for

each of the three types of shark skin surfaces consisted of a shark skin membrane of a given denticle size on each side of this yellow plastic backbone (Figure 3.3). The yellow plastic support was laser cut with an extra 1cm in chord length (with three holes at the end – see Figure 3.3) so that the foil could be attached to the robotic flapping device described below.

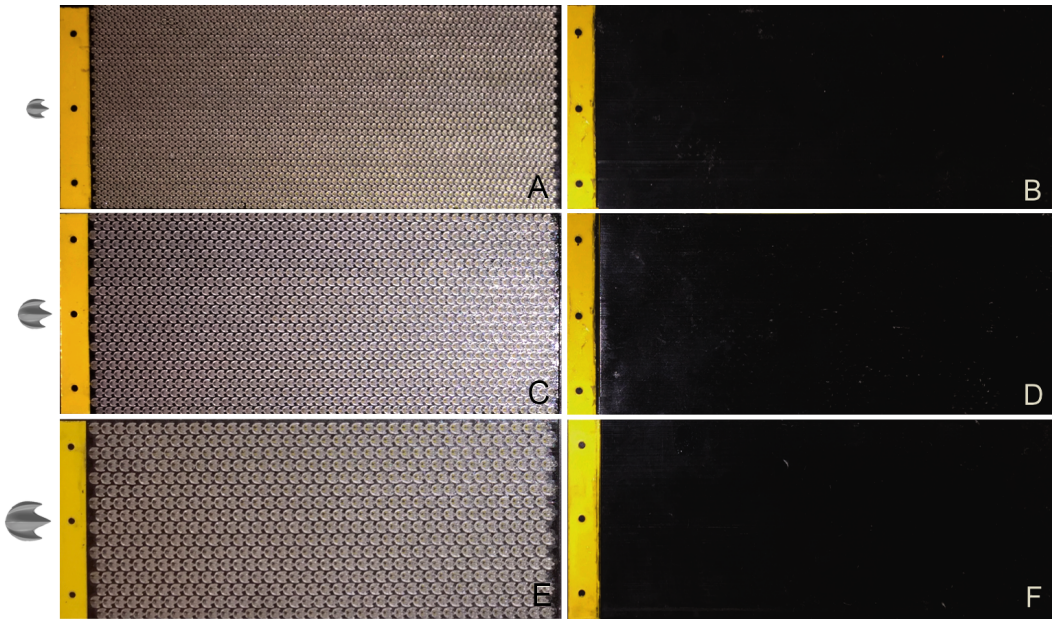

Figure 3.3: Images of the six foils tested in this study: biomimetic shark skin foils on the left and the corresponding smooth control foils of the same mass on the right. Denticle images scaled relative to each other are shown to the left of the foils. The black material pictured above is flexible so that all of the foils move in a fish-like motion when dynamically tested. The size of rigid denticles embedded in the biomimetic shark skin foils was varied, and the mass of the control adjusted accordingly. (A) shows the 1x denticle foil (l_c = 2.1mm) while (B) shows its corresponding smooth control foil, (C) shows the 1.5x denticle foil (l_c = 3.15mm) while (D) shows its corresponding smooth control foil, (E) shows the 2x denticle foil (l_c = 4.2mm) while (F) shows its corresponding smooth control foil. The yellow tab to the left of each foil was 10mm in width and was used to attach the foils to the robotic flapping device. The foils chord and span length were 157mm and 68mm, respectively.

Each of the three denticle foils had its own denticle-free control foil of identical total mass (a 3D printed plain, smooth black flexible membrane with the

same mass, chord and span length as the denticle-containing foils). To accomplish this, the control thickness was adjusted relative to the denticle foils to match the mass of the respective denticle foil (ensuring that inertial effects would not play a role in the dynamic testing when comparing each denticle foil to their control). The small increase in thickness did not observably affect the stiffness of the membranes since the flexural stiffness of the entire assembled foil (Figure 3.3) was dominated by the stiffness of the central plastic backbone (also see Wen et al. (2015) for further discussion of this point) (20). Using the above mentioned naming schemes, we will refer to these control foils as the "1x control", "1.5x control", and "2x control". In general, our approach to designing and manufacturing the flexible foils was similar to that used in our previous work investigating shark skin denticle performance (9,18-20). The parameters for each of the 6 foils tested in this study (as shown in Figure 3.3) can be found in Table 3.1 which provides key characteristics of each of the tested denticle foils and their corresponding controls.

Table 3.1: Parameters for each of the 6 foils tested in this study: 3 biomimetic shark skin foils and their 3 corresponding smooth controls (values include both sides of the foil). S_s is the spanwise distance between denticles and S_l is the distance along the chord between denticles.

Sharkskin Morphology	1x Control	1x Scales	1.5x Control	1.5x Scales	2x Control	2x Scales
S_s (mm)	-	2.05	-	3.075	-	4.10
S_l (mm)	-	2.05	-	3.075	-	4.10
# of Denticles	0	4950	0	2200	0	1184
Denticle Surface Area (mm^2)	0	42006	0	41998	0	40189
Membrane Surface Area (mm^2)	21352	17628	21352	17626	21352	17788
Total Surface Area (mm^2)	21352	59634	21352	59624	21352	57977

3.2.3 Imaging Biological Shark Skin and Biomimetic Shark Skin Surfaces

Imaging the skin of three species of sharks (figure 3.1) and the biomimetic denticle and control membrane surfaces (Figure 3.4) was performed using gel-based surface profilometry (GelSight Incorporated, Waltham, Mass, USA) as described previously by Wainwright and Lauder (2016) and Wainwright et al. (2017, 2018) (21-23). Each of the resulting 3D data sets had dimensions of 4.5 by 3 cm in x and y and contained 18 million x, y, z coordinates providing a detailed representation of surface elements and their patterning. Image resolution was 5208 by 3476 pixels, with additional z (height) data for each pixel. Surface profile data were analyzed using MountainsMap software (v. 7 Digital Surf, Besançon, France) to generate image maps of surface height (Figures 3.1, 3.4) and to quantify the surface roughness parameter Sq. Sq was calculated as the square-

root of the sum of the squared distances of each point from the mean height (units are in µm).

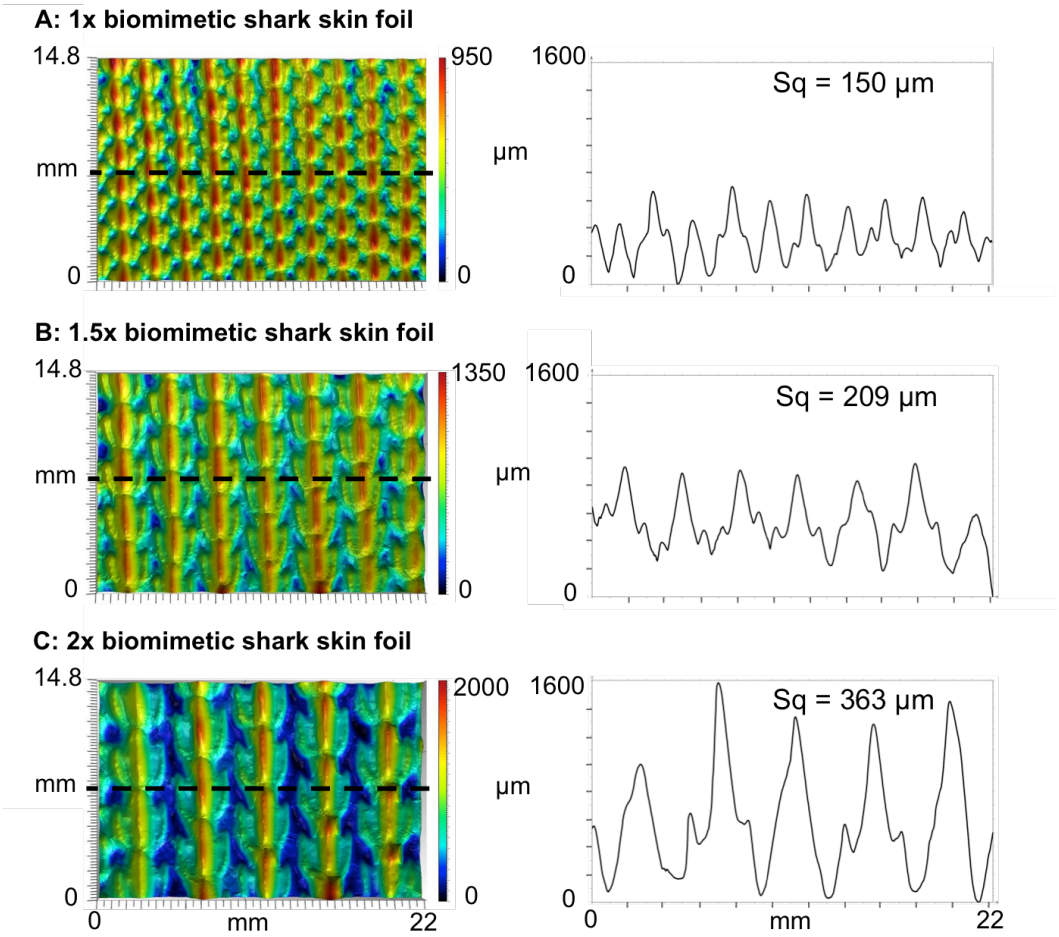

Figure 3.4: Surface patterning in the three biomimetic foils tested to illustrate height variation and denticle spacing among the different flexible biomimetic membranes. The upper panels show the 1x denticle size (A), the middle panels the 1.5x denticle size (B), and the bottom panels the 2x size (C). The surface of each membrane was imaged in three dimensions using gel-based surface profilometry (see Methods). For each foil, a surface image is shown with height indicated in color (left), and a height profile at the location of the dashed line (right). Measurements of surface roughness (Sq, see Methods) are given above each profile.

Due to resolution limitations of modern multi-material 3D printers, we were not able to print denticles at the smallest sizes present on living shark species (Figure 3.1). Attempts to print at denticle sizes with l_c less than 2 mm

(Figure 3.2) resulted in an unacceptable distortion of smaller surface features such as the ridges, valleys, and posteriorly pointed tips on the denticle surface (also see the discussion on printing denticles in Wen et al. 2015) (20). As a result, the smallest size denticles tested here were 2 – 5 times the denticle size common in many sharks, and more than 10 times larger than for fast open ocean pelagic sharks such as the mako (Figure 3.1; 5). The ability to print arrays of thousands of rigid denticles on a flexible substrate at a denticle size of 0.5 mm or smaller with accurate surface features on the order of 25 microns in size (or less) awaits new advances in 3D printing technology.

3.2.4 STATIC TESTING

Each of the 6 foils were tested statically (held still, with no motion of the leading edge) in a recirculating water flow tank with working dimensions 26 cm x 26 cm x 80 cm. The testing apparatus was the same as that used in previous studies on foil propulsion and shark denticle hydrodynamics (9,20,24,25). Each foil was attached to a mounting rod that held the foil under water with the foil placed in the center of the tank and oriented parallel to the incident flow. Using a six-axis load cell (Nano-17, ATI Industrial Automation Inc., Apex, NC, USA), drag forces were measured by finding the average force on the foil parallel to the direction of flow over a period of ten seconds. Drag forces were recorded at speeds ranging from 0.1 ms^{-1} to 0.5 ms^{-1} in increments of 0.05 ms^{-1}. With a membrane chord length of 157 mm for each foil, this gave a Re_C (Reynolds number with chord as characteristic length) range of approximately $1.5x10^4$ –

$8x10^4$. Each foil was tested at each flow speed a total of 6 times, and the standard error for the drag force measurements at each speed was determined.

Drag coefficients for static foil tests were calculated using the following equation:

$$C_D = \frac{2F_D}{\rho A U^2} \quad [3.1]$$

where A is the foil area, $\rho \approx 1000$ kg/m^3 is the density of water, U is the flow speed, and FD is the drag force experimentally measured for each foil at each given flow speed.

3.2.5 Dynamic Testing

For dynamic testing, where the foils were moved and propelled or swam against oncoming flow, the holding rod to which the foils were attached was connected to a rotary motor (Pittman, GM8724S009). In order to attain a fish-like swimming motion for the foils, the rotary motor generated a pitch motion of the rod in a sinusoidal pattern to create undulatory waves in the foil surface (26). From the six-axis load cell (ATI Nano-17: ATI Industrial Automation, Apex, NC, USA) attached to the holding rod, forces and torques were measured during propulsion. Using this experimental arrangement, two forms of dynamic testing were carried out: (*i*) measurement of self-propelled swimming speed for a given set of foil motion parameters (referred to as a motion program), and (*ii*) determining power coefficient curves over a range of motions under conditions of self-propulsion following procedures outlined in Saadat et al. (2017) (26).

For the first set of dynamic tests – finding self-propelled swimming speeds (SPS) for a given locomotion – a range of leading edge pitch motions (θ) and frequencies (*f*) were chosen for each of the foils, to generate a fish-like swimming motion. Previous research by Oeffner and Lauder 2012 (18) had shown that this range of leading edge pitches and frequencies generate foil curvatures that approximate those of freely-swimming sharks. As the front of the foil is pitched by the holding rod, a traveling undulatory wave is sent down the body of the foil, and this fish-like flapping motion allows the foil to generate thrust (26). Self-propelled speed, where average thrust is zero over a flapping cycle (27), was determined using a custom LabView program that altered the imposed free-stream flow and measured average thrust at each speed. This procedure to determine self-propelled swimming speeds was repeated five times for each motion and standard error for each measurement was calculated. Note that for each of the three different denticle foils, three motion programs to explore self-propelled speeds were chosen that corresponded to each of the foils' most efficient swimming-like motion (these motion programs were identified based on the results obtained from additional dynamic testing discussed in the following sections). Cost of transport (COT) was also reported for all of the swimming motions as the locomotor power (which was computed as the torque generated by the foil, T_z, times the angular velocity of the pitching motion, v_p) divided by the self-propelled swimming speed, SPS, for that motion.

$$C_D = \frac{2F_D}{\rho A U^2} \quad [3.2]$$

$$COT = \frac{Power}{SPS} \quad [3.3]$$

For the second set of dynamic testing experiments, obtaining power coefficient curves over a range of motions when the foil is self-propelling (see 26), testing was conducted at two chord-based Reynolds numbers: $Re_C = 3x10^4$ and $5.3x10^4$. The frequency-amplitude space of the motion of the foil (body waves created by the pitching of the foil) was explored at each Reynolds number in order to discover which frequency and pitching amplitude parameters generated a desired self-propelled swimming speed. Essentially, the imposed free-stream flow was set to the value of that of the desired self-propelled swimming speed, and as the foil dynamically moved at a given pitch amplitude, a series of pitch frequencies were input until the net force parallel to the flow on the foil was zero (meaning that it was then swimming at the desired self-propelled speed). Then, for the frequency at which the foil was self-propelling at that given pitch input, the side-to-side amplitude of the trailing edge was measured (using high speed videos taken at 2000Hz and at a resolution of 1024 pixels by 1024 pixels with a Photron mini-UX100 high-speed video camera). Measured amplitudes were then divided by the length of the foil to obtain non-dimensional amplitude, $A^* = A/L$. Power input to the foil was measured as described above to calculate a power coefficient (C_p) for each experimental test. These measurements were performed for a series of different imposed leading edge pitch amplitudes to construct a C_p vs. A^* curve (as in Figure 3.9). C_p is calculated as follows:

$$C_p = \frac{2P}{\rho U^3 S} \qquad [3.4]$$

where P is the measured power, ρ is the density of water (1000kg/m3), U is the imposed free-stream flow speed, and S is the undeformed planform area of the

foil. This curve describes the amount of power required for the foil to self-propel at a given trailing edge amplitude. Finally, following the procedures outlined in Saadat et al. (2017) (26), we plotted non-dimensionalized trailing edge amplitude A^* against nondimensionalized frequency f^* (=fL/U) to capture and better understand the dynamics of the undulatory propulsion of the various denticle foils.

3.3 RESULTS

3.3.1 STATIC TESTING

Experimental results of static drag testing are shown in Figure 3.5. In this plot, the Ds/Dm ratio evaluates whether the denticle foil surfaces are reducing or increasing drag compared to the smooth control surfaces. D_s is the drag force experienced by a denticle foil, while D_m is the drag force experienced by the denticle foils' corresponding smooth control surface. Thus, $D_s/D_m = 1$ (which is shown as the dashed line in Figure 3.5) corresponds to no difference in drag force between the denticle foil and its corresponding smooth control, whereas $D_s/D_m < 1$ (below the dashed line in Figure 3.5) demonstrates drag reduction for the denticle foil.

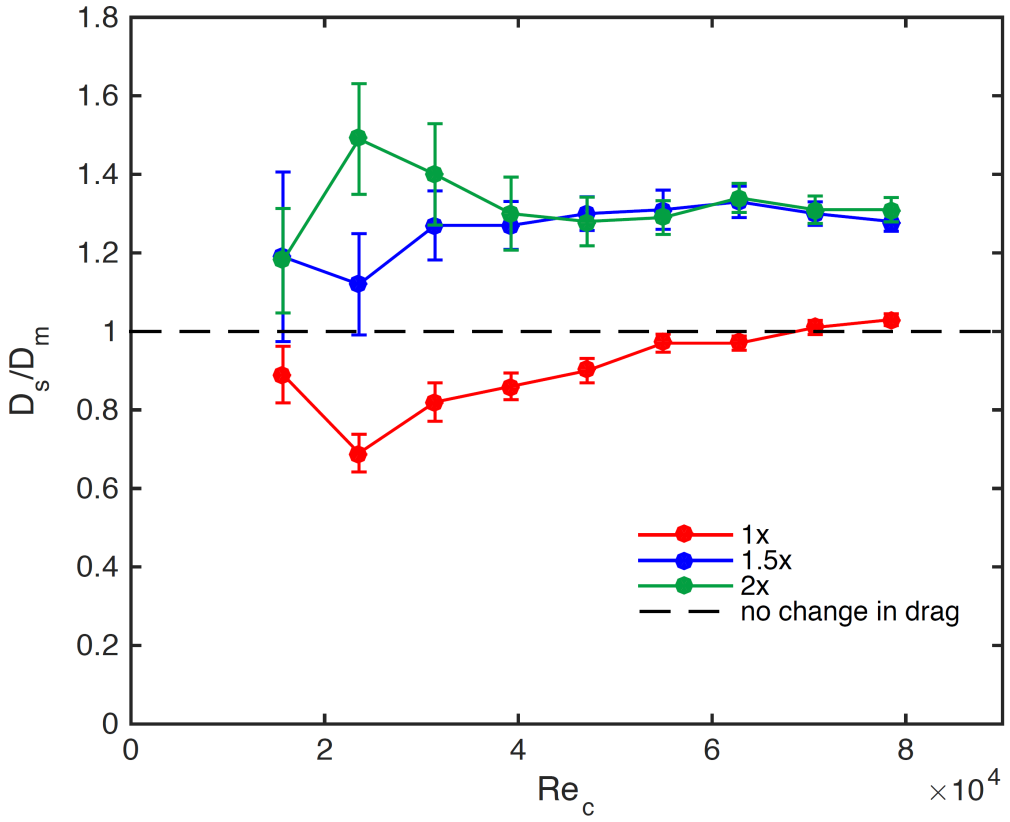

Figure 3.5: Static testing of drag forces experienced by each of the three tested biomimetic foils relative to their corresponding control plotted versus Reynolds number (Re_C - the Reynolds number based on the foil chord). D_s represents the drag experienced by a given shark skin foil at a given Re_C, whereas D_m represents the drag experienced by the shark skin's corresponding smooth control foil. Thus, D_s/D_m is a measure of how much the shark denticles are either increasing or decreasing drag compared to the corresponding control surfaces under uniform flow conditions. The dashed line represents $D_s/D_m = 1$, which is the case in which the shark skin foil and its corresponding control are producing the same amount of drag. Error bars are standard errors, N = 6 trials.

Only the 1x shark skin foil exhibited drag reduction compared to the smooth control (Figure 3.5), and it did so at seven of the nine Reynolds numbers tested. At lower speeds, drag reduction of the 1x shark denticle foil was most pronounced; however, at higher speeds the drag experienced by the 1x foil became greater than that of the control (D_s/D_m = 0.89, 0.69, 0.82, 0.86, 0.90, 0.97,

0.97, 1.01, 1.03 at Re_C = 1.57x104, 2.36x104, 3.14x104, 3.93x104, 4.71x104, 5.50x104, 6.28x104, 7.07x104, 7.85x104, for the 1x denticle foil respectively). For the larger denticles, drag reduction compared to their respective controls was never seen at any flow speed: denticle foils of the 1.5x and 2x sizes exhibited higher drag relative to the smooth control at all tested speeds (Figure 3.5). (D_s/D_m = 1.19, 1.12, 1.27, 1.27, 1.30, 1.31, 1.33, 1.30 and D_s/D_m = 1.18, 1.49, 1.40, 1.30, 1.28, 1.29, 1.34, 1.31, 1.31 at Re_C = 1.57x104, 2.36 x104, 3.14x104, 3.93x104, 4.71 x104, 5.50x104, 6.28x104, 7.07x104, 7.85x104, for the 1.5x and 2x denticle foils respectively).

Drag coefficients (C_D) for the various foils swimming at different flow speeds, and hence Reynolds numbers, are reported in Figure 3.6. All denticle foils exhibited lower drag coefficients compared to the corresponding control foils when the total wetted surface area was used in the C_D calculation (Figure 3.6*A*), since the denticle foils have a much larger wetted surface area due to their complex surface undulations and overlapping geometries (Table 3.1). In Figure 3.6*B*, when using the planform area for all tested foils to calculate drag coefficients, shark skin foils exhibited drag coefficients that were usually higher than their respective controls, except for speeds at which the 1x denticle foil showed reduced drag compared to its control.

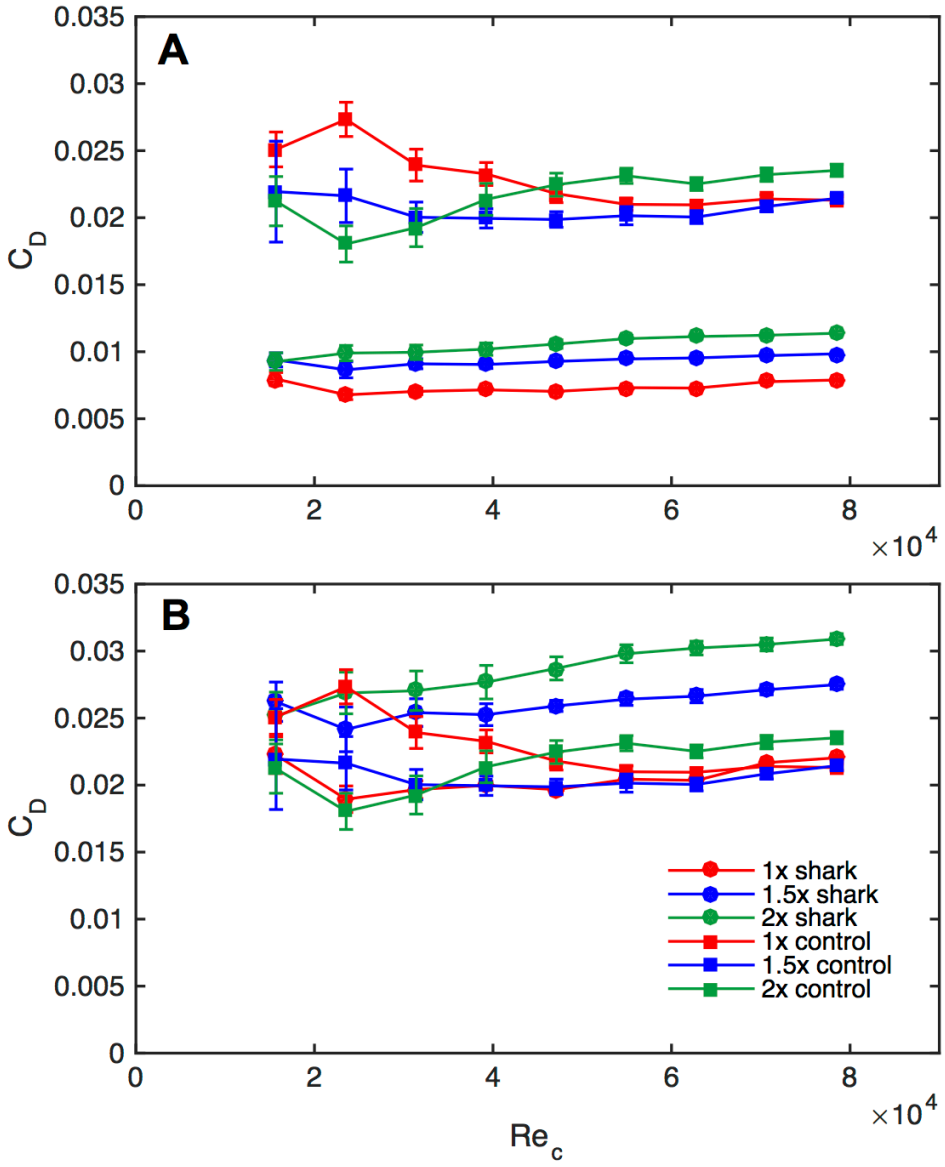

Figure 3.6: Experimental drag coefficient (C_D) data from static testing as a function of the Reynolds number based on the foil chord (Re_C) for each of the six foils (three shark skin foils of different size denticles as well as their corresponding controls). In (A), drag coefficients are calculated using the total wetted surface area (see Table 3.1), whereas in (B), drag coefficients are calculated using the planform area of the surface. Error bars are standard errors, N = 6 trials.

3.3.2 Dynamic Testing

Results for self-propelled swimming speed (SPS) measurements and the cost of transport (COT) calculations for the 1x denticle foil and its corresponding control are shown in Table 3.2 (the location that these motions lie on the C_p vs. A^* plane is labeled 1-9 in both Figure 3.7 and the various tables of the Results section), with corresponding results for the 1.5x and 2x foils in Tables 3.3 and 3.4, respectively. For all three motion programs, the 1x denticle foil had a higher SPS than its respective control (Table 3.2) despite having a wetted surface area more than twice that of the smooth control (Table 3.1). For the 1.5x foil tests, the self-propelled speed was higher for this denticle foil at the highest frequency (2.5 Hz), similar for the middle frequency (2 Hz), and slower for the lowest tested frequency (1.25 Hz) (Table 3.3). The largest denticle foil size (2x) showed slower SPS for all three tested frequencies (Table 3.4).

Table 3.2: Self-propelled swimming speeds and cost of transport for each of the various swimming motions tested for the 1x biomimetic shark skin foil and its corresponding control. See Figure 3.7 to locate where these pitch/frequency motions lie on the power coefficient-amplitude plane.

Point from Figure 3.7	Pitch [deg.]	Frequency [Hz]	SPS of Control (m/s)	SPS of Shark Membrane (m/s)	COT of Control (J/m)	COT of Shark Membrane (J/m)
1	15	2	0.184 ± 0.0104	0.199 ± 0.0035	0.082 ± 0.0046	0.086 ± 0.0016
2	20	1	0.157 ± 0.0019	0.195 ± 0.0020	0.072 ± 0.0009	0.096 ± 0.0023
3	25	1.5	0.202 ± 0.0025	0.235 ± 0.0048	0.138 ± 0.0123	0.163 ± 0.0034

Table 3.3: Self-propelled swimming speeds and cost of transport for each of the various swimming motions tested for the 1.5x biomimetic shark skin foil and its corresponding control. See Figure 3.7 to locate where these pitch/frequency motions lie on the power coefficient-amplitude plane.

Point from Figure 3.7	Pitch [deg.]	Frequency [Hz]	SPS of Control (m/s)	SPS of Shark Membrane (m/s)	COT of Control (J/m)	COT of Shark Membrane (J/m)
4	15	2.5	0.169 ± 0.0055	0.199 ± 0.0119	0.172 ± 0.0056	0.145 ± 0.0087
5	20	2	0.200 ± 0.0064	0.190 ± 0.0109	0.155 ± 0.0049	0.174 ± 0.0010
6	25	1.25	0.188 ± 0.0054	0.169 ± 0.0030	0.132 ± 0.0038	0.190 ± 0.0034

Table 3.4: Self-propelled swimming speeds and cost of transport for each of the various swimming motions tested for the 2x biomimetic shark skin foil and its corresponding control. See Figure 3.7 to locate where these pitch/frequency motions lie on the power coefficient-amplitude plane.

Point from Figure 3.7	Pitch [deg.]	Frequency [Hz]	SPS of Control (m/s)	SPS of Shark Membrane (m/s)	COT of Control (J/m)	COT of Shark Membrane (J/m)
7	20	2	0.189 ± 0.0157	0.155 ± 0.0099	0.218 ± 0.0180	0.228 ± 0.0146
8	25	1.5	0.219 ± 0.0060	0.195 ± 0.0092	0.215 ± 0.0059	0.196 ± 0.0092
9	30	1	0.204 ± 0.0050	0.169 ± 0.0024	0.217 ± 0.0054	0.222 ± 0.0031

The 1x denticle foil always had a higher COT than its respective control, although the COT values for the 2 Hz tests were not significantly different. For the 1.5x and 2x denticle foils, one motion program had a lower COT for each (2.5 Hz and 1.5 Hz respectively), while the other tested motion programs resulted in a higher COT for the denticle foils. The 1.5x denticle foil performed best relative

to the control when tested at 15° pitch and 2.5 Hz in the sense of having both a higher SPS and a lower COT, although the 1x denticle foil had a higher SPS with an equivalent COT compared to its smooth control foil at 2 Hz.

Figure 3.7 shows power curves with the power coefficient for each denticle foil and its control plotted against dimensionless amplitude A^* =A/L of trailing edge undulatory motion. All curves represent conditions of self-propulsion, and follow roughly the same pattern: a region of low power consumption (where C_p is lowest) around A^* = 0.1-0.3 when self-propelling at Re_C = 3x104, and increasing power consumption when the imposed motion program generates large trailing edge amplitudes. The tight range of 0.1-0.3 for non-dimensional trailing edge amplitude is associated with optimal swimming at cruise condition as discussed by Saadat et al. (2017) (26). The values for optimal trailing edge amplitude obtained here fall in the range of observed tail-beat amplitude for diverse species of fish under the free swimming/self-propelled condition (26). Most curves initially start with a slightly larger power coefficient before decreasing to a minimum power region. In Figure 3.7, denticle foils always have a higher power coefficient at any given motion (A^*) compared to their respective controls. Thus, it appears that at this moderate self-propelling swimming speed, the smooth controls are swimming more efficiently in terms of power use than their corresponding denticle foils.

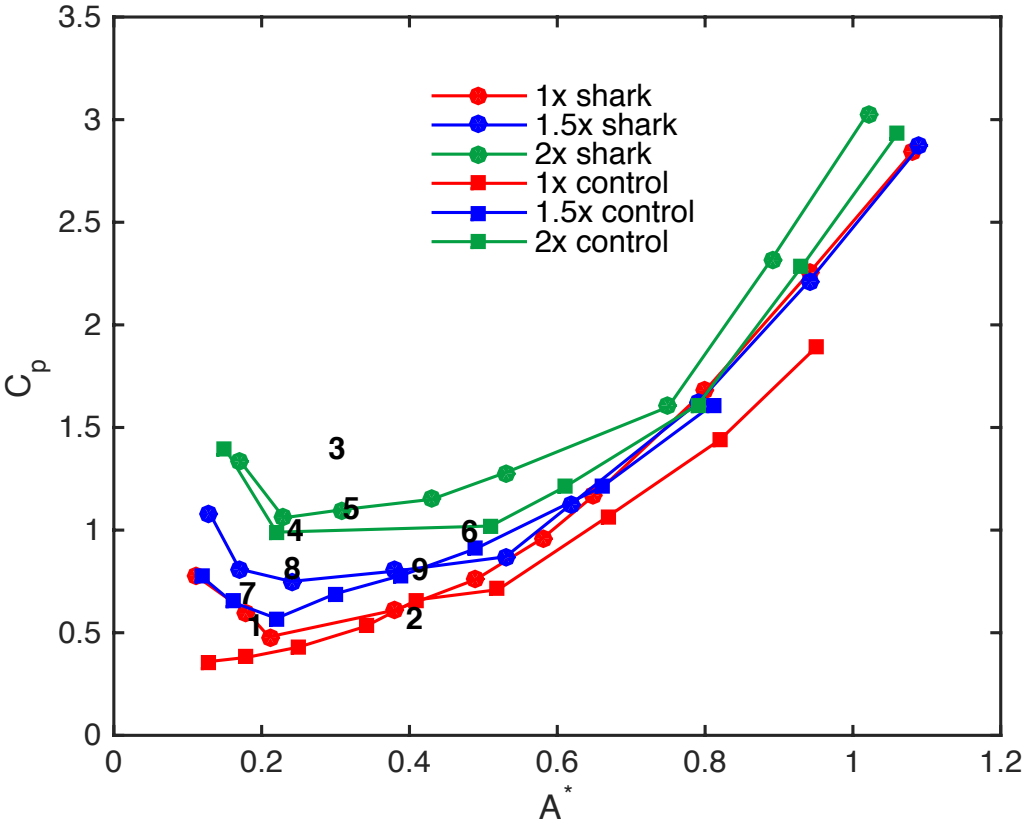

Figure 3.7: Measured C_p (coefficient of power) as a function of motion (which is considered here to be dimensionless tip-to-tip amplitude, $A^*=A/L$) at a self-propelled speed corresponding to a Reynolds number based on the foil chord (Re_C) of $3x10^4$ for the six different foils considered in this study (3 biomimetic shark skin foils as well as their 3 corresponding controls). The 1-9 numbered markers in the plot above show the location on this C_p vs. A^* plane of where the testing parameters were chosen for each of the foils for the other type of dynamic testing (i.e. finding self-propelled swimming speeds for a given locomotion). Tables 3.2, 3.3, and 3.4 provide the testing parameters and results corresponding to these 1-9 numbered marks. Note that some A^* values were challenging to obtain due to the high pitch frequencies and amplitudes required that could damage the robotic flapping device and/or the force transducer, and these experimental parameters were not tested.

Figure 3.8 illustrates dimensionless speed contours for tests at Re_C = $3x10^4$ for the 1x and 2x denticle foils and their controls of the same mass. These curves present the complete kinematic envelope for our flapping foils at cruise

condition whereby frequency and amplitude are controllable parameters (inputs) and the speed is a dependent variable (outcome). The choice of non-dimensional amplitude (A^*=A/L) and frequency (f^*=fL/U) arise in the dimensional analysis of a cruising swimmer as presented in Saadat et al. (2017) (26). One aspect of the locomotion studied here shown by Figure 3.8 is the constancy and independence of Strouhal number of the motion from the kinematics of the flapping when A^* is maintained at a value around 0.2. The constancy of St results in cruising speed being linearly related to the frequency of flapping. For dimensionless amplitudes, A^*, below 0.4, there is a clear mass effect with the larger denticle foil and its control producing higher relative trailing edge motions at all f^* =fL/U. For these experiments, biomimetic shark skin surfaces are not distinguishable from their smooth controls.

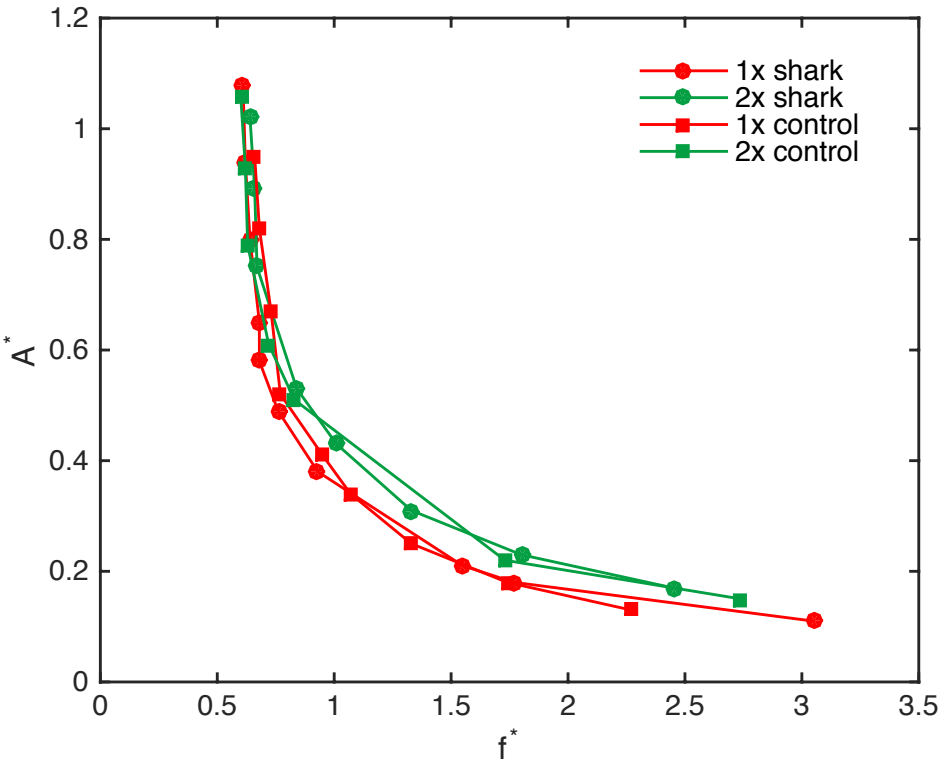

Figure 3.8. Dimensionless speed contours (dimensionless tip-to-tip amplitude A^*=A/L vs. dimensionless frequency, f^* = fL/U) for the 1x and 2x shark skin foils and the corresponding control surfaces at a self-propelled speed corresponding to a Reynolds number based on the foil chord (Re_C) of $3x10^4$.

The same procedure that was used to measure the power coefficient curves for all of the foils at the moderate Reynolds number based on the foil cord (Re_C = $3x10^4$) shown in Figure 3.7, was also used for a higher self-propelled speed (Re_C = $5.3x10^4$): the results for this higher self-propelled speed are shown in Figures 3.9 and 3.10. In Figure 3.9, the power coefficient is plotted at various A^* values for the 1x denticle and control foils at both the previously reported moderate speed (for comparison) and also for the higher self-propelled speed. At this higher Re_C, several of the 1x denticle foil power coefficients were lower than their respective controls at the higher A^* values between 0.5 and 0.7. These results

indicate that the 1x denticle foils are consuming lower power while swimming than their respective controls at motion programs that generate higher trailing edge amplitudes. Figure 3.10 shows dimensionless speed contours for tests at Re_C = 5.3x10^4 for the 1x and 2x denticle foils and their controls of the same mass. In general, for higher values of A^*, the 1x denticle foil swam with lower f^* than its corresponding control.

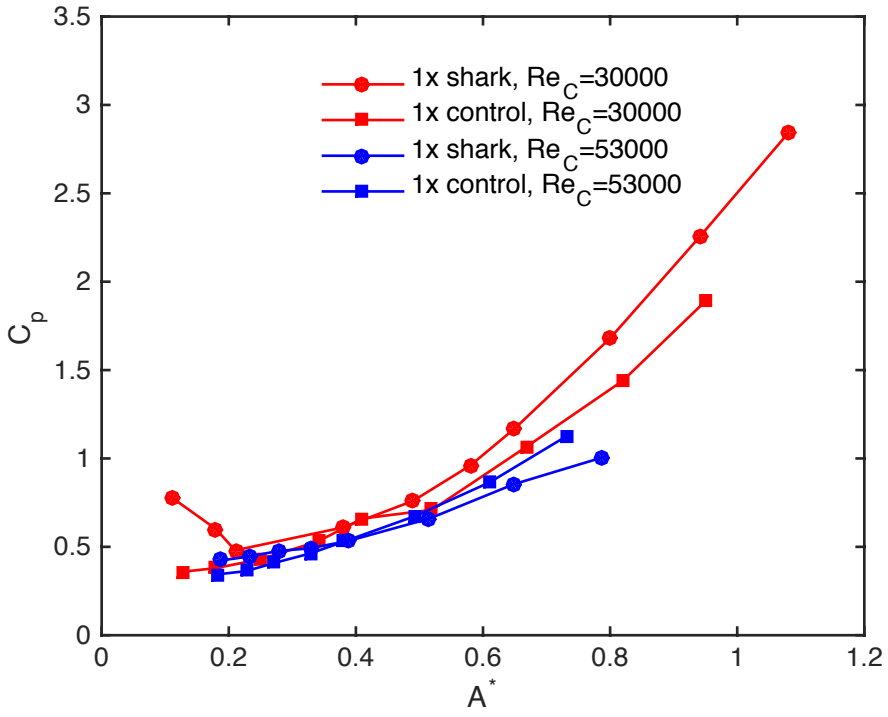

Figure 3.9: Measured C_p (coefficient of power) as a function of motion (dimensionless tip-to-tip amplitude, A^* =A/L) at self-propelled speeds corresponding to Reynolds numbers based on the foil chord (Re_C) of 3x10^4 and 5.3x10^4 for the 1x foils.

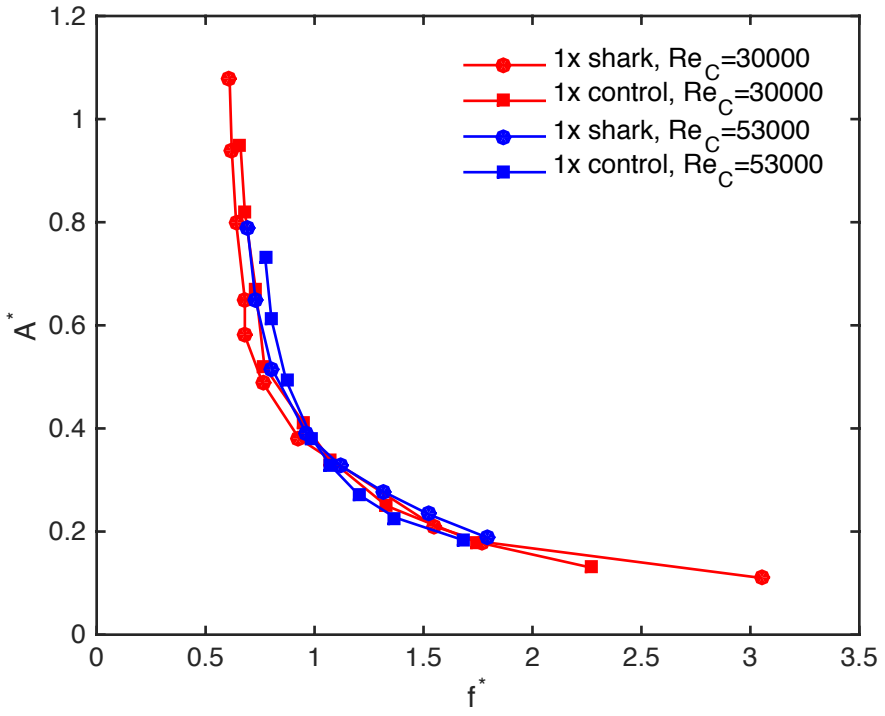

Figure 3.10: Dimensionless speed contours (dimensionless tip-to-tip amplitude, A^*=A/L vs. dimensionless frequency, f^* = fL/U) for the 1x shark and control foils at self-propelled speeds corresponding to a Reynolds number based on the foil chord (Re_C) of $3x10^4$ and $5.3x10^4$.

3.4 DISCUSSION

We found that denticle-containing foils performed better with smaller denticles and at higher swimming speeds when tested dynamically, and we identified several conditions of frequency and leading edge pitch at which the denticle foils swam with a higher self-propelled speed (SPS) as well as with lower energetic cost of transport (COT) than their corresponding smooth controls. These results demonstrate that even though foils with denticles on their surfaces have more than twice the total surface area of smooth controls of equivalent mass due to the presence of denticles, there are still motion parameters and denticle size combinations that result in improved swimming performance. Furthermore,

despite findings in the computational literature suggesting that shark denticle shapes on a membrane surface produce increased drag (13), we measured significant drag reduction relative to smooth controls during static tests for the smallest denticle size, while increasing denticle size on the foils resulted in higher drag relative to smooth controls.

Despite the new functional insights gained from the present study, two overall limitations stem from (*i*) current constraints on the size limits at which small shark denticles and flexible membranes can be accurately 3D printed together, and (*ii*) our inability to test dynamically under conditions of both high flapping frequencies and large pitch amplitudes at high Reynolds numbers. In these studies, we 3D printed the 1x denticles at the smallest size at which the final 3D printed denticles (Figures 3.3, 3.4) still retained sufficient detail to approximate those found in real shark skin (Figure 3.1; 5). While the resulting morphology of the 3D printed denticles was biologically accurate, their larger size resulted in a corresponding increase in surface roughness from 150 μm for the 1x foils to 363 μm for the 2x foils. Attempts to print denticles at smaller sizes resulted in unacceptably distorted surfaces that did not resemble shark skin closely. Surface roughness of our 3D printed biomimetic shark skin foils also exceeded that of real shark skin. Measured biological shark skin roughness (Sq) values ranged from 15.1 μm to 33.4 μm (Figure 3.1), while the biomimetic shark skin foil surfaces had surface roughnesses that varied from 150 μm to 363 μm (Figure 3.4). In addition, the maximal pitch motor torque of our experimental flapping system limited the extent to which we could impose rapid high amplitude

motion to the leading membrane edge and execute flapping at high Reynolds numbers (Re), which restricted our dynamic tests to a maximum Re_C of $5.3x10^4$.

Shark species vary widely in denticle size and shape (Figure 3.1; 5,7,19,28), and we believe that our results both represent the range of effects of a denticle surface on swimming dynamics, and point toward future analyses with smaller denticles when manufacturing capabilities allow for such. Shark denticles vary from around 210 μm in length in mako sharks, to almost 1 millimeter in gulper sharks (5). Many species have denticles in the range of 300 to 600 μm. Thus, while the smallest 1x denticle size tested here is still nearly twice the size of larger shark denticles, our results, with caveats, still suggest that smaller denticles confer hydrodynamic benefits. It should be noted, however, that the hydrodynamic effects of different sized denticles may not change dramatically with denticle size alone, as such effects will be dominated by the boundary layer thickness length scale. Boundary layer thickness, orthogonal to the denticle surface, can vary considerably during complex motions, and as such, is highly sensitive to both swimming speed and body oscillation, which induces complex fluctuation in the thickness length scale (29). It is thus difficult to determine just how denticle size alone will affect boundary layer thickness in the absence of direct measurements of the boundary layer over biomimetic shark skin membranes. Preliminary measurements of this kind were presented for biomimetic shark skin by Lauder et al. (2016), but boundary layer thickness was not quantified over a body oscillation cycle relative to that on a control surface (19).

3.4.1 Static Drag Reduction by Denticles

Our results are generally similar to those reported by Wen et al. (2015), whose tests on a biomimetic staggered-overlapped shark skin foil exhibited reduced drag in static testing (20). We see a similar trend in drag reduction with the 1x denticle pattern described here, which exhibits reduced drag at lower flow speeds, and increased drag at faster flow speeds (Figure 3.5). Since all tested foils with different denticle sizes have the same Reynolds number based on the foil chord (Rec), the different patterns of response to increasing flow that we observed for the three foils with differently sized denticles cannot simply be attributed to Re_C. The foil with the smallest denticles (1x) is the only one that exhibited drag reduction, and both foils with larger denticles never showed a reduction in drag relative to a smooth control (Figure 3.5). Reynolds numbers for the three tested foils (1x, 1.5x, and 2x) based on denticle size (Re_D) varied from 200 to 1000, 300 to 1500, and 400 to 2000 respectively, and it is reasonable to expect that as denticle fabrication at smaller and smaller length scales becomes possible, drag reduction may also become evident at higher free-stream flow speeds. For a 1 m length shark swimming at a speed of 1 m/s, the Re_D ranges from 150 to 600 for denticles of 150 μm to 600 μm in size. This contrasts to a whole animal Re using body length as the characteristic length of Re = 1 x 106 or greater at high shark swimming speeds. The smallest 1x denticle foil at the slowest test speeds thus has Re_D values that are only slightly higher than the Re_D of the mako shark based

on its denticles, a value at which, we observe the best drag reduction in this study (Figure 3.5).

A recent report that examined the role of ridged surfaces on drag reduction (30) used a numerical approach to show that using the chord Reynolds number alone is not a good metric for evaluating drag reduction. These authors define a new Reynolds number ($Re_{\lambda/L}$) that was based on chord length L and the wavelength between adjacent ridges, λ. Raayai-Ardakani and McKinley showed that at slower speeds and with certain ridge aspect ratios (the ratio of two times the height of the ridge to the wavelength between ridges), drag forces were reduced relative to a smooth surface (30). The study also showed that for chord Reynolds numbers greater than 10^4 (which is in the range of speeds tested in this study), values of unity for this aspect ratio tend to be best for drag reduction. Based on the images shown in Figure 3.1 and Figure 3.4 comparing shark denticle patterns to that of our biomimetic foils, if we assume that ridges as defined by Raayai-Ardakani and McKinley are equivalent to the pattern and spacing of middle denticle ridges on sharks, we note that the aspect ratios of both the biomimetic denticles as well as the biological denticles is roughly unity (30). Although there are many differences between the three-dimensional denticle morphology in sharks and the long continuous triangular ridge used by Raayai-Ardakani and McKinley, it is noteworthy that our foils function in the general region of $Re_{\lambda/L}$ identified by Raayai-Ardakani and McKinley (2017) as a drag-reducing zone (30).

The recent study of Boomsma and Sotiropoulos (2016) has called into question the ability of shark skin and biomimetic shark skin foils to reduce drag compared to their smooth controls. Boomsma and Sotiropoulos (2016) used an immersed boundary method to compute flow over a shark denticle surface, and they estimated that a denticle surface increases drag by 44%-50% (13). This result is similar to the maximal increase that we observed for the largest (2x) denticle sizes (Figure 3.5) but stands in sharp contrast to the reduction in drag seen experimentally for the 1x denticle foil both here (Figure 3.5) and by Wen et al. (2015) (20). Despite these radically different outcomes, these simulations were run using the same denticle parameters as those of the biomimetic surfaces that reduce drag both in our present study and those of Wen et al. (2015) (20). It is important to note, however, that the employed methods deviate from each other in that their Reynolds number (2800) was much lower than the lowest Reynolds number used in the present study, a slow speed that we were unable to precisely test with our current flow tank setup and force transducer. Although there are many differences between the computational domain of Boomsma and Sotiropoulos (2016) and the experimental configuration and free-stream speeds tested here, the differences in results are nonetheless perplexing. Boomsma and Sotiropoulos (2016) do compute a drag reduction of 5% for riblet configurations in general accordance with previous experimental data (13, 31-33), so the lack of concordance with the experimental demonstration of drag reduction with biomimetic denticle surfaces demonstrates the complexity of these interactions and needs further study.

3.4.2 Dynamic Testing of Propulsion

The importance of using dynamic tests for understanding the function of shark denticle surfaces has been emphasized previously by Lauder et al. (2016) and Wen et al. (2014; 2015) (9,19,20). Although Domel et al. (2018) recently shed light on the effects of denticle morphology on vortex generation on airfoils, all tests in that study were carried out under static conditions with the airfoil at a range of (fixed) angles of attack (10). To obtain a more complete picture of the hydrodynamic function of denticles, dynamic tests are needed as denticles experience dynamic flow conditions when sharks swim with undulatory propulsion. Testing under conditions of propulsion in which the denticle-embedded surface deforms during undulatory motion and undergoes cyclic curvature which interacts with free-stream flow is more biologically relevant to shark locomotion than static testing alone, in which the shark skin models do not move. The surface of swimming sharks undergoes changes in angle of attack throughout a tail beat cycle during locomotion (34-38), and so testing of shark skin effects should include conditions that mimic these time-dependent flow conditions as closely as possible. Also, comparison of water flow patterns between static tests and flapping propulsion by Lauder et al. (2016) revealed considerable differences between the two types of testing, and suggest that flow alteration on the skin surface by denticles changes substantially when motion of the surface occurs (19). In particular, flow in and among denticles was greatly reduced during many phases of the flapping cycle compared to static test conditions (19).

Although the vast majority of literature on shark skin denticles addresses the possibility of drag reduction as a result of the roughened surface, both Oeffner and Lauder (2012) and Domel et al. (2018) have demonstrated that denticle surfaces can alter thrust and lift forces and hence affect propulsion by affecting the formation and position of separation bubbles on the skin surface (10,24). The effects of denticle shape and arrangement on lift and thrust have yet to be comprehensively explored, but based on this previous work, we might expect that the effects of dynamic testing under conditions of denticle surface motion could reveal different effects and patterns of denticle size than emerge from static tests alone. It is also worth noting that we are not able to quantitatively compare changes in cost of transport and power consumption between previous work on the propulsion of real shark skin samples (18) and the biomimetic foils studied here, as force and power were not measured in the previous research on propulsion of real shark skin. As such, additional experiments on the propulsion of real shark skin samples and the alteration of surface configuration while measuring power consumed during swimming are required and are an active area of ongoing research.

The dynamic tests conducted here, with several combinations of leading edge pitch and frequency at two swimming speeds, result in undulatory propulsion of the manufactured denticle foils that permit calculation of locomotor self-propelled speeds as well as efficiency and cost of transport (26). Our results show that the effect of denticle size and Reynolds number (ReC) on propulsion vary with the imposed motion program. For some combinations of size, pitch,

and frequency, the denticle foils demonstrated a slower SPS than their corresponding smooth control and a higher COT (Tables 3.2, 3.3, 3.4): for the two largest sizes of denticle surfaces, five of the six tests showed reduced SPS by the denticles compared to their smooth control, while one test showed equivalent swimming performance. However, for the 1x denticle size, all three test conditions resulted in improved denticle foil SPS relative to the control. These results suggest that the larger denticle sizes result in either increased drag or reduced effects on lift and thrust, or both, that reduce swimming performance relative to a smooth control.

When the flexible membranes of the biomimetic shark skin foils bend during undulatory propulsion, individual denticles can interact with each other due to their close proximity and tightly packed and overlapping pattern (Figures 3.3, 3.4), and such interactions might be expected to increase the COT depending on the imposed motion program (20). Our results show that many of the motion programs and denticle sizes result in increased swimming costs (Tables 3.2, 3.3, 3.4) and that this effect is not dependent on denticle size, at least for the sizes tested here. Five of the nine tested experimental conditions resulted in increased COT, two were equivalent between the control and denticle surface, while two tests showed reduced COT of denticle surfaces relative to their smooth control. Only one test, the 1.5x foil at 2.5 Hz and 15° pitch, generated both increased SPS and reduced COT for the shark skin surface. Motta et al. (2012) and Lang et al. (2014) have noted that for mako sharks, the denticles are passively mobile within the skin and that denticles may change orientation based on surface flow

characteristics (8,15). But another possible explanation for shark denticles that are flexibly embedded within the skin is to reduce COT, which results from bending the skin during undulatory propulsion. Denticles on real shark skin can overlap considerably (Figure 3.1) and skin curvature that occurs during body bending would result in increased energetic cost if denticles were rigidly embedded. In our manufactured denticle membranes, however, the modulus of the basal substrate to which the denticles were embedded was not low enough to facilitate such mobility. While this may be the case, future advances in the multi-material additive manufacturing of elastomers with moduli in the kPa range could be used to test this cost of transport hypothesis in biomimetic shark skins by directly altering the extent to which individual denticles can move relative to the skin surface.

Our measurement of swimming kinematics and power requirements followed the procedures outlined in Saadat et al. (2017) who suggested plotting power coefficients against non dimensionalized trailing edge amplitude A^* (A/L) and frequency f^* (fL/U) to capture the dynamics of undulatory propulsion (26). The data on the biomimetic and control foils' propulsion (Figures 3.7-3.10) show that size effects dominate differences between the smallest and largest foils. It is not surprising that power requirements should increase with foil mass (for both the denticle and smooth control foils), and that as foil inertia increases during flapping propulsion, the power required to swim at a given speed also increases. Denticles on the foil surface also change the power required for the foils in most of the tests, and as a result, power coefficients for denticle foils are generally

higher than for controls at a given value of A^* at the lower Re_C tested (Figures 3.7, 3.8). However, when the smallest denticles (1x size) were tested at a higher self-propelling speed, we observed that for some motion programs, this denticle foil used less power to swim than its respective control (Figure 3.9). We predict that as testing becomes possible at higher Re_C values that begin to approach that of large sharks swimming rapidly (on the order of 500,000 or so) and as our ability to manufacture smaller denticles improves, we will see a greater reduction for the biomimetic foils in power consumption relative to smooth-surfaced controls. These results that showed that power requirements increased with foil mass also suggest that there may be natural selection for reduced denticle mass in rapidly swimming sharks and that the thin and flattened crowns of mako and white shark denticles, for example (Figure 3.1), may act to reduce power requirements of bending the body during swimming by reducing denticle-denticle interactions in concave regions during undulation.

Finally, when both the static and dynamic test results are considered together for the biomimetic denticles tested here, we find that drag reduction (static tests) is improved at low speeds, while improved propulsion (dynamic tests) occurs at higher Re_C and higher flapping frequencies. These results suggest that denticles may have different hydrodynamic functions depending on body orientation (and hence the local fluid environment) and locomotory style. The fluid environment around the body of a swimming shark varies tremendously over the head, tail, pectoral fins, and different body regions (due to the tilted swimming postures common in many sharks) and likely have differing turbulence levels and

differing patterns of flow separation that change as the body and fins move (38-41). Differing levels of oscillatory amplitude along the shark body from head to tail are also likely to impose different hydrodynamic conditions on the skin, although specifics of how flow varies in the near skin region around the body are largely unknown (41).

Different locomotor behaviors such as steady swimming, gliding, accelerations, and rapid turning maneuvers also are all likely to result in altered flow patterns at any one location on the body, and the static and dynamic results reported here may provide insight into different aspects of shark locomotion. Our static drag testing results may be most relevant to slower speed gliding behavior where the body is held relatively steady, while our dynamic testing results may be more relevant during undulatory locomotion. These two modes of locomotion are commonly used in conjunction with one another during normal shark swimming as can be observed when a shark will tend to move quickly and dynamically to generate thrust and then glide following a bout of undulation. Our dynamic testing results may also reflect changes in both thrust and lift and drag forces generated by denticle surfaces under dynamic motion (see also Domel et al. 2018) (10). The changing angle of attack that denticles experience as the shark body undergoes undulatory locomotion is reflective of the dynamic tests here as the denticle surface of different regions of the swimming foils experiences time-dependent changes in incident flow. Because denticle structure, which exhibits site-specific variability across the body surface (5,7), may reflect a functional compromise that reflects both dynamic and static flow patterns, there remains considerable scope

for future research to develop an understanding of precisely how and why different denticle surface structures affect flow, and how flow varies in the near-skin region during swimming. The results presented here not only provide important insight into shark locomotor hydrodynamics, but also provide conceptual guidelines for the design of aquatic or aerial bio-inspired robots. More generally, any dynamic system moving through a fluid medium could potentially benefit from both drag reduction and thrust enhancement through the incorporation of these shark-inspired surface coatings.

3.5 REFERENCES

[1] Hamlett, W. C. ed, (1999). Sharks, Skates, and Rays. *The Biology of Elasmobranch Fishes*. Baltimore: Johns Hopkins Univ. Press.

[2] Castro, J. I. (2011). *The Sharks of North America*. Oxford: Oxford Univ. Press.

[3] Carrier, J. C., Musick J. A., and Heithaus, M R. (2012). *Biology of Sharks and Their Relatives*. Boca Raton: CRC Press.

[4] Klimley, A. P., (2013). *The Biology of Sharks and Rays*. University of Chicago Press.

[5] Ankhelyi, M., Wainwright, D. K., and Lauder, G. V. (2018). Diversity of dermal denticle structure in sharks: skin surface roughness and three-dimensional morphology. *J. Morphol*., doi.org/10.1002/jmor.20836.

[6] Bechert, D. W., Hoppe, G., and Reif, W. E. (1985). On the drag reduction of the shark skin. *AIAA Journal.,* 85-0546, 1-18.

[7] Reif, W. E. (1985). Squamation and Ecology of Sharks Cour. *Forsch.-Inst. Senckenberg*, 78, 1-255.

[8] Motta, P., Habegger, M. L., Lang, A., Hueter, R., and Davis, J. (2012). Scale morphology and flexibility in the shortfin mako Isurus oxyrinchus and the blacktip shark Carcharhinus limbatus. *J Morphol*., 273.

[9] Wen L., Weaver J. C., and Lauder, G. V. (2014). Biomimetic shark skin: design, fabrication, and hydrodynamic function. *J. Exp. Biol*., 217, 1656-66.

[10] Domel, A. G., Saadat, M., Weaver, J. C., Haj-Hariri, H., Bertoldi, K., and Lauder, G. V. (2018). Shark denticle-inspired designs for improved aerodynamics. *J. Roy. Soc. Inter*., 15, 20170828.

[11] Dillon, E. M., Norris, R. D., and O'Dea, A. (2017). Dermal denticles as a tool to reconstruct shark communities. *Mar. Ecol. Prog*., Ser. 566, 117-34.

[12] Díez, G., Soto, M. and Blanco, J. M. (2015). Biological characterization of the skin of shortfin mako shark Isurus oxyrinchus and preliminary study of the hydrodynamic behaviour through computational fluid dynamics. *J. Fish. Biol*., 87, 123–37.

[13] Boomsma, A. and Sotiropoulos, F. (2016). Direct numerical simulation of sharkskin denticles in turbulent channel flow. *Phys. Fluids*., 28, 035106.

[14] Lang, A. W., Motta, P., Hidalgo, P., and Westcott, M. (2008). Bristled shark skin: a microgeometry for boundary layer control?. *Bioinsp. Biomimet*., 3, 046005.

[15] Lang, A. W., Bradshaw, M. T., Smith, J. A., Wheelus, J. N., Motta, P. J., Habegger, M. L., and Hueter, R. E. (2014). Movable shark scales act as a

passive dynamic micro-roughness to control flow separation. *Bioinsp. Biomimet*., 9, 036017.

[16] Dean, B. and Bhushan, B. (2010). Shark-skin surfaces for fluid-drag reduction in turbulent flow: a review. *Philosophical Transactions of the Royal Society A: Mathematical, Physical and Engineering Science*s, 368, 4775-806.

[17] Yuehao, L., Deyuan, Z., and Huawei, C. (2012). Research on Manufacturing Vivid Trans-Scale Shark Skin Surface and Drag-Reducing Effect Simulation. *Advanced Science Letters,* 5, 49-55.

[18] Oeffner, J. and Lauder, G. V. (2012). The hydrodynamic function of shark skin and two biomimetic applications. *J. Exp. Biol*., 215, 785-95.

[19] Lauder, G. V., Wainwright, D. K., Domel, A. G., Weaver, J. C., Wen, L., and Bertoldi, K. (2016). Structure, biomimetics, and fluid dynamics of fish skin surfaces. *Physical review Fluids,* 1, 060502.

[20] Wen, L., Weaver, J. C., Thornycroft, P. J. M., and Lauder, G. V. (2015). Hydrodynamic function of biomimetic shark skin: effect of denticle pattern and spacing. *Bioinsp. Biomimet*., 10, 1-13.

[21] Wainwright, D. K. and Lauder, G. V. (2016). Three-dimensional analysis of scale morphology in bluegill sunfish, Lepomis macrochirus. *Zoology*, 119, 182-95.

[22] Wainwright, D. K., Lauder, G. V., and Weaver, J. C. (2017). Imaging biological surface topography in situ and in vivo. *Methods in Ecology and Evolution*, 8, 1626–38.

[23] Wainwright, D. K. and Lauder, G. V. (2018). Mucus matters: the slippery and complex surfaces of fish, In *Functional Surfaces in Biology III*, ed E Gorb and S Gorb. Berlin: Springer Verlag.

[24] Lauder, G. V., Flammang, B. E., and Alben, S. (2012). Passive robotic models of propulsion by the bodies and caudal fins of fish Int. *Comp. Biol*., 52, 576–87.

[25] Shelton, R. M., Thornycroft, P. J. M. and Lauder, G. V. (2014). Undulatory locomotion by flexible foils as biomimetic models for understanding fish propulsion. *J. Exp. Biol*., 217, 2110-20.

[26] Saadat, M., Fish, F. E., Domel, A. G., Di Santo, V., Lauder, G. V., and Haj-Hariri, H. (2017). On the rules for aquatic locomotion. *Physical Review Fluids*, 2, 083102.

[27] Lauder, G. V., Lim, J., Shelton, R., Witt, C., Anderson, E. J., and Tangorra, J. (2011). Robotic models for studying undulatory locomotion in fishes. *Marine Tech. Soc. J*., 45, 41-55.

[28] Castro, J. I. (1983). *The Sharks of North American Waters*. College Station: Texas A&M University Press.

[29] Yanase, K. and Saarenrinne, P. (2015). Unsteady turbulent boundary layers in swimming rainbow trout. *J. Exp. Biol*., 218, 1373-1385.

[30] Raayai-Ardakani, S. and McKinley, G. H. (2017). Drag reduction using wrinkled surfaces in high Reynolds number laminar boundary layer flows. *Phys. Fluids*., 29, 093605.

[31] Bechert, D. W., Bruse, M., and Hage, W. (2000). Experiments with three-

dimensional riblets as an idealized model of shark skin. *Exp. Fluids*., 28, 403-12.

[32] Bechert, D. W. and Hage, W. (2007). Drag reduction with riblets in nature and engineering, In *Flow Phenomena* in Nature. Vol. 2. Inspiration, learning, and application, ed R Liebe. Southampton. UK: WIT Press. pp 457-69.

[33] Dean, B. (2011). The Effect of Shark Skin Inspired Riblet Geometries on Drag in Rectangular Duct Flow Masters Thesis in Mechanical Engineering, Ohio State University, pages.

[34] Webb, P. W. and Keyes, R. S. (1982). Swimming kinematics of sharks. *Fish. Bull*., 80, 803-12.

[35] Donley, J. and Shadwick, R. (2003). Steady swimming muscle dynamics in the leopard shark Triakis semifasciata. *J. Exp. Biol*., 206, 1117-26.

[36] Shadwick, R. and Gemballa, S. (2006). Structure, kinematics, and muscle dynamics in undulatory swimming. In *Fish Biomechanics*. Vol. 23 in Fish Physiology, ed R E Shadwick and G. V. Lauder. San Diego: Academic Press. pp 241-80.

[37] Lauder, G. V. (2006). Locomotion*,* In *The Physiology of Fishes*, Third Edition, ed D. H. Evans and J. B. Claiborne. Boca Raton: CRC Press. pp 3-46.

[38] Lauder, G. V. and DiSanto, V. (2015). Swimming mechanics and energetics of elasmobranch fishes, In *Fish Physiology* Vol. 34A, Physiology of Elasmobranch Fishes: Structure and Interaction with Environment, ed R E

Shadwick, et al. New York: Academic Press. pp 219-53.

[39] Wilga, C. D. and Lauder, G. V. (2000). Three-dimensional kinematics and wake structure of the pectoral fins during locomotion in leopard sharks Triakis semifasciata. *J. Exp. Biol*., 203, 2261-78.

[40] Wilga, C. D. and Lauder, G. V. (2002). Function of the heterocercal tail in sharks: quantitative wake dynamics during steady horizontal swimming and vertical maneuvering. *J. Exp. Biol*., 205, 2365-74.

[41] Anderson, E. J,, McGillis, W., and Grosenbaugh, M. A. (2001). The boundary layer of swimming fish. *J. Exp. Biol*., 204, 81-102.

This work was done in collaboration with Prof. George Lauder, Prof. Katia Bertoldi, James Weaver, Li Wen, and Dylan Wainwright. This work has already been published, and the relevant citation for the work is: Lauder, G. V., Wainwright, D. K., Domel, A. G., Weaver, J. C., Wen, L., & Bertoldi, K. (2016). Structure, biomimetics, and fluid dynamics of fish skin surfaces. Physical Review Fluids, 1(6). https://doi.org/10.1103/physrevfluids.1.060502.

4

Structure, Biomimetics, and Fluid Dynamics of Fish Skin Surfaces

4.0 ABSTRACT

The interface between the fluid environment and the surface of the body in swimming fishes is critical for both physiological and hydrodynamic function. The skin surface in most species of fishes is covered with bony scales or tooth-like denticles (in sharks). Despite the apparent importance of fish surfaces for understanding aquatic locomotion and near-surface boundary layer flows, relatively little attention has been paid to either the nature of surface textures in fishes or possible hydrodynamic effects of variation in roughness around the body surface within an individual and among species. Fish surfaces are remarkably diverse and in many bony fishes scales can have an intricate surface texture with projections, ridges, and comb-like extensions. Shark denticles (or scales) are tooth-like, and project out of the skin to form a complexly textured surface that interacts with free-stream flow. Manufacturing biomimetic foils with fish-like surfaces allows hydrodynamic testing, and we emphasize here the importance of dynamic test conditions where the effect of surface textures is assessed under conditions of self-propulsion. We show that simple two-dimensional foils with patterned cuts do not perform as well as a smooth control surface, but that biomimetic shark skin foils can swim at higher self-propelled speeds than smooth controls. When the arrangement of denticles on the foil surface is altered, we find that a staggered-overlapped pattern outperforms other arrangements. Flexible

foils made of real shark skin outperform sanded controls when foils are moved with a biologically realistic motion program. We suggest that focus on the mechanisms of drag reduction by fish surfaces has been too limiting, and an additional role of fish surface textures may be to alter leading edge vortices and flow patterns on moving surfaces in a way that enhances thrust. Analysis of water flow over an artificial shark skin foil under both static and dynamic conditions shows that a shear layer develops over the denticle surface, and we propose that there is limited flow under the expanded surfaces of shark denticles. The diversity of fish scale types and textures and the effect of these surfaces on boundary layer flows and fish locomotor energetics is a rich area for future investigation.

4.1 INTRODUCTION

For a swimming fish, the interface between the fluid environment and the body is critical for both physiological and hydrodynamic function. Processes such as the exchange of ions, carbon dioxide, and oxygen all occur across the surface area of body tissues, and frictional and pressure forces that arise during locomotion are significantly affected by surface texture and conformation. Interfacial phenomena are of general importance in biofluid dynamics, but for swimming fish, the nature of the interface between the body and fluid is a key factor determining both the energetic cost of locomotion in the short term, as well as being responsible for evolutionary specializations such as drag reducing features on longer time scales.

Despite the apparent importance of fish surfaces for understanding aquatic locomotion, relatively little attention has been paid to the nature of the skin surface texture in fishes and the possible hydrodynamic effects of variation in texture around the body surface as well as among species. For example, the surfaces of bony fish are substantially different from the skin surface of sharks and rays, and yet we understand little about the hydrodynamic consequences of these different surface types. Furthermore, the three-dimensionality of biological fish surfaces is not well characterized, and the extent to which textural elements extend into the boundary layer as fish swim is unknown, as is the extent of movement (either active or passive) among skin surface elements. Moreover, there are few experimental models that can replicate *in vivo* fish surface function during locomotion and allow measurement of parameters such as swimming speed, the energetic cost of locomotion, and thrust and drag forces under dynamic swimming conditions.

Fish surfaces are composed of arrays of individual scales (often termed denticles in sharks and rays) that form a textured surface. In sharks, the denticles have a complex shape (see below) and penetrate the epidermal skin layer to make direct contact with the water. Shark denticles are homologous to mammalian teeth (1): each denticle possesses an interior pulp cavity with nervous and arterial supply, a coating of dentine and enamel, as well as a "root" or expanded base embedded within the dermis. In bony fish, individual scales are composed of bone arranged in thin layers to make a laminated composite structure (2-4). Scales are embedded within the skin's epidermal layer, and in most species scales

do not make direct contact with the water due to the epidermal coating. Bony fish surfaces are also often well-supplied with mucus glands, and a mucus coating can obscure some features of scale surface texture.

The skin of sharks has attracted the most attention as a biological surface that might possess special drag-reducing properties in the water, and a number of simple physical models have been suggested that might replicate shark-skin function (5-10). These studies have focused on static testing, analyzing drag forces on rigid surfaces as a function of flow speed, and examining the effect of surface feature spacing on the magnitude of observed drag reduction. Riblet models as a general abstraction of a shark-like textured surface also have been analyzed for drag reducing properties (8,11-13), and recent computational models have assessed the ability of shark skin surfaces to possibly reduce drag (14,15), again under static conditions.

In considering the effect of surface structures on drag, it is useful to consider both the Reynolds number and a dimensionless S+ number (5,16,17). However, the characteristic length scale for Reynolds numbers relevant to fish locomotion can range from propulsor (or fish) body length, down to the spacing between surface roughness elements and boundary layer thickness. For the types of data and experiments described here, whole propulsor (foil or animal) Re ranges from ~$1*10^3$ to $2*10^5$ although large pelagic fishes such as tuna certainly swim at higher Re than this. Using the distance between adjacent riblet-like ridges on shark skin denticles as a characteristic length, and free-stream flow velocities of typical laboratory experiments in water, the Re is on the order of 15.

Clearly a range of interesting fluid dynamic phenomena may be involved in understanding how fish scales interact with their fluid environment.

In addition, the dimensionless S+ parameter has been used in studies of drag reduction as the Reynolds number may not be the most relevant metric when fish surface structures have a much smaller size scale than that of the whole body (13,17-19). S+ is a function of the spacing between surface projections, fluid kinematic viscosity, density, and average surface shear stress. Values of S+ between approximately 5 and 25 have been shown to represent conditions where surface textures may result in reduced friction drag.

In this paper we present an overview of fish surface structures and their hydrodynamic effects studied under dynamic conditions. First, we provide a synopsis of the diversity of three-dimensional fish surfaces. There is a remarkable and unappreciated diversity of fish surface textures, and new technologies have recently allowed measurement of the surface topography of fish skin. Second, we discuss experimental platforms that allow dynamic testing of a variety of alternative fish surface designs that range from simple two-dimensional physical models to 3D-printed shark skin, to pieces of actual shark skin. Finally, we present the results of dynamic tests of swimming performance of these different skin models, and review previous hydrodynamic results suggesting that fish skin textures may enhance propulsion by improving thrust, in addition to possible effects of drag reduction.

We believe that the near-exclusive focus on the possibility of drag reduction by fish surfaces has been too limiting, and that an additional role of fish

surface textures may be to alter leading edge vortices and flow patterns on moving surfaces in a way that enhances thrust. Most importantly, we wish to emphasize the importance of dynamic testing in which model fish skin surfaces are analyzed under time-dependent conditions. Replicating the locomotor conditions of freely-swimming fishes to test hydrodynamic effects of surface structures is critical; bending of the body and active motion of fins are key features of fish propulsion (20-22). We believe that static testing circumstances, which do not replicate patterns of skin bending, changing angles of attack through time, and self-propulsion where thrust and drag forces are balanced over a flapping cycle, are unlikely to reveal the key physical phenomena associated with fish skin surface effects during aquatic propulsion.

4.2 Materials and Methods

4.2.1 Imaging

Imaging fish surfaces is challenging. In particular, imaging the surface of live fishes and the broader pattern of surface elements so that the arrangement of textural elements can be seen as they occur *in vivo* poses special difficulties. Traditionally, scanning electron microscopy (SEM) has been used to image bony fish scales, but published SEM images are almost exclusively of individual scales and do not reveal the overlapping patterns of scales and associated soft tissues in bony fishes. SEM has also been used to image the surfaces of shark skin (Figure 4.1; 23,24), and micro-computed tomography (μCT) scans have provided surface images of shark skin scales (or denticles) as well as for one species of bony fish

(25). For the smaller surface features of shark skin scales to be seen, μCT scanning at a resolution on the order of a micron may be necessary (19), and such scans have been used to make three-dimensional models of the individual denticles for additive manufacturing of biomimetic shark skin (26).

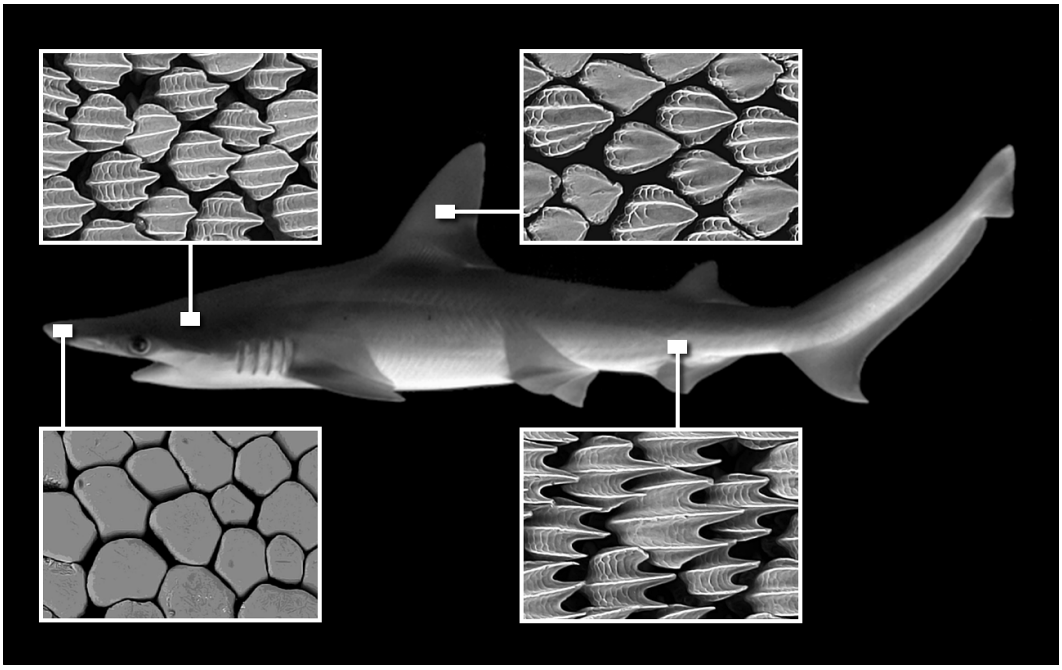

Figure 4.1: Scanning electron micrographs (SEM) showing the diversity of denticles around the body and head of a bonnethead shark, *Sphyrna tiburo*. Individual denticles are all 100 - 200 μm in length (see 19,29). Denticles near the leading edge of the head are flatter with greatly reduced or absent ridges, while denticles on the mid- and posterior-body regions have prominent ridges and posterior projections oriented in the stream-wise direction.

A new approach to imaging the surface of fish skin that provides images relevant to both propulsion and measurement of surface textural roughness is to use gel-based contact surface profilometry (27,28). Wainwright and Lauder (25) used contact profilometry to analyze the textures of scale patterns on the surface

of bluegill sunfish, and below we provide sample images using this technique for several species of both bony fishes and sharks (Figures 4.2, 4.3).

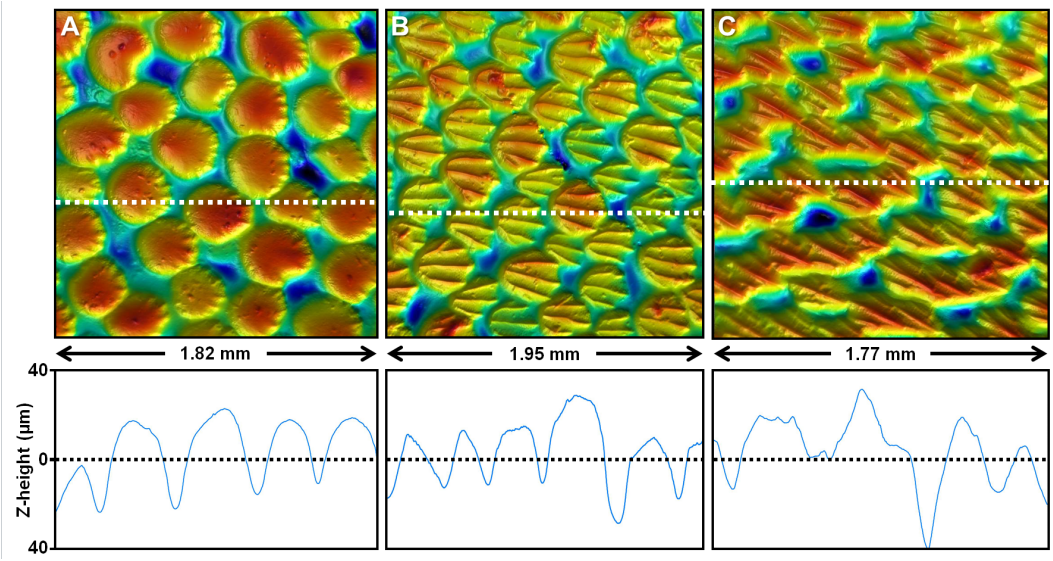

Figure 4.2: Surface topography of a blue shark (*Prionace glauca*). A, surface of the dorsal side of the anterior-most tip of the head. B, topography of the dorsal side of the head between the eyes. C, topography of denticles from the trailing edge of the tail. All images are arranged so that anterior is left, and dorsal is up; color indicates surface height, with blue representing the lowest regions, and red color the regions that project the greatest extent from the surface. Dotted lines in each image show the location of the vertical profiles below each image. Shark surface roughness varies considerably around the body.

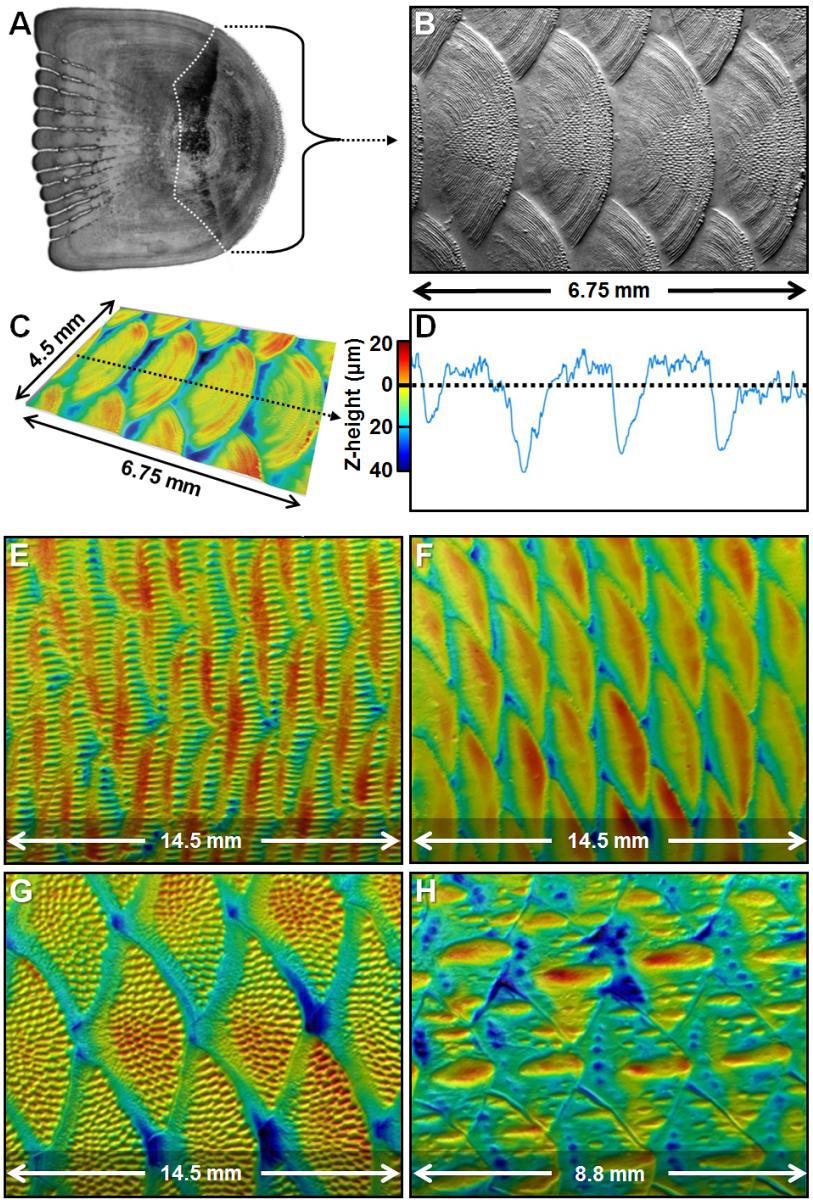

Figure 4.3: Bony fish surfaces. A, photograph of a single bluegill sunfish (*Lepomis macrochirus*) scale (dashed white line indicates the limit of the portion of the scale exposed to the water). B, group of scales located in the center of the body from a bluegill sunfish to show the overlapping arrangement. C, a 45 degree view with height enhanced (by 3%) of the same image in A, with a vertical profile along the dashed line shown to the right. E, the surface of a gulf menhaden (*Brevoortia patronus*). F, the surface of a Hawaiian dascyllus (*Dascyllus albisella*). G, the surface of a sargassum triggerfish (*Xanthichthys ringens*) just posterior to the tip of the pectoral fin. H, the surface of a rainbow smelt (*Osmerus mordax*). All images show surfaces where anterior is left and dorsal is up. For images C, E – H, color indicates height with dark blue representing the lowest point, and red the highest point on the fish surface. Maximum feature height ranges from ~150 µm to 350 µm.

4.2.2 FOIL MANUFACTURE

In order to study the hydrodynamic effect of fish surface textures under dynamic conditions of self-propulsion where fish skin or skin models are moved with a heave (side to side) or pitch (rotational) motion program to generate thrust, fish skin models must be assembled into flexible foils or panels that can be attached to mechanical controllers. To generate simple two-dimensional physical models with patterned surfaces in which water can flow from one side of the swimming panel to the other, we used a laser cutter to slice differently shaped "scales" into flexible plastic panels (Artus color-coded shim stock; http://www.artuscorp.com) that vary in stiffness (Figure 4.4). Cutting shapes into plastic panels of various stiffnesses allowed individual elements to "pop-up" from the panel surface during swimming. The propulsive performance of these different patterns was tested as described below under several movement programs.

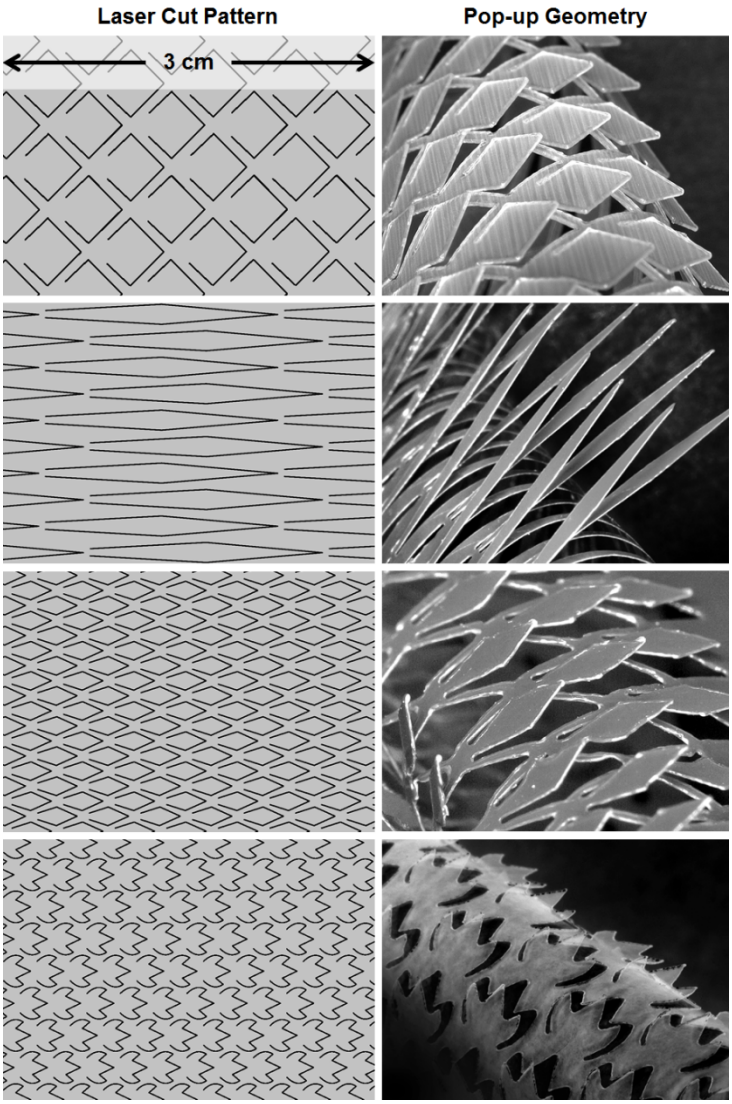

Figure 4.4: Two-dimensional biomimetic foils with different patterns laser-cut into thin flexible plastic panels. Images in the left column show the cut pattern (all illustrated at the same scale), used to generate deformable fish scale-like components. Images to the right show bent foils and the resulting pop-up geometry. Water can flow from one side to the other of the swimming foil when the cut elements deform. Patterns are cut into different thickness plastic materials to vary the extent of the pop-up behavior during bending. From top to bottom, foil thicknesses are 0.19 mm, 0.05 mm, 0.05 mm, and 0.025 mm.

To produce membranes of shark skin for hydrodynamic testing, Oeffner and Lauder (29) excised pieces of skin from freshly caught sharks (Figure 4.8*A*), cleaned the skin samples of underlying muscle and connective tissue to produce

strips of skin (Figure 4.8*B*), and assembled these strips into both rigid (by gluing skin strips to aluminum panels) and flexible (by gluing the skin strips to each other and attaching them to a leading edge rod, Figure 4.8*C*) panels for testing. The swimming performance of these skin strip panels was compared to panels in which the surface denticles had been carefully sanded off (29).

To manufacture biomimetic shark skin that allowed us to control both denticle structure and arrangement on the panel surface, we used micro-CT (μCT) scanning to generate a three-dimensional denticle model, arranged the individual model denticles into arrays of various types, and used additive manufacturing to print artificial shark skin membranes in which the denticles are made of rigid material with their expanded bases embedded into a flexible substrate (Figure 4.5). This approach allowed us to generate flexible biomimetic skin models in which denticles change their relative spacing as the skin changes from concave to convex during undulatory propulsion (Figure 4.5*F*).

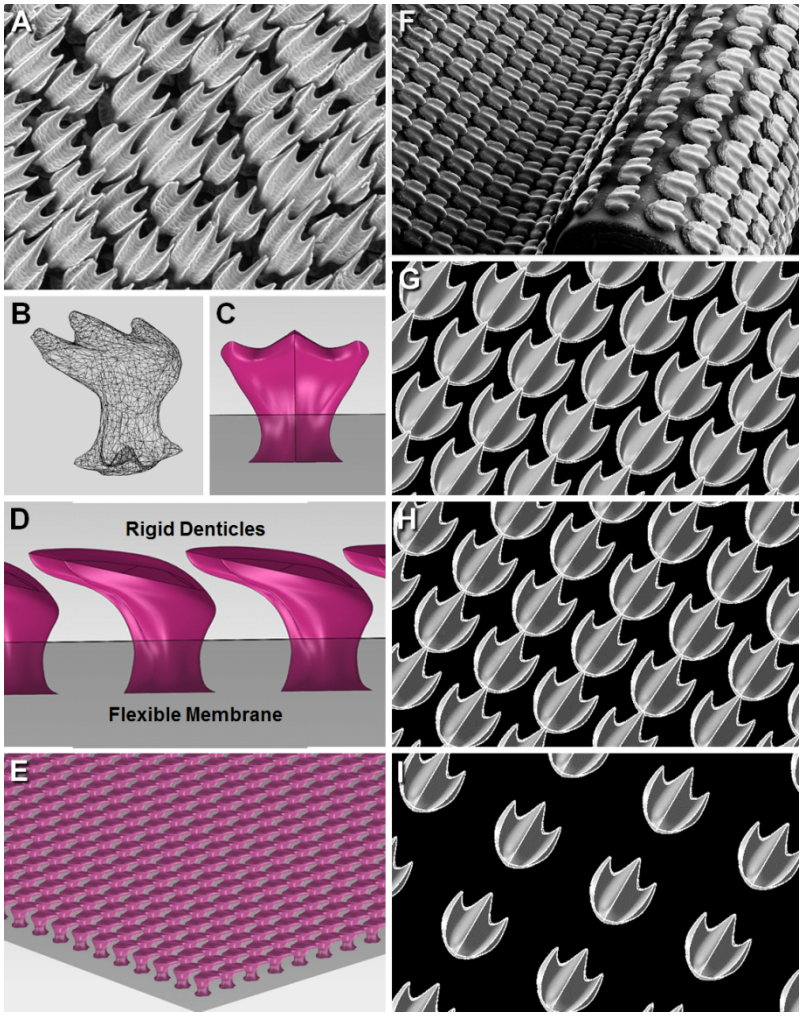

Figure 4.5: Shark denticle models and biomimetic skin membranes. A, Bonnethead shark (*Sphyrna tiburo*) denticles from near the anal fin (scales are ~ 200 µm in length). B, three-dimensional mesh and rendered model (C) of an individual denticle. D, a row of denticles, showing how the top of one denticle overlaps the base of the adjacent one. E, two-dimensional denticle array in which rigid denticles are laid out on a flexible membrane substrate. F, fabricated biomimetic synthetic shark skin membrane used for hydrodynamic testing in which rigid denticles are arrayed on a flexible substrate. Individual denticles are ~1 mm in length. G, H, I, diagrams of three different denticle patterns and densities used for testing the effect of changing denticle arrangements on propulsion. Adapted from (19,22,26,29).

Both denticle-covered artificial shark skin membranes and the smooth controls have near identical flexural stiffnesses, due to the central supporting plastic element (Figure 4.9C) to which the flexible foil surfaces were attached.

This central plastic support dominates the flexural stiffness of the entire assembly, and the presence of denticles did not noticeably alter flexural stiffness.

To explore the possibility of printing shark-like denticles at very small size scales, we used a Nanoscribe printer (Photonic professional, GmbH, Germany) and two-photon lithography to fabricate a single shark skin denticle at a size that is ten times smaller than its real scale. Figure 4.6 shows the optical and SEM images of a 3D-printed single shark skin denticle attached to a glass coverslip.

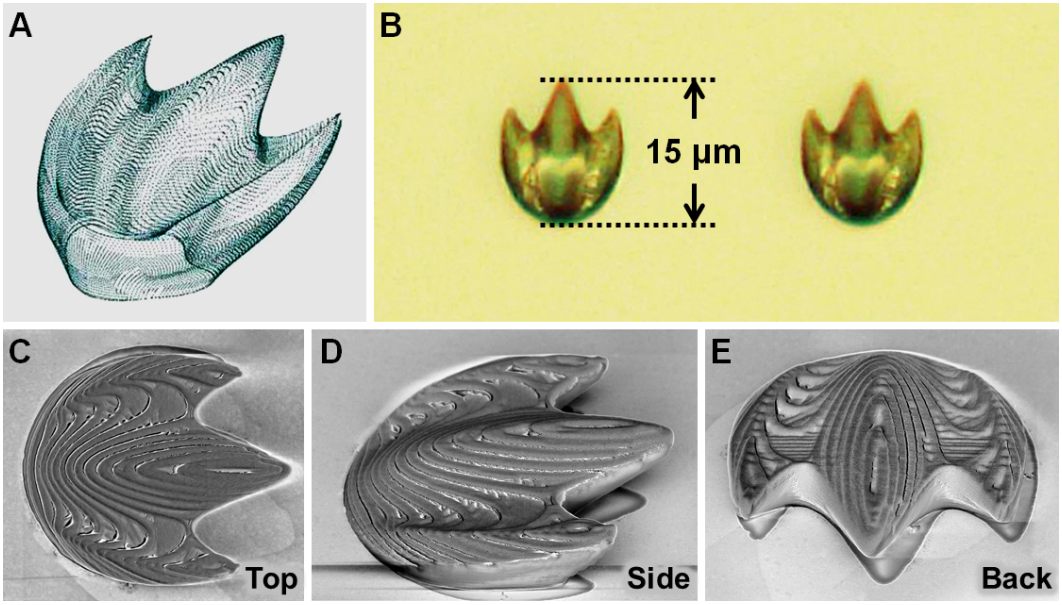

Figure 4.6: Images of a high-resolution 3D print of a shark skin denticle. (A) Volumetric model of a denticle generally similar to those of mako sharks (Isurus oxyrinchus). (B) Optical microscopic image of the fabricated denticle in top view showing the size scale. Scanning electron microscopic images of the denticle are shown in top (C), side (D), and posterior (E) views. The 3D printed denticle is mounted on a glass coverslip, and manufactured using two-photon lithography.

The shark skin denticle model was first designed in Solidworks (Solidworks Corp., Waltham, MA, USA), and then converted into volumetric pixels in Matlab. UV-curable photoresist material (IP-Dip, Nanoscribe, GmbH,

Germany) was exposed by a laser beam at the positions of the volumetric pixels following the designed denticle shape. A thin layer of post-exposed baked SU-8 resist material was used to ensure the polymerized shark skin denticle reliably bonded to the underlying glass coverslip for SEM imaging. Polymerizing the single shark skin denticle (15μm in length and 10μm in width) took approximately 25 minutes. Once the polymerization process was finished, unexposed regions including the denticle undercut area were removed with a developer bath using 2-methoxy-1-methylethyl acetate (PGMA). After baking the polymerized denticle at 120 °C for 30 min, the solidified shark skin denticle is rigid with a Young's modulus of approximately 4GPa.

4.2.3 HYDRODYNAMIC TESTING

Dynamic testing of fish skin model panels and membranes made from real shark skin was accomplished with a mechanical controller that allows programming of heave (side-to-side) and pitch (rotational) motions (30). Foils are held at the leading edge by a supporting rod, which is in turn attached above the water to heave and pitch motors through a force/torque sensor (see Figures 4.8C and 4.9A). A recirculating water flow tank with programmable speed control allows testing of diverse swimming motions under a range of speeds. A number of recent studies of the dynamics of swimming flexible panels have used this apparatus to measure swimming forces and torques with a 6-axis ATI nano-17 transducer (ATI Inc., Apex, NC) (e.g., 31,32-35). Synchronized high-speed video cameras allow measurement of foil motion as forces are recorded.

Measurement of the self-propelled swimming speed of foils is accomplished by first picking a particular motion program of heave, frequency, and pitch, and then measuring the mean thrust across a range of imposed flow speeds. Self-propulsion, for a particular motion program, occurs at the speed where the average thrust over a flapping cycle is zero.

Flow visualization over the surface and in the wake of flapping foils is accomplished using particle image velocimetry as in our previous research. We have analyzed the vortical structure on the surface of swimming foils (19,29), and in the wake (e.g., 36,37,38) to document how changing surface characteristics and motion patterns alter flow structures. Here we present flow visualizations over the surface of a static and dynamic biomimetic shark skin foil with widely spaced denticles (arrangement of Figure 4.5*I*) to allow flow in between individual denticles to be seen, as well as the pattern of surface flow (Figure 4.10).

4.3 RESULTS

4.3.1 FISH SURFACE TOPOGRAPHY

There is considerable regional variation in fish scale structure, and different locations on the body can have scales with dramatically different morphology (25). In sharks (Figure 4.1), scales near the leading edge of the head tend to be more paver-like with flattened and smooth upper surfaces exposed to the water, while along the body the scale surface has ridges and three or more posterior finger-like projections (23,29). Images and elevation profiles of blue shark (*Prionace glauca*) denticles (Figure 4.2) also show the smooth upper

surface of each denticle at the front (leading edge) of the head, and ridged surfaces on denticles further back along the body. The amplitude of surface roughness in blue sharks ranges from 40 μm near the head to almost 80 μm along the body (Figure 4.2), and denticles are not covered by epidermis so this texture would be seen by water moving over the undulating body and tail. There is a great diversity of sizes and shapes of shark denticles (see, e.g., 39). Sizes of individual denticles range from approximately 120 μm in open ocean sharks to more than 1 mm (39) in more benthic and slow-moving species, and denticles may be widely spaced or can be arranged in close proximity with essentially no gaps among denticles (Figure 4.2). Denticles of moderate to fast-swimming species have overlapping posterior extensions so that an individual upstream denticle overlaps the surface of the next downstream denticle (Figure 4.5*A*). Denticles in shark species with this overlapping structure are generally arrayed into a staggered pattern (Figure 4.2) where adjacent rows are offset from each other (also shown schematically in Figure 4.5*G*).

In bony fish (Figure 4.3), there is also variation around the body in scale structure (25). Bony fish scales overlap considerably and approximately half of each individual scale overlaps the next most anterior scale (Figure 4.3*B*). Scales are flattened and are arranged into a tight array; surface profiles again show approximately a 40 – 50 μm surface topography, although some of the smaller-scale roughness would be covered by epidermis in life. A survey of bony fish scale topography using gel-based surface contact profilometry reveals a great diversity of surface structures that vary considerably in amplitude. Four examples

of this diversity are shown in Figure 4.3. The exposed portion of scales can have numerous posteriorly-pointing ridges, be covered with prominent bumps, have smooth posterior edges, or possess large central ridges surrounded by smaller surface projections.

4.3.2 Swimming Dynamics of Biomimetic Fish Surfaces

Although we initially believed that the use of simple flexible (essentially two-dimensional) panels with patterned cuts that could bend and flex and "pop-up" away from the panel surface during locomotion and allow water to pass from one side to the other (Figure 4.4) would enhance propulsion, we were unable to find any foil of this type that outperformed a smooth control. For example, Figure 4.7 shows the results of measuring the self-propelled swimming speed of two different cut foils. The high-aspect ratio cut (Figure 4.4*D*) swam dramatically slower, at approximately one-fourth the speed of the smooth control (Figure 4.7*A*), and the cut foil exhibited an increased mean cost of transport (in Joules/m) nearly five times that of the control.

The cut foil pattern shown in Figure 4.4*A* was tested under two different motion programs, one with heave and pitch continually adjusted to give a zero angle of attack (see 40) (Figure 4.7*B*), and one with heave-only motion at the leading edge (Figure 4.7*C*). In both cases, the cut foil swam more slowly, and exhibited an increase in the cost of transport. While we did not explore a large parameter space of possible motion programs, and the possibility remains that some other movement patterns of these cut panels could result in improved

swimming performance, we believe that the reduced effective surface area as the cut elements bend away from the panel surface reduces swimming performance in most cases. Fluid flow from one side of the panel to the other may indeed change swimming dynamics, but quantifying this effect remains a future task.

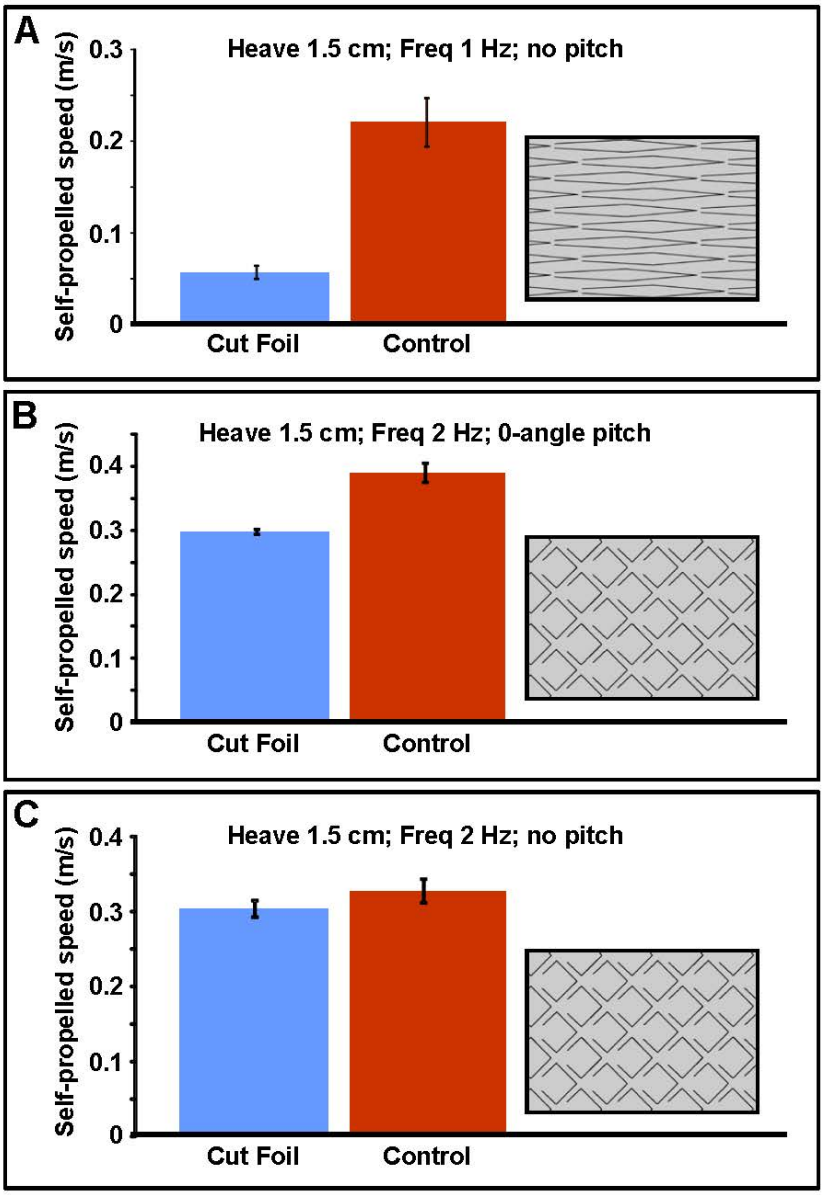

Figure 4.7: Analysis of self-propelled swimming speeds for two of the two-dimensional cut foils shown in Figure 4.4. The three motion programs used for testing are explained in the text. Images to the right show the foil cut pattern for each test condition. Error bars are +/- one standard error.

Cost of transport (J/m) for each foil type: A, control (0.021), cut foil (0.096); B, control (0.045), cut foil (0.047); C, control (0.104), cut foil (0.108).

Swimming tests of *flexible* panels made from actual shark skin (Figure 4.8) demonstrated that for a variety of motion programs, both with pitch and heave-only, the intact shark skin surface resulted in improved self-propelled speeds compared to a control in which the surface denticles were removed by sanding. Oeffner and Lauder (29) noted, however, that their tests of *rigid* shark skin panels attached to aluminum plates (which are not able to bend) did *not* show improved swimming performance: intact skin either performed similarly to sanded skin, or in one case worse than the control. These data provide evidence that *flexibility* of the skin membranes is critical to generating improved propulsive performance.

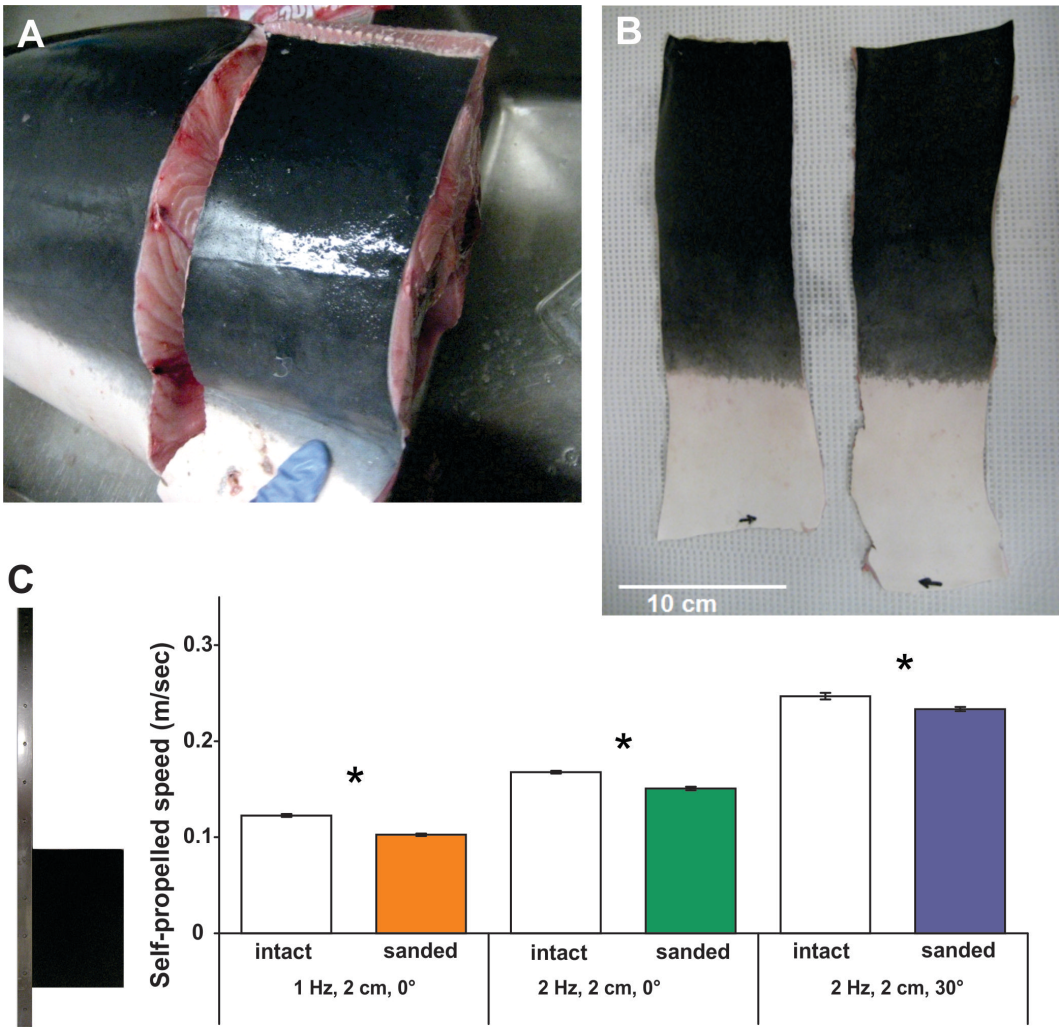

Figure 4.8: Fabrication of a flexible skin foil from mako shark skin, and analysis of the self-propelled swimming speed of this foil under three motion programs, compared to a smoother sanded foil in which most of the denticles have been removed. A, removal of sections of skin from a mako shark (Isurus oxyrinchus). Skin is then cleaned of underlying tissue (B) and the orientation marked (black arrow at the bottom of each skin strip). Two skin strips are glued to each other with each denticle surface facing the water, trimmed into a rectangular flexible foil, and attached to a rod for testing (C). Histograms show the self-propelled swimming speed for three different motion programs in which the leading edge of the shark skin foil is moved in heave (either 1Hz or 2Hz at +/- 2 cm), and with no pitch or with 30° pitch. In each of the three tested cases, the intact shark skin foil swims significantly faster than the smoother control (*). Adapted in part from (29); photographs in (A) and (B) courtesy of Johannes Oeffner.

Analysis of the swimming speeds of biomimetic shark skin panels relative to a 3D-printed control of the same mass (Figure 4.9*C*), tested at a heave amplitude and frequency of ±1.5 cm and 1Hz respectively, but at a variety of pitch values, shows that the shark skin surface swims significantly faster than the control at the intermediate pitch values of 5 to 15°, but slower or equivalently at lower and higher pitch angles. The effect of a shark skin-like surface thus depends on the movement pattern, and we should not expect improved performance under all motion programs.

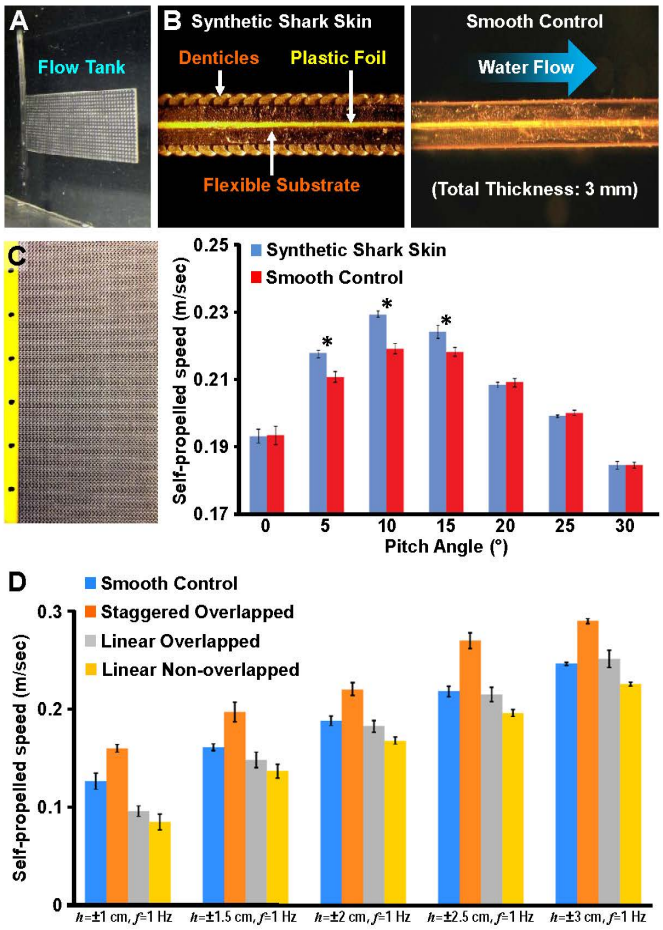

Figure 4.9: Hydrodynamic function of biomimetic shark skin models. A, Dynamic testing in a flow tank of a synthetic shark skin membrane in a mechanical flapping controller. B, cross-sections of biomimetic shark skin and the smooth control, both manufactured to be of equal total mass; blue arrow indicates the direction of water flow. C, a flexible plastic foil (yellow, 0.5 mm thickness) is covered on both sides with 3D printed flexible synthetic shark skin to allow testing; foil is 177 mm in height and 77 mm chord width. Histogram shows results of testing the self-propelled speed of this synthetic shark skin membrane with respect to the smooth control surface at different leading edge pitch values; heave amplitude was ± 1.5 cm and frequency was 1 Hz for all tests. At pitch angles of 5°, 10°, and 15° (asterisks), the swimming speeds of the biomimetic shark skin foils were significantly greater than those of the controls; at the other four pitch angles, the swimming speeds were similar. D, tests of the swimming speeds of three different denticle patterns (see Figure 4.5) relative to a smooth control at five different leading edge heave values. Error bars represent ±1 standard error of the mean. Adapted in part from (19,26).

Modifying the pattern of biomimetic shark skin denticles on the foil surface (Figure 4.9*D*) significantly affects propulsion, and under the test conditions of 1 Hz flapping frequency with no pitch, the staggered array of denticles (Figure 4.5*G*) performs much better than a linear array and also better than the smooth control, without any increase in the cost of transport at the lower heave motions (26).

Analysis of the pattern of water flow over the surface of shark skin compared to a sanded control showed that the roughened surface alters the intensity and location of the leading vortex formed during the flapping motion (29). Oeffner and Lauder (29) suggested that due to the timing of flow separation and the location of the vortex center closer to the foil surface, denticles on shark skin may enhance thrust by increasing leading edge suction. Shark tails appear to possess an attached leading edge vortex during most phases of the tail beat (41), and the textured surface thus can act as a thrust-enhancer in body regions where flow separates at appropriate times in the undulatory cycle. Flow separation has also been observed on shark pectoral fins during maneuvering when pectoral fins change their angle of attack, but does not occur during steady swimming, at least when smaller sharks swim freely under laboratory conditions (42,43). In addition, the cost of transport in flexible biomimetic shark membranes with overlapping denticles is increased under certain motion programs, which suggests that physical interactions among denticles are increasing the flexural stiffness of the membrane during swimming, and therefore could be reduced by making each denticle slightly mobile at the base (26). In fact, mobile denticle bases have been

noted in mako sharks (23,44), and this mobility may function to reduce the cost of bending the skin back and forth, where contact among adjacent scales would otherwise increase skin bending stiffness. However, many other sharks such as leopard sharks and spiny dogfish do not possess highly flexible denticles, and the extent to which different shark species possess mobile denticles is currently unknown. For bony fish, relative motion of scales is most likely common, although scale movement during locomotion has never been measured, and the forces needed to bend bony fish skin are unknown.

One key question that remains unanswered is the extent to which water penetrates the layer of denticles on shark skin and forms vortices underneath the expanded and ridged outer surfaces. Such vortex formation might increase drag (14), but to date there are no experimental observations of such flows. Given the extensive surface provided by the upper regions of denticles (Figure 4.2), it might seem unlikely that there is significant flow among the denticle stalks that protrude from the epidermal surface. Studying a model system with widely spaced denticles in which such flows are visible could provide an indication of the extent of within-denticle flow, because observing such flows in freely-swimming sharks represents substantial challenges that are not likely to be resolved any time soon. Figure 4.10 shows the results of both static and dynamic (flapping) flow visualization using the biomimetic denticle membrane of Figure 4.5*I*.

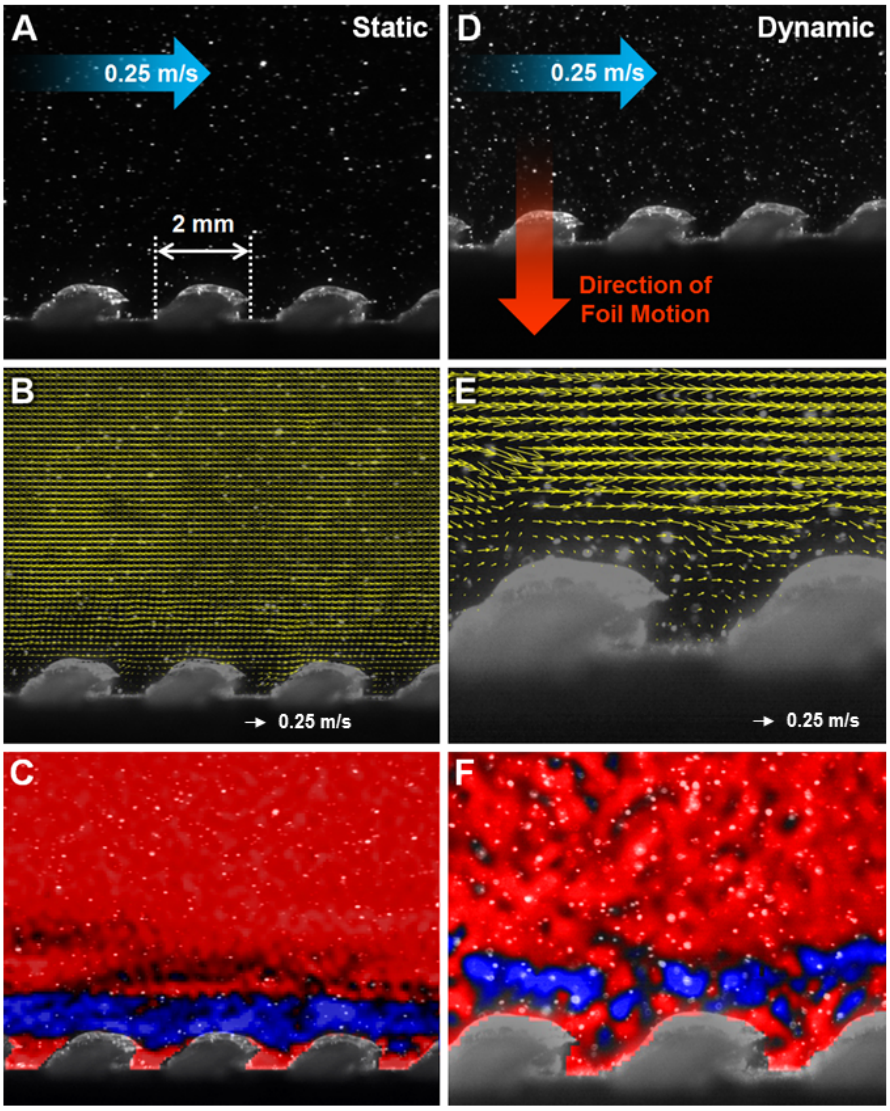

Figure 4.10: Flow over a synthetic shark skin membrane with widely spaced denticles (see Figure 4.5*I*) during static testing (A-C) and under dynamic conditions of 2 Hz leading edge oscillation and a free stream flow of 25 cm/s (D-F). Top images show the biomimetic shark skin membrane; blue and red arrows indicate the direction of water and foil motion respectively. Middle panels show velocity vector fields representing flow over the membrane. C, average vorticity (mean over 0.4 s) on the surface of the static shark skin panel; vorticity (s^{-1}) ranges from maximum positive (red) of 0.025 to maximum negative (blue) of -0.4. F, instantaneous vorticity (s^{-1}) over the shark skin panel surface; vorticity ranges from maximum positive (red) of 120 to maximum negative (blue) of -400. Size of the denticles is shown in panel A.

The relatively wide spacing of the denticles allows visualization of the flow in between adjacent denticles, as well as analysis of near-denticle surface flows. Although some flow can be seen separating behind denticles and forming a recirculation zone for both static and dynamic cases, a well-developed shear layer forms over the top of the denticles and across the gaps between adjacent denticles (Figure 4.4,4.10 *C,F*). This suggests that water may interact with the ridged denticle surface but not form internal vortical patterns that affect propulsion as has been previously suggested for widely spaced and erect denticles (45). And the observation of such a distinct surface shear layer in a model system with widely-spaced denticles strongly suggests that in tightly-packed natural denticle configurations as shown in Figure 4.2, that sub-surface among-denticle flows could be minimal, especially if a mucus coating exists above the epidermis and around the denticle stalks.

4.4 DISCUSSION

Perhaps the most significant issue for which we still lack a clear answer is the extent to which the surface structures on fish skin discussed here interact with near-surface flows and affect the boundary layer. Measurements of vortex location on the surface of swimming panels of shark skin allowed measurement of flow within a few millimeters of the skin surface, and were able to detect alterations in vortex structure when denticles were removed (29). But boundary layer profiles have yet to be measured on panels of flapping shark skin. Some fish skin structures can project hundreds of microns above the mean surface, and

it is likely that surface roughness has significant effects on flow near the surface and alters the boundary layer profile compared to a smooth surface. In order to understand the functional significance of the diversity of fish surface structures, we need to measure boundary layer profiles along the body during swimming, as static models will not reflect the effects of pressure gradients that develop as the body bends back and forth, and pressure changes substantially along the fish body during locomotion (46).

Quantifying boundary layer profiles along the length of swimming fishes is challenging, and high resolution and high frequency imaging of flows in small areas on the order of 1-5 mm^2 are needed to visualize boundary layer profiles and their evolution through time. The boundary layer of freely-swimming fishes has only been measured in two previous studies, and in both cases it was not possible to determine the effect of surface roughness on flow structure or separation point. The first paper to measure the boundary layer of a swimming fish is that of Anderson et al. (47) who were able to quantify profiles along the body in one bony fish species (scup, *Stenotomus chrysops*), and one shark, the smooth dogfish (*Mustelus canis*) during free swimming. They showed that there was little flow separation along the body at the swimming speeds studied (Reynolds numbers up to 3×10^5) and proposed that there is minimal body pressure drag at these speeds. Furthermore, their results suggest that there is substantially increased total friction on an undulating fish body compared to the same rigid body towed at the swimming speed. A similar conclusion that body undulations increase frictional drag forces has been reached by (48,49), who support the "Bone-Lighthill

hypothesis" that changes in boundary layer thickness as a result of body undulation increase frictional drag forces.

Yanase and Saarenrinne (50) have recently measured boundary layer profiles on the body surface of trout swimming at a Reynolds number of 4×10^5, and have shown that boundary layers can be unsteady and turbulent at certain locations on the fish. These authors report finding small recirculation regions near the trout surface that are similar to laminar separation bubbles that result from adverse pressure gradients and cause flow separation. Areas of flow separation result in *upstream* flow at the skin surface at this localized region. Because trout possess small scales that are coated with a mucus layer, and the trout skin surface is thus very smooth, we do not expect to see effects of scales on boundary layer profiles in this species. But in other bony fish such as bluegill sunfish where the scales on many regions of the body have posteriorly projecting small "teeth" or ctenii (25) that pierce the mucus layer and enter the boundary layer, such effects may be evident (Figure 4.3).

We emphasize the importance of measuring the local flow environment on the skin surface to understand the effect of different scale structures on boundary layer flow. If there are regions of flow separation, then flow at the skin surface will be moving in the *opposite* direction to the free stream, and scales with ctenii or other asymmetrical shapes and features may function very differently than if flow were uniformly downstream along the body. Such an effect has been seen in swimming shark skin membranes (29), where flow next to the denticle surface is in the opposite direction to free stream flow due to the presence of a large

separation bubble that forms on the foil. We should not assume that shark denticles or bony fish scales are designed to function with flow acting only in the free stream direction along their surface.

The extent to which individual scales are mobile during fish swimming is unknown, but fish lack direct muscular attachments to individual scales and so any scale mobility will be the result of external forces. Scale motion could certainly affect the boundary layer, and movement that does occur is most likely a passive response to body bending, to pressure changes within the body cavity, or to tension applied to dermal collagen fibers that invest the skin. Fish skin is remarkably complex and in this paper we have focused on the pattern of surface ornamentation in sharks and bony fishes. But fish skin also possesses an extensive dermal array of embedded collagen fibers (51,52), and some fish species have scales embedded within the dermis that will likely affect the material properties and hence the pattern of skin deformation during locomotion. The extent to which scale motion affects skin hydrodynamic function is unknown, but linking skin structure to locomotor hydrodynamics is a promising area for future work.

4.5 REFERENCES

[1] Liem, K. F., Bemis, W. E., Walker, W. F., and Grande, L. (2001). *Functional Anatomy of the Vertebrates. An evolutionary perspective. Third Edition* (Harcourt College Publishers, Fort Worth).

[2] Allison, P. G. et al. (2013). Mechanical properties and structure of the biological multilayered material system, *Atractosteus spatula* scales. *Acta Biomaterialia,* 9, 5289.

[3] Bigi, A., Burghammer, M., Falconi, R., Koch, M. H. J., Panzavolta, S., and Riekel, C. (2001). Twisted plywood pattern of collagen fibrils in teleost scales: an X-ray diffraction investigation. *Journal of structural biology,* 136, 137.

[4] Bruet, B. J. F., Song, J., Boyce, M. C., and Ortiz, C. (2008). Materials design principles of ancient fish armour, *Nature Mater*., 7, 748.

[5] Dean, B. and Bhushan, B. (2010). Shark-skin surfaces for fluid-drag reduction in turbulent flow: a review. *Philosophical Transactions of the Royal Society A: Mathematical, Physical and Engineering Sciences,* 368, 4775.

[6] Bechert, D. W., Bartenwerfer, M., Hoppe, G., and Reif, W. E. (1986). Drag reduction mechanisms derived from shark skin. *AIAA,* 2, 1044.

[7] Bechert, D. W. and Hage, W. (2007). *Flow Phenomena in Nature. Volume 2. Inspiration, learning, and application*, edited by R. Liebe (WIT Press, Southampton, UK), pp. 457.

[8] Büttner, C. C. and Schulz, U. (2011). Shark skin inspired riblet structures as aerodynamically optimized high temperature coatings for blades of aeroengines. *Smart Mater. Struct.,* 20, 094016.

[9] Luo, Y. H., Li, X., Zhang, D. Y., and Liu, Y. F. (2016). Drag reducing surface fabrication with deformed sharkskin morphology. *Surface Engineering*, 32(2), 157–163.

[10] Lang, A., Motta, P., Habegger, M. L., Hueter, R., and Afroz, F. (2011). Shark skin separation control mechanisms. *Marine Tech. Soc. J.,* 45, 208.

[11] Sirovich, L. and Karlsson, S. (1997). Turbulent drag reduction by passive mechanisms. *Nature,* 388, 753 .

[12] Luchini, P., Manzo, F., and Pozzi, A. (2006). Resistance of a grooved surface to parallel flow and cross-flow. *J. Fluid Mech*., 228, 87.

[13] Bechert, D. W., Bruse, M., and Hage, W. (2000). Experiments with three-dimensional riblets as an idealized model of shark skin. *Exp. Fluids,* 28, 403.

[14] Boomsma, A. and Sotiropoulos, F. (2016). Direct numerical simulation of sharkskin denticles in turbulent channel flow. *Phys. Fluids,* 28, 035106.

[15] Díez, G., Soto, M., and Blanco, J. M. (2015). Biological characterization of the skin of shortfin mako shark *Isurus oxyrinchus* and preliminary study of the hydrodynamic behaviour through computational fluid dynamics. *J. Fish. Biol.,* 87, 123.

[16] Videler, J. (1994). Body surface adaptations to boundary-layer dynamics. *Symposia of the Society for Experimental Biology,* 49, 1.

[17] Bechert, D. W., Bruse, M., Hage, W., Van Der Hoeven, J. G. T., and Hoppe, G. (1997). Experiments on drag-reducing surfaces and their optimization with an adjustable geometry. *J. Fluid Mech*., 338, 59.

[18] Anderson, E. J., MacGillivray, P. S., and Demont, M. E. (1997). Scallop shells exhibit optimization of riblet dimensions for drag reduction. *Biol. Bull.,* 192, 341.

[19] Wen, L., Weaver, J. C., and Lauder, G. V. (2014). Biomimetic shark skin: design, fabrication, and hydrodynamic function. *J. Exp. Biol.,* 217, 1656.

[20] Shadwick, R. E., and Lauder, G. V. (2006). *Fish Biomechanics* (Academic Press, San Diego), Vol. 23.

[21] Shadwick, R. and Gemballa, S. (2006). in *Fish Biomechanics. Volume 23 in Fish Physiology*, edited by R. E. Shadwick, and G. V. Lauder (Academic Press, San Diego), pp. 241.

[22] Lauder., G. V. (2015). Fish locomotion: recent advances and new directions. *Ann. Rev. Marine Sci*., 7, 521.

[23] Motta, P., Habegger, M. L., Lang, A., Hueter, R., and Davis, J. (2012). Scale morphology and flexibility in the shortfin mako *Isurus oxyrinchus* and the blacktip shark *Carcharhinus limbatus*. *J. Morphol*., 273, 1096.

[24] Reif, W. E. (1985). Squamation and Ecology of Sharks. *Cour. Forsch.-Inst. Senckenberg,* 78, 1.

[25] Wainwright, D. K., and Lauder, G. V. (2016). Three-dimensional analysis of scale morphology in bluegill sunfish. *Lepomis macrochirus*, *Zoology,* 119, 182.

[26] Wen, L., Weaver, J. C., Thornycroft, P. J. M., and Lauder, G. V. (2015). Hydrodynamic function of biomimetic shark skin: effect of denticle pattern and spacing. *Bioinsp. Biomimet.,* 10, 1.

[27] Li, R. and Adelson, E. (2013). in *Proceedings of the IEEE Conference on Computer Vision and Pattern Recognition*), pp. 1241.

[28] Li, R., Platt, R., Yuan, W., ten Pas, A., Roscup, N., Srinivasan, M. A., and Adelson, E. (2014). in *Intelligent Robots and Systems (IROS), 2014 IEEE/RSJ International Conference on* (*IEEE*), pp. 3988.

[29] Oeffner, J. and Lauder, G. V. (2012). The hydrodynamic function of shark skin and two biomimetic applications. *J. Exp. Biol.,* 215, 785.

[30] Lauder, G. V., Anderson, E. J., Tangorra, J., and Madden, P. G. A. (2007). Fish biorobotics: kinematics and hydrodynamics of self-propulsion. *J. Exp. Biol.,* 210, 2767.

[31] Quinn, D. B., Lauder, G. V., and Smits, A. J. (2015). Maximizing the efficiency of a flexible propulsor using experimental optimization. *J. Fluid Mech*., 767, 430.

[32] Lauder, G. V., Flammang, B. E., and Alben, S. (2012). Passive robotic models of propulsion by the bodies and caudal fins of fish. *Int. Comp. Biol*., 52, 576.

[33] Shelton, R. M., Thornycroft, P. J. M., and (2014). G. V. Lauder. Undulatory locomotion by flexible foils as biomimetic models for understanding fish propulsion. *J. Exp. Biol*., 217, 2110.

[34] Lim, J., and Lauder, G. V. (2016). Mechanisms of anguilliform locomotion in fishes studied using simple three-dimensional physical models. *Bioinsp. Biomimet*., 11, 046006.

[35] Alben, S., Witt, C., Baker, T. V., Anderson, E. J., and Lauder, G. V. (2012). Dynamics of freely swimming flexible foils. *Phys. Fluids,* 24, 051901.

[36] Wen, L. and Lauder, G. V. (2013). Understanding undulatory locomotion in fishes using an inertia-compensated flapping foil robotic device. *Bioinsp. Biomimet*., 8, 046013.

[37] Quinn, D. B., Lauder, G. V., and Smits, A. J. (2014). Scaling the propulsive performance of heaving flexible panels. *J. Fluid Mech*., 738, 250.

[38] Quinn, D. B., Lauder, G. V., and Smits, A. J. (2014). Flexible propulsors in ground effect. *Bioinsp. Biomimet.,* 9, 1.

[39] Castro, J. I. (2011). *The Sharks of North America* (Oxford Univ. Press, Oxford).

[40] Lucas, K. N., Thornycroft, P., Gemmell, B. J., Colin, S. P., Costello, J. H., and Lauder, G. V. (2015). Effects of non-uniform stiffness on the swimming performance of a passively-flexing, fish-like foil model. *Bioinsp. Biomimet.,* 10, 056019.

[41] Borazjani, I. and Daghooghi, M. (2013). The fish tail motion forms an attached leading edge vortex. *Proceedings. Biological Sciences / The Royal Society,* 280, 20122071.

[42] Wilga, C. D. and Lauder, G. V. (2000). Three-dimensional kinematics and wake structure of the pectoral fins during locomotion in leopard sharks *Triakis semifasciata*. *J. Exp. Biol*., 203, 2261.

[43] Wilga, C. D. and Lauder, G. V. (2001). Functional morphology of the pectoral fins in bamboo sharks, *Chiloscyllium plagiosum*: benthic versus pelagic station holding. *J. Morphol*., 249, 195.

[44] Lang, A. W., Bradshaw, M. T., Smith, J. A., Wheelus, J. N., Motta, P. J., Habegger, M. L., and Hueter, R. E. (2014). Movable shark scales act as a passive dynamic micro-roughness to control flow separation. *Bioinsp. Biomimet*., 9, 036017.

[45] Lang, A. W., Motta, P., Hidalgo, P., and Westcott, M. (2008). Bristled shark skin: a microgeometry for boundary layer control?. *Bioinsp. Biomimet*., 3, 046005.

[46] Gemmell, B. J., Colin, S. P., Costello, J. H., and Dabiri, J. O. (2015). Suction-based propulsion as a basis for efficient animal swimming. *Nature Commun.,* 6.

[47] Anderson, E. J., McGillis, W., and Grosenbaugh, M. A. (2001). The boundary layer of swimming fish. *J. Exp. Biol.,* 204, 81.

[48] Ehrenstein, U. and Eloy, C. (2013). Skin friction on a moving wall and its implications for swimming animals. *J. Fluid Mech.,* 718, 321.

[49] Ehrenstein, U., Marquillie, M., and Eloy, C. (2014). Skin friction on a flapping plate in uniform flow. *Philosophical Transactions of the Royal Society of London A: Mathematical, Physical and Engineering Sciences,* 372, 20130345.

[50] Yanase, K. and Saarenrinne, P. (2015). Unsteady turbulent boundary layers in swimming rainbow trout. *J. Exp. Biol.,* 218, 1373.

[51] Motta, P. J. (1977). Anatomy and functional morphology of dermal collagen fibres in sharks. *Copeia,* 1977, 454.

[52] Wainwright, S. A., Vosburgh, F., and Hebrank, J. H. (1978). Shark skin: function in locomotion. *Science,* 202, 747.

This work was done in collaboration with Prof. Katia Bertoldi, James Weaver, Prof. Li Wen, Zhexin Xie, Ning An, Connor Green, Tianmiao Wang, Zheyuan Gong, and Elias M. Knubben.

5

Octopus Arm-Inspired Tapered Soft Actuators with Suckers for Improved Grasping

5.0 Abstract

Octopuses can employ their tapered arms to catch prey of all shapes and sizes because of their dexterity, flexibility, and gripping power. Intrigued by variability in arm taper angle between different octopus species, we explored its utility in the design of soft actuators exhibiting a distinctive conical geometry, which is in stark contrast to previous more traditional cylindrical forms. We found that the octopus-inspired conical-shaped actuators exhibited a wide range of bending curvatures that could be tuned by simply altering their taper angle. The taper angle and bending curvature were inversely related, while taper angle and applied bending force were directly related. Using insights gained from these results, two taper angles were chosen for the design and fabrication of complete octopus arm-inspired grippers, which incorporated suction cups for improved functionality, similar to their biological counterparts. This design allowed for a novel, multifunctional soft actuator which combined bending (via a tapered actuator) and suction (via rows of flexible suckers) for powerful gripping. By choosing appropriate taper angles with integrated suction cups, the two tapered soft actuators with suckers were able to grip, move, and place a remarkably wide range of objects with flat, nonplanar, smooth, or rough surfaces, as well as retrieve objects through narrow openings. The results from these studies not only provide new design insights into the creation of next-generation soft robotic

actuators for gripping a wide range of morphologically diverse objects, but also contribute to our understanding of the functional significance of arm taper angle variability across octopus species.

5.1 Introduction

Biological systems have inspired the design of a wide range of materials and devices capable of addressing modern engineering challenges (1-7). Octopuses represent one such example. They can effectively catch prey of different shapes and sizes, perform remarkably complex tasks, and retrieve objects from constrained environments by combining two important capabilities: (i) the highly coordinated motion of their arms and (ii) the integration of linear arrays of suckers (Figure 5.1*A*-*C*) (8-12). Because of their flexibility, agility and adaptability for efficiently grasping a wide range of structurally diverse objects, octopus arms have served as model systems for the development of robust soft robotic prototypes, ranging from single powerful actuators (13-16) to more complex multi-actuator systems (17-20). These soft robots offer many advantages over their more traditional rigid counterparts, in that they are significantly easier and cheaper to manufacture, are safer to operate around human subjects, and can achieve complex outputs with simple inputs (21-31). Despite the fact that octopus arms exhibit a characteristic cone-shaped geometry, tapering from the base to the tip, most soft actuators (including octopus-inspired forms) exhibit a constant cross-sectional diameter along their length (19, 23, 25-27). While this taper angle of octopus arms is highly variable between different species (see Figure B.1), little is known regarding the functional significance of this observed diversity.

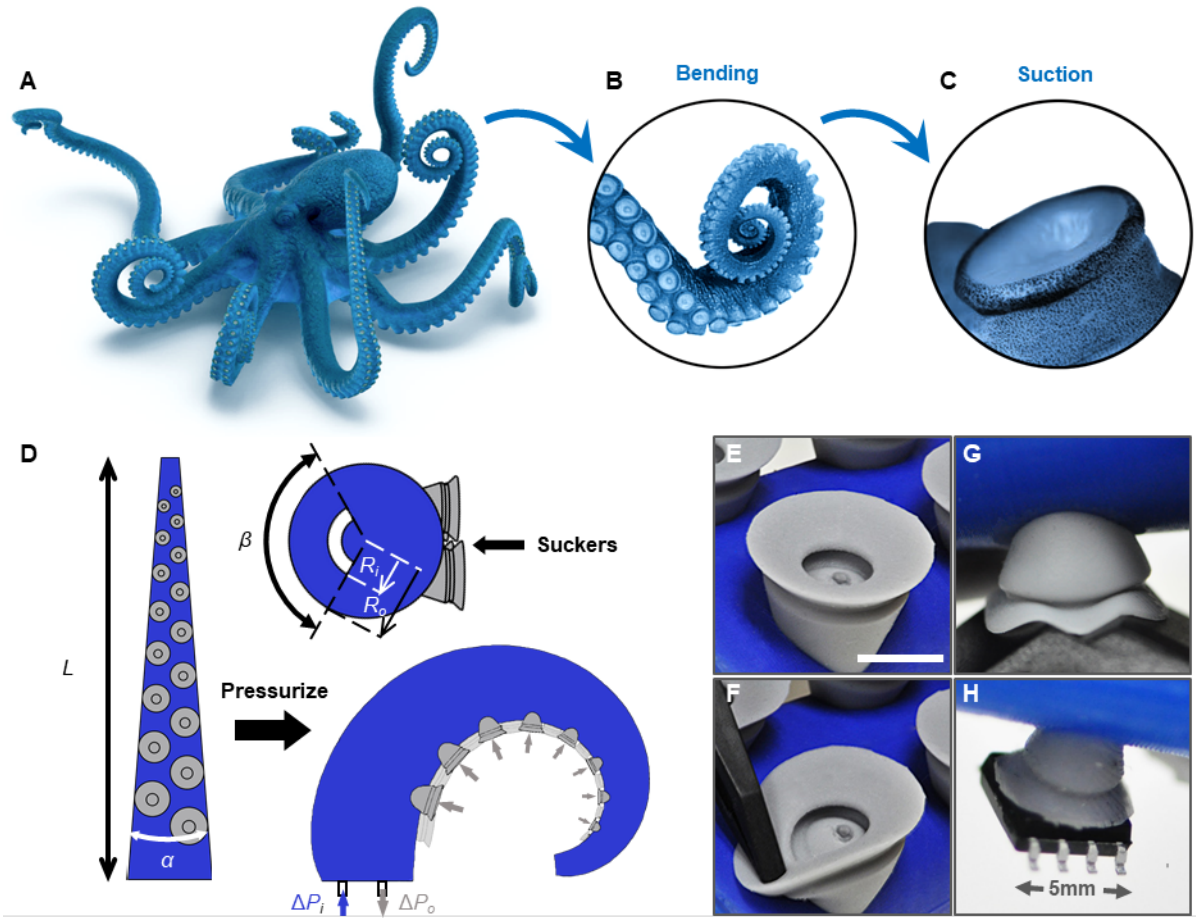

Figure 5.1: Octopus arm-inspired tapered soft actuators with suckers for improved grasping. (A-C) Octopus arms are tapered and incorporate both bending and suction functionalities. Here, we use them as inspiration for the design of soft robotic actuators with improved grasping. (D) Schematics of our tapered soft actuators with suckers. (E)-(H) Our suckers are flexible, conformable, and can attach to small objects.

Inspired by investigations into the morphological diversity of octopus arms, in the present work, we explore the potential trade-offs between dexterity and gripping power in tapered soft actuators. In contrast to previous studies on octopus-inspired robots, which focused primarily on either arm motion (13-15, 17), or sucker action alone (32-35), the present study integrates both concepts. First, we numerically study the bending kinematics and applied forces of tapered

soft actuators. Then, we use these findings to guide the design and fabrication of an octopus arm-inspired soft robot with integrated suckers for improved gripping (Figure 5.1*D*-*H*). We demonstrate that our fluidic tapered soft actuator with suckers can effectively grasp a variety of geometrically diverse objects, including flat and curved forms with diverse moduli and surface roughness, as well as retrieve objects through narrow openings. The results from this study thus provide new design cues for the realization of soft robotic actuators capable of gripping a wider range of nonplanar objects, as well as new insights into how variability in octopus arm taper angle may affect grasping strength and prey item choice.

5.2 Results

5.2.1 Octopus Arms

In this study, we focus on two important features of octopus arms: the taper angle and the suckers. To explore the diversity in octopus arm taper angle, we performed detailed measurements from online photographs (of living specimens) acquired from ten different octopus species (see supplementary section B.1 and Figure B.1). We found that arm taper angle can vary widely, ranging from $< 4°$ for the very slender arms of *Octopus macropus* to $> 9°$ for the comparatively broader arms found in *Eledone cirrhosa* (Figure 5.2), detailed data can be found in table S1. Guided by these measurements, in this study we considered taper angles ranging from $\alpha = 3°$ to $\alpha = 13.5°$ and investigated their effects on both actuator bending curvature and applied bending force.

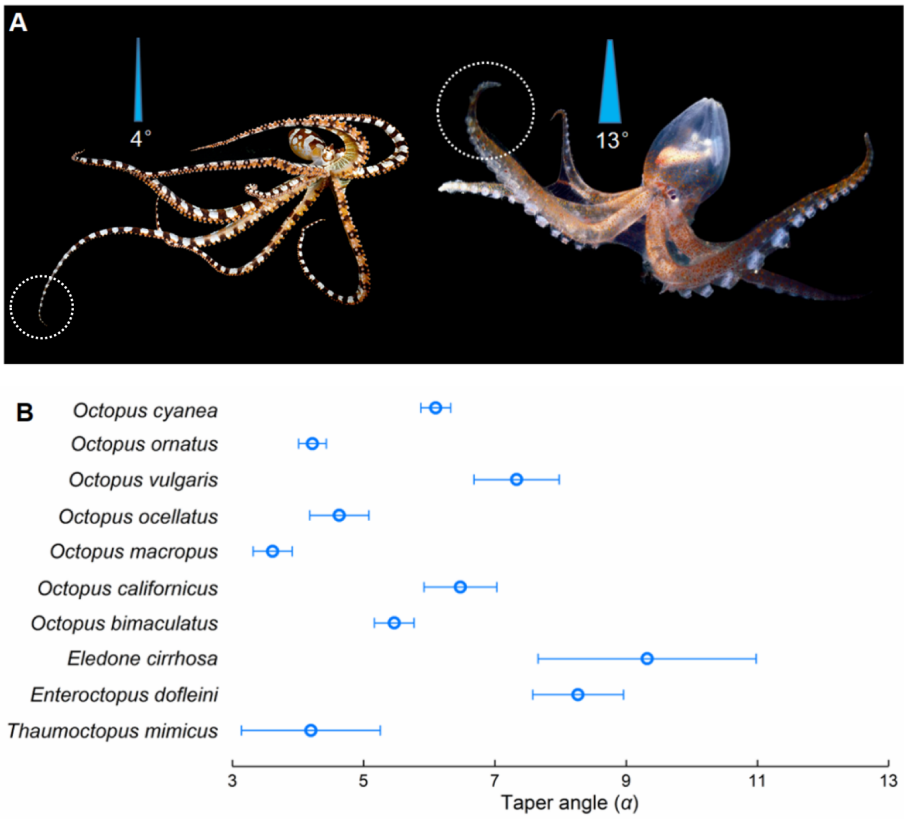

Figure 5.2: Arm taper angle diversity among various octopus species. (A) Photographs of two representative octopus species that exhibit low (left, *Wunderpus photogenicus*) and high (right, *Vitrelladonella richardi*) arm taper angles. (B) Taper angle measurements from ten different octopus species (multiple individuals of each species were considered).

In most octopus species, two rows of suckers are distributed in a staggered arrangement along the ventral surface of each arm, with diameters ranging from a few millimeters to a few centimeters (36, 37). They comprise an exposed disc-like infundibulum and a central cavity acetabulum and allow for strong attachment not only to large flat surfaces, but also to irregular surfaces and even objects smaller than a single sucker (38, 39). In this study, we mimicked the general structure and distribution when designing our soft robotic suckers for integration into our tapered soft actuators.

5.2.2 Effect of Taper Angle on Bending Curvature and Applied Bending Force

We first investigated, numerically, via finite element (FE) simulations the properties of tapered pneumatic soft actuators (without suckers), focusing on the effect of the taper angle on both bending curvature and applied bending force. Specifically, we considered tapered soft actuators, each of the same length (L = 200 mm) and tip diameter (D_{tip} = 8.4 mm), but with taper angles ranging from $\alpha = 3°$ to $\alpha = 13.5°$ (see Section B.2 for more design details). To induce bending via inflation, a single hollow internal ring-shaped chamber was placed along their length (see Figure B.2*A* for schematic), at a fixed normalized distance from the outer radius.

All models were constructed using 8-node linear brick elements (Abaqus element type C3D8H) and the material behavior was captured using an incompressible Gent model (40) with initial shear modulus μ = 195 kPa and stiffening parameter J_m = 12 (see Section B.3 for more details). Static non-linear simulations were performed using Abaqus/Standard and, in order to induce bending, each actuator's inner chamber was pressurized from P = 0 kPa to P = 200 kPa with the bottom end of the actuator being held in a fixed position. To evaluate the effect of the taper angle on the bending curvature, no additional constraint was added and at each incremental 2 kPa increase in pressure, the maximum, minimum, and average curvature along the bending profile of the actuator was measured (see Section B.4 for more details). To study the effect of taper angle on applied bending force, the actuators were placed at a horizontal distance d = 30 mm away from a

rigid body surface (representing a hypothetical load cell) and frictional surface to surface contact (with a coefficient of friction of 0.5) was employed between the actuator and the hypothetical load cell. When an input pressure was applied to each of these actuators (with the actuator base fixed), they would bend towards this rigid surface and the applied force was monitored.

To begin with, we validated our numerical simulations by comparing the numerical results to those obtained experimentally for actuators fabricated from Mold Star 30 (Smooth-On Inc., PA) silicone rubber (see Section B.4 and Figures S10 and S12). Since we found an excellent agreement between the two data sets in terms of both bending curvature and bending force over a wide range of pressures, we then proceed to use FE simulations for a much more extensive exploration of the actuator design space. We started by numerically investigating the effect of the taper angle on the bending curvature. The results shown in Figure 5.3*A* demonstrate that the bending curvature of the tapered actuators depend highly on both the taper angle α and the pneumatic pressure P. Specifically, the bending curvature increases as pressure P increases, but decreases as the taper angle α increases. For example, the average bending curvature (κ) decreased by over 2-fold (from $\kappa = 0.0282$ mm^{-1} to $\kappa = 0.0134$ mm^{-1}) by increasing the taper angle from $\alpha = 3°$ to $\alpha = 13.5°$ at P = 200 kPa, and changed from $\kappa = 0.0009$ mm^{-1} to $\kappa = 0.0134$ mm^{-1} by increasing the pneumatic pressure from P = 100 kPa to P = 200 kPa for $\alpha = 13.5°$. (See Section B.5 and Figure B.11 for more detailed simulation results of bending curvature). It should also be noted that for a given pressure and taper angle, the maximum,

minimum, and average curvatures varied along the length of the actuator, thus permitting the grasping of different sized objects at a single actuating pressure.

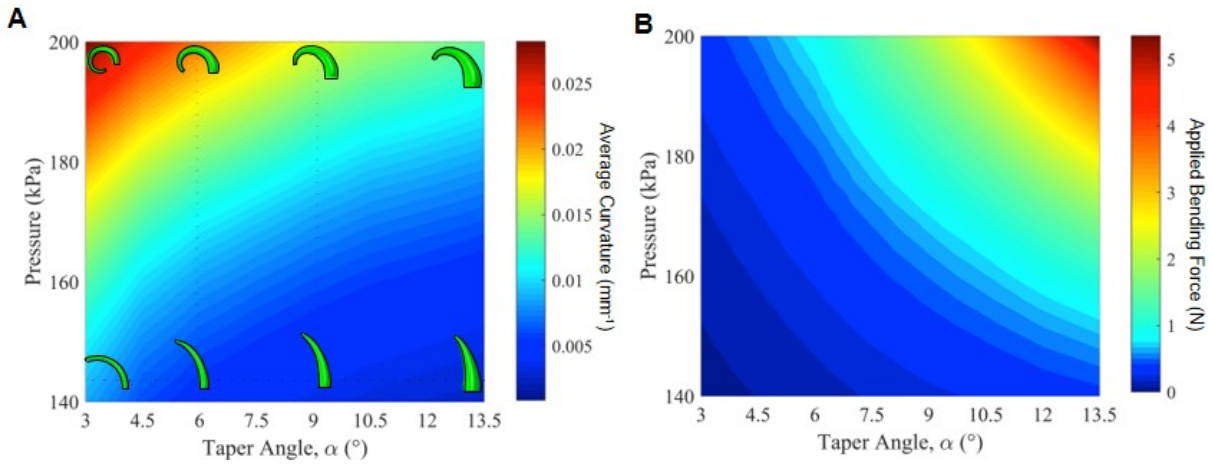

Figure 5.3: Modeling the effects of arm taper angle on bending curvature and applied bending force. (A) Numerical results illustrating the average bending curvature (κ) as a function of taper angle (α) and input pressure (P). Bending profile snapshots obtained from the simulations at P = 150 kPa and P = 200 kPa are overlaid on the heat map. (B) Numerical results illustrating the applied bending force (F_N) as a function of taper angle (α) and input pressure (P).

After characterizing bending curvature as a function of taper angle, we next investigated the exerted bending force as a function of pressure. Interestingly, the numerical results reported in Figure 5.3*B* show that the taper angle produced opposite responses in terms of bending force and bending curvature (Figure 5.3*B* and see Section B.4 and Figure B.9 for results of other measured distances other than d = 30 mm). For example, the bending force increased from 0.33 N to 5.35 N when the taper angle was increased from α = 3° to α = 13.5° at P = 200 kPa (Figure 5.3*B*) while the bending curvature decreased from κ = 0.0282 mm^{-1} to κ = 0.0134 mm^{-1} when the taper angle was increased from α = 3° to α = 13.5° at P =200 kPa

(Figure 5.3*A*). Therefore, when taking both the bending force and bending curvature results into account, we discovered an inherent tradeoff between the two. Overall, models with lower taper angles output a lower force but could bend with much larger curvature (with the opposite being true for larger taper angles).

5.2.3 The Complete Octopus Arm-Inspired Prototype

Guided by these numerical results, we next sought to build an octopus arm-inspired robot consisting of a tapered soft actuator with integrated suckers for further improved grasping ability. Given the observed trade-off between bending curvature and bending force, one could select either a taper angle that places a premium on bending curvature or bending force, or a taper angle that balances both at moderate levels. In this study, we chose: (i) an intermediate taper angle ($\alpha = 9°$) that leads to a good balance between high force-application and moderate bending curvature; and (ii) a relatively small taper angle ($\alpha = 4.5°$) that places a premium on bending curvature over applied bending force.

Our octopus-inspired prototypes included silicone rubber suction cups (made from Dragon Skin FX-Pro, Smooth-On Inc., PA) which were integrated into the design using a multi-step molding process (Section B.6 and Figure B.13). The flexible suckers were designed and fabricated by mimicking the geometries of the infundibulum and acetabulum of Octopus vulgaris (Figure 5.1*C*) (41), and a vacuum generator was used to lower the pressure inside each of the suckers. Upon evacuation, the suckers could conform and attach to small objects (Figure 5.1*H*) and even those with irregular surfaces (Figure 5.1*G*). To account for the tapered actuator, the sizes of the suction cups decreased from the base of the actuator to the

tip, as is seen in its biological counterpart, and no appreciable differences in the bending curvatures (κ) were found between actuators with suckers and those without. Additionally, we found no mechanical interference between adjacent suckers even under large pneumatic pressures thanks to the spacing and distribution pattern of the suckers on the actuator (see Figures S14 and S15).

With the tapered soft actuator with suckers constructed, we then characterized the attachment behavior of the suckers to substrates exhibiting a variety of different geometries and surface roughnesses (see Section B.7 for details). We began by characterizing the attachment of the suckers to planar substrates (Figure 5.4*A*) since planar objects are often difficult to grasp using bending actuators alone. To this end, we measured via a substrate-integrated load cell the force when pulling the unpressurized actuator in direction perpendicular to the flat surface. We found that for a tapered actuator with $\alpha = 9°$ the pull-off force is 6.59 ± 0.32 N (Figure 5.4*B*). When such force was reached, the suckers eventually detached from the surface in a sequential fashion (Figure 5.4*A*), resulting in a post-yield stairstep-like failure mode (Figure 5.4*B*). During detachment, the edge of each sucker lip deformed toward the center of the sucker, eventually caving inward and causing detachment, with the attachment force dropping to zero once suction failure occurred. The results for the same test with the $\alpha = 4.5°$ actuator can be found in Figure B.16. The results are very similar to that of the $\alpha = 9°$ actuator but with just lower maximum pull-off force being exerted because larger taper angle results in stiffer actuator with proportionally larger suckers, and thus lead to larger pull-off force. Because of the compliant

nature of the suckers, they were also able to successfully attach to surfaces exhibiting a wide range of surface roughnesses (Figure 5.4*C*). For example, a tapered actuator with $\alpha = 9°$ required a pull-off force of 6.59 ± 0.32 N on a smooth surface, 8.43 ± 0.35 N on a medium-roughness surface (R_a = 20 µm), and 3.12 ± 0.50 N on a rough surface (R_a = 200 µm) (Figure 5.4*C*). While surface roughness did affect the required pull-off force, the suckers were able to maintain a reasonably high force even at the highest roughness, an effect which could be further enhanced by increasing the sucker modulus (see Section B.7 and Figure B.16 for additional details). A very similar result was observed with the various surface roughnesses for the $\alpha = 4.5°$ actuator as well, but once again with lower maximum pull-off force as previously explained.

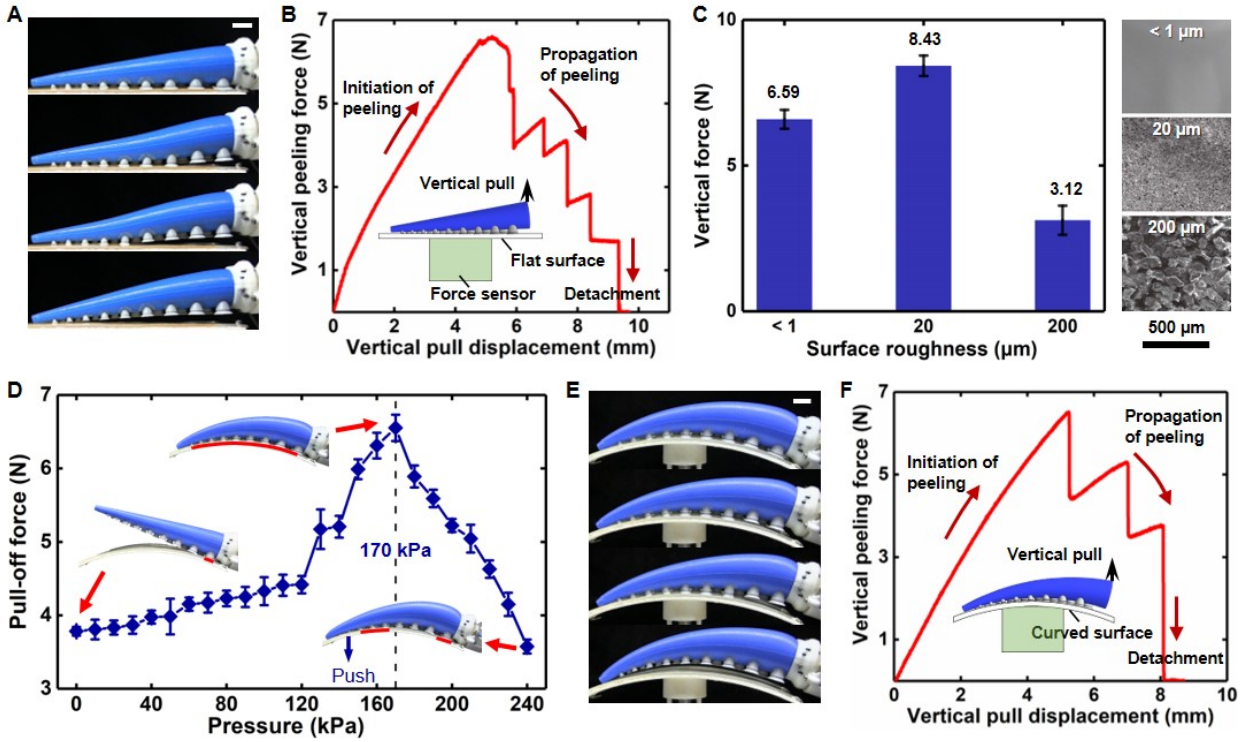

Figure 5.4: Sucker attachment force measurements. (A) Side-view photographs showing the sequential pull-off of an α = 9° actuator with its suckers activated (vacuum on) from a smooth planar surface (scale bar, 20 mm) and (B) its corresponding load-displacement curve. (C) The high flexibility of the integrated suckers permits successful attachment to materials exhibiting diverse surface roughnesses (R_a < 1 μm, 20 μm, 200 μm, SEM image widths, 500 μm). (D) Scanning a wide range of input pressures permits the identification of the optimal input pressure for maximizing pull-off force from non-planar substrates. The vertical dashed line indicates the "critical" pneumatic pressure values for maximizing the pull-off forces for the curvature of this specific surface (260 mm^{-1}). (E) Side-view photographs showing the sequential pull-off of an α = 9° actuator with its suckers actuated from a smooth curved surface (scale bar, 20 mm) and (F) its corresponding load-displacement curve (which is nearly identical to that shown in (B)).

We next characterized the attachment abilities of the tapered actuators with suckers to curved surface. One of the key advantages of our tapered soft actuators design is that attachment can be improved by pressuring the actuator to closely approximate the surface curvature of the object being grasped, so that all of the suckers can be engaged to the surface. To demonstrate this point, we focused on a surface with curvature 1/260 mm^{-1} and investigated how a α = 9° tapered actuator with suckers adhered to it as a function of the input pressure. The results shown in Figure 5.4*D* indicate that the attachment of the tapered soft actuator with suckers to the surface is highly dependent on the pressure input since this determines how many suckers engaged to the surface. After determining the optimal pressure (P = 170 kPa) for this combination of actuator and surface curvature (Figure 5.4*D*), then this pressure was used to obtain the results shown in Figure 4E, F. Looking at these pull-off force results, we see that the actuator can achieve almost identical pull-off force on both flat (6.59 ± 0.32 N) and curved surfaces (6.55 ± 0.18 N) with a statistically non-significant difference (Figures 5.4*A,B* and 5.4*E,F*). This remarkable behavior is enabled by the interplay of bending and suction, since the

bending curvature of the actuator directly affects how many suckers are engaged with the non-planar surface and therefore affects the overall pulling strength of the actuator. While in Figures 5.4*D-F* we focus on the $\alpha = 9°$ actuator, the results for the $\alpha = 4.5°$ actuator are shown in Figure B.16. As for the $\alpha = 9°$ actuator, we find that the pressure alters the amount of suckers engaged to the surface and, therefore, significantly affects the pull-off force. However, in full agreement with our previous results and with our numerical analyses, the pull-off force for $\alpha = 4.5°$ actuator is lower than for the $\alpha = 9°$ actuator.

After characterizing the sucker's capabilities and required peeling forces, we explored the real world applications of our two prototypes with taper angle $\alpha = 4.5°$ and $\alpha = 9°$. We first demonstrated their abilities to attach, wrap, transport and deliver an object of interest, which necessitated the use of both bending and suction functionalities (Figure 5.5*A*). Specifically, a thin plastic sheet was grasped from an initially planar geometry and then transported and delivered in a rolled-up orientation - an operation that could be useful in assembly line applications involving thin membranes. In this example, the actuator characterized by $\alpha = 4.5°$ was able to move the thin sheet in three steps (see Figure 5.5*A*): i) Starting with the non-pressurized actuator (0 s) the suction cups made contact with the planar surface and a vacuum was applied. ii) Once the system detected the pressure change from the suckers, the robotic arm lifted the sheet to a predefined height above the workspace (4 s). At ~ 6 s (a preset time delay), the actuator was then pressurized (P = 250 kPa) to "wrap" the sheet into a roll (6.5 s). iii) The robotic arm transported the sheet quickly (8 s) and at a constant speed, and then delivered it to a human

hand at 12 s (by releasing the vacuum and inflation pressure). Figure B.17 shows the inflation and vacuum pressures as a function of time during this process. Based on the pressure sensory feedback, the "attach, wrap, transport and deliver" motion could be utilized in a semi-autonomous way, and could achieve safe and efficient assistance when interacting with a human subject. Similar results were also demonstrated with the α = 9° actuator, but the wrapping abilities were reduced based on the actuator's bigger taper angle leading to smaller curvatures.

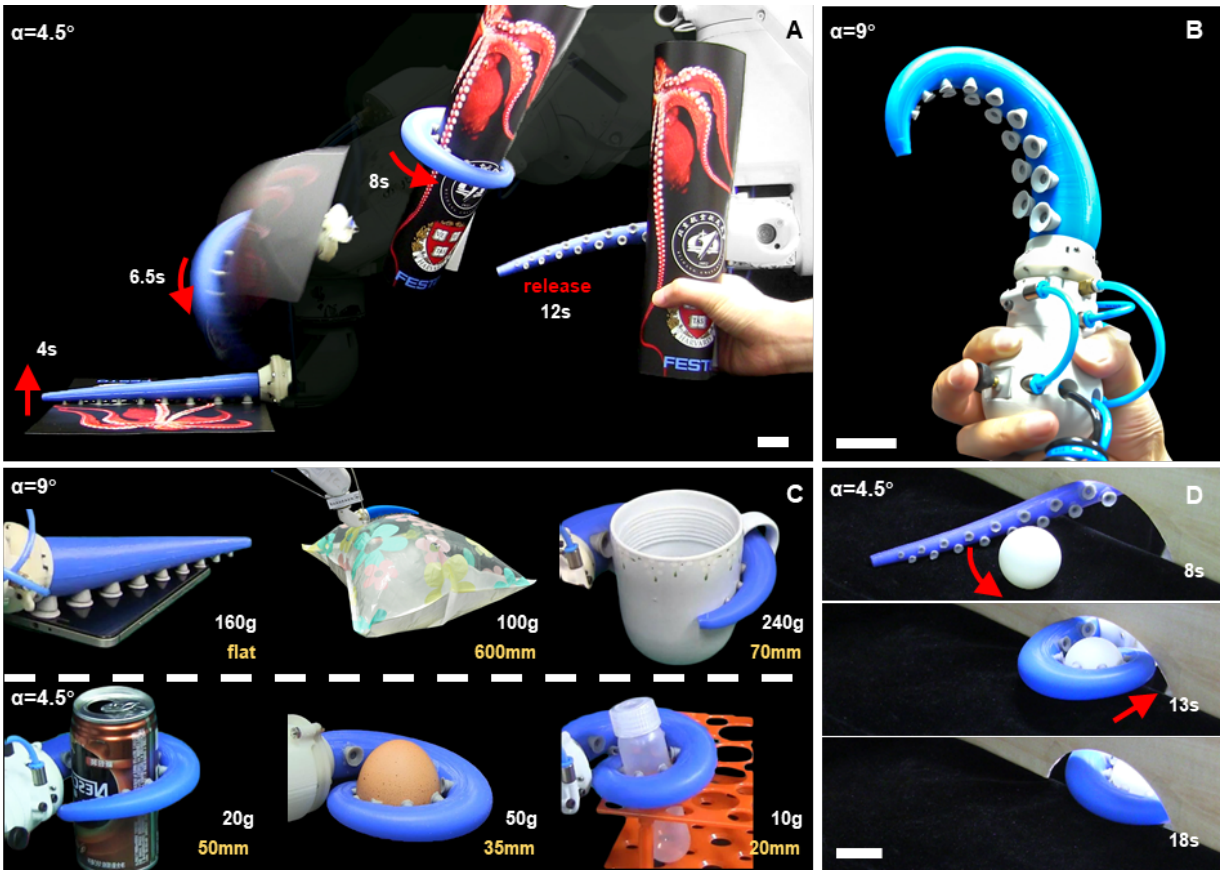

Figure 5.5: Exploring the application space for the tapered soft actuator with suckers. (A) Suction and bending for picking up, rolling, and placing a printed plastic sheet. This specific task is termed "attach, wrap, transport, and deliver" (scale bar, 30 mm). (B) In a modified configuration, a two-button bulb-like controller that integrates a pressure valve and vacuum regulator is used, allowing for simple, one-hand operability (scale bar, 30 mm). (C) The tapered soft actuator with suckers can grip a wide range of objects using this handheld controller. Upper row: $\alpha = 9°$ actuator; lower row: α

= 4.5° actuator. (D) The tapered actuator can also navigate narrow spaces through a reaching movement, implemented by a robotic arm, to fetch an object through bending and suction and pulling it back through the opening (scale bar, 30 mm).

To further expand on the practical applications of our design, we sought to create a seamless human-machine interface to control pressurization and depressurization. As an initial step in this direction, we constructed a device that integrated a pressurization valve and vacuum generator into a bulb-shaped handle (60 mm in diameter), with two buttons operable by a single human hand (Figure 5.5*B*). Using this bulb-shaped handle, we then examined the prototype's ability to grasp common objects (Figure 5.5*C*). Both prototypes were able to adequately grasp objects, such as a mug, a test tube, or a pillow; however, each actuator clearly has its strengths and weaknesses based on the previously observed trade-offs between curvature and applied bending force. The actuator with $\alpha = 4.5°$, for example, was able to more easily grasp the light weight items with higher curvatures, such as the can, egg, and test tube, whereas the $\alpha = 9°$ prototype struggled to do so (Figure 5.5*C*). This is because the actuator with $\alpha = 4.5°$ can bend into a larger curved state (a spiral shape with the tip of the robot curling past its base) with significant less time (0.3 s) than the actuator with $\alpha = 9°$ (1.2 s) (Figure B.18*A*). However, the $\alpha = 9°$ prototype was able to more easily grasp the heavier and bulkier objects with lower curvatures, such as the mug and pillow (Figure 5.5*C*), and a bucket of water weight up to 27 N, which is over 24 times the weight of the prototype (Figure B.18*B*). These results confirm that the combination of bending (with choosing the appropriate taper angle) and suction can allow for

the grasping of an extremely wide range of objects, including planar and non-planar geometries, rigid and soft, and rough and smooth objects.

Since octopuses are well known for the ability to retrieve objects from confined spaces (9), we also investigated whether our octopus-inspired actuator with suckers could perform similar functions. To carry out these studies, we considered a wall with a 4 cm diameter hole, and then we placed an object of interest on one side (Figure 5.5*D*) and the $\alpha = 4.5°$ actuator (which was barely small enough to fit through the opening) connected to a robotic arm (MOTOMAN MH3F, YASKAWA Inc., Japan) on the other one. The tapered design allowed for the actuator to extend most of its body through the opening (8 s), and then the resulting non-constant curvature of the pressurized tapered actuator allowed for the robot to grip the object (13 s) while still being tightly wound enough to return through the small opening with the object (18 s). The successful demonstration of this retrieving behavior was only possible with our streamlined tapered actuator design, and thus highlights the further usefulness of this conical geometry for object manipulation in constrained environments. We also mounted the actuator on an elephant trunk-like (or octopus arm-like) appendage to demonstrate a large-scale continuum of motion in three-dimensional space that could be safely operated in the company of human bystanders.

5.3 Discussion

In the present report, we demonstrated the tradeoff between bending curvature and force output in tapered octopus-inspired soft actuators. We then applied the learned tradeoff to guide the design and fabrication of a multifunctional

tapered soft actuator with suckers, and evaluated its gripping ability over a wide range of structurally diverse objects. We found that the actuators can display a range of different functionalities by simply altering the taper angle. When compared to the design strategies presented here, it should be noted that most other octopus-inspired gripper and soft robotic designs bend with a constant curvature (19, 25, 26). This constant curvature is based on the fact that conventional soft actuators, since they usually maintain a constant diameter along their length (Figure B.19). In contrast, our tapered actuators can achieve non constant bending curvature along its length and a more spiral-like shape due to their tapered form. The varying bending curvature along the length is an intriguing and potentially useful phenomenon in that it enables the actuators to grip objects with a much wider size range than those typically manipulated employing a non-tapered geometry.

The pneumatic pressure input (and the resulting bending curvature) was also seen to play an important role in the interfacial attachment of the suckers to non-planar surfaces, and could thus be employed to maximize the attachment performance of the suckers to such surfaces. As a result, and in contrast to previously documented soft machines employing other mechanisms of biologically inspired adhesion (42-45), our tapered actuators with suckers can easily grip a variety of flat, curved, smooth and rough items through the combined action of bending and suction. Compared to grippers that require several actuators organized into a hand-like geometry (23, 28, 29, 31, 46), our system requires only a single actuator to complete tasks thanks to its tapered form and combined bending and

suction features. This streamlined, high aspect ratio, multifunctional architecture thus enables the actuators to perform tasks in narrow and constrained conditions (Figure 5.5*D*), behaviors which are functionally similar to those observed in living octopus (47).

While in this study, our actuators design mimics only the bending motion of an octopus arm, future prototypes could also incorporate three-dimensional (out of plane) bending and elongation (48, 49), material stiffness variability (50), or the incorporation of reinforcing fibrous components (24) for added functionality. In the current study, because of the compact design of the actuators, we employed a simplified vacuum system to actuate the suckers, but we imagine that the acetabular contraction could be more closely mimicked in future studies with different types of soft actuators, including those based on dielectric elastomers (51, 52), shape memory polymers (53), or hydrogels (35, 54, 55). It should also be noted that the arm's taper angle can be dynamically altered in living octopuses when catching prey items of different sizes or weights (56), and could, in theory, be replicated in our soft robotic analogs using some of the design strategies and materials systems outlined above. The results and diverse octopus-inspired design elements described here could thus help lay the foundation for the future design of dynamically morphable soft robots that can adapt in real time to perform specific tasks of interest.

Finally, our results have implications for understanding the biomechanics of octopus arms. In nature, an octopus with a small arm taper angle (e.g., Octopus macropus, 3.58° ± 0.33°), and with a correspondingly thinner muscular structure,

produces smaller bending radii to catch small preys compared to an octopus with a larger arm taper angle (e.g., Eledone cirrhosa, 9.32° ± 1.66°) with a thicker muscular structure (57). The ecological and evolutionary consequences of this variability may be related to (i) size, strength, and speed of potential prey items, (ii) habitat structural heterogeneity, or (iii) depth-dependent food availability and related octopus energetics. While the precise reasons for this observed diversity of arm tapering angle is still largely unknown, the results reported here may shed new light on this matter and may stimulate further hypothesis testing into the various possibilities outlined above.

5.4 Materials and Methods

The biological data of octopus arm taper angles were analyzed using Matlab (Mathworks, USA), and details can be found in section B.1. The design geometry of the tapered actuator and its suckers investigated in this study is detailed in section B.2. The fabrication details of the tapered soft actuators used in the validation of the finite element simulations and the characterization of the material mechanical response can be found in section B.3. The bending curvature and bending force experiments on tapered soft actuators without suckers can be found in section B.4. The finite element simulations for bending curvature and applied bending force were conducted with Abaqus (SIMULIA, Providence, RI), and details can be found in section B.5. Using the insights from the results of the finite element simulations, the tapered actuators with suckers were ultimately fabricated with a multi-step molding and casting process. The tapered soft actuators were

made of Mold Star 30 (Smooth-On Inc., PA), and the suckers were made of Dragon Skin FX-Pro (Smooth-On Inc., PA). Details for this fabrication can be found in section B.6. The experiments of sucker attachment forces are detailed in section B.7. And finally, demonstrations of the complete tapered actuators with suckers can be found in section B.8.

5.5 REFERENCES

[1] Li, C., Zhang, T. and Goldman, D.I. (2013). A terradynamics of legged locomotion on granular media. *Science,* 339, 1408–1412.

[2] Kizilkan, E., Strueben, J., Staubitz, A., Gorb., S.N. (2017). Bioinspired photocontrollable microstructured transport device. *Sci. Robot.,* 2, eaak9454.

[3] Çulha, U.. Iida, F. (2016). Enhancement of finger motion range with compliant anthropomorphic joint design. *Bioinspir. Biomim.,* 11, 026001.

[4] Koh, J.S., Yang, E., Jung, G.P., Jung, S.P., Son, J.H., Lee, S.I., Jablonski, P.G., Wood, R.J., Kim, H.-Y., Cho., K.-J. (2015). Jumping on water: Surface tension–dominated jumping of water striders and robotic insects. *Science,* 349, 517–521.

[5] Wen, L., Weaver, J.C., Lauder., G.V., (2014). Biomimetic shark skin: Design, fabrication and hydrodynamic function. *J. Exp. Biol.,* 217, 1656–1666.

[6] Wang, Y., Yang, X., Chen, Y., Wainwright, D.K., Kenaley, C.P., Gong, Z., Liu, Z., Liu, H., Guan, J. T., Wang, Weaver, J. C., Wood, R. J. and Wen., L.

(2017). A biorobotic adhesive disc for underwater hitchhiking inspired by the remora suckerfish. *Sci. Robot.,* 2, eaan8072.

[7] Domel, A. G., Saadat, M., Weaver, J. C. Haj-Hariri, H., Bertoldi, K., Lauder, G. V. (2018). Shark skin-inspired designs that improve aerodynamic performance. *J. R. Soc. Interface.,* 15, 20170828.

[8] Vail, A. L., Manica, A., Bshary, R. (2013). Referential gestures in fish collaborative hunting. *Nat. Commun.,* 4, 1765.

[9] Richter, J. N. , Hochner, B., Kuba., M. J. (2015). Octopus arm movements under constrained conditions: adaptation, modification and plasticity of motor primitives. *J. Exp. Biol.,* 218, 1069-1076.

[10] Smith, A. (1996). Cephalopod sucker design and the physical limits to negative pressure. *J. Exp. Biol*., 199, 949-958.

[11] Sumbre, G. Gutfreund, Y., Fiorito, G., Flash, T., Hochner, B. (2001). Control of octopus arm extension by a peripheral motor program. *Science,* 293, 1845-1848.

[12] Margheri, L., Laschi, C., Mazzolai, B. (2012). Soft robotic arm inspired by the octopus: I. From biological functions to artificial requirements. *Bioinspir. Biomim.,* 7, 025004.

[13] Calisti, M., Giorelli, M., Levy, G., Mazzolai, B., Hochner, B., Laschi, C., Dario, P. (2011). An octopus-bioinspired solution to movement and manipulation for soft robots. *Bioinspir. Biomim.,* 6, 036002.

[14] Mazzolai, B., Margheri, L., Cianchetti, M., Dario, P., Laschi, C. (2012). Soft-robotic arm inspired by the octopus: II. From artificial requirements to innovative technological solutions. *Bioinspir. Biomim.,* 7, 025005.

[15] Laschi, C., Cianchetti, M., Mazzolai, B., Margheri, L., Follador, M., Dario, P. (2012). Soft robot arm inspired by the octopus. *Adv. Robot.,* 26, 709-727.

[16] Pikul, J. H., Li, S., Bai, H., Hanlon, R. T., Cohen, I., Shepherd, R. F. (2017). Stretchable surfaces with programmable 3D texture morphing for synthetic camouflaging skins. *Science,* 358, 210-214.

[17] Walker, I. D., Dawson, D. M., Flash, T., Grasso, F. W., Hanlon, R. T., Hochner, B., Kier, W. M., Pagano, C. C., Rahn, C. D., M. Zhang, Q. (2005). Continuum robot arms inspired by cephalopods. *Proceedings of the 2005 SPIE Conference on Unmanned Ground Vehicle Technology IV,* 5804, 303-315.

[18] Cianchetti, M., Calisti, M. , Margheri, L., Kuba, M., Laschi, C. (2015). Bioinspired locomotion and grasping in water: the soft eight-arm Ocotopus robot. *Bioinspir. Biomim.,* 10, 035003.

[19] Katzschmann, R. K., Marchese, A. D., Rus, D. (2015). Autonomous object manipulation using a soft planar grasping manipulator. *Soft Robotics*, 2, 155-164.

[20] Marchese, A. D., Rus, D. (2016). Design, kinematics, and control of a soft spatial fluidic elastomer manipulator. *Int. J. Robot., Res.* 35, 840-869.

[21] Rus, D., Tolley, M. T. (2015). Design, fabrication and control of soft robots. *Nature*, 521, 467.

[22] Majidi, C. (2014). Soft robotics: a perspective—current trends and prospects for the future. *Soft. Robot,* 1, 5-11.

[23] Shepherd, R. F., Stokes, A. A., Nunes, R., Whitesides, G. M. (2013). Soft machines that are resistant to puncture and that self seal. *Adv. Mater.*, 25, 6709-6713.

[24] Connolly, F., Walsh, C. J., Bertoldi, K. (2017). Automatic design of fiber-reinforced soft actuators for trajectory matching. *Proc. Natl. Acad. Sci.,* 114, 51-56.

[25] Mosadegh, B., Polygerinos, P., Keplinger, C., Wennstedt, S., Shepherd, R. F., Gupta, U., Shim, J., Bertoldi, K., Walsh, C. J., Whitesides, G. M. (2014). Pneumatic networks for soft robotics that actuate rapidly. *Adv. Funct. Mater.,* 24, 2163-2170.

[26] Polygerinos, P., Wang, Z., Overvelde, J. T., Galloway, K. C., Wood, R. J., Bertoldi, K., Walsh, C. J. (2015). Modeling of soft fiber-reinforced bending actuators. *IEEE Trans. Robot,* 31, 778-789.

[27] Galloway, K. C., Polygerinos, P., Walsh, C. J., Wood, R. J. (2013). Mechanically programmable bend radius for fiber-reinforced soft actuators. *Proceedings of the 16th International Conference on Advanced Robotics (ICRA)*, Montevideo, Uruguay, 25 to 29 November.

[28] Kwok, S. W., Morin, S. A., Mosadegh, B., So, J. H., Shepherd, R. F., Martinez, R. V., Smith, B., Simeone, F. C., Stokes, A. A., Whitesides, G. M. (2014). Magnetic assembly of soft robots with hard components. *Adv. Funct. Mater.,* 24, 2180-2187.

[29] Deimel, R., Brock, O. (2016). A novel type of compliant and under-actuated robotic hand for dexterous grasping. *Int. J. Robot. Res.,* 35, 161–185.

[30] Shepherd, R. F., Ilievski, F., Choi, W., Morin, S. A., Stokes, A. A., Mazzeo, A. D., Chen, X., Wang, M., Whitesides, G. M. (2011). Multigait soft robot. *Proc. Natl. Acad. Sci.,* 108, 20400-20403.

[31] Terryn, S., Brancart, J., Lefeber, D., Van, A. G., Vanderborght, B.. (2017). Self-healing soft pneumatic robots. *Sci. Robot.,* 2, eaan4268.

[32] Baik, S., Park, Y., Lee, T. J., Bhang, S. H., Pang, C. (2017). A wet-tolerant adhesive patch inspired by protuberances in suction cups of octopi. *Nature,* 546, 396.

[33] Hou, J., Wright, E., Bonser, R. H., Jeronimidis, G. (2012). Development of biomimetic squid-inspired suckers. *J. Bion. Engineer.,* 9, 484-493.

[34] Choi, M. K., Park, O. K., Choi, C., Qiao, S., Ghaffari, R., Kim, J., Lee, D. J., Kim, M., Hyun, W., Kim, S. J., Hwang, H. J., Kwon, S. H., Hyeon, T., Lu, N., Kim, D. H. (2016). Cephalopod-Inspired Miniaturized Suction Cups for Smart Medical Skin. *Adv. Health. Mater.,* 5, 80-87.

[35] Lee, H., Um, D. S., Lee, Y., Lim, S., Kim, H. J., Ko, H.. (2016). Octopus-Inspired Smart Adhesive Pads for Transfer Printing of Semiconducting Nanomembranes. *Adv. Mater.,* 28, 7457-7465.

[36] Tramacere, F., Beccai, L., Kuba, M. J., Mazzolai, B. (2013). Octopus suckers identification code (OSIC). *Mar. freshw. behav. phy.,* 46, 447-453.

[37] Smith., A. M. (1996). Cephalopod sucker design and the physical limits to negative pressure. *J. Exp. Biol.,* 199, 949-958.

[38] Kier, W. M., Smith, A. M. (1990). The morphology and mechanics of octopus suckers. *Biol. Bullet.,* 178, 126-136.

[39] Kier, A., W. M., Smith, M. (2002). The structure and adhesive mechanism of octopus suckers. *Integr. Comp. Biol.,* 42, 1146-1153.

[40] Gent, A. N. (1996). A new constitutive relation for rubber, *Rub. Chem. Tech.,* 69, 59-61.

[41] Tramacere, F., Follador, M., Pugno, N. M., Mazzolai, B. (2015). Octopus-like suction cups: from natural to artificial solutions. *Bioinspir. Biomim.,* 10, 035004.

[42] Autumn, K., Liang, Y. A., Hsieh, S. T., Zesch, W., Chan, W. P., Kenny, T. W., Fearing, R., Full, R. J. (2000). Adhesive force of a single gecko foot-hair. *Nature,* 405, 681.

[43] Song, S., Drotlef, D. M., Majidi, C., Sitti, M. (2017). Controllable load sharing for soft adhesive interfaces on three-dimensional surfaces. *Proc. Natl. Acad. Sci.,* 114, E4344-E4353.

[44] Glick, P., Suresh, S., Ruffatto, D. III, Cutkosky, M., Tolley, M. T., Parness, A. (2018). A soft robotic gripper with gecko-inspired adhesive. *IEEE Robot. Autom.* Lett., 3, 903-910.

[45] Li, J., Celiz, A. D., Yang, J., Yang, Q., Wamala, I., Whyte, W., Seo, B. R., Vasilyev, N. V., Vlassak, J. J., Suo1, Z., Mooney, D. J. (2017). Tough adhesives for diverse wet surfaces. *Science,* 357, 378-381.

[46] Hao, Y., Gong, Z., Xie, Z., Guan, S., Yang, X., Ren, Z., Wang, T., Wen, L. (2016). Universal soft pneumatic robotic gripper with variable effective

length. *Proceedings of the 35th IEEE Control Conference (CCC)*, Sichuan, China, 27 to 29 July 2016.

[47] UC Berkeley. (2015). Octopus to Shrimp. *YouTube*, https://www.youtube.com/watch?v=mc6fIuNTNEQ.

[48] Robertson, M. A., Paik, J. (2017). New soft robots really suck: Vacuum-powered systems empower diverse capabilities. *Sci. Robot.,* 2, eaan6357.

[49] Kim, S. J., Lee, D. Y., Jung, G. P., Cho, K. J. (2018). An origami-inspired, self-locking robotic arm that can be folded flat. *Sci. Robot.,* 3, eaar2915.

[50] Bartlett, N. W., Tolley, M. T., Overvelde, J. T. B., Weaver, J. C., Mosadegh, B., Bertoldi, K., Whitesides, G. M., Wood, R. J. (2015). A 3D-printed, functionally graded soft robot powered by combustion. *Science,* 349, 161-165.

[51] Shian, S., Bertoldi, K., Clarke, D. R. (2015). Dielectric elastomer based "grippers" for soft robotics. *Adv. Mater.,* 27, 6814-6819.

[52] Shintake, J., Rosset, S., Schubert, B., Floreano, D., Shea, H. (2016). Versatile soft grippers with intrinsic electroadhesion based on multifunctional polymer actuators. *Adv. Mater.,* 28, 231-238.

[53] Z. Zhao, K. Zhang, Y, Liu, J. Zhou, M. Liu. (2017). Highly Stretchable, Shape Memory Organohydrogels Using Phase-Transition Microinclusions. *Adv. Mater.,* 29.

[54] Fu, F., Shang, L., Chen, Z., Yu, Y., Zhao, Y. (2018). Bioinspired living structural color hydrogels. *Sci. Robot.,* 3, eaar8580.

[55] Kim, Y. S., Liu, M., Ishida Y., Ebina, Y., Osada, M., Sasaki, T., Hikima, T., Takata, M., Aida, T. (2015). Thermoresponsive actuation enabled by permittivity switching in an electrostatically anisotropic hydrogel. *Nat. Mater.,* 14, 1002.

[56] Kier, W. M., Stella, M. P. (2007). The arrangement and function of octopus arm musculature and connective tissue. *J. Morphol.,* 268, 831-843.

[57] Steer, A., Semmens, J. M. (2003). Pulling or drilling, does size or species matter? An experimental study of prey handling in Octopus dierythraeus (Norman, 1992). *J. Exp. Marine Biol. Ecol.,* 290, 165-178.

6

Conclusion and Summary

In this thesis, it has been shown how inspiration can be drawn from nature to guide human design for different engineering applications. This thesis started by looking closely at shark skin and analyzing the tiny tooth-like structures (denticles) that cover it, and from these analyses, inspiration was drawn to design structures and surfaces that can positively affect man-made aerial devices and dynamic systems. This work showed the novel concept that these denticles can be used as low-profile vortex generators on an airfoil to not only decrease the drag but also to simultaneously enhance the lift of the airfoil, which can ultimately lead to more efficient aerial systems. The results shown here have the potential to outperform all previously reported results for traditional low-profile vortex generators. Furthermore, the enhanced normal force (lift) shown by the denticles in this study also has implications in understanding the functional benefit conferred to a living shark by these denticles, with respect to increasing thrust when swimming. Further, when creating and testing the full biomimetic shark skin surfaces with a robotic flapping device, in addition

to their engineering applications, our findings also have implications in understanding how these denticles function on living sharks. Specifically, we saw that as the biomimetic denticles approached the size of the actual biological denticles, drag reduction/thrust improvement was achieved, further improving as we approached the true swimming parameters of a real shark. These findings also contribute to guiding the design of more efficient locomotory systems.

Finally, it was shown how inspiration could be taken from the arm of an octopus to develop a versatile soft robotic gripper. With the novel combination of suction (via biomimetic suckers) and bending (via a tapered soft actuator), the soft robotic gripper is able to grasp and manipulate a myriad of objects, including rigid flat objects, soft flat objects, rigid curved objects, and even delicate curved objects, just to name a few. This work, based on the measured biological range of taper angles of octopus arms from a variety of species, demonstrated how this range of taper angles affects the bending curvature and applied bending force of the soft robotic gripper. This work further reveals the added benefits of incorporating these concepts with a novel pneumatic sucker design.

From these various projects, it is clear that nature provides an array of features and structures – from the morphologically complex surface of shark skin, to the flexible and agile arms of an octopus – that can inspire future technological innovations.

A

Supporting Information for Chapter 2

A.1 GEOMETRY

In this section, we provide geometric details on all of the different foils considered in this study. All the airfoils tested in this study are based on a symmetric NACA0012 airfoil with aspect ratio W/L=2.8 (L=68mm being the chord length and W denoting the span length – see Figure A.1). We first characterized the aerodynamic performance of the smooth airfoil, and then investigated how the coefficients of lift and drag are affected when different geometric perturbations are arranged on its suction side.

Models of all foils were created using SolidWorks (SolidWorks Corp., Waltham, MA, USA). These models were exported as stl files and 3D printed using an Objet Connex500 3D printer (Stratasys Ltd, Eden Prairie, MN, USA). The foils were printed from a transparent photopolymer (RGD810) on the Connex500 3D printer. Any supporting material used to print the foil was easily removed using a water jet (1). Because this 3D printer has some precision limitations with which smooth surfaces can be printed, the leading edge of the foils had some slight roughness with a root-mean-square height of roughly 8 microns, measured using surface profilometry (2, 3).

A.1.1 SMOOTH CONTROL

In Figure A.1 we show a model of the airfoil used as the smooth control in this study. It consists of a symmetric NACA0012 airfoil with aspect ratio W/L=2.8 and no perturbation on its faces.

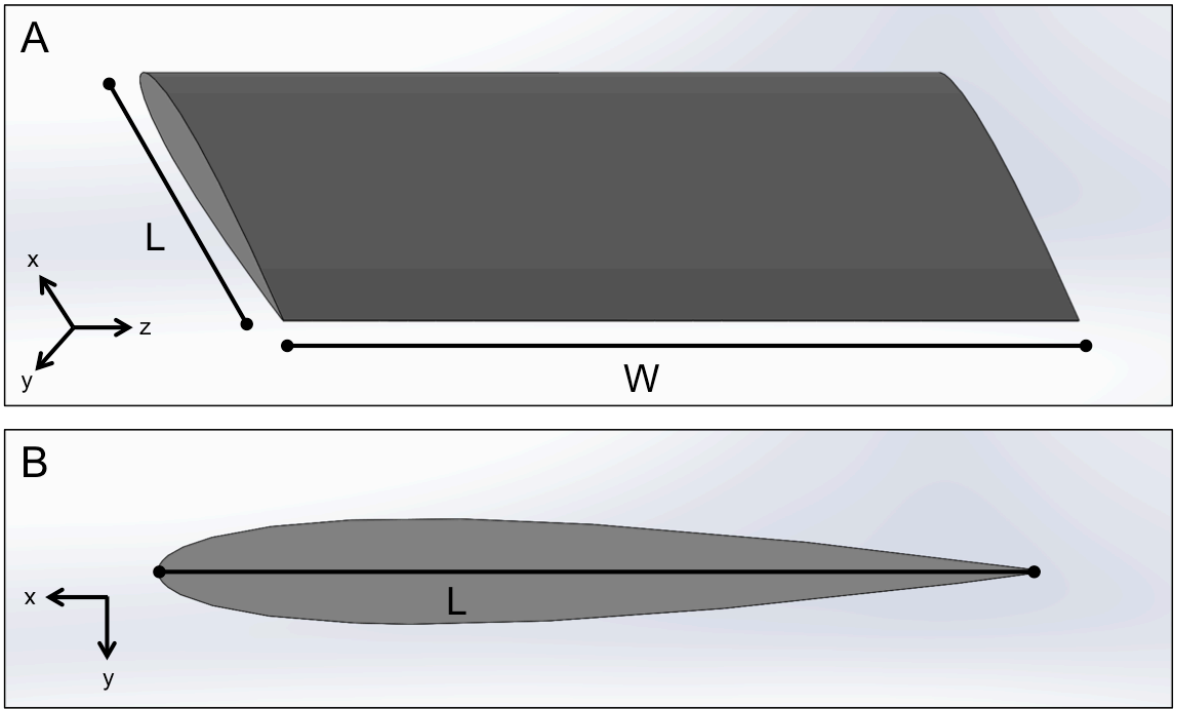

Figure A.1: (A) Isometric and (B) cross-sectional views of the smooth NACA0012 airfoil.

A.1.2 AIRFOILS WITH SHARK DENTICLES

We designed 20 airfoils characterized by different arrangements, sizes, and tilt angles of representative models of shark denticles attached to their suction side (see Figure A.2).

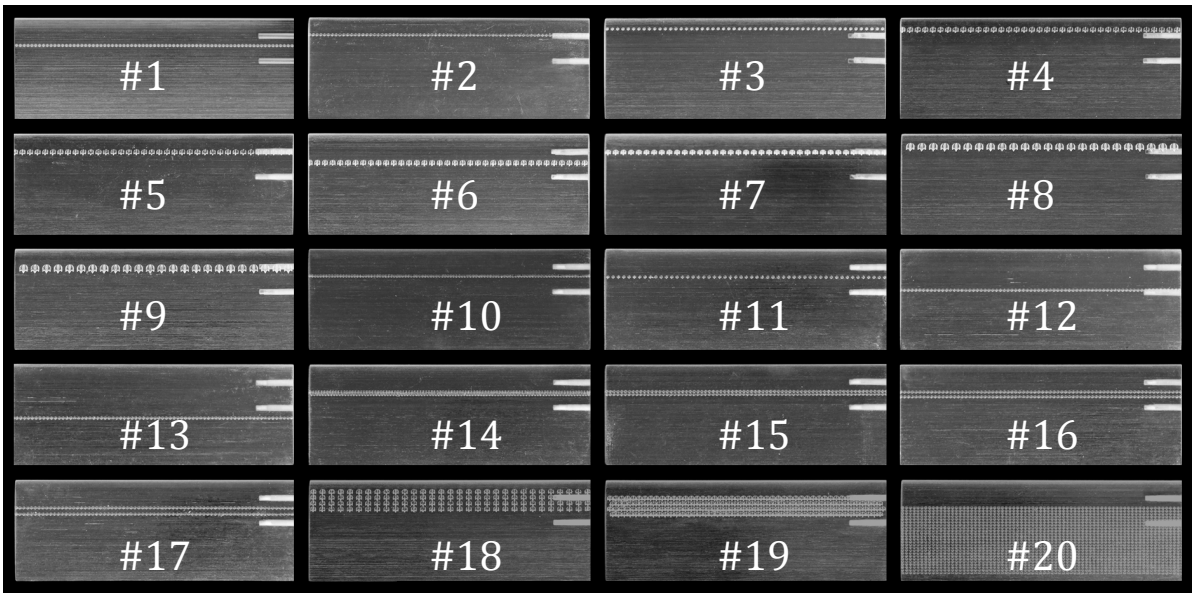

Figure A.2: Image of all 20 shark denticle foils tested. The two holes on the upper right of each foil were used to attach the foil to the testing apparatus.

Representative model of shark denticles: The 3D parameterized model of a single representative denticle from a shortfin mako shark (Isurus oxyrinchus) was constructed using a microCT scanner (XradiaVersaXRM-500, at Cornell University, Institute of Biotechnology) and meshed using Mimics 3D (Materialise Inc., Leuven, Belgium). Details of shark denticle modeling are also available in Wen et al. (2014, 2015) (1, 4). A representative model is shown in Figure A.3. There, l_c is the chordwise length of the middle ridge, l_r is the chordwise length of the side ridges, l_s is the spanwise length between the outside ridges (the middle ridge is placed in the middle between these two ridges), h_1 is the height of the

middle ridge, and h_2 is the height of the side ridges. Based on measurements of the shark denticles, in our study we kept l_c/l_s = 1.37, l_c/l_r = 1.25, h_1/h_2 = 1.40, and l_c/h_1 = 2.95 constant for all foils. Moreover, all denticles (except those arranged on foil #7) were placed with a 15° angle of tilt (θ) (see Figure A.3*D*). An additional 15° of tilt (meaning the denticles were rotated 15° further counterclockwise about their center) was given to the denticles arranged on foil #7. Additional details on the geometry of the denticles arranged on the 20 different foils considered in this study are provided in Table A.1.

Denticle arrangement: All denticles were placed on the suction side of the airfoils with their grooves aligned parallel to the chordwise direction (see Fig S2). 13 foils (Foils #1 - #13) comprise a single row of denticles placed at different distances, *d/L*, along the chord (*d* denoting the distance from the leading edge to the front of the row of denticles – see Fig S4*A*) and with a spanwise separation *b* varying between 0 and 3 mm (see Figure A.4*B* and Table A.1 for details). The remaining 7 foils (Foils #14 - #20) comprise multiple rows of denticles, arranged either according to a linear (see Figure A.4*C*) or staggered pattern (see Figure A.4*D*). Note that for these foils the geometric parameter *d* as specified in Table A.1 indicates the distance from the leading edge to the front of the first row of denticles. Moreover, in Table A.1 "closely packed" refers to denticles spaced as closely as possible without physically touching, as shown in Figure A.4*D*.

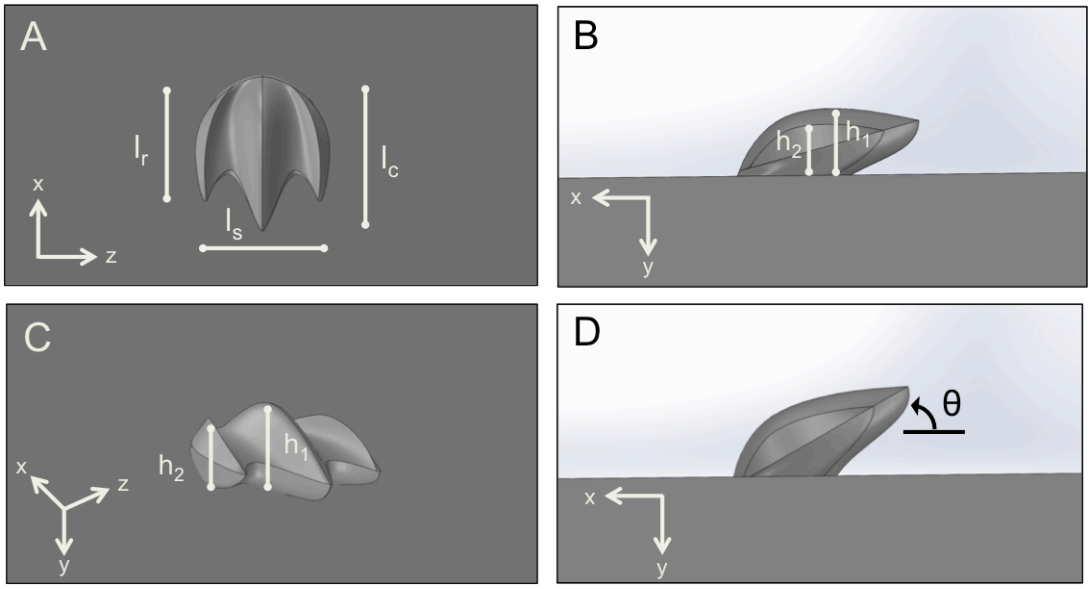

Figure A.3: (A) Top, (B) side, and (C) isometric view of the representative model of the shark denticle used in this study, along with the corresponding geometric parameters. (D) A tilt angle q=15° was used for all denticles except for foil #7, for which q=30°.

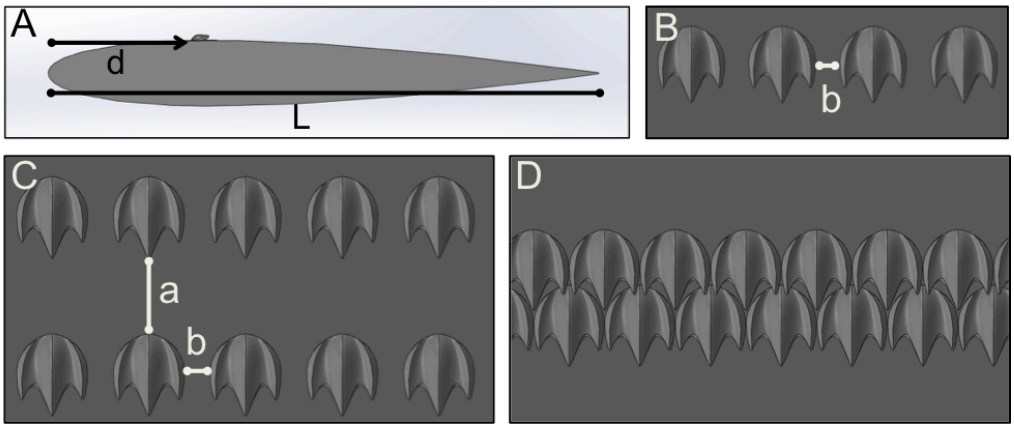

Figure A.4: (A) Side view of the foil showing the chordwise placement of the denticles on its suction side. (B) Foils #1 - #13 have a single row of denticles with a spanwise separation *b*. (C)-(D) Foils #14 - #20 comprise multiple rows of denticles arranged either on a (C) linear or a (D) staggered pattern.

Table A.1: Geometric parameters characterizing the 20 different shark denticle foils considered in this study. Images of all 20 shark denticle foils are shown in Figure A.2.

Foil #	Pattern	# of Rows	Chordwise Separation, a [mm]	Spanwise Separation, b [mm]	Location along Chord, d/L	Size of Denticle, l_c [mm]	Tilt Angle of Denticle, θ [deg.]
1	linear	1	n/a	1	0.26	2	15
2	linear	1	n/a	1	0.16	2	15
3	linear	1	n/a	2	0.10	2	15
4	linear	1	n/a	2	0.10	4	15
5	linear	1	n/a	2	0.16	4	15
6	linear	1	n/a	2	0.26	4	15
7	linear	1	n/a	2	0.16	4	30
8	linear	1	n/a	3	0.10	6	15
9	linear	1	n/a	3	0.16	6	15
10	linear	1	n/a	0	0.26	2	15
11	linear	1	n/a	2	0.26	2	15
12	linear	1	n/a	1	0.38	2	15
13	linear	1	n/a	1	0.50	2	15
14	staggered	2	closely packed	closely packed	0.26	2	15
15	linear	2	closely packed	1	0.26	2	15
16	linear	2	1	1	0.26	2	15

17	linear	2	2	1	0.26	2	15
18	linear	4	closely packed	3	0.10	4	15
19	staggered	4	closely packed	closely packed	0.16	4	15
20	linear	26	closely packed	1	0.26	2	15

A.1.3 AIRFOIL WITH 2D BUMP PROFILE

To further understand the effect of the denticles on the aerodynamic performance of the foils, we then considered a foil in which one row of denticles is replaced with a simple 2D bump profile, which has non-zero curvature only in the chordwise direction.

Figure A.5 below shows the morphology of the 2D bump foil. The leading edge curvature matches the shark denticle middle ridge leading edge curvature. However, rather than having an overhang like the shark denticle does, the bump attaches to the foil downstream from where the shark denticle middle ridge ends. This gives the 2D bump a streamlined nature so as to reduce pressure drag. Note that all parameters and dimensions (h_1, l_s, d, L, W) shown in Figure A.5 match exactly that of the best shark denticle foil (Foil #1). Specifically, h_1=0.7mm, l_c=2mm, d/L=0.26, L=68mm and W/L=2.8.

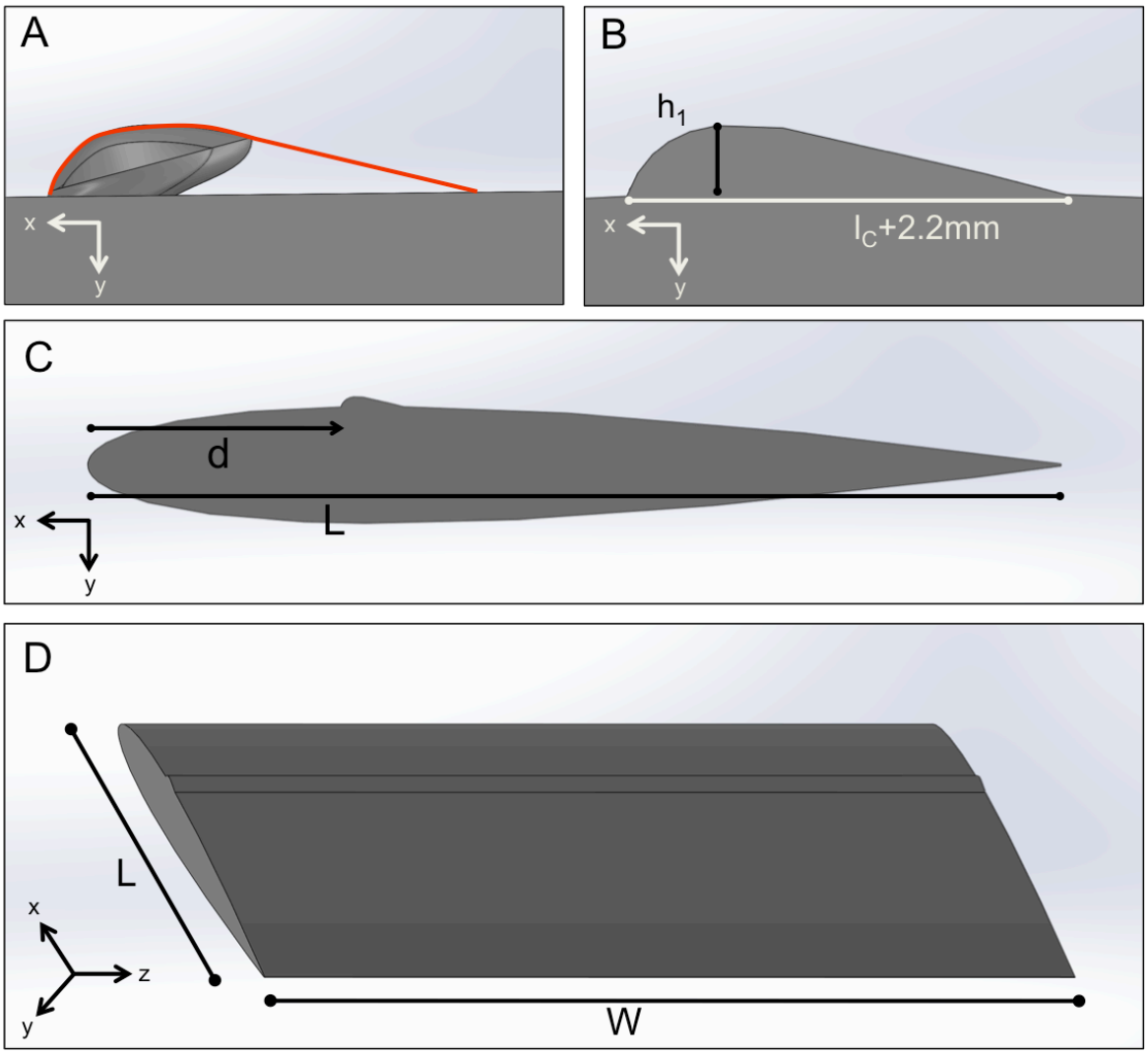

Figure A.5: (A) Comparison between the profile of the 2D bump (red line) and the representative model of the shark denticle. (B) Side view of the 2D bump. (C) Chordwise placement of the 2D bump on the foil (d/L=0.26). (D) Isometric view of the 2D bump foil.

A.1.4 Airfoil with Continuous Shark-Inspired Profile

Guided by our experiments, we then tried to improve the aerodynamic performance of the airfoil by designing a geometric perturbation that takes advantage of the multiple mechanisms that were seen to be beneficial in airfoils with the shark denticles and the 2D bump profile. More specifically, we designed a geometric perturbation that merges the ridges of the shark denticle with the continuous chordwise curved profile of the 2D bump profile. As such, we refer to this morphology as the continuous shark-inspired profile.

In Figure A.6 we show top, side, and isometric views of the continuous shark-inspired profile. Essentially, this morphology can be thought of as one continuous shark denticle that runs the full span of the foil at a chordwise placement of d/L = 0.26. The leading edge chordwise curvature matches that of the shark denticle (just like the 2D bump profile did). This morphology also has an extremely similar structure as that of the denticle with a long chordwise middle ridge between two smaller side ridges (the side ridges have been extended an extra 1.3mm and the middle ridge an extra 2.2mm so as to give this profile a very streamlined extended shape like that of the 2D bump profile, yet with pronounced chordwise ridges like that of the denticle). Similarly to foil #1, h_1=0.7mm, h_2=0.5mm, l_s=1.5mm, l_c=2mm, l_r=1.6mm, d/L=0.26, L=68mm, W/L=2.8.

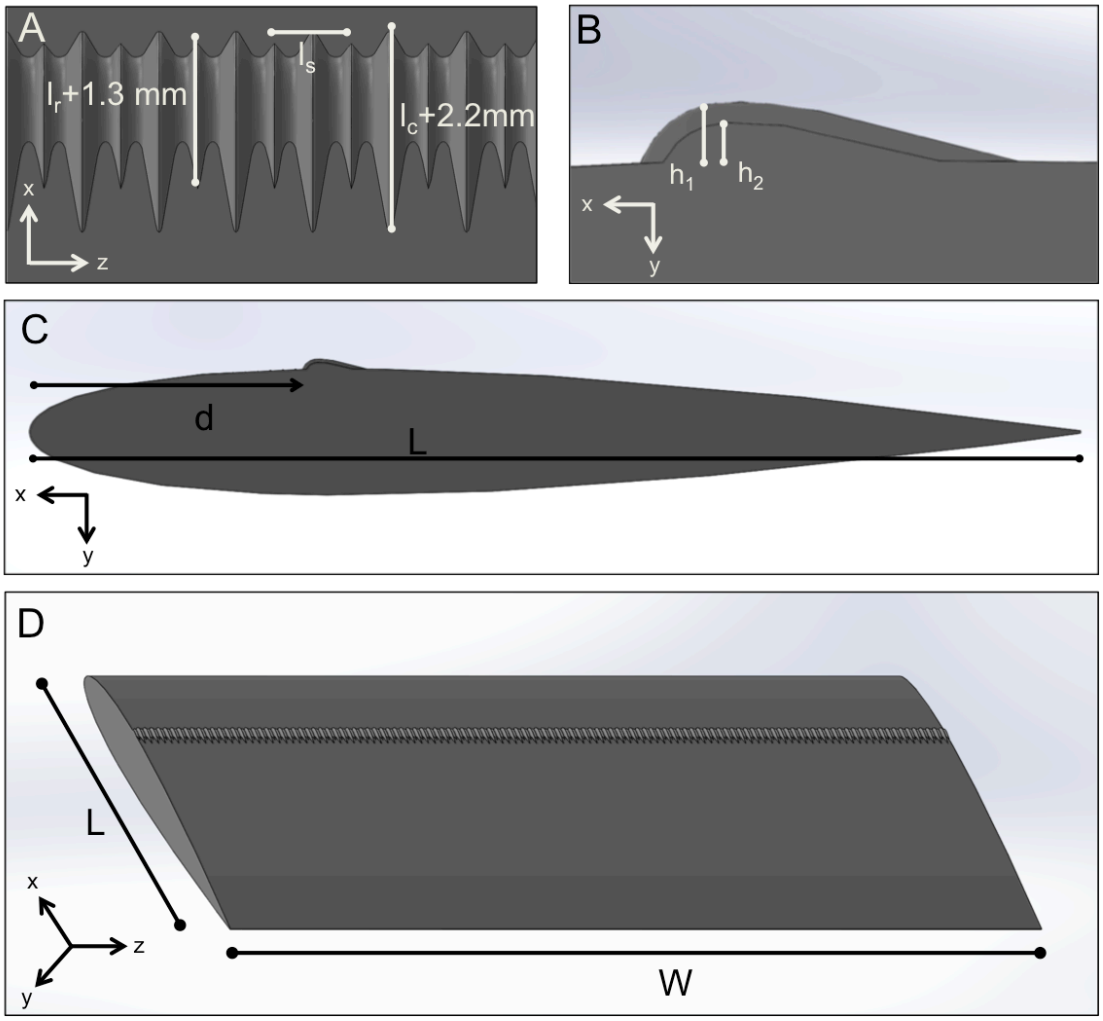

Figure A.6: (A) Top and (B) side views of the continuous shark-inspired profile. (C) Chordwise placement of the profile on the foil (*d/L*=0.26). (D) Isometric view of the continuous shark-inspired foil.

A.2 Experimental Setup

Each foil's aerodynamic performance was tested in steady state within the water flow tank shown in Figure A.7 (kinematic viscosity υ=1x10^{-6} m^2/s). All tests were conducted in the laminar regime with a flow speed of U=0.58m/s, which corresponds to a chord Reynolds number of $Re_c=UL/\upsilon\approx$4x10^4. PIV was conducted using this water tank as well. 10g of neutrally-buoyant, sliver-covered glass particles were added to the water tank, and a 10W continuous-wave argon-ion laser (Innova 300, Coherent Laser Group, CA, USA) was focused at the middle of each foil for which PIV was conducted. Using a Photron mini-UX100 high-speed video camera, high speed videos at 2000Hz and at a resolution of 1024 pixels by 1024 pixels were taken. Then, using LaVision's DaVis software (v 7.3.1), the videos were post-processed to obtain the streamlines.

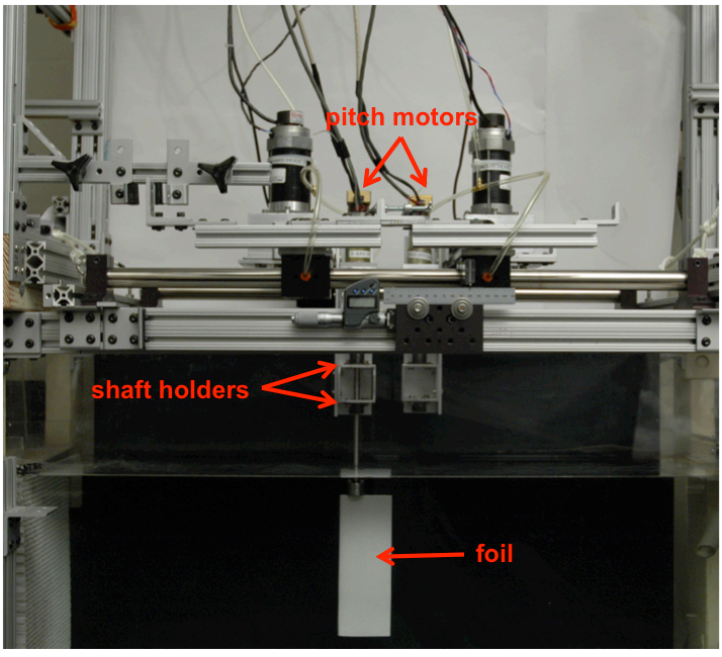

Figure A.7: Experimental flow tank setup used to test the foils. The pitch motors are used to determine the angle of attack of the foil. The shaft holders support the foil within the tank. The tanks working section dimensions are 26cm x 26cm x 80cm.

It is important to note that, at the moderate Reynolds numbers considered in this study, the response of the foils is strongly influenced by the unavoidable small imperfections introduced both during fabrication and testing (8). Therefore, the following points need to be considered when comparing the results reported in this study with available foil data in the literature.

1. **Surface roughness of the airfoil.** Surface roughness of an airfoil can certainly influence flow separation and measured C_L and C_D values, and no manufactured airfoil is completely smooth. We measured the surface roughness of our 3D printed foils using quantitative surface profilometry and report a root-mean-square surface feature height of 8 microns (2, 3).
2. **Turbulence intensity.** Turbulence intensity in the tank can also influence patterns of the fluid flow over a foil. The turbulence intensity values measured for our experimental setup are roughly 3-5%.
3. **Drag on the holding rod.** We measured forces on the holding rod in the absence of the foil over a range of angles of attack (since rotating the holding rod could potentially affect measured drag). Mean values of rod drag and lift were subtracted at each point for the data reported in this study.
4. **Tip effects and surface waves.** The upper and lower edges of the tested foils were roughly 3cm from the tank bottom and free water surface. Some interaction of flow over the foil and these surfaces is inevitable, but we were not able to detect any effects of foil surface interactions that affected our experimental data.

5. **Trailing edge thickness.** 3D printed airfoils are subject to the challenges of 3D printing resolution in general, and a perfectly sharp tailing edge is particularly difficult to achieve. Our foils were printed at high resolution on an Objet Connex 500 printer which has state-of-the art resolution capability, but the trailing foil edge is likely not as sharp as might occur in manufactured and polished aluminum airfoils.
6. **Asymmetry in manufactured airfoils.** Even though there are necessarily some minor asymmetries due to additive printing, we made every effort to ensure that our 3D printed airfoils were symmetrical and met NACA0012 profile standards.
7. **Calibration and airfoil alignment.** Airfoil calibration and alignment is one of the most critical and yet challenging issues in conducting static tests on airfoils (8). We expended considerable effort to ensure that our calibration was accurate and that airfoil alignment provided accurate, symmetric results for the smooth control foil. Symmetrical data were obtained when the control foil was moved in both directions (i.e., measurements of lift and drag forces showed similar patterns when the foil was rotated both clockwise and counterclockwise). In order to be able to obtain these accurate, symmetric results, the data had to be calibrated from the raw forces read by the transducer. Because it is very difficult to perfectly align the transducer with the foil, some β angle must be introduced to calibrate, calculate, and ensure symmetric and accurate results in the smooth control foil. Specifically, since the force transducer is locked in with the foil during experiments, it rotates

with the foil as the foil is rotated to test the different angles of attack. If we denote with F_x and F_y the forces along the x- and y-direction read by the transducer (see Figure A.8), it follows that the lift and drag force on the foil can be calculated as

$$\boldsymbol{F_D = F_x * cos(\alpha + \beta) + F_y * sin(\alpha + \beta)} \qquad [A.1]$$

$$\boldsymbol{F_L = F_y * cos(\alpha + \beta) - F_x * sin(\alpha + \beta)} \qquad [A.2]$$

where a is the angle of attack of the foil andβis the calibration angle to ensure symmetrical results for the foils (see Figure A.8).

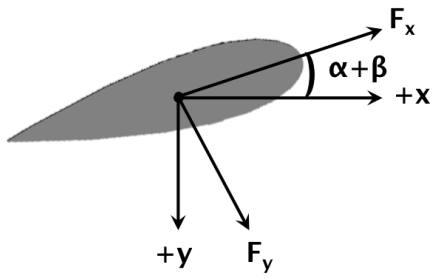

Figure A.8: Schematic for calibration.

In addition, we note that the C_L and C_D values of our smooth control at zero angle of attack align well with the literature (8). Differently, a wide range of values of lift and drag has been reported in literature for angles of attack past zero (8). This is undoubtedly due to a rather considerable variation of the parameters (i.e. 7 points described above) among the different investigators.

A.3 Experimental Results for All Shark Denticle Foils

In this section, we present the experimentally measured C_L, C_D, and C_L/C_D curves for the considered 20 different shark denticle foils, grouped by the different parameters that were varied. In all plots each data point is based on at least six total tests, and standard error bars are included (error bars are sometimes small enough to be contained within the plotted symbol). Although in the main text we discuss in detail the response of the best performing shark denticle foil (Foil #1 in Table A.1), these experimental data show that there are several other foils that also perform pretty well.

A.3.1 Varying Chordwise Position and Size of Denticles

In this section, we consider airfoils with denticles of different sizes and at different chordwise positions (Foils #1-6, #8-9 as shown in Figure A.9). Data for each of these foils can be found in Figures B.10-S14.

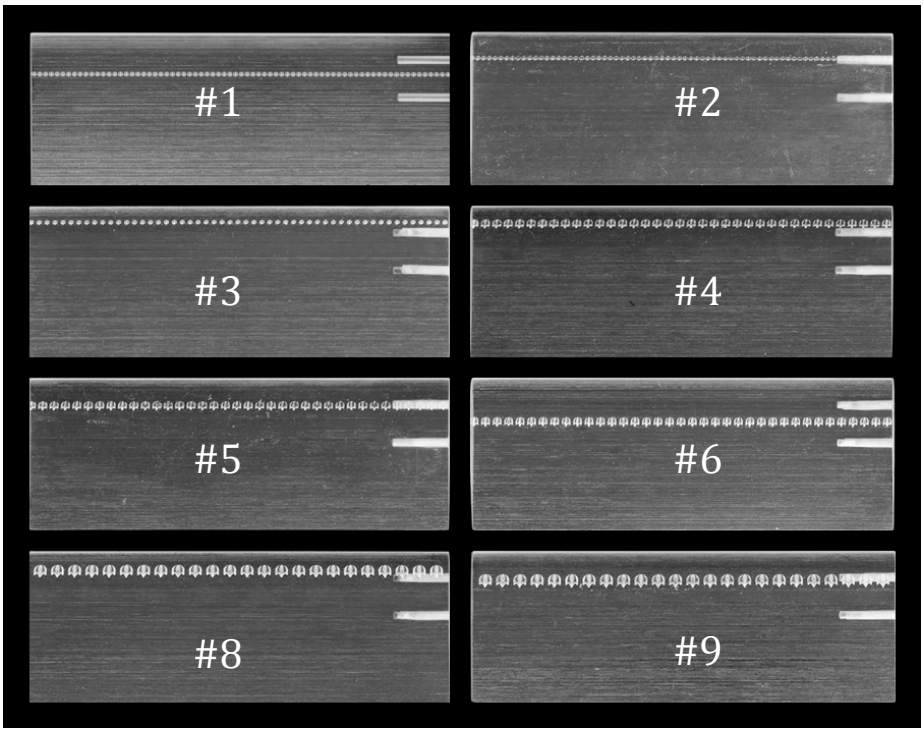

Figure A.9: Image of the 8 shark denticle foils comprising a single row of denticles with different chordwise position and denticle size.

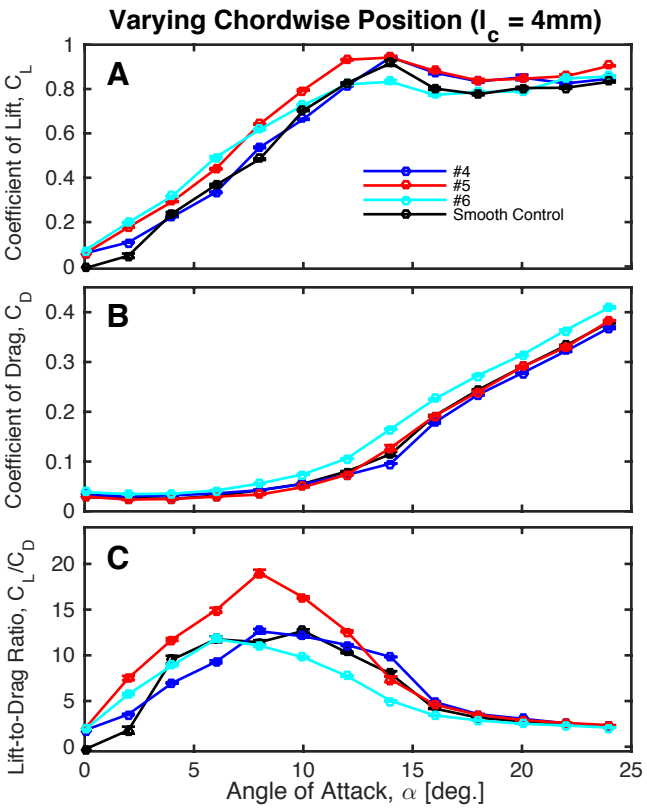

Figure A.10: Experimental results for foils #4, #5 and #6. Evolution of (A) lift coefficient, (B) drag coefficient and (C) lift-to-drag ratio as a function of the angle of attack.

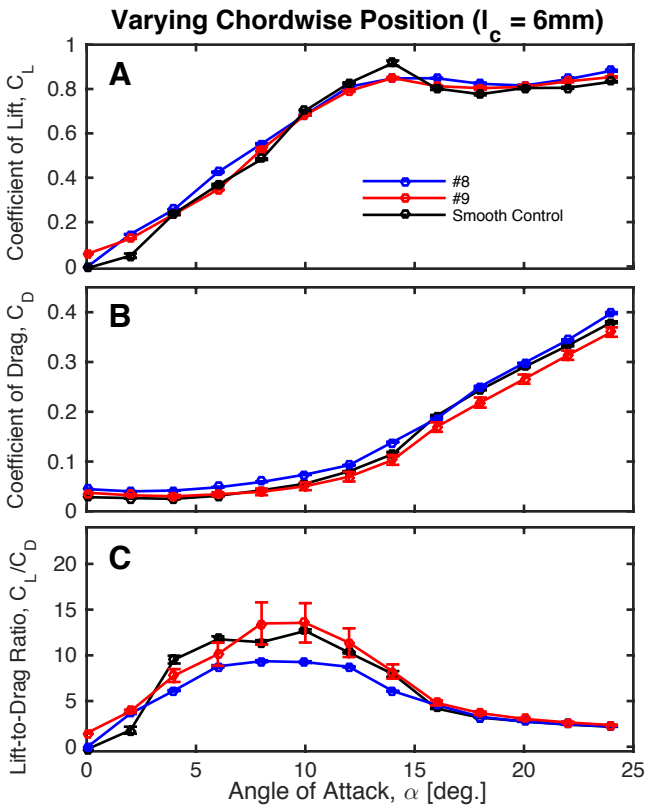

Figure A.11: Experimental results for foils #8 and #9. Evolution of (A) lift coefficient, (B) drag coefficient and (C) lift-to-drag ratio as a function of the angle of attack.

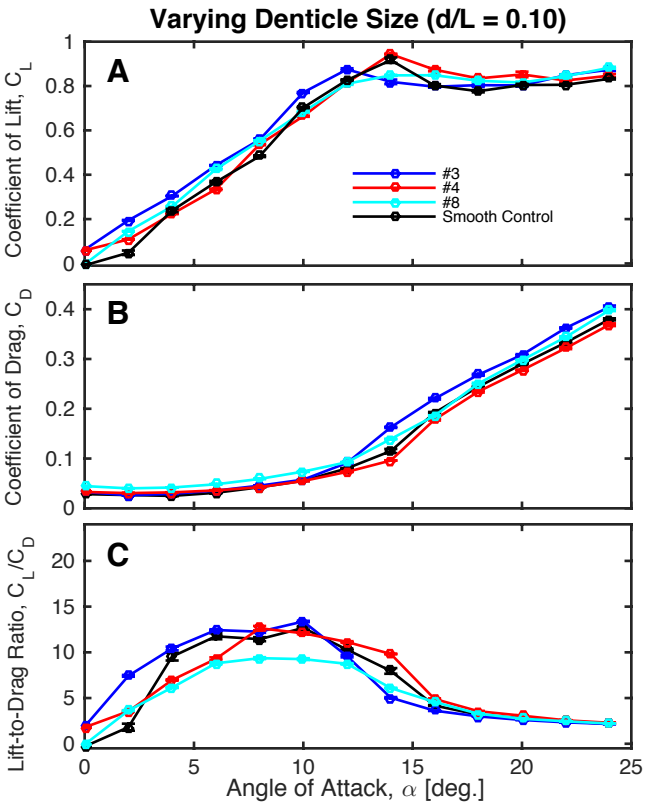

Figure A.12: Experimental results for foils #3, #4 and #8. Evolution of (A) lift coefficient, (B) drag coefficient and (C) lift-to-drag ratio as a function of the angle of attack.

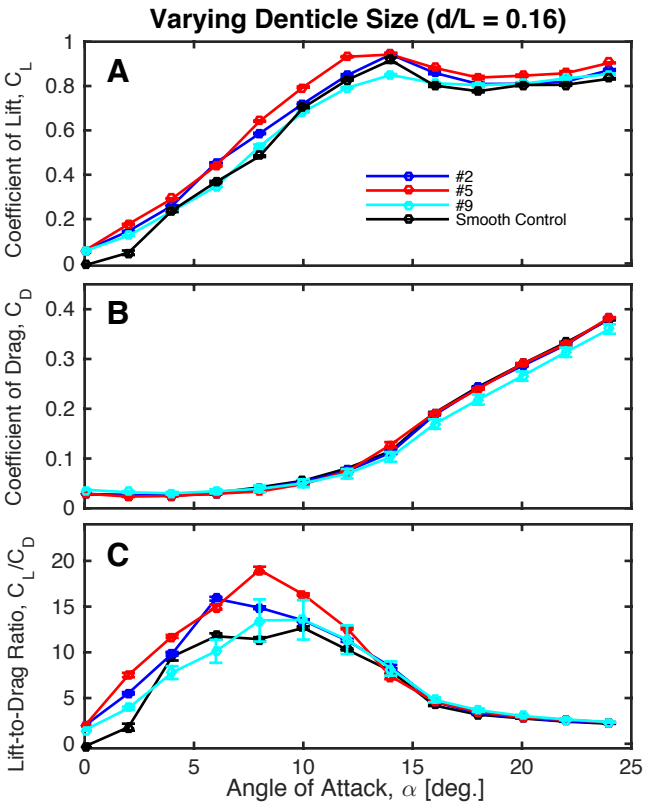

Figure A.13: Experimental results for foils #2, #5 and #9. Evolution of (A) lift coefficient, (B) drag coefficient and (C) lift-to-drag ratio as a function of the angle of attack.

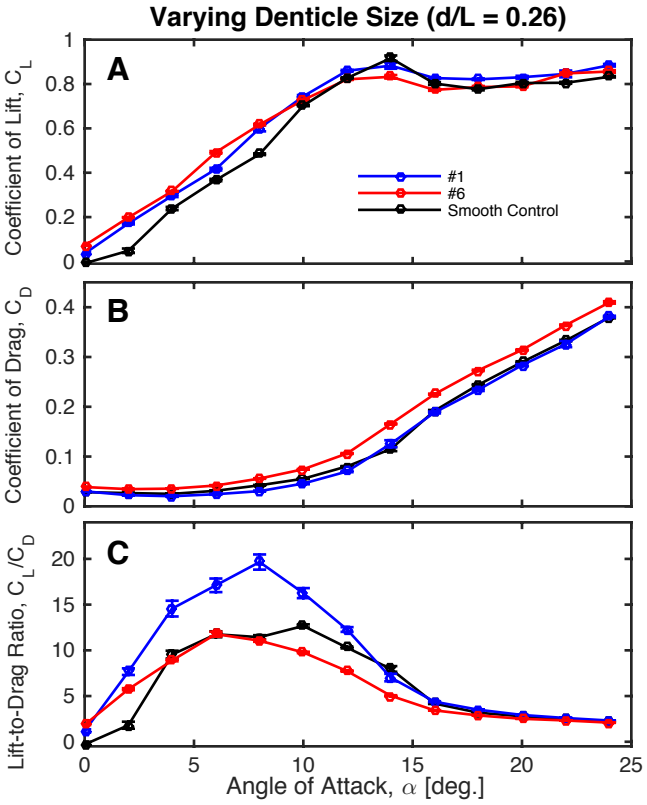

Figure A.14: Experimental results for foils #1 and #6. Evolution of (A) lift coefficient, (B) drag coefficient and (C) lift-to-drag ratio as a function of the angle of attack.

A.3.2 VARYING CHORDWISE POSITION FOR L_C = 2MM

In this section, we consider airfoils with denticles characterized by l_c=2mm, but different chordwise positions (Foils #1-3, #12-13 - see Figure A.15). Data for these foils can be found in Figure A.16.

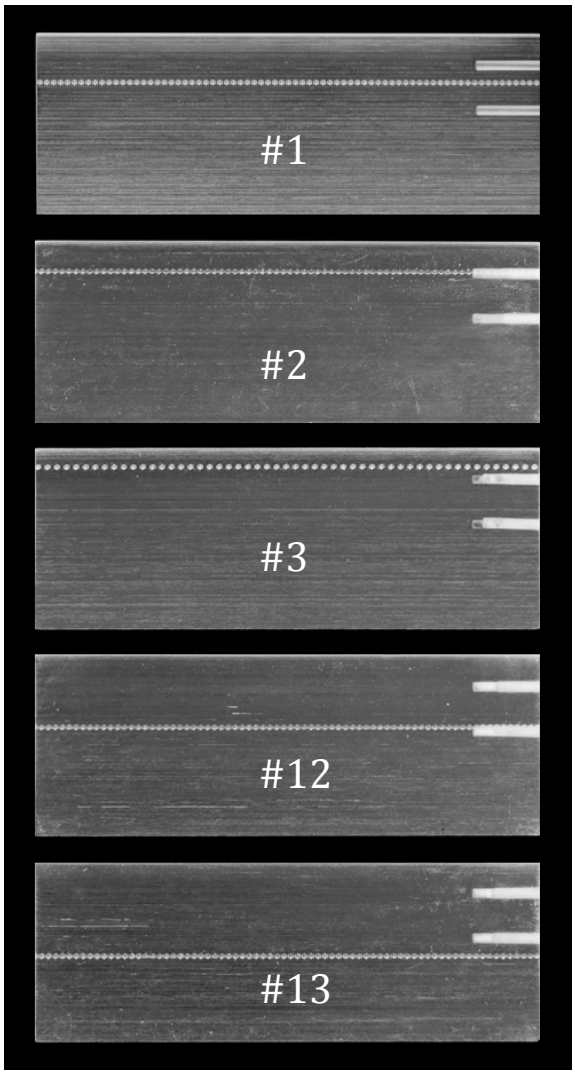

Figure A.15: Image of the 5 shark denticle foils comprising a single row of denticles with l_c = 2mm and different chordwise position.

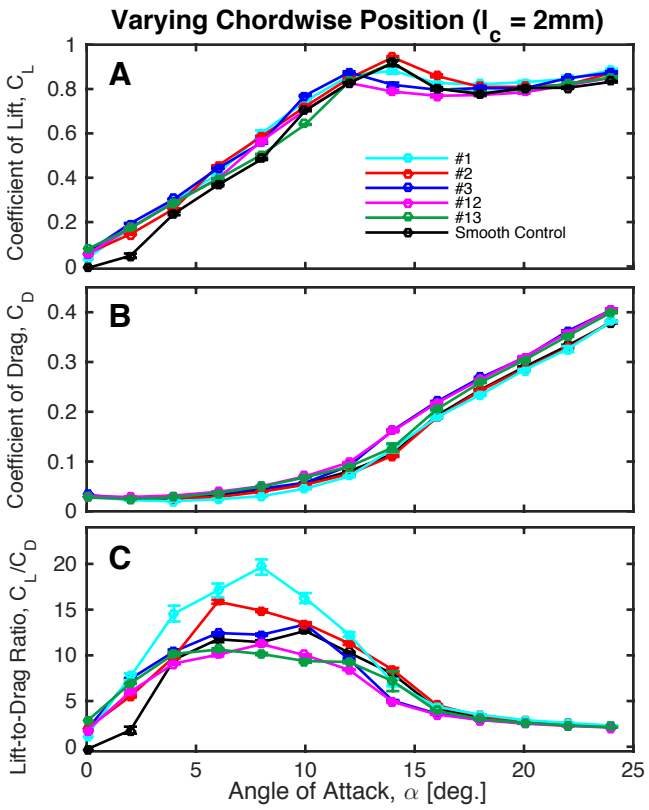

Figure A.16: Experimental results for foils #1, #2, #3, #12, and #13. Evolution of (A) lift coefficient, (B) drag coefficient and (C) lift-to-drag ratio as a function of the angle of attack.

A.3.3 VARYING TILT ANGLE OF DENTICLES

In this section, we consider airfoils with a row of denticles characterized by l_c=4mm, but different tilt angles (Foils #5, #7 – see Figure A.17). Data for these foils can be found in Figure A.18.

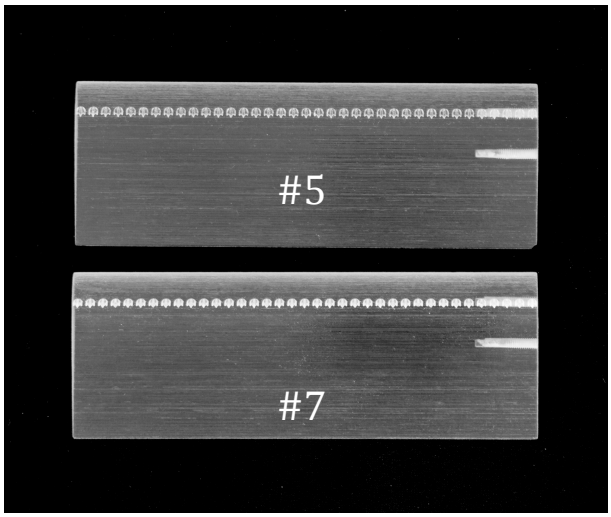

Figure A.17: Images of the 2 shark denticle foils comprising a single row of denticles with l_c = 4mm and different tilt angles.

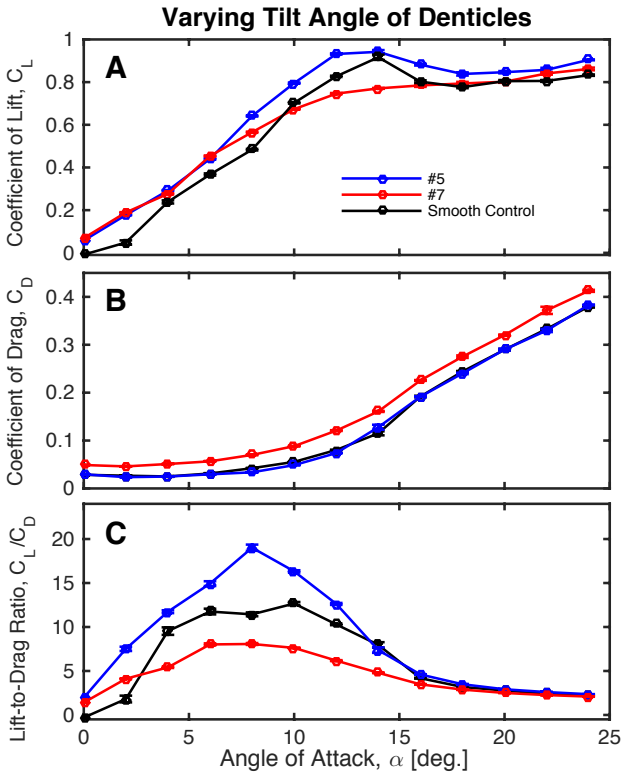

Figure A.18: Experimental results for foils #5 and #7. Evolution of (A) lift coefficient, (B) drag coefficient and (C) lift-to-drag ratio as a function of the angle of attack.

A.3.4 Varying Spanwise Separation of Denticles

In this section, we consider airfoils with a single row of denticles with l_c=2mm placed at d/L=0.26, but with different spanwise separations between denticles (Foils #1, #10-11 - see Figure A.19). Data for these foils can be found in Figure A.20.

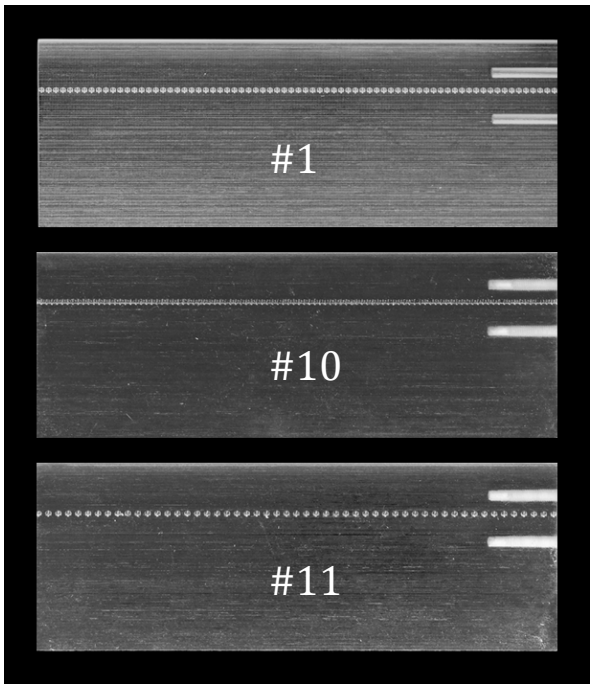

Figure A.19: Images of the 3 foils comprising a single row of denticles with l_c=2mm placed at d/L=0.26, but with different spanwise separations.

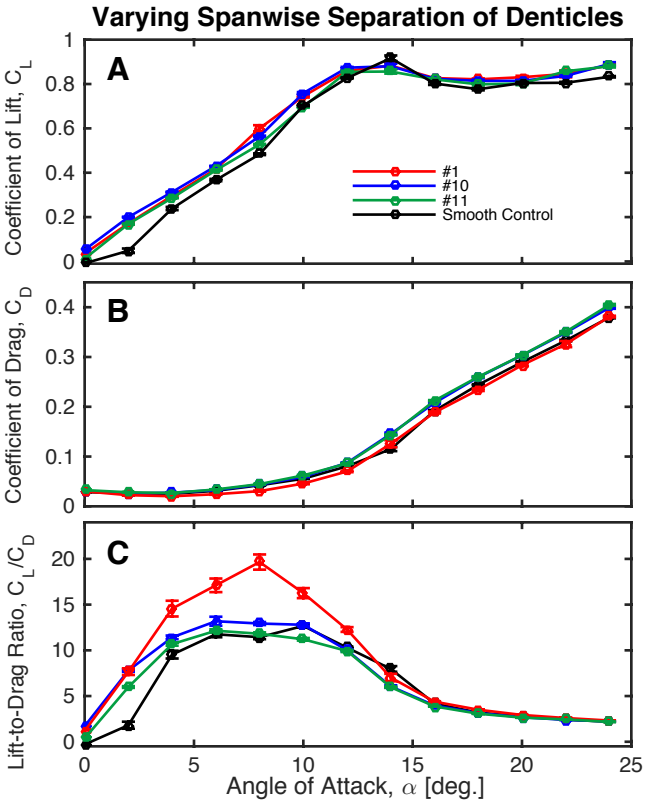

Figure A.20: Experimental results for foils #1, #10 and #11. Evolution of (A) lift coefficient, (B) drag coefficient and (C) lift-to-drag ratio as a function of the angle of attack.

A.3.5 Varying Chordwise Separation with Two Rows of Denticles

In this section, we consider airfoils comprising two rows of denticles arranged according to the linear pattern with d/L=0.26 with l_c=2mm, but different chordwise separation between rows (Foils #15-17 - see Figure A.2). Data for these foils can be found in Figure A.22.

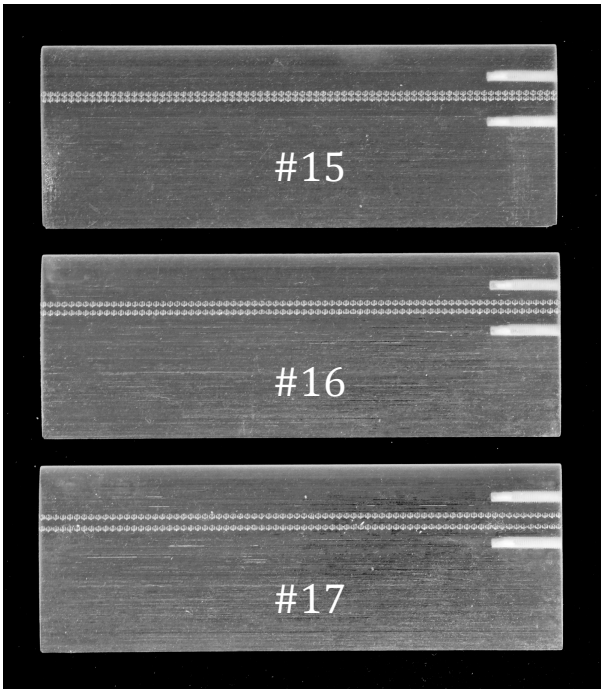

Figure A.21: Images of the 3 foils comprising two rows of denticles with different chordwise separation between rows.

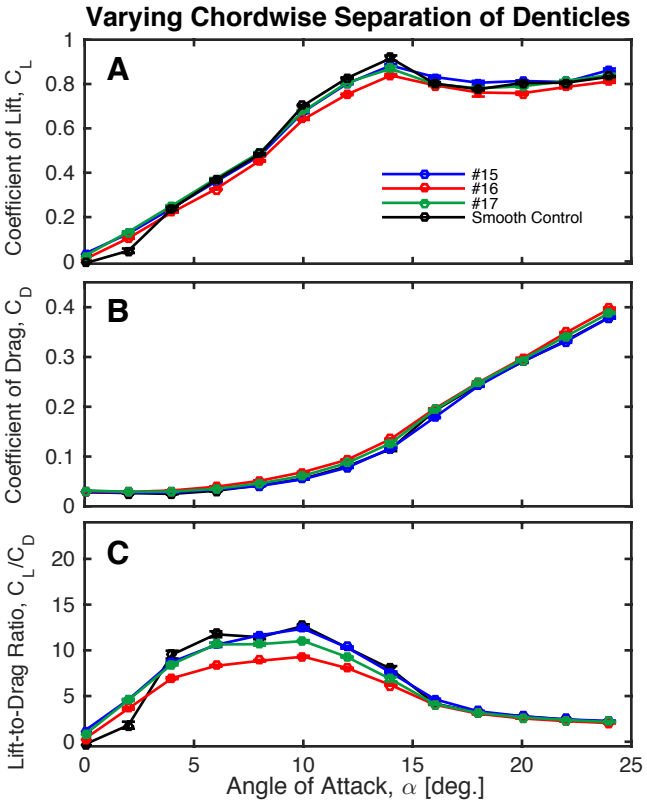

Figure A.22: Experimental results for foils #15, #16 and #17. Evolution of (A) lift coefficient, (B) drag coefficient and (C) lift-to-drag ratio as a function of the angle of attack.

A.3.6 Varying Pattern with Two Rows of Denticles

In this section, we consider airfoils comprising two rows of denticles with d/L=0.26 and l_c=2mm, but different arrangements (Foils #14-15 - see Figure A.23). Data for these foils can be found in Figure A.24.

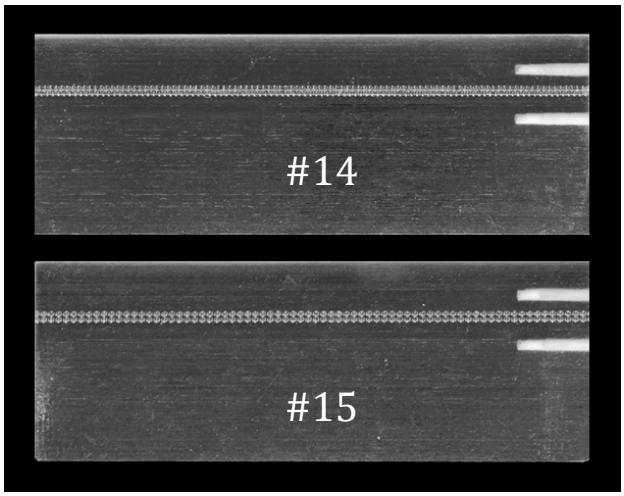

Figure A.23: Images of the 2 foils comprising different patterns: staggered (Foil #14) vs. linear (Foil #15).

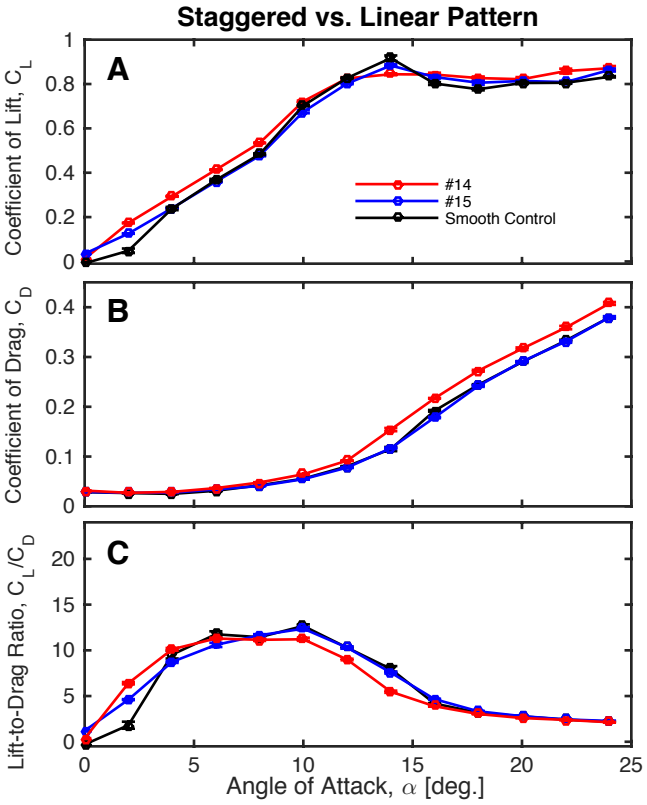

Figure A.24: Experimental results for foils #14 and #15. Evolution of (A) lift coefficient, (B) drag coefficient and (C) lift-to-drag ratio as a function of the angle of attack.

A.3.7 Foils with 4 or More Rows of Denticles

In this section, we consider airfoils comprising multiple rows (ranging from 4 to 26 rows) of denticles with a variety of different parameters (Foils #18-20 - see Figure A.25). Data for these foils can be found in Figure A.26.

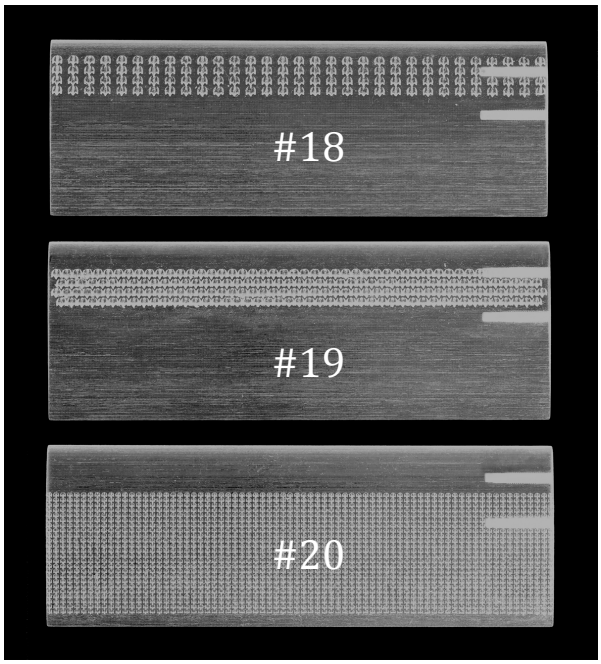

Figure A.25: Images of the 3 foils with multiple rows of denticles.

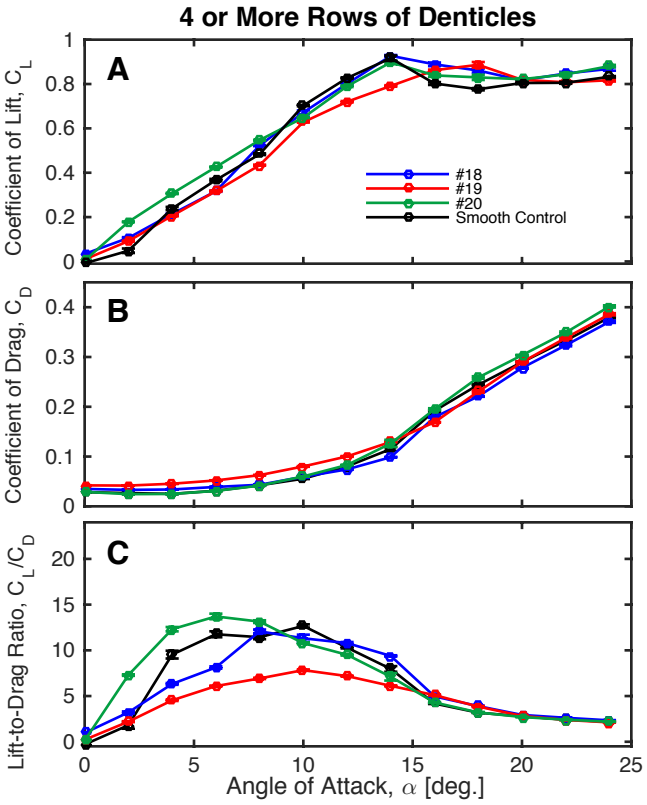

Figure A.26: Experimental results for foils #18, #19 and #20. Evolution of (A) lift coefficient, (B) drag coefficient and (C) lift-to-drag ratio as a function of the angle of attack.

A.4 Comparison of the Results for the Foils Discussed in the Main Text

In this section, we compare the results of the three foils analyzed in the main text (i.e. best shark denticle, 2D bump profile, and continuous shark-inspired profile foils). Specifically, in Figure A.27 we report the lift-to-drag ratio (L/D) improvement of each of the foils in comparison with the smooth control as a function of angle of attack a. Note that, since the control foil is symmetric and therefore has an L/D of zero at a=0°, the plot begins at a=2°.

The results of Figure A.27 show two key features. First, all three foils provide great improvements in L/D at low angles of attack (i.e. at a=2°), with the shark denticle and continuous shark-inspired profile foils performing significantly better. This is because, although the 2D bump profile enhances lift over twice that of the shark denticle at a=0°, it loses a lot of those lift benefits at higher angles of attack and does not produce a lot of drag reduction since it is not a vortex generator. Second, the continuous shark-inspired profile is outperforming the other two foils at the majority of angles of attack. This is because this profile, which combines aspects of the 2D bump profile and the shark denticle, is able to produce the same lift benefits as the 2D bump at a=0° without losing these lift benefits as much at higher angles of attack (like the 2D bump does), in addition to greatly reducing drag at these higher angles.

In Figure A.27 we also indicate with a filled in marker the angle at which the max L/D occurs for each foil. Note that at this angle the foil can move with its most advantageous lift-to-drag ratio. So for example, if a given application

does not have a mandatory angle of attack at which it must move, then this angle of attack would be the most advantageous to use for generating a lot of lift without producing too much drag. We see from Figure A.27 that, like in the case of most angles of attack, the continuous shark-inspired profile produces the greatest improvements at this max L/D (as seen by comparing the filled in markers for each foil).

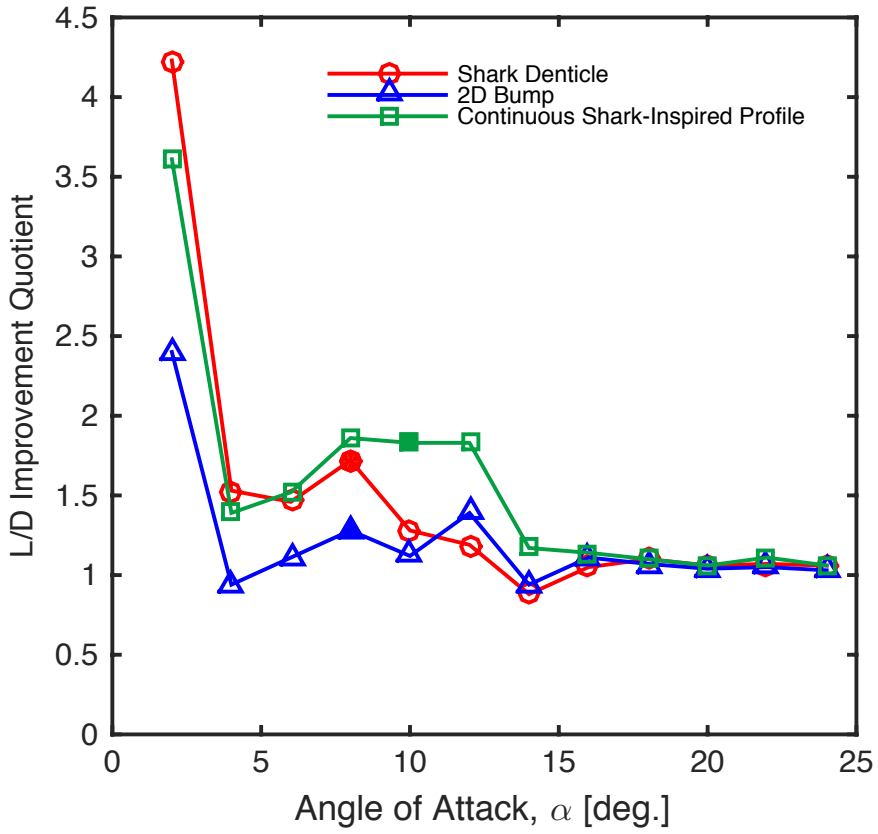

Figure A.27: Comparison between the airfoils analyzed in the main text. The red, blue, and green markers correspond to $C_{L/D}^{shark}/C_{L/D}^{control}$, $C_{L/D}^{2Dbump}/C_{L/D}^{control}$, and $C_{L/D}^{cont.}/C_{L/D}^{control}$, respectively. The markers that are filled in represent the angle at which the max L/D for that foil occurs.

A.5 Comparison of Shark Skin-Inspired Designs and Traditional Low-Profile Vortex Generators

In this section, we compare the results obtained for the shark skin-inspired designs presented in this study to those of traditional low-profile vortex generator designs. Specifically, we consider the following set of data available in the literature for low-profile vortex generators:

- counter-rotating and co-rotating trapezoid-wing vortex generators arranged on a cambered airfoil. For this system, lift-to-drag ratio measurements as a function of angle of attack at $Re_c \approx 9x10^6$ are reported in Figure 17 of (9) and Figure 15 of (10).
- wedge-type vortex generators tested on a "rooftop" section of an airplane wing in transonic flow with M = 0.71. Lift-to-drag ratio measurements as a function of C_L are reported in Figure 12 of (11).
- co-rotating vane-type vortex generators tested on a "10%-scale configuration of a near-term technology, low-observable, multi-role fighter derivative concept." Lift-to-drag ratio measurements as a function of C_L at a Re≈ 1,300,000 per foot are reported in Figure 8 of (12).

It is important to note that the vortex generators described above were tested in a much different environment than the study presented here. Although it may be difficult to make a direct comparison, it allows for some reference to the present study.

In Figure A.28 we compare the lift-to-drag ratio (L/D) improvement of our bio-inspired designs (best shark denticle foil and continuous shark-inspired foil)

to counter-rotating and co-rotating trapezoid-wing vortex generators described above (9,10), which are the best-reported traditional low-profile VGs as reported in Lin's literature review (13). It appears that on a whole the bio-inspired designs presented here are relatively comparable to the results of these more traditional vortex generators at higher angles of attack near stall and the max L/D. However, the bio-inspired designs presented here show even better improvements at low angles than the traditional low-profile vortex generators. This low angle of attack improvement has potential significance for many systems such as drones, airplanes, and aquatic autonomous vehicles, which can often experience similar low angles of attack in use. Moreover, we see that the continuous shark-inspired profile is producing greater L/D improvements at its max L/D (filled in markers) than any other airfoil is. Once again, this is very beneficial for applications at which the angle of attack is not set, since at this angle the system can move with its most advantageous L/D.

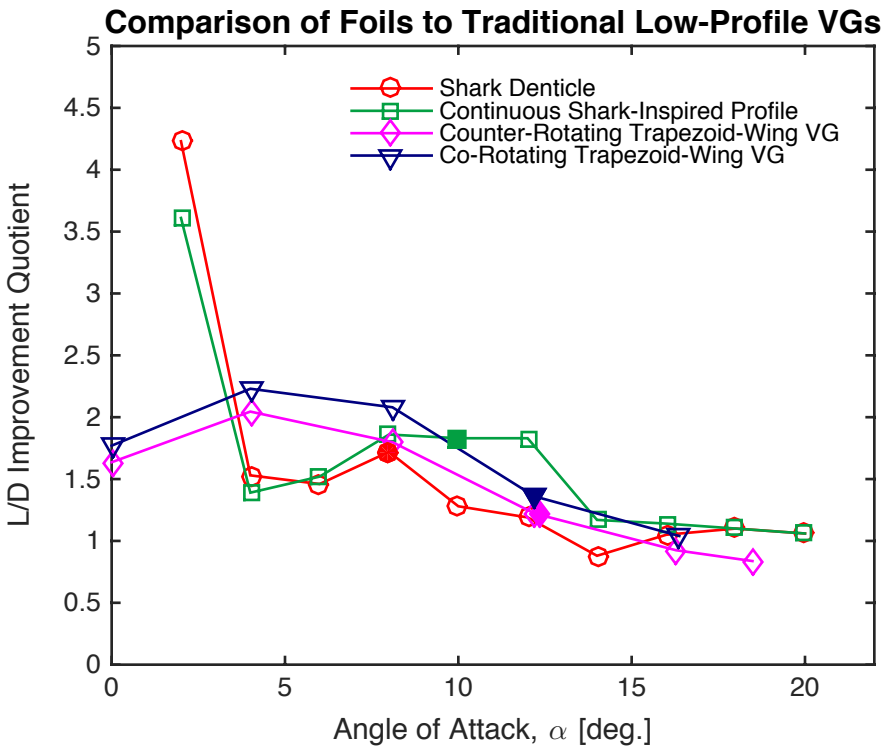

Figure A.28: Comparison between the shark skin-inspired designs presented in this study and some of the traditional best low-profile vortex generators reported in the literature. Red, green, magenta, and dark blue markers correspond to $C_{L/D}^{shark}/C_{L/D}^{control}$, $C_{L/D}^{cont.}/C_{L/D}^{control}$, $C_{L/D}^{CTR}/C_{L/D}^{control}$ (CTR denoting counter-rotating trapezoid wing vortex generators), and $C_{L/D}^{COR}/C_{L/D}^{control}$ (COR denoting co-rotating trapezoid wing vortex generators), respectively. The markers that are filled in represent the angle at which the max L/D for that foil occurs.

Finally, in Figure A.29 we compare the lift-to-drag ratio improvements of our best shark skin-inspired designs (best shark denticle foil and continuous shark-inspired profile) to that measured for the wedge-type vortex generators reported in (11) and the co-rotating vane-type vortex generators described in (12). Note that in the plot the L/D improvement is reported as a function of the coefficient of lift, as in (11,12). Analyzing Figure A.29, we find that the shark denticle foil and continuous shark-inspired profile foil show significant improvements compared to the roughly 5% increases that the other studies see. This holds true for all values of C_L tested in these other studies. In addition, just as we saw for the previous two plots, the continuous shark-inspired profile is producing the highest L/D improvements at its max L/D.

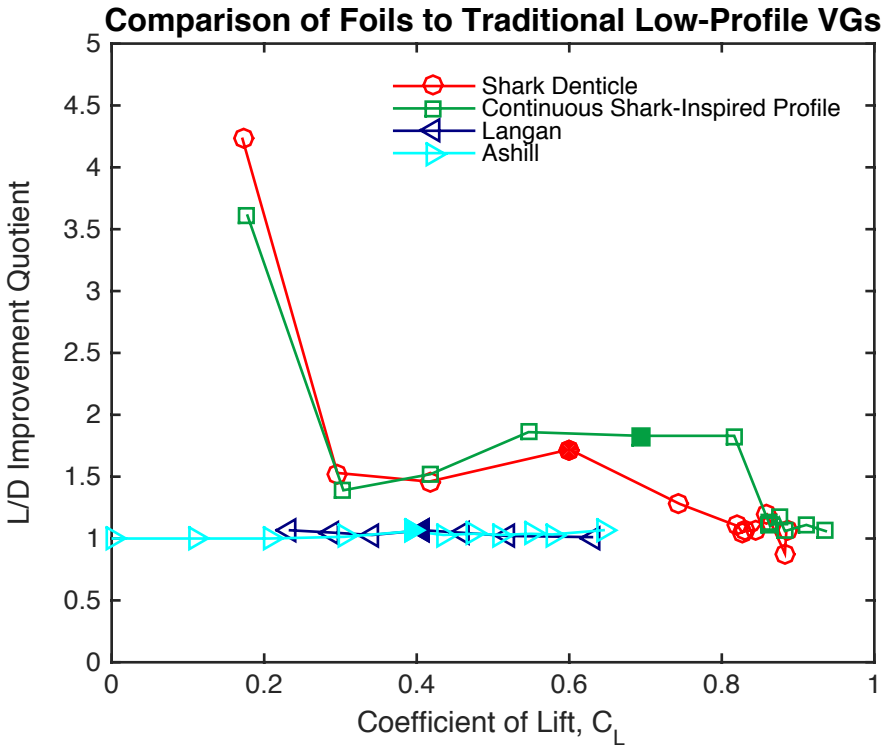

Figure A.29: Comparison between the shark skin-inspired designs presented in this study and some of the traditional low-profile vortex generators. Red, green, blue, and cyan markers correspond to $C_{L/D}^{shark}/C_{L/D}^{control}$, $C_{L/D}^{cont.}/C_{L/D}^{control}$, $C_{L/D}^{COR}/C_{L/D}^{control}$ (COR denoting the co-rotating vane-type vortex generators), and $C_{L/D}^{WED}/C_{L/D}^{control}$ (WED denoting the wedge-type vortex generators), respectively. The markers that are filled in represent the angle at which the max L/D for that foil occurs.

A.6 CFD ANALYSIS

We used the commercial computational fluid dynamic (CFD) package ANSYS® CFX, release 16.0 to carry out the calculations of flow over the shark denticle design on a flat plate (as discussed in the main text) and the 2D bump foil. This code employs a hybrid finite-volume/finite-element approach to discretize the Navier Stokes equations (14). The equations are solved by an unsteady fully-implicit, fully-coupled multigrid solver in the inertial reference frame of the lab. The Shear Stress Transport (SST) turbulence model (15), which combines the *k*-ω model near the wall and the *k*-ε model away from the wall, is used throughout the study. The choice of turbulence model allows for accurate prediction of onset and amount of flow separation under adverse pressure gradient conditions, and can handle the transition of the flow from laminar to turbulent. The airfoil is placed inside a rectangular fluid domain. An O-type structured mesh is refined around the airfoil and coarsened away from the airfoil. The physical normal distance of the first mesh node above the surface of the airfoil is kept fixed for all the cases. The maximum non-dimensional distance corresponding to the first node above the airfoil surface among all the cases is $y^+ \approx 0.3$. The dimensionless wall distance y^+ is defined as $y^+ = u^* y/\nu$, where u^*, y, and u correspond to the nearest-wall friction velocity, normal distance away from the wall, and kinematic viscosity, respectively.

A.6.1 Analysis of 2D Bump Foil

Because of the geometric simplicity of the 2D bump foil compared to the shark denticle foil, 2D simulations of this system were conducted. As done with the experiments, CFD data were computed for angles of attack that extended past stall. For the CFD results shown in Figure A.30, we observe similar results to those seen in the experiments. Positive lift is being generated at zero angle of attack by the 2D bump profile (C_L = 0.22), and we calculate a 946% and 11% increase in lift generated at a=2° and a=4° respectively compared to the control (see Figure A.30*A*). In addition, we notice that lift enhancements by the 2D bump foil are lost at higher angles of attack just as was the case in experiments (see Figure A.30*A*). At low angles of attack, a separation bubble is formed by the 2D bump profile, which leads to separation, and which in turn likely ultimately degrades the performance of the 2D bump foil at higher angles. In regards to drag, it is important to note that at zero angle of attack a very similar drag coefficient is seen in CFD (see Figure A.30*B*) compared to the experiments (both just a bit below 0.03). Because of these lift and drag results, we see an overall qualitatively similar L/D curve as was seen in experiments (see Figure A.30*C*).

Figure A.30*D* shows the CFD streamlines for the 2D bump and control for two low angles of attack at which lift is being enhanced by the 2D bump profile (a=0° and a=4°). Analyzing these images, we see that at 0° a short separation bubble is being generated by the 2D bump foil yet not in the smooth control (as was the case with the shark denticle foil). At 4° we do see a separation bubble developing at the trailing edge of the smooth control. However, this separation

bubble is fairly large and does not quite reattach at the trailing edge of the foil, negatively affecting lift. In the 2D bump foil, we see the separation bubble in both CFD and PIV at a=4° much further upstream, which is a more beneficial location in regards to the pressure gradient along the chord as previously discussed.

We should note, however, that there are some differences in the experimental and CFD results, such as the angle at which each of the foils stall and the maximum lift and drag being generated. The 2D CFD calculations here are inherently somewhat different than the 3D experiments which include three-dimensional effects; CFD is a much more idealized version of the experiments. In the experiments, for example, tip vortices may reduce the size of the separation bubble. In spite of some inherent differences between the two, we have shown that there are qualitative similarities between the CFD and experiments, including the following: (*i*) a positive lift enhancement at low angles of attack, (*ii*) non-zero lift at zero angle of attack, and (*iii*) the loss of lift increase relative to the control near and at stall. Furthermore, similar flow mechanisms are seen in both the CFD and PIV streamlines, where short separation bubbles form downstream from the trailing edge of the 2D bump profile.

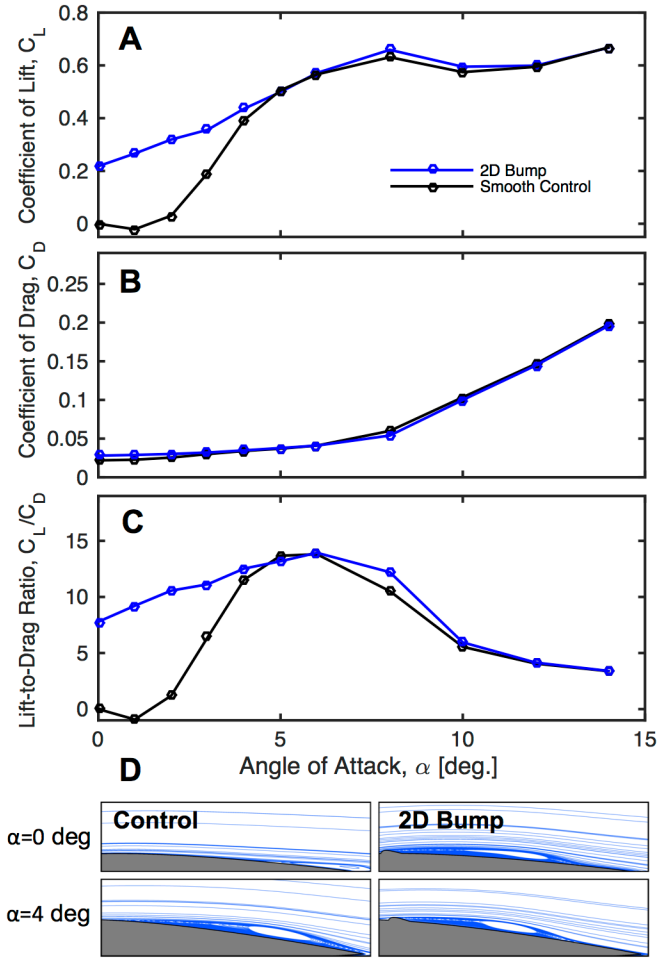

Figure A.30: Computational fluid dynamic (CFD) results. Evolution of (A) lift coefficient, (B) drag coefficient and (C) lift-to-drag ratio as a function of the angle of attack. (D) Numerical snapshots showing the streamlines for the control and 2D bump at a=0^o and 4^o.

A.7 REFERENCES

[1] Wen, L., Weaver, J. C., Lauder, G. V. (2014). Biomimetic shark skin: design, fabrication and hydrodynamic function. *J Exp Biol.,* 217, 1656–1666.

[2] Wainwright, D. K. and Lauder, G. V. (2016). Three-dimensional analysis of scale morphology in bluegill sunfish, *Lepomis macrochirus*. *Zoology,* 119, 182-195.

[3] Wainwright, D. K., Lauder, G. V., and Weaver, J. C. (2017). Imaging biological surface topography in situ and in vivo. *Methods in Ecology and Evolution*, 8, 1626–38.

[4] Wen, L., Weaver, J. C., Lauder, G V. (2015). Hydrodynamic function of biomemtic shark skin: effect of denticle pattern and spacing. *Bioinspir. Biomim.,* 10, 06601.

[5] Lauder, G. V., Wainwright, D. K., Domel, A. G., Weaver, J. C., Wen, L., and Bertoldi, K. (2016). Structure, biomimetics, and fluid dynamics of fish skin surfaces. *Physical Review Fluids,* 1, 060502.

[6] Saadat, M., Fish, F. E., Domel, A. G., Di Santo, V., Lauder, G. V., and Haj-Hariri, H. (2017). On the rules for aquatic locomotion. *Physical Review Fluids*, 2, 083102.

[7] Shelton, R. M., Thornycroft, P. J. M., and Lauder, G. V. (2014). Undulatory locomotion by flexible foils as biomimetic models for understanding fish propulsion. *J. Exp. Biol.,* 217, 2110-2120.

[8] Tank, J., Smith, L., Spedding, G. R. (2017). On the possibility (or lack

thereof) of agreement between experiment and computation of flows over wings at moderate Reynolds number. *Interface Focus,* 7(1):20160076.

[9] Lin, J. C., Robinson, S. K., McGhee, R. J., Valarezo, W. O. (1994). Separation control on high-lift airfoils via micro-vortex generators. *J Aircr,* 31, 1317–1323.

[10] Kerho, M., Hutcherson, S., Blackwelder, R. F., Liebeck, R. H. (1993). Vortex generators used to control laminar separation bubbles. *J Aircr,* 30, 315–319.

[11] Ashill, P., Fulker, J., Hackett, K. (2001). Research at DERA on sub boundary layer vortex generators (SBVGs). *39th Aerospace Sciences Meeting and Exhibit,* doi:10.2514/6.2001-887.

[12] Langan, K., Samuels, J. (1995). Experimental investigation of maneuver performance enhancements on an advanced fighter/attack aircraft. *33rd Aerospace Sciences Meeting and Exhibit,* doi:10.2514/6.1995-442.

[13] Lin, J. C. (2002). Review of research on low-profile vortex generators to control boundary-layer separation. *Prog Aerosp Sci,* 38(4-5):389–420.

[14] ANSYS® Academic Research, Release 14.0, Help System, ANSYS CFX-Solver Theory Guide, ANSYS, Inc.

[15] Menter, F. R. (1993). Zonal Two Equation k-ω Turbulence Models for Aerodynamic Flows. *AIAA Paper,* 93, 2906.

B

Supporting Information for Chapter 5

B.1 Measuring the Taper Angles of Octopus Arms

To measure the taper angles of biological octopus arms, we obtained images of biological octopus specimens from online sources. In total, we selected 33 images of 10 different octopus species with clear views of their arms (all the 33 images can be found in the SI "33 octopus images.zip" file). Using Matlab (Mathworks, USA) we outlined the border of each arm and calculated the tip angle variability between species, as shown in Figure B.1. Table B.1 shows all the 33 measurements across the ten octopus species. For a single octopus, *Thaumoctopus mimicus* had the slenderest arms with a taper angle of 2.95°, while *Eledone cirrhosa* had comparatively wider arms with a taper angle of 13.32°.

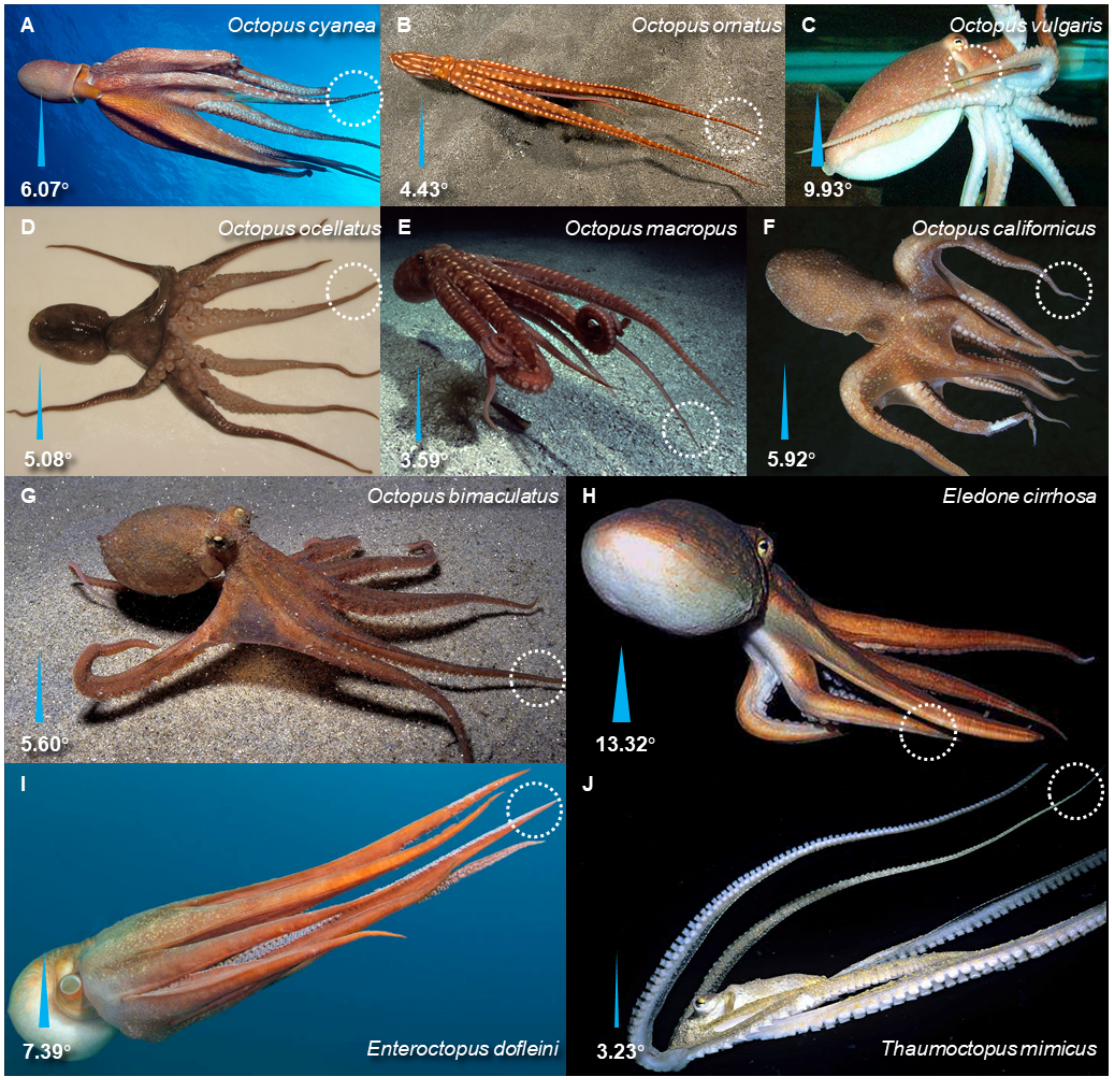

Figure B.1: Images of ten species of octopus for taper angles measurements. (A)-(J) *Octopus cyanea* (6.07°), *Octopus ornatus* (4.43°), *Octopus vulgaris* (9.93°), *Octopus ocellatus* (5.08°), *Octopus macropus* (3.59°), *Octopus californicus* (5.92°), *Octopus bimaculatus* (5.60°), *Eledone cirrhosa* (13.32°), *Enteroctopus dofleini* (7.39°), and *Thaumoctopus mimicus* (3.23°).

Table B.1: Taper angles of biological octopus arms.

Octopus species	Taper angles α (°)						
Octopus cyanea	5.55	6.07	6.12	6.66			
Octopus ornatus	4.01	4.43					
Octopus vulgaris	5.51	5.61	6.83	6.86	7.21	9.37	9.93
Octopus ocellatus	4.18	5.08					
Octopus macropus	3.01	3.59	4.14				
Octopus californicus	5.92	7.03					
Octopus bimaculatus	4.89	5.60	5.91				
Eledone cirrhosa	6.25	6.95	10.76	13.32			
Enteroctopus dofleini	7.39	7.78	9.63				
Thaumoctopus mimicus	2.95	3.23	6.31				

B.2 Geometry of the Tapered Soft Actuator and Its Suckers

As shown in Figure B.2*A*, the actuators considered in this study are cone-shaped with a taper angle α, length L = 200 *mm* and tip radius R_{tip} = 4.2 mm. As such, the outer radius $R_o(z)$ and cross sectional area $S_o(z)$ of the actuator at a distance z ($0 < z < L$) from the tip is given by

$$R_o(z) = R_{tip} + z\tan\frac{\alpha}{2} \quad [B.1]$$

and

$$S_o(z) = \pi R_o(z)^2. \quad [B.2]$$

A single inner pneumatic chamber running the length of the actuator was used for a simple, effective way to induce bending in the actuator (1,2). This chamber has a β = 120° swept ring-shaped cross-section, an outer radius $R_i(z)$ *and*

an inner radius $R_m(z)$ (see cross-section in Figure B.2*A*). The chamber was placed at a fixed normalized distance from the outer radius of the actuator; specifically, the chamber placement was defined so that

$$\frac{R_o(z)}{R_o(z)-R_i(z)} = K\,, \qquad \text{[B.3]}$$

where K denotes a constant that determines the placement of the chamber cross-section with respect to the edge of the actuator's cross-section (see Figure B.2*B*). Note that by varying K, we can study how the normalized distance from the outside of the chamber to the outside of the actuator affects the bending of the actuator. It follows from Eq. B.3 that the chamber's outer radius, $R_i(z)$, at a distance z from the tip is given by

$$R_i(z) = \frac{K-1}{K} R_o(z)\,. \qquad \text{[B.4]}$$

Moreover, the ratio of the cross-sectional area of the inner chamber, $S_i(z)$, to the cross-sectional area of the actuator, $S_o(z)$, was kept constant along the length

$$\frac{S_i(z)}{S_o(z)} = 0.05\,. \qquad \text{[B.5]}$$

It follows that to satisfy Eq. B.5, the inner radius of the chamber $R_m(z)$ is given by

$$R_m(z) = \sqrt{R_o(z)^2 - \frac{0.05\, S_0(z)}{\pi}}\,. \qquad \text{[B.6]}$$

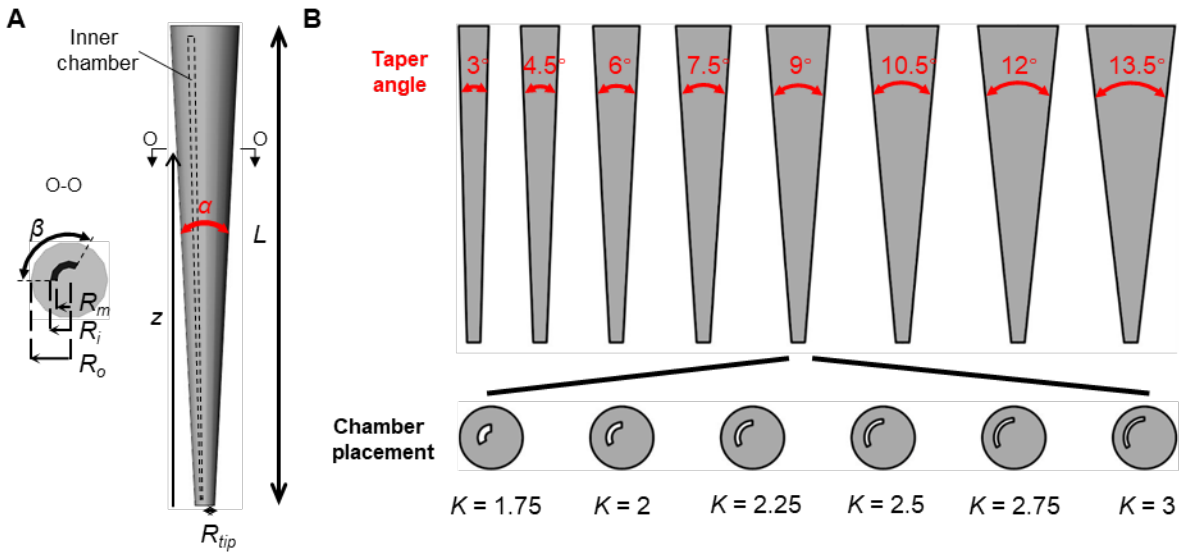

Figure B.2: Geometry of the tapered soft actuator. (A) Cross-sectional view and side view of the actuator with a ring-shaped inner chamber for pressurization. The actuator length (L), taper angle (α), outer radius (R_o), chamber outter radius (R_i), and chamber inner radius (R_m) are indicated in the image. (B) 8 actuators of different taper angles (α from 3° to 13.5° with an interval of 1.5°, K = 2) and 6 actuator of different chamber placements (K from 1.75 to 3 with an interval of 0.25, α = 9°) were considered in this study.

To improve the grasping ability of these tapered actuators, we next integrated suckers into their design. The shape of our suckers mimic that of the *infundibulum* and *acetabulum* of *Octopus vulgaris* (see Figures B.3*A-D*). Specifically, for the *j-th* sucker with outer diameter d_j, we choose the *infundibulum* height, e_j, and inner diameter, f_j, (Figures B.3*A-E*) as

$$e_j = \frac{d_j}{4} \qquad [B.7]$$

and

$$f_j = \frac{d_j}{2}. \qquad [B.8]$$

Moreover, as Figure B.3*G* shows, the sucker's diameter d_j is chosen to be

$$d_j = R_o(z_j). \quad [B.9]$$

where z_j denotes the location of the *j*-th sucker along the actuator.

Based on the octopus images we analyzed, we arranged 17 suckers with decreasing diameters in a staggered pattern along the tapered actuator (see Figures B.3*E-G*). The position of the center point for the *j-th* sucker (see black dot in Figure B.3*F*) is defined by coordinates z_j and x_j, which are given by

$$z_j = \begin{cases} L - \frac{5R_o(L)\cos\frac{\alpha}{2}}{4} & j = 1 \\ L + \frac{R_o(L)\cos\frac{\alpha}{2}}{100}j^2 - \frac{17R_o(L)\cos\frac{\alpha}{2}}{25}j - \frac{29R_o(L)\cos\frac{\alpha}{2}}{50} & j = 2, 3, \ldots, 17 \end{cases} \quad [B.10]$$

and

$$x_j = R_{tip} + z_j \tan\frac{\alpha}{2} + \frac{9R_o(L)}{25\cos\frac{\alpha}{2}} - \frac{3R_o(L)}{200\cos\frac{\alpha}{2}}j, \quad [B.11]$$

where $R_o(L)$ is the radius at the base of the actuator ($z = L$), which is defined by Eq. B.3.

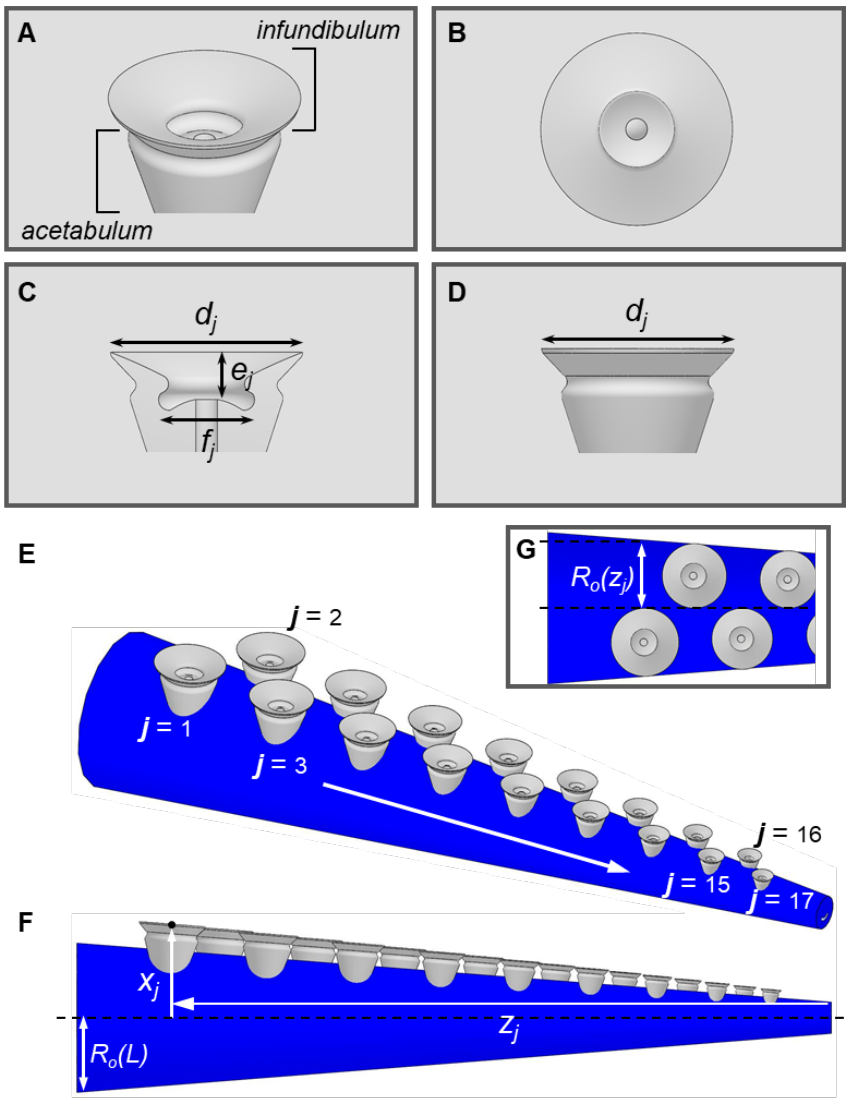

Figure B.3: Design details of the soft suckers. (A) Isometric view, (B) top view, (C) cross sectional view and (D) side view of the sucker model with the corresponding design parameters (41). (E)-(G) Views of the tapered actuator with suckers arranged on its surface with a staggered distribution.

B.3 Fabrication of Tapered Soft Actuators without Suckers and Characterization of the Material Response

In order to validate the finite element simulations, we began by fabricating the tapered soft actuators without suckers for testing. A molding and casting process was used to fabricate the tapered soft actuators (Figure B.4). All the molds for the casting process were designed in SolidWorks and printed using a 3D printer (Makerbot Replicator X5, MakerBot Industries LLC, HK, China). The molds were assembled and held together firmly with tightly looped rubber rings while a 3D-printed rod with a β = 120° swept ring-shaped cross-section was positioned inside the tapered mold for the creation of the internal pneumatic chamber of the actuator. A 3D-printed cap was placed on top of the mold to hold the rod in place. A silicone elastomer with Young's modulus of E = 0.66 MPa (Mold Star 30, Smooth-On Inc., PA) was then poured into the mold (Figure B.4*A*), and degassed in a vacuum chamber for ten minutes. The elastomer was then left for 6 hours at room temperature to cure. After curing, the tapered mold and rod was removed, which created a core used for the actuator's inner pneumatic chamber. Finally, the actuator was sealed with adhesives (Sil-Poxy, Smooth-On Inc., PA) (Figure B.4*B*).

For this study, we fabricated eight actuators, all characterized by K=2 and with α = 3°, 4.5°, 6°, 7.5°, 9°, 10.5°, 12°, and 13.5° (Figure B.5), which were used to experimentally measure bending curvature and bending force for the purpose of validating the simulations.

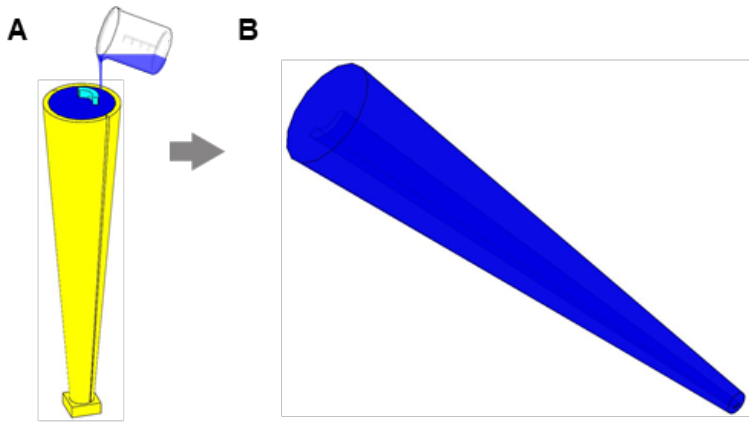

Figure B.4: Fabrication of the tapered soft actuator. (A) 3D-printed molds are used to cast the actuators. (B) The cured tapered soft actuator.

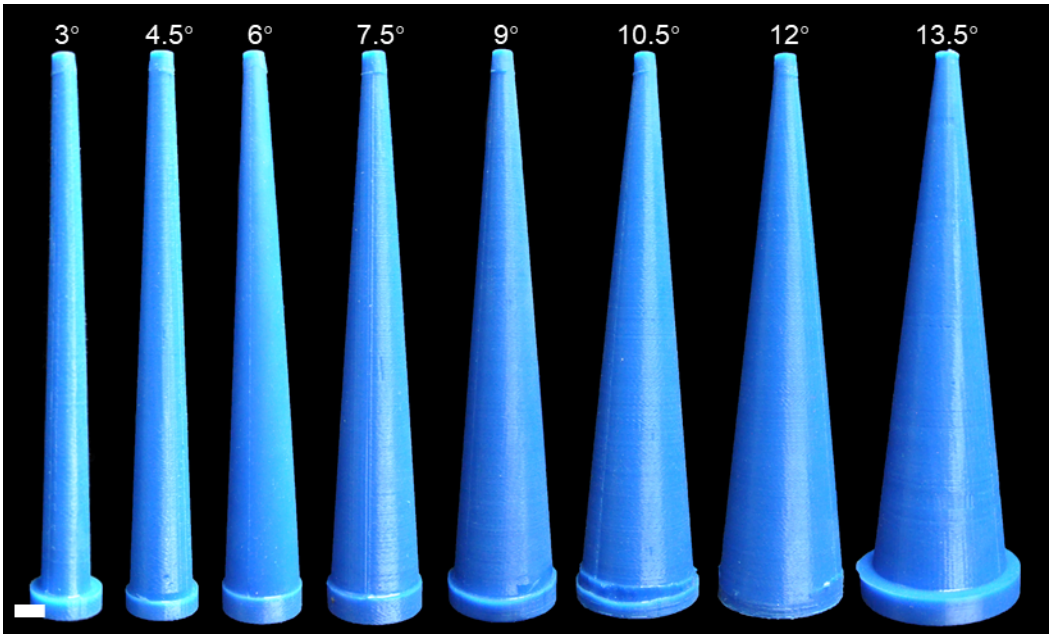

Figure B.5: Tapered soft actuators. Eight tapered soft actuators with taper angle α ranging from 3° - 13.5° were fabricated (scale bar, 10 mm).

To characterize the mechanical response of the silicon rubber used to fabricate our actuators, we tested dogbone-shaped samples (ASTM standard) made out of Mold Star 30 under uniaxial tension. To this end, we used a single-

axis Instron (model 5566, Instron, Inc.) with a 100 N load cell. The material behavior up to a strain of 1.5 (i.e. until failure) is reported in Figure B.6. We find that the material response is nicely captured by an incompressible Gent hyperelastic model (3), whose strain energy is given by

$$W = -\frac{\mu J_m}{2}\ln\left(1-\frac{I_1-3}{J_m}\right), \quad \text{[B.12]}$$

where μ is the initial shear modulus of the material, J_m is a constant related to the limiting stretch, and I_1 is the first invariant of the three principal stretch ratios λ_1, λ_2, and λ_3

$$I_1 = \lambda_1^2+\lambda_2^2+\lambda_3^2 \quad \text{[B.13]}$$

The principal nominal stresses s_i can then be obtained as a function of W, λ_i, and the Lagrange multiplier p as

$$s_i = \frac{\partial W}{\partial \lambda_i} - \frac{p}{\lambda_i} \quad \text{[B.14]}$$

Considering a sample subjected to uniaxial stress state and letting the stretch along the axis of loading be $\lambda_1 = \lambda$, incompressibility ($\lambda_1\lambda_2\lambda_3 = 1$) dictates that the stretches in the directions transverse to the loading axis are

$$\lambda_2 = \lambda_3 = \lambda^{-1/2} \quad \text{[B.15]}$$

Next, since there is no stress in the directions transverse to the loading axis

$$s_2 = s_3 = \frac{\partial W}{\partial \lambda_2} - \frac{p}{\lambda_2} = \frac{\mu J_m}{-\lambda^2-2\lambda^{-1}+J_m+3}\cdot\lambda^{-\frac{1}{2}} - \frac{p}{\lambda^{-\frac{1}{2}}} = 0 \quad \text{[B.16]}$$

we find that

$$p = \frac{\mu J_m}{-\lambda^2 - 2\lambda^{-1} + J_m + 3} \cdot \lambda^{-1} \qquad [B.17]$$

By combining equation [B.14] with [B.17], we get:

$$s_1 = \frac{\partial W}{\partial \lambda_1} - \frac{p}{\lambda_1} = \frac{\mu J_m}{-\lambda^2 - 2\lambda^{-1} + J_m + 3}(\lambda - \lambda^{-2}) \qquad [B.18]$$

where the stretch l is related to the applied strain e as $\lambda = 1 + \varepsilon$. Finally, we fit equation [B.18] to our measured stress-strain data, and find that the material response is best captured with μ = 195 kPa and J_m = 12 (see Figure B.6).

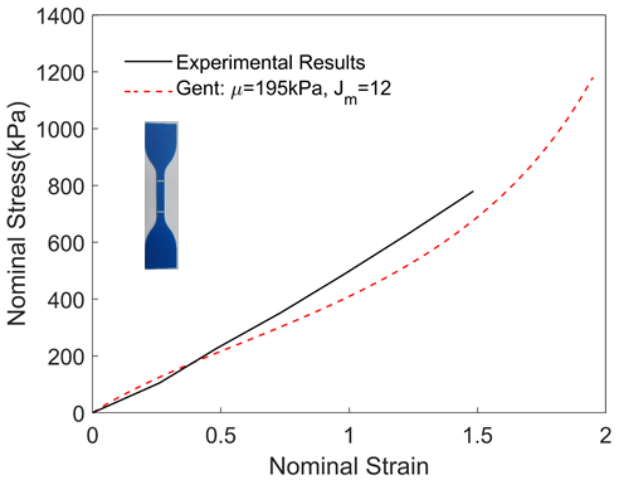

Figure B.6: Material behavior. Stress-strain curve for Mold Star 30 as measured in experiments (continuous line) and predicted using a Gent hyperelastic material model (dashed line).

B.4 Experiments on Tapered Soft Actuators without Suckers

B.4.1 Bending Curvature

We first began by investigating the effect of the taper angle on bending curvature (note that these experiments were performed on actuators without suckers). Two representative actuators characterized by α = 6° and α = 10.5° (for

both actuators $K = 2$) were pressurized from $P = 0$ kPa to $P = 200$ kPa while holding their bottoms fixed. During inflation, at every 2 kPa increment we took a photograph of the deformation of the actuators, which we processed to extract the minimum, maximum, and average curvatures along the length. Specifically, for each photograph we identified the line running along the inner gripping side of the actuator (shown in red in Figure B.7) and divided it into 40 equally-sized segments. For the i-th segment we then determined the radius R_i of the circle that best fits its bent shape and calculated its average curvature as $\kappa_i = 1/R_i$ (see Figure B.7). Remarkably, we find that, in contrast to the case of cylindrical soft actuators, the bending curvature varies along the length of the tapered actuator – a feature that may facilitate grasping differently sized objects. In Figure B.8 we report the evolution of the maximum, minimum, and average curvatures as a function of the applied pressure for the two fabricated actuators. We find that the curvature increases as taper angle decreases.

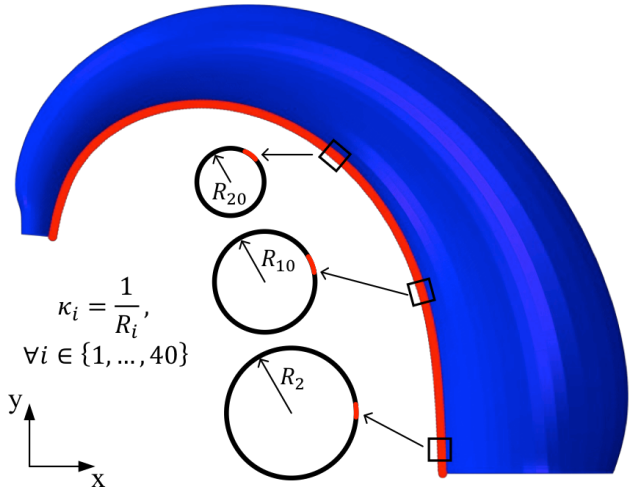

Figure B.7: Curvature (α = 10.5° tapered actuator). Schematic highlighting the procedure used to calculate the bending curvature along the length of the tapered actuator.

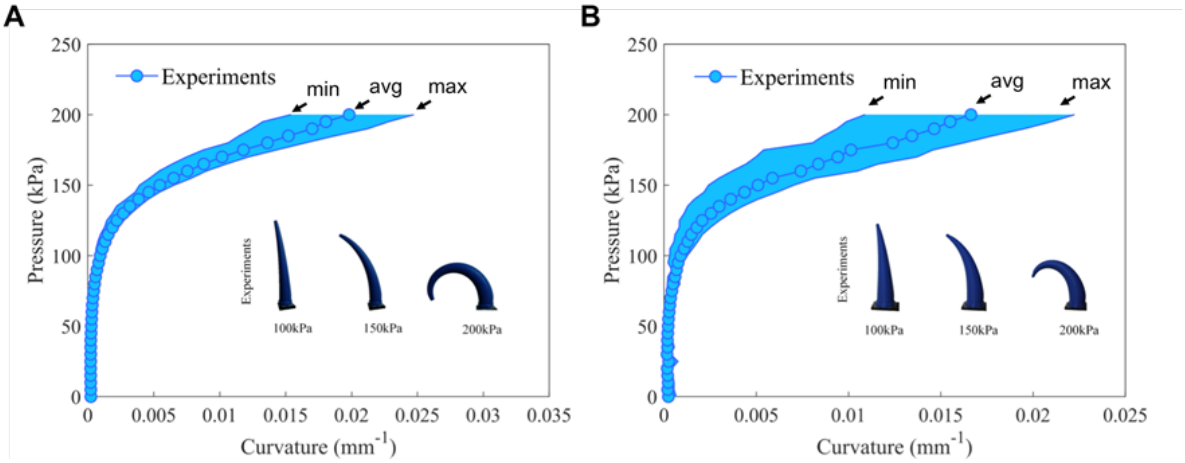

Figure B.8: Experimental results of bending curvature for α = 6° and α = 10.5° tapered actuators. Experimental minimum, average, and maximum curvatures as a function of pressure for tapered actuators characterized by **(A)** α = 6° and **(B)** α = 10.5°. The snapshots of the deformed actuator at different pressures (P = 100 kPa, 150 kPa, and 200 kPa) are shown as insets.

B.4.2 Bending Force Measurements

Next, we measured the force applied by the actuators upon inflation. To do this, eight actuators with taper angles α = 3°, 4.5°, 6°, 7.5°, 9°, 10.5°, 12°, and 13.5° were tested using the setup shown in Figure B.9*A*. Specifically, each actuator was fixed at its base and placed at a distance d from a six-axis force transducer (Mini 40 F/T sensor, ATI Technologies Inc., USA). When the actuator would bend upon pressurization, the tip would press against the force transducer to create a tip force, which was acquired by a data acquisition board (PCI 6284, National Instruments Corp., TX, USA) and LabVIEW (National Instruments Corp., 2012) with a sampling frequency of 1000 Hz. For each of the 8 actuators, experiments (N = 5 trials) were conducted for d = 10 mm, 20 mm, 30 mm and 40 mm with pressure input ranging from P = 0 kPa to P = 200 kPa. The experimental results reported in Figure B.9*B*-*E* show that for all considered horizontal distances d the bending force increases as both pressure and taper angle increase.

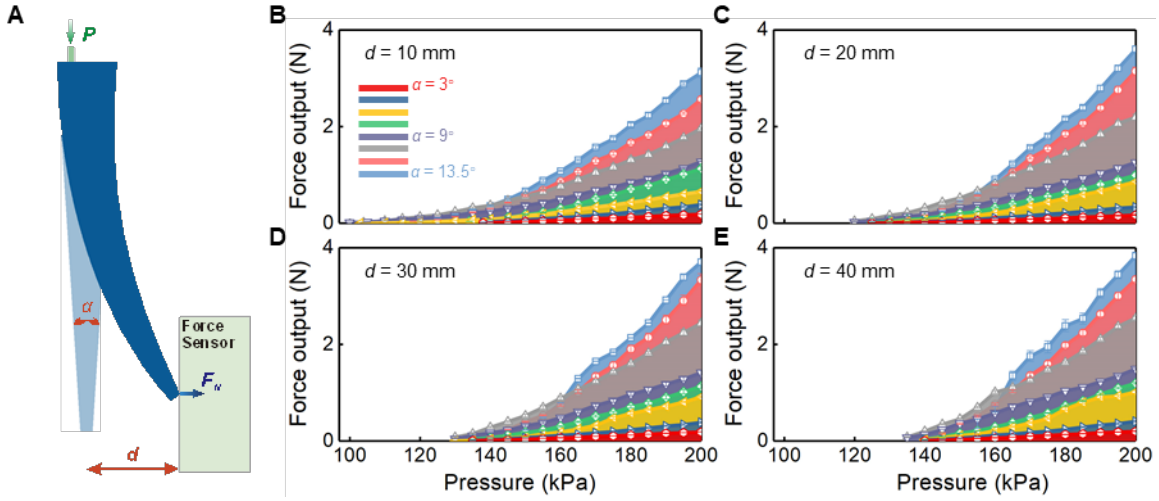

Figure B.9: Experimental results of bending force measurements. (A) Schematic of the setup used to measure the bending force. **(B)-(E).** Bending force as a function of the applied pressure for soft

actuators with different taper angle α (3° to 13.5° with an interval of 1.5°) located at distance **(B)** d = 10 mm, **(C)** d = 20 mm, **(D)** d = 30 mm and **(E)** d = 40 mm from the force sensor.

B.5 Numerical Simulations

To evaluate the effect of the taper angle on the response of the designed soft actuators (without suckers), static non-linear finite element (FE) simulations were carried out using Abaqus/Standard (SIMULIA, Providence, RI), a commercial finite element software. The models were constructed using 8-node linear brick elements (Abaqus element type C3D8H), and the Gent hyperlastic material model (3) (implemented via a UHYPER user subroutine) was used to capture the material response.

B.5.1 Simulating Bending in Free Space

We started by numerically investigating the effect of the taper angle on the bending curvature. In these simulations, the same procedure as the experiments was carried out: the bottom of the actuator was held fixed, a pressure load ranging from P = 0 kPa to P = 200 kPa was applied to the inner chamber, and the minimum, maximum, and average curvatures along the length of the actuators were measured at every 2 kPa (using the same procedure as in experiments). To validate our finite element simulations, we first compared the numerical results to the experimental data shown in Figure B.8. Remarkably, we find that the FE simulation model agrees well with the experimental results obtained from the fabricated actuators (see Figure B.10).

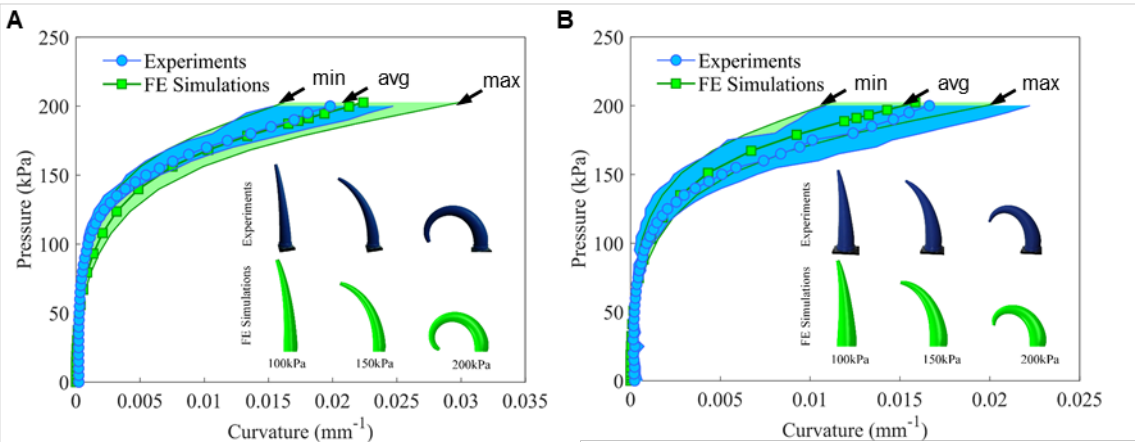

Figure B.10: Comparisons between numerical and experimental results for the bending curvature of the α = 6° and α = 10.5° actuators. Experimental (blue) and numerical (green) minimum, average, and maximum curvatures as a function of pressure for tapered actuators characterized by **(A)** α = 6° and **(B)** α = 10.5°. The snapshots of the deformed actuators at different pressures (P = 100 kPa, 150 kPa, and 200 kPa) are shown as insets.

With the simulations matching the experiments well, numerical modeling could then be carried out to completely and rapidly explore the parameter design space. From exploring this parameter space via FE, we found that the bending curvature of the tapered actuator (including min., avg. and max. κ) depended highly on both the taper angle α and the pneumatic pressure P (Figure B.11*A*-*C*). For a given chamber placement (K = 2), we find that the bending curvature increases as pressure P increases, but decreases as the taper angle α increases. For example, the average bending curvature (κ) decreased by over 2-fold (from κ = 0.0282 mm^{-1} to κ = 0.0134 mm^{-1}) by varying the taper angle from α = 3° to α = 13.5° at P = 200 kPa, and changed from κ = 0.0009 mm^{-1} to κ = 0.0134 mm^{-1} by increasing the pneumatic pressure from P = 100 kPa to P = 200 kPa for α = 13.5°.

We also numerically investigated the effect of K (i.e. chamber placement) on the bending curvature by considering an actuator with α = 9°. The results

shown in Figure B.11*D-F* indicate that the bending curvature increases with larger values of K (i.e. for chambers closer to the outer edge of the actuators – see Figure B.11*D-F*). For example, the average bending curvature (κ) increased roughly 4-fold (from κ = 0.0075 mm^{-1} to κ = 0.0312 mm^{-1}) by varying chamber placement K from 1.75 to 2.5 at P = 200 kPa.

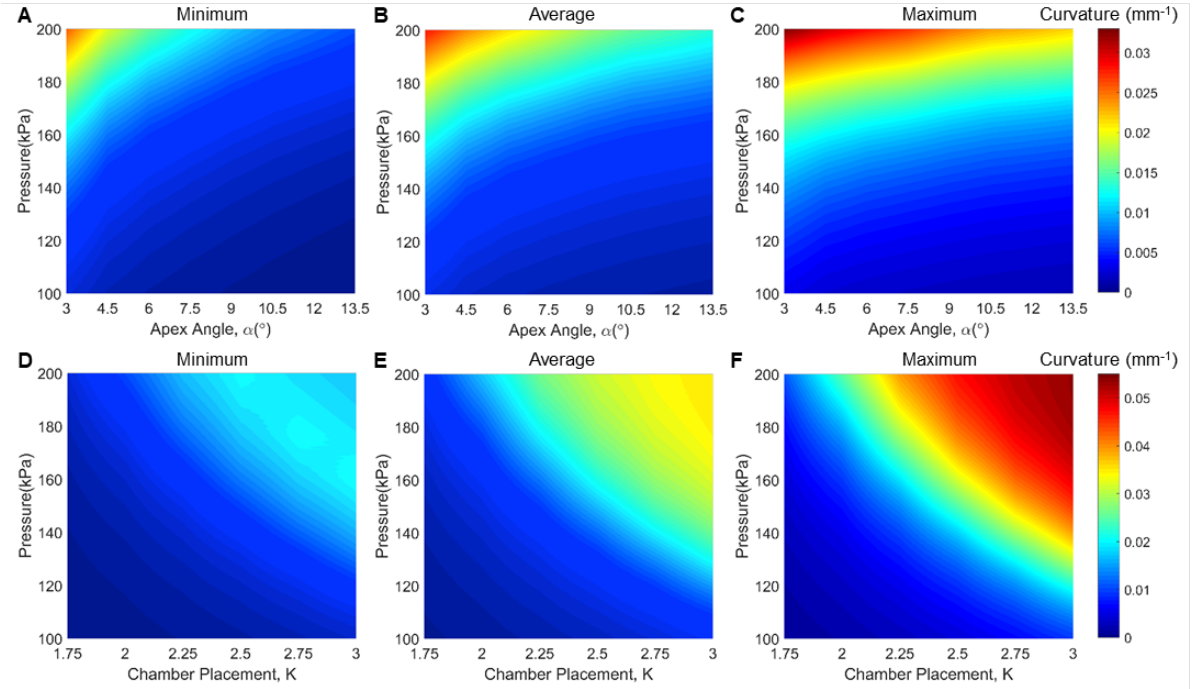

Figure B.11: Simulation results of bending curvature of the tapered soft actuators. Heat map illustrating the minimum **(A)**, average **(B)** and maximum **(C)** bending curvature (κ) as a function of taper angle (α) and input pressure (P), and heat map illustrating the minimum **(D)**, average **(E)** and maximum **(F)** bending curvature (κ) as a function of the chamber placement (K) and input pressure (P).

B.5.2 Simulating Bending Force

We also investigated numerically the effect of the tapering angle a on the applied bending force. In these simulations the bottom end of the actuator was held

fixed, a pressure load was applied to the surface of the inner chamber (each actuator was pressurized from P = 0 kPa to P = 200 kPa), and the actuators were placed at a horizontal distance (d = 30 mm) away from a rigid body surface. This rigid body surface acted as a hypothetical load cell upon which the actuator could bend and apply force to. Frictional surface to surface contact (coefficient of friction of 0.5) was employed between the rigid body surface and the actuator. As input pressure into the actuator was increased, the actuator would bend towards and apply force to the hypothetical load cell. As shown in Figure B.12, the simulated bending force agrees well with the experimental results obtained from the fabricated actuators. Both the simulated and experimental results indicate that the bending force of the tapered actuator depends highly on both the taper angle α and pneumatic pressure P. Specifically, the bending force increases as pressure P increases and as the taper angle α increases.

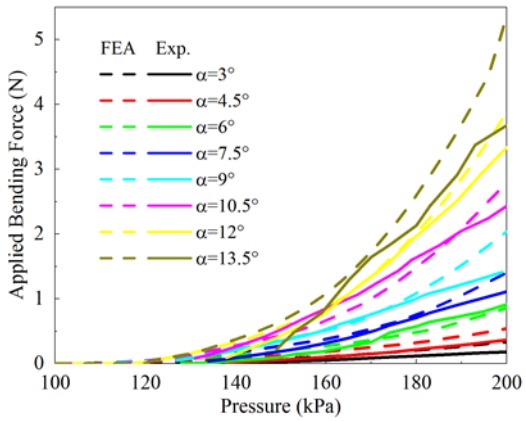

Figure B.12: Comparisons between the numerical and experimental bending forces. Experimental (solid lines) and numerical (dashed lines) results for applied bending force as a function of pressure (up to P = 200 kPa) for 8 taper angles. As can be seen from the plot, the numerical bending force results match the experimental results well.

B.6 Fabrication of the Tapered Soft Actuator with Suckers

A multi-step molding and casting process was used to fabricate the tapered soft actuator with suckers (Figure B.13). As described in section B.3, the molds for the casting process were designed in SolidWorks and printed using a 3D printer. The difference between the fabrication process of the actuator with suckers and without suckers is the following: when fabricating with suckers, holes were left on the outer tapered actuator mold and threaded with silicone tubes for use in the sucker vacuum generation (Figure B.13*A*).

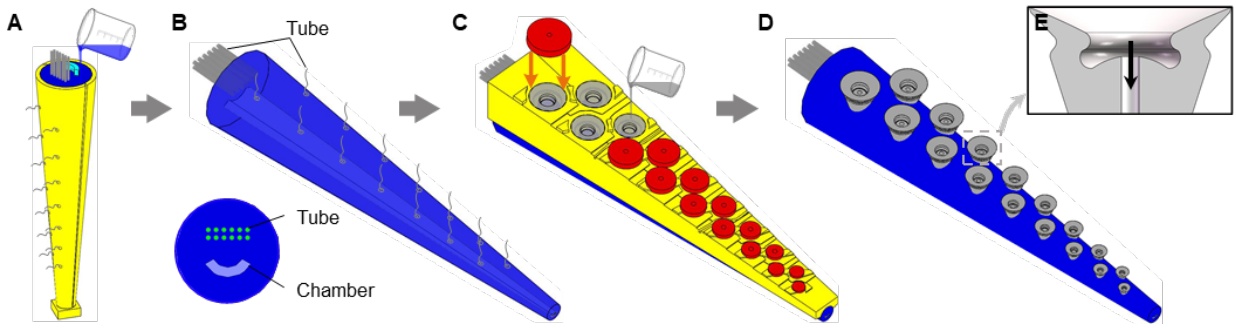

Figure B.13: Fabrication process of the tapered soft actuator with suckers. (A) 3D printed molds are used to cast the robot using elastomer Mold Star 30. **(B)** The cured soft actuator has silicone tubes embedded inside, which were ultimately used to apply a vacuum to the suckers. The cross-sectional view shows the arrangement of the inner chamber and silicone tubes within the actuator. **(C)** A 3D printed mold for the suckers is assembled on the actuator and elastomer was poured into the mold. Then, 3D printed caps were laid on the mold to create the shape of the suckers as the elastomer cured. **(D)** The fully cured tapered actuator with suckers was then complete. **(E)** A cross-sectional view of the suction cup is shown. The aforementioned silicone tubes were embedded within each of the suckers to apply a vacuum (the arrow indicates the vacuum air flow).

As done before for the fabrication without suckers, after curing, the tapered mold and rod were removed, which created a core used for the actuator's inner pneumatic chamber. Additionally, the previously mentioned silicone tubes

(for vacuum suction) were left embedded inside the robot (Figure B.13*B*). Next to fabricate the suckers onto the actuator with embedded silicone tubes, a 3D-printed mold for casting the suckers was attached to the inside surface of the actuator and tightened to avoid leakage of the fluidic elastomer. Silicone elastomer with Young's modulus of 0.25 MPa (Dragon Skin FX-Pro, Smooth-On Inc., PA) was dyed grey with a coloring agent (Ignite, Smooth-On Inc., PA) and then poured into the mold (Figure B.13*C*). The elastomer used for the suckers was much softer than that used for the actuator to ensure the flexibility of the suckers. Caps were designed and 3D-printed to fit each sucker's inner infundibulum shape, and a hole was left in the center for a silicone tube to pass through. These caps were placed onto the freshly poured elastomer to create the shape of the suckers and threaded with the silicone tubes previously left in the mold (Figure B.13*C*). The elastomer was left for 40 minutes at room temperature to cure. After the elastomer cured, the molds were removed. The exposed excess silicone tubes coming out of the suckers were trimmed with scissors, and the robot was fully sealed with adhesives (Sil-Poxy, Smooth-On Inc., PA) (Figure B.13*D*). The fully fabricated tapered soft actuators with suckers are shown in Figure B.14.

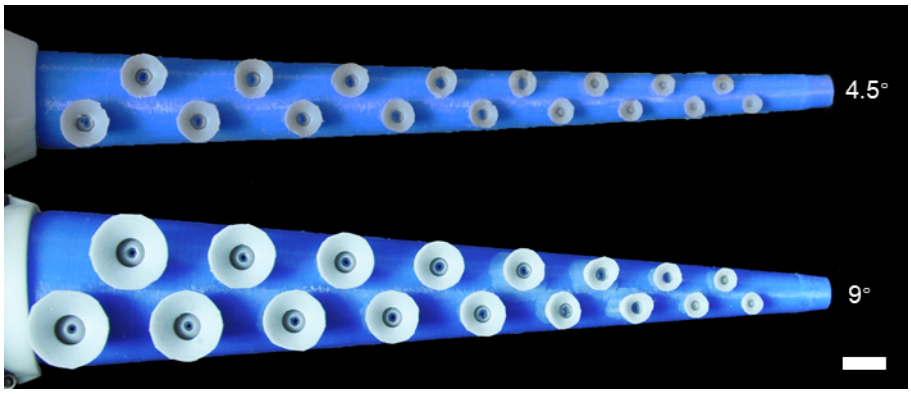

Figure B.14: Two tapered soft actuators with suckers with taper angle α = 4.5° and α = 9° (scale bar, 10 mm).

After that, 3D-printed clamps were mounted on the actuator, and two air connectors are left for the actuation of bending and suction, respectively. Moreover, to improve the human-machine interface, we developed an integrated hand-held controller to allow simple manipulation of the tapered soft actuator with suckers. Two on-off valves and a vacuum generator were placed in a 3D-printed bulb-shaped shell (60 mm in diameter). Two buttons were installed on the handle to independently control the bending and suction (Figure 5.5*B*).

The fabricated α = 9° tapered soft actuator with suckers was actuated at a pressure of P = 200 kPa and compared with α = 9° tapered actuator without suckers actuated at the same pressure. The results show no distinct difference between the bending of the α = 9° tapered actuator with and without suckers (Figure B.15). This result demonstrates that the fabricated suckers do not alter the actuator's bending during pressurization.

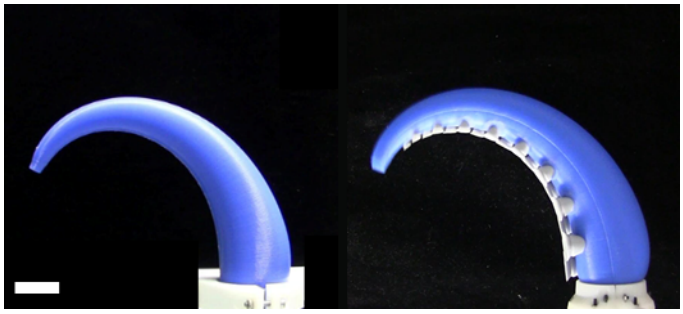

Figure B.15: Bending comparisons between actuators with suckers and without suckers at P = 200 kPa. This result demonstrates that the suckers do not alter the actuator's bending during pressurization (scale bar, 2 cm).

B.7 Sucker Attachment Force Measurements

In this section, we detail the sucker attachment force measurements for the α = 4.5° and α = 9° tapered actuators with suckers. We investigated the engagement of the suckers on three planar surfaces of different roughnesses (R_a < 1 µm, 20 µm, 200 µm) as well as one curved surface of roughness R_a < 1 µm.

B.7.1 Experimental Substrates

Four surfaces (three planar surfaces of increasing roughness: R_a < 1 µm, 20 µm, 200 µm, and then also one smooth surface, R_a < 1 µm, with a curvature of 1/260 mm^{-1}) were used in this study. To control for the effects of material stiffness, wettability, surface chemistry, and temperature, and to focus on the effect of surface roughness alone on adhesion with the suckers, the surfaces were all fabricated with the same epoxy resin material (EpoxAcast 650, Smooth-On Inc., PA, USA).

We first created the substrate surface with R_a ~20 µm roughness. A female die was made from Dragon Skin 20 with a cast of sandpaper with the

desired roughness (FEPA Grit designation P600, corresponding to an average particle diameter of ~20 μm). Next, casting epoxy was poured into the female die, allowed to cure for 24 hours, and removed from the die. Then, the same procedure was used to create another substrate surface with a roughness around R_a ~200 μm (with FEPA Grit designation P80 sandpaper, corresponding to an average particle diameter of ~200 μm). Finally, the smooth flat substrate surface (R_a < 1 μm) was created with a mold made from glass. The three flat substrates were then fastened to a 3D-printed plastic base plate fixed onto a force transducer to measure suction force (Figure B.16*A*).

For the smooth surface with a curvature of 1/260 mm^{-1}, casting epoxy was poured into the glass mold as done before for the flat surface and allowed to cure for 12 hours, after which the substrate surface was semi-solidified. Then the substrate was removed from the glass mold and laid on a 3D-printed plastic base plate with curvature of 1/260 mm^{-1}. Because of its semi-solidified state, the substrate surface cured over the next 12 hours to the same curvature as that of the plastic base plate (1/260 mm^{-1}). The curved substrate was also fastened to the 3D-printed base plate and fixed to the force transducer.

B.7.2 Experimental Setup for Measuring Sucker Attachment Force

To measure the actuator's sucker attachment force, we designed and built the system shown in Figure B.16*A*. A six-axis ATI force transducer (Mini 40 F/T sensor, ATI Technologies Inc., USA) was mounted on the ground with its *z*-axis parallel to the ground. A 3D-printed plastic base was fixed on the force transducer

with one of the four substrate surfaces (whichever was currently being tested) fastened to it. The actuator was then mounted with its base fixed to a robotic arm (MOTOMAN MH3F, YASKAWA Inc., Japan). For the suction force measurements on the three flat surfaces, the actuator's suckers were positioned parallel to the substrate, the tapered actuator was not inflated and only the sucker vacuum (-80 kPa) was applied to attach to actuator to the substrates (the initial position of the robotic arm is shown in Figure 5.4*A*). For the curved surface measurements, the actuator's bottom sucker was initially positioned tangent to the edge of the substrate (Figure 5.4*E*). The tapered actuator was subsequently pressurized (P = 0 kPa to P = 240 kPa with an interval of 10 kPa) to adapt to the substrate curvature, and the sucker vacuum (-80 kPa) was then applied (Figure 5.4*D*, inserted schematic). The robotic arm was programmed to move vertically upwards at a constant speed of 0.1 mm/s until the suckers completely lost contact with the substrate surface. For each experiment, N = 3 trials were conducted to produce an error measurement. The force data were acquired by a data acquisition board (PCI 6284, National Instruments Corp., TX, USA) and LabVIEW (National Instruments Corp., 2012) with a sampling frequency of 1000 Hz.

B.7.3 Results of the Sucker Attachment Force Measurements

Figures B.16*B,C* show the force time histories of the α = 9° and α = 4.5° actuator peeling-off from flat surfaces with different roughnesses (R_a < 1 μm, 20 μm, 200 μm). They all resulted in a post-yield stairstep-like failure mode, and the peeling-off process of the α = 4.5° actuator from its base on the smooth flat

surface are provided in Figures B.16*D,E* (the results for the $\alpha = 9°$ acutator are all shown in Figure 5.4). Just as was the case with the $\alpha = 9°$ actuator as discussed in the main text, the $\alpha = 4.5°$ actuator was also able to successfully attach to surfaces exhibiting a wide range of surface roughnesses and the results are shown in Figure B.16. The $\alpha = 4.5°$ actuator required a pull-off force of 1.31 ± 0.08 N on a smooth surface, 1.86 ± 0.09 N on a medium-roughness surface (R_a = 20 μm), and 0.81 ± 0.06 N on a rough surface (R_a = 200 μm) (Figure B.16*F*).

Additionally, we chose one of the actuators ($\alpha = 9°$) and changed the material used to fabricate its suckers. We found that the sucker force could be further enhanced by increasing the sucker modulus. The $\alpha = 9°$ actuator with stiff suckers (Young's modulus 660 kPa) generated a considerable pull-off force of up to 26.14 ± 0.54 N (error values are ± SEM) on a smooth surface ($R_a < 1$ μm), 19.52 ± 0.31 N on a medium-rough surface (R_a = 20 μm), and 2.11 ± 0.29 N on a rough surface (R_a = 200 μm). With soft suckers (Young's modulus 260 kPa) the $\alpha = 9°$ actuator produced 6.59 ± 0.32 N on a smooth surface, 8.43 ± 0.35 N on a medium-rough surface (R_a = 20 μm), and 3.12 ± 0.50 N on a rough surface (R_a = 200 μm) (Figure B.16*F*).

Finally, we also investigated the effects of bending on the adhesive performance of the $\alpha = 4.5°$ actuator on a curved surface (1/260 mm^{-1}) under different pneumatic pressures, the results from which, can be found in Figure B.16*G*. Similar to the $\alpha = 9°$ actuator (as shown and discussed in the main text), the attachment of the $\alpha = 4.5°$ actuator to the surface is highly dependent on the pressure input since this determines how many suckers engage to the surface.

After determining the optimal pressure (P = 130 kPa) for this combination of actuator and surface curvature (Figure B.16*G*), then this pressure was used to obtain the results shown in Figures B.16*H,I*. Looking at these pull-off force results, we see that the actuator can achieve a pull-off force similar on both flat (1.31 ± 0.08 N) and curved surfaces (1.85 ± 0.05 N), as all suckers made full contact with both surfaces (Figures B.16*D,E* and S16*H,I*).

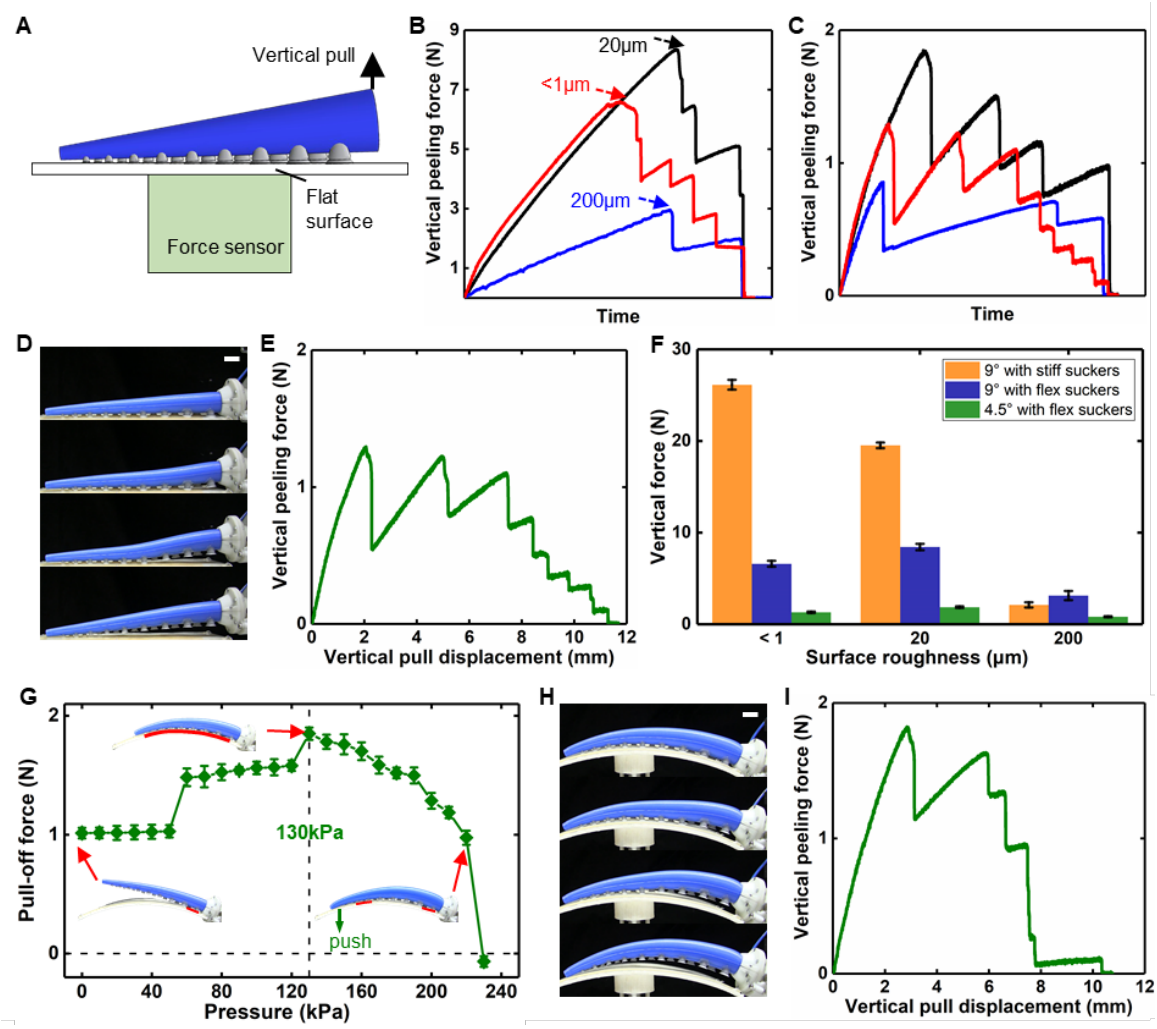

Figure B.16: Attachment force comparisons between the α = 4.5° and α = 9° actuators with suckers against different surfaces. (A) Experimental setup schematic of sucker attachment force measurements. The force sensor was mounted on the ground. A 3D printed plastic base was fixed on the force sensor with the substrate surfaces fastened on it. We set the initial position of the actuator to ensure the suckers attachment on the surface. A robotic arm fixed to the base of the

actuator was programmed to move straight upwards at a constant speed of 0.1 mm/s until the suckers completely detached from the substrate surface. Vertical peeling forces plotted against time of (B) $\alpha = 9°$ actuator and (C) $\alpha = 4.5°$ actuator on surfaces of various roughness (R_a: < 1 μm, 20 μm, 200 μm). Side-view photographs (D) showing the sequential pull-off of an $\alpha = 4.5°$ actuator with its suckers actuated from a smooth planar surface and its corresponding load-displacement curve (E). (F) The attachment forces of the $\alpha = 9°$ actuator with stiff suckers (Young‘s Modulus: 660 kPa) and flexible suckers (Young's Modulus: 260 kPa) and $\alpha = 4.5°$ actuator with flexible suckers on planar surfaces of various roughness (R_a: < 1 μm, 20 μm, 200 μm). Scanning a wide range of input pressures with the $\alpha = 4.5°$ actuator permits the identification of the optimal input pressure (and therefore curvature) for maximizing pull-off force from non-planar substrates (G). The vertical dashed line indicates the “critical” pneumatic pressure values for maximizing the pull-off forces of the $\alpha = 4.5°$ actuator for the curvature of this specific surface (260 mm^{-1}). Side-view photographs showing the sequential pull-off of an $\alpha = 4.5°$ actuator with its suckers actuated from a smooth curved surface (H) and its corresponding load-displacement curve (I), which is very similar to that shown in (E).

B.8 Tapered Actuator Demonstrations

Figure B.17 shows the inflation and vacuum pressures time series of the tapered actuator during a semi-autonomous “attach, wrap, transport, and deliver” process as discussed in the main text. As Figure 5.5*A* shows, the $\alpha = 4.5°$ actuator was mounted on the robotic arm. Starting with the non-pressurized $\alpha = 4.5°$ tapered soft actuator with suckers (t = 0 s), firstly the robotic arm was programed to reach the plastic sheet and a -60 kPa vacuum was applied to the suction cups (t = 2 s). Once the suckers were attached to the plastic sheet, the vacuum pressure rapidly raised to -80 kPa (t = 4 s), and the system detected the pressure change from the suckers. Then, a 2-second time delay is set for the robotic arm to lift up the attached plastic sheet. The actuator was then pressurized (P = 250 kPa) to “wrap” the sheet into a roll (t = 6.5 s). After that, the robotic arm transported the

sheet quickly (t = 8 s) in a programmed trajectory and then delivered it to a human hand at t = 12 s (the vacuum and inflation pressure returned to P = 0 kPa at this time). In this process, the suckers not only worked to assist grasping, but also acted as feedback elements for the control system. Based on this pressure sensory feedback principle, the tapered actuator with suckers can achieve more significant application in industry, especially applications involving human interaction.

Next, we were interested in the bending kinematics and velocity of the actuators with suckers. Based on the tradeoff (between bending curvature and applied bending force) as a function of taper angle we presented earlier, the α = 4.5° and α = 9° actuators show obvious different characteristics. To compare the bending kinematics and velocity of actuators with different taper angles, we actuated each actuator (α = 4.5° and α = 9°) with a miniature compressor (LRMA-QS-4, FESTO Inc), which delivered compressed air at a maximum flow rate of 40 L/min (Movies S4 and S5). This compressor fully bent to the α = 9° actuator in 1.2 ± 0.11 seconds (N = 5) and the α = 4.5° actuator in 0.3 ± 0.06 seconds (N = 5). Figure B.18*A* shows snapshots taken from movies (Movies S6 and S7) of the two actuators bending. The α = 4.5° actuator showed an interesting and potentially useful spiral bending behavior with the tip of the actuator curling past its own base.

It should be noted that the spiral shape is due to the actuator's taper angle, whereas a traditional cylindrically-shaped actuator self-intervenes by coming into contact with its own base at high pressures (Figure B.19). However, despite the bending kinematics and velocity, the α = 9° actuator has an advantage in the

grasping force on the other hand. As shown in Figure B.18*B*, we actuated the α = 9° actuator at a pressure of P = 250 kPa, and the α = 9° actuator was able to lift a bucket of water weighing up to 27 N — over 24 times the weight of the prototype.

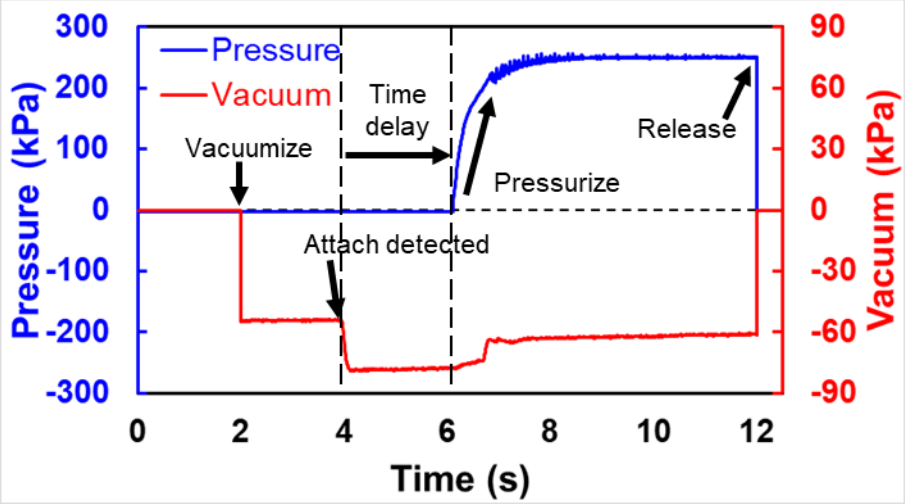

Figure B.17: The inflation and vacuum pressures as a function of time during the "attach, wrap, transport, and deliver" process. Starting with the non-pressurized α = 4.5° tapered soft actuator with suckers (t = 0 s), a vacuum was applied to the suction cups firstly (t = 2 s), the system detected the pressure change from the suckers at t = 4 s, after 2-seconds' time delay (time for the robotic arm lifting up the attached plastic sheet) the actuator was then pressurized (P = 250 kPa) to "wrap" the sheet into a roll (t = 6.5 s). After that, the robotic arm transported the sheet quickly (t = 8 s) and then delivered it to a human hand at t = 12 s (the vacuum and inflation pressure returned to P = 0 kPa).

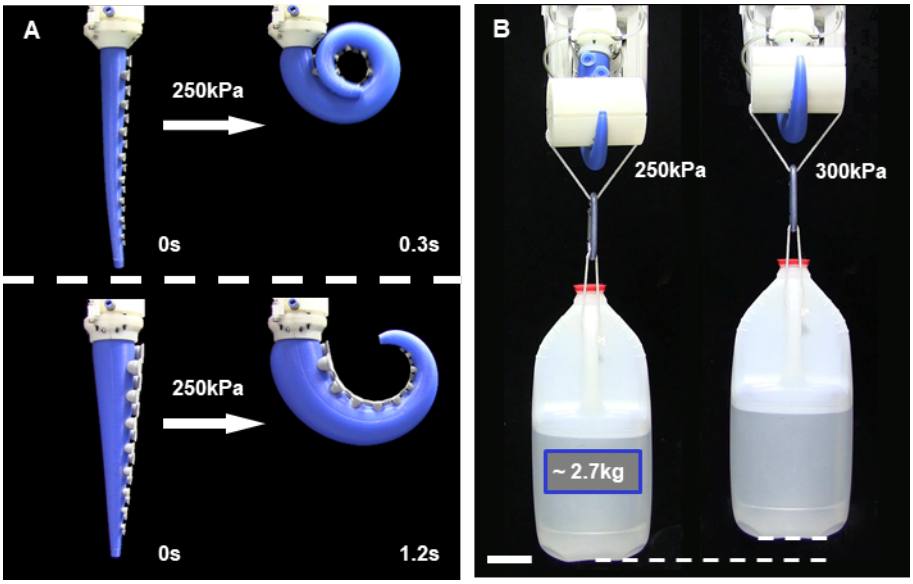

Figure B.18: Motion of $\alpha = 4.5°$ and $\alpha = 9°$ actuators and load capability of $\alpha = 9°$ actuator. (A) High-speed images of the initial and final positions of the actuators when pressurized from $P = 0$ kPa to $P = 250$ kPa. The $\alpha = 4.5°$ actuator bended into a spiral shape (upper) while the $\alpha = 9°$ actuator bended into an arc shape with non-uniform curvature (lower). The $\alpha = 4.5°$ actuator displayed a faster response (t = 0.3 s) than the $\alpha = 9°$ actuator (t = 1.2 s). **(B)** The $\alpha = 9°$ actuator can lift up a weight of 2.7 kg at input pressures of $P = 250$ kPa (left) and $P = 300$ kPa (right) (scale bar, 5 cm).

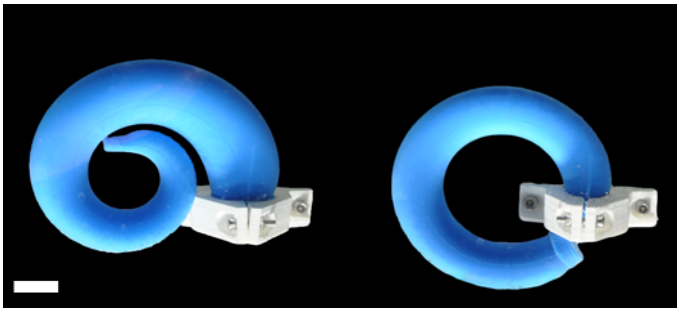

Figure B.19: Bending comparisons: tapered and cylindrically-shaped soft actuator. (scale bar, 2 cm).

B.9 REFERENCES

[1] Martinez, R. V., Branch, J. L., Fish, C. R., Jin, L., Shepherd, R. F., Nunes, R. M., Suo, Z., Whitesides, G. M. (2013). Robotic tentacles with three-dimensional mobility based on flexible elastomers. *Adv. Mater.,* 25, 205-212.

[1] Elsayed, Y., Vincensi, A., Lekakou, C., Geng, T., Saaj, C. M., Ranzani, T., Cianchetti, M., Menciassi, A. (2014). Finite element analysis and design optimization of a pneumatically actuating silicone module for robotic surgery applications. *Soft. Robot.,* 1, 255-262.

[3] Gent, A. N. (1996). A new constitutive relation for rubber, *Rub. Chem. Tech.,* 69, 59-61.